A catalog of variable high-energy gamma-ray sources and prospects for polarization measurement with the *Fermi* Large Area Telescope

Dissertation

zur Erlangung des akademischen Grades

doctor rerum naturalium

(Dr. rer. nat.)

im Fach Physik
Spezialisierung Experimentalphysik

eingereicht an der
Mathematisch-Naturwissenschaftlichen Fakultät
der Humboldt-Universität zu Berlin

von
M. Sc. Matteo Giomi

Präsidentin der Humboldt-Universität zu Berlin:
Prof. Dr.-Ing. Dr. Sabine Kunst

Dekan der Mathematisch-Naturwissenschaftlichen Fakultät:
Prof. Dr. Elmar Kulke

Gutachter: 1. Dr. Gernot Maier, Deutsches Elektronen-Synchrotron, Zeuthen.
2. Prof. Dr. Thomas Lohse, Humboldt-Universität zu Berlin.
3. Prof. Dr Jamie Holder, University of Delaware.

Tag der mündlichen Prüfung: 9. Oktober 2017

A Giada e Mia.

Summary

The *Fermi* Large Area Telescope (LAT) is a space-based pair-conversion telescope sensitive to gamma-rays with energies from $\sim$ 30 MeV to several hundreds of GeV. Observing gamma rays in this energy range, we gain information on the sources and acceleration mechanisms of cosmic rays (CRs) of energies from $\sim$ 1 GeV to $\sim$ 10 TeV. Studying the emission of gamma-ray sources during periods of enhanced activity (flares) provides a sensitive probe of the production mechanisms of CRs, as it makes it possible to investigate the distributions of the freshly-accelerated particles.

The main part of this work presents the latest catalog of variable gamma-ray sources above 100 MeV, the second *Fermi* All-sky Variability Analysis catalog (2FAV). The 2FAV catalog contains more than 4500 flares detected at high significance in the first 7.4 years of LAT observations and the 518 sources from which these flares originate. Probable counterparts, mostly active galactic nuclei (AGN), have been found for 441 sources in the 2FAV. The remaining 77 sources have no reliable counterparts in other gamma-ray or blazar catalogs; they are potentially new gamma-ray sources. Studying the spectra of the 2FAV flares, we observe a harder-when-brighter behavior for the entire sample of flares associated with flat spectrum radio quasars, a class of AGN. We also observe a minimum value in the distribution of the photon index Γ of the flares, corresponding to $\Gamma \gtrsim 1.5$. In a simple leptonic scenario, assuming that the distribution of accelerated particles is isotropic in the source reference frame, this limit on the spectral hardness implies that the spectra of the accelerated particles responsible for the flare is never harder than $dN/dE \propto E^{-2}$.

Another way to probe the environments where CRs are accelerated is by measuring the polarization of the gamma rays. A preliminary study of the LAT sensitivity to linear polarization of astrophysical gamma-rays is presented in the last part of this thesis. In the pair-production regime, linear polarization of the gamma-rays induces a modulation in the azimuthal angle of the planes where the electron-positron pairs are produced. Although not designed as a polarimeter, the LAT has the potential to measure this modulation using low energy ($\lesssim$ 200 MeV) events converting in the silicon detector layers of its tracker. A selection of these events using supervised machine learning algorithms is presented and used as a basis to estimate the statistical and systematic uncertainties affecting the measurement. Considering only statistical uncertainties, a degree of polarization of $\sim 30-50\%$ could be detected at the 5σ confidence level for the Vela pulsar and the Crab pulsar-wind nebula after 10 years of observation. By including systematic uncertainties, a 5σ sensitivity limit corresponding to a polarization degree of $\sim 46\%$ is estimated, using a stack of AGN as an unpolarized test source and comparing the data with detailed Monte Carlo simulations. This analysis addresses for the first time all the steps of a real measurement and can therefore provide the basis for future measurements of gamma-ray polarization with the LAT.

Zusammenfassung

Das *Fermi* Large Area Telescope (LAT) ist ein satellitengestütztes Gammastrahlungs-Teleskop zur Messung von Gammastrahlung im Energiebereich zwischen $\sim$ 30 MeV und mehreren hundert GeV. Der Nachweis extraterrestrischer Gammastrahlung in diesem Energiebereich erlaubt Rückschlüsse auf die astrophysikalischen Quellen der Gammastrahlung und Beschleunigungsmechanismen kosmischer Strahlung mit Energien zwischen 1 GeV und $\sim$ 10 TeV. Die Beobachtung von Quellen während Phasen vorübergehend erhöhter Gammastrahlungsflüsse ('Flares') ermöglicht dabei eine besonders empfindliche Untersuchung der Produktionsmechanismen kosmischer Strahlung in den Quellen, da die Eigenschaften kürzlich beschleunigter Teilchen unmittelbar studiert werden können.

Der Hauptteil dieser Dissertation stellt das neueste Verzeichnis zeitlich variabler Gammastrahlungsquellen über 100 MeV vor, den zweiten 'Fermi All-sky Variability Analysis' Katalog (2FAV). Der 2FAV Katalog enthält über 4500 Flares, welche in den ersten 7.4 Jahren der LAT Datennahme auf einem hohen Vertrauensniveau gemessen und an 518 verschiedenen Himmelspositionen beobachtet wurden. 441 dieser Quellpositionen im 2FAV können Aktiven Galaktischen Kernen (AGN) zugeordnet werden. Die verbleibenden 77 Quellpositionen besitzen keine sichere Entsprechung in anderen Verzeichnissen von Gammastrahlungs- oder Blazarquellen und stellen möglicherweise neue Gammastrahlungsquellen dar. Bei der Untersuchung der Spektren der 2FAV Flares, welche sogenannten 'Flat-Spectrum' Radioquasaren (FSRQ) - eine Unterklasse der AGN - zugeordnet werden können, wurde durchweg ein härteres Gammastrahlungsspektrum während Phasen erhöhter Gammastrahlungsemission beobachtet. Zudem wurde eine Untergrenze in der Verteilung der spektralen Exponenten, $\Gamma \gtrsim 1.5$, in der Stichprobe der untersuchten Flares festgestellt. Unter der Annahme eines einfachen leptonischen Modells und dass die Verteilung beschleunigter Teilchen im Inertialsystem der Quelle isotrop ist, folgt daraus, dass die Energiespektren der kosmischen Strahlung, welche die Gammastrahlungs-Flares verursachen, mit $dN/dE \propto E^{-2}$ oder stärker abfallen.

Eine andere Möglichkeit, die Beschleunigungsmechanismen kosmischer Strahlung zu untersuchen, ist die Messung der Polarisation der begleitenden Gammastrahlung. Der letzte Teil dieser Dissertation enthält eine vorläufige Studie zur Messbarkeit linearer Polarisation astrophysikalischer Gammastrahlung mit dem LAT-Instrument. Bei Konversion hochenergetischer Photonen in Elektron-Positron-Paare verursacht eine lineare Polarisation der Gammastrahlung eine Modulation des Azimutwinkels der Ebenen, in denen die Elektron-Positron-Paare erzeugt wurden. Obwohl der LAT ursprünglich nicht als Polarimeter konzipiert wurde, ermöglicht das Instrument eine Messung dieser Modulation für niederenergetische Primärteilchen ($\lesssim 200$ MeV), welche in den Silikonschichten des Detektors konvertieren. Eine Auswahl solcher Ereignisse, selektiert durch Algorithmen überwachten maschinelles Lernens ('supervised machine learning'), wird verwendet um die statistischen und systematischen Messunsicherheiten abzuschätzen, denen eine Messung unterworfen ist. Werden allein statistische Unsicherheiten berücksichtigt, ist der LAT in der Lage, einen Polarisationsgrad von 30$-$50% der Gammastrahlungsflüsse vom Vela-Pulsar und vom Krebs-Pulsarwindnebels nach einer Beobachtungszeit von zehn Jahren auf einem Vertrauensniveau von 5σ nachzuweisen. Werden zusätzlich systematische Unsicherheiten berücksichtigt, wird abgeschätzt, dass ein Polarisationsgrad von $\sim$ 46% auf einem Vertrauensniveau von 5σ nachweisbar ist, indem eine Auswahl von AGN als unpolarisierte Testprobe verwendet und mit umfangreichen Monte-Carlo Simulationen verglichen wird. Die Analyse in dieser Dissertation berücksichtigt zum ersten Mal sämtliche Aspekte einer polarization-sensitiven Ereignissrekonstruktion und dienst damit als Grundlage für zukünftige Nachweisversuche der Polarisation astrophysikalischer Gammastrahlung mit dem LAT.

Contents

Summary **v**

Zusammenfassung **vii**

1 Physics of gamma-ray astronomy **1**
1.1 Particle acceleration at the sources . . . 3
1.1.1 Diffusive shock acceleration . . . 3
1.1.2 Magnetic reconnection . . . 6
1.2 Radiative processes: from cosmic rays to gamma rays . . . 8
1.3 Simple radiative models . . . 15

2 Observing high-energy gamma rays **19**
2.1 Detection principle . . . 20
2.2 The Fermi Large Area Telescope . . . 23
2.2.1 Design . . . 24
2.2.2 From trigger to high-level science data . . . 26
2.2.3 Response functions . . . 27
2.2.4 Observations . . . 29

3 The high-energy gamma-ray sky **31**
3.1 Taxonomy of gamma-ray sources . . . 33
3.1.1 Galactic . . . 34
3.1.2 Extragalactic . . . 37
3.2 Variability in gamma-rays . . . 40
3.2.1 Flux Variability . . . 41
3.2.2 Spectral Variability . . . 43

4 The Second Fermi All-sky Variability Analysis Catalog **47**
4.1 Introduction . . . 48
4.2 FAVA analysis . . . 49
4.2.1 Photometric all-sky search . . . 49
4.2.2 Likelihood follow-up analysis . . . 52
4.2.3 Angular resolution and sensitivity . . . 57

4.3 Construction of the catalog . . . 58
4.3.1 Flare selection . . . 60
4.3.2 Sensitivity . . . 61
4.3.3 Clustering of the flares . . . 64
4.3.4 Association procedure . . . 69
4.4 The second FAVA catalog . . . 71
4.4.1 Likely counterparts . . . 73
4.4.2 Unassociated sources . . . 79
4.4.3 Comparison with the 1FAV . . . 80
4.5 2FAV flare spectra . . . 81
4.5.1 Blazars . . . 83
4.5.2 Non-blazar sources . . . 86
4.6 Outlook and conclusions . . . 88

5 Estimate of the *Fermi*-LAT sensitivity to gamma-ray polarization 91
5.1 Principle of the measurement . . . 93
5.2 Selection of silicon-converted events . . . 96
5.2.1 Instrument Response Functions for silicon events . . . 102
5.3 The minimum detectable polarization . . . 104
5.4 Estimating systematic uncertainties . . . 106
5.4.1 A stack of AGN as a test source . . . 107
5.4.2 Data and Monte Carlo simulation . . . 109
5.5 Azimuthal distributions . . . 113
5.6 Conclusions and outlook . . . 115

List of Figures 121

List of Tables 125

Bibliography 127

Acknowledgment 147

Chapter 1

Physics of gamma-ray astronomy

This chapter reviews the physical processes involved in the production of energetic ($\gtrsim 10$ MeV) photons (hereafter gamma rays) of astrophysical origin. Such energies are too large for these photons to be of thermal origin. For radiation in thermal equilibrium, the energy at which most of the photons are emitted is related to the temperature by $T[\mathrm{K}] \sim 2.3 \times 10^3\, E[\mathrm{eV}]$ (see, e.g., Rybicki and Lightman, 1979). No known place in the universe is hot enough to produce a significant amount of $\gg 10$ MeV thermal radiation. Astrophysical gamma-ray sources are capable of accelerating charged particles to relativistic energies (Hinton and Hofmann, 2009). In the environment of these sources, gamma rays are produced as the accelerated particles lose their energy in the interaction with ambient matter or radiation fields.

Long before the first astronomical observations in the gamma-ray band, the detection of cosmic rays (CRs) provided direct evidence that the universe must contain such 'natural' particle accelerators. CRs were first observed at the beginning of the twentieth century as the cause of discharge in isolated electroscopes. In a series of underwater experiments, Domenico Pacini proved that this ionizing radiation could not be explained by natural radioactivity of the Earth's crust. He concluded that the observed radiation must have an air-borne component (the original paper is from 1911. A translated version is available in Pacini, 2010). One year later, with his famous balloon flights, Victor Hess proved that CRs are indeed of extra-terrestrial origin (Hess, 1912)[1]. More than a century later, our phenomenological knowledge of CRs has greatly improved thanks to the numerous experiments that have been dedicated to their study (see, e.g. Verzi, 2016; Maestro, 2015, for an overview of the latest experimental results). At around $\sim$ 1 GeV, CRs are made up of $\sim$85% hydrogen, 12% helium nuclei and 2% electrons. Heavier nuclei and antimatter are also present in smaller fractions.

Figure 1.1 presents a recent compilation of measurements of the all-particle differential energy

[1] Pacini made important contributions to the discovery of CRs. However, he is seldom acknowledged. Although Hess was aware of Pacini's work, he never cited him in his publications. An interesting reading on the history of the discovery of CRs, including the correspondence between Hess and Pacini, can be found in Carlson and de Angelis (2010).

spectrum (i.e., number of particles per unit time, surface, solid angle, and energy) of CRs as measured from ground based detectors. The main features of the CR spectrum are (Patrignani et al., 2016):

- the CR spectrum covers a huge energy range of more than tens orders of magnitude. The spectrum is well described by a set of power-law functions[1] $dN(E)/dE \propto E^{-\alpha}$.
- there are two marked changes in the slope α of the spectra: the so-called 'knee' at $\sim 10^{15}$ eV, where the spectrum steepens from $\alpha \sim -2.7$ to $\alpha \sim -3.1$, and the 'ankle' around 5×10^{18} eV. A second knee is also visible around $\sim 10^{17}$ eV.
- a cutoff of the spectra above $\sim 10^{20}$ eV, often interpreted as the result of the interaction of ultra-high energy (UHE) CRs with the cosmic microwave background radiation, the so-called GZK cutoff (Greisen, 1966; Zatsepin and Kuz'min, 1966).

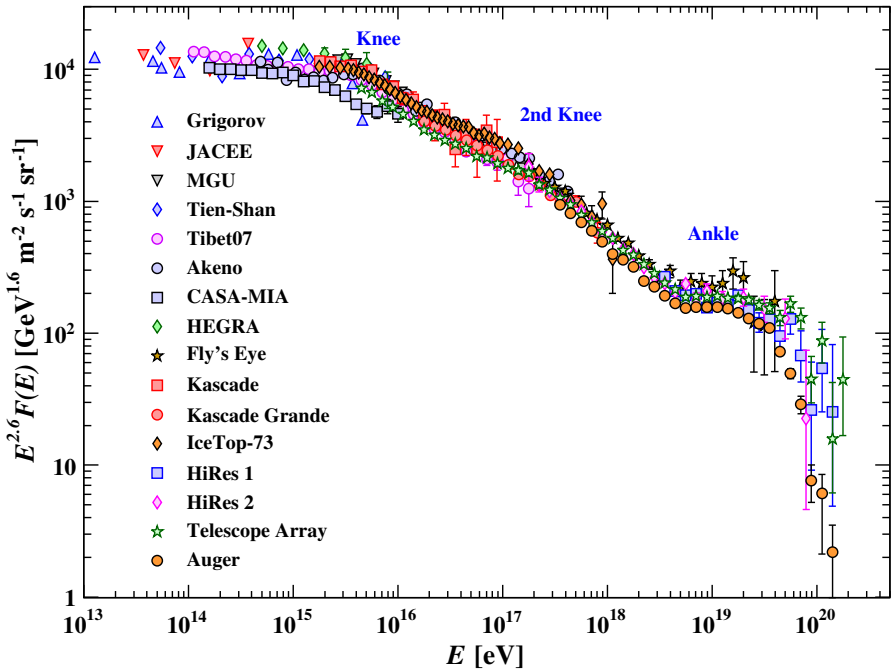

Figure 1.1: The all-particle CRs spectrum as a function of the energy per nucleus, as measured from various air shower detectors. The spectrum has been multiplied by $E^{2.6}$ to better display the spectral features. Image taken from Patrignani et al. (2016).

[1] Power laws are ubiquitous in a wide range of natural and sociological phenomena. As we will see, they approximate not only the spectra of many gamma-ray sources, but also the properties of their temporal variability. Power laws also describe the magnitude of earthquakes and meteor impacts, how population is distributed in cities, the frequencies of words in text, and the scale of wars among countries, just to give a few examples. For an interesting reading on the subject, see Newman (2005).

Despite this wealth of data, the sources of CRs have not been identified with certainty. The features of the CR spectrum can be interpreted as the result of the interplay of different source populations. The commonly accepted paradigm is that CRs below the knee originate from Galactic sources, while the ones above $\sim 10^{18}$ eV might be of extragalactic origin. What exactly the sources are, and where the transition between Galactic and extragalactic ones lies is still under debate (see, e..g., Aharonian et al., 2012, and references therein). These questions cannot be answered in a straightforward way. Being charged particles, CRs are deflected by Galactic and extragalactic magnetic fields as they propagate. When they are detected on Earth their arrival directions are almost isotropic (Aab et al., 2015). As the sources of CRs cannot be observed directly, measurements of neutral secondary particles like energetic photons (gamma rays) or neutrinos, produced in the same sources, are necessary for source identification. Supernova remnants, for example, have long been suspected to be (one of) the sources of Galactic CRs (e.g. Ginzburg and Syrovatskii, 1964). These explosions of massive stars are powerful and frequent enough to be able to sustain the energy flux of CRs. However, a conclusive proof of proton acceleration in these objects came only with sensitive observations of their emission in high-energy ($\gtrsim 50$ MeV) gamma rays (Ackermann et al., 2013b).

1.1 Particle acceleration at the sources

In gamma-ray sources, energy is transferred via electromagnetic fields to kinetic energy of charged particles. Several acceleration mechanisms have been proposed to accomplish this. The most commonly invoked are particle acceleration at shocks and magnetic reconnection. In the following, we will state the main results and ideas behind these two acceleration mechanisms. For acceleration at shock fronts, a detailed review of the classical theory can be found in Blandford and Eichler (1987) and a more recent account on the relativistic case in Sironi et al. (2015). Reviews on magnetic reconnection mechanism can be found in Zweibel and Yamada (2009) and Kagan et al. (2015).

1.1.1 Diffusive shock acceleration

The basics of this acceleration mechanism were first laid out by Enrico Fermi (Fermi, 1949). In the original formulation of this process, the particles gain energy as a consequence of repeated elastic scatterings with moving 'magnetic mirrors' associated with irregularities of the magnetic fields. The magnetic mirrors are assumed to be infinitely massive and move with a Lorentz factor $\gamma = (1 - \beta^2)^{-1/2}$, with $\beta = uc$ being the speed of the mirror in units of the speed of light c. A basic sketch of the process is presented in Fig 1.2.

The particles gain energy when colliding head-on with these mirrors and lose it in the case of following collisions. The relative energy gain per collision is proportional to β. In a randomized environ-

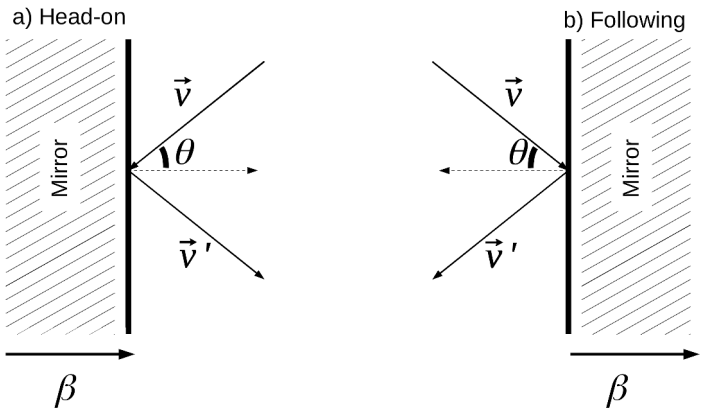

Figure 1.2: Sketch of the second-order Fermi acceleration mechanism, illustrating the elastic scattering of a particle with velocity **v** against a magnetic mirror moving with a speed βc. Head on and following collision are presented in the left and right part of the sketch, respectively.

ment, head-on collisions are favored over following ones again by factor $\sim \beta$. The resulting average energy gain is $\langle \frac{\Delta E}{E} \rangle \sim \beta^2$, of the second order in β. For this reason this acceleration mechanism is often called second-order Fermi process. The relative energy gain is independent on the particle energy. The energy of the particles will increase exponentially with the number of scatterings. If the probability for the particles to escape the acceleration region is finite and constant, the resulting energy distribution is a power law $N(E > \tilde{E}) \propto \tilde{E}^x$. Despite its success in explaining the shape of the CR spectra, it was soon realized that this mechanism is probably too inefficient to explain the presence of CRs of energies higher than ~ 1 PeV.

Diffusive shock acceleration overcomes this problem. In this case, particles are scattered off turbulent magnetic fields on both sides of shock waves, which can, for example, be generated by supersonic ejection of stellar matter in supernovae (see Section 3.1.1). This process is sketched in Fig. 1.3.

The shock wave moves in the unperturbed upstream region with a velocity u. In the case of an adiabatic shock in an ideal plasma, the gas in the downstream region follows the shock with a velocity of $3/4u$ (e.g. Longair, 1994). As in the second-order Fermi mechanism, as a particle crosses the shock and enters the downstream region, its energy increases by $\Delta E/E \sim u/c$. The particle is then scattered by irregularities in the magnetic field. Its motion is isotropized with respect to the turbulent gas downstream of the shock, and the particle has a probability to diffuse back into the upstream region. In the frame of reference of the shocked gas, the material in the upstream region appears to flow inwards with a velocity $3/4u$. The situation, as seen from the two frames of reference, is therefore identical. Contrary to second-order Fermi acceleration, the particle will gain energy at every crossing of the shock. The average energy gain is therefore linear with $\beta = u/c$. For this reason this process is often referred to as first-order Fermi mechanism. A proper calculation (e.g. Longair, 1994) of the relative

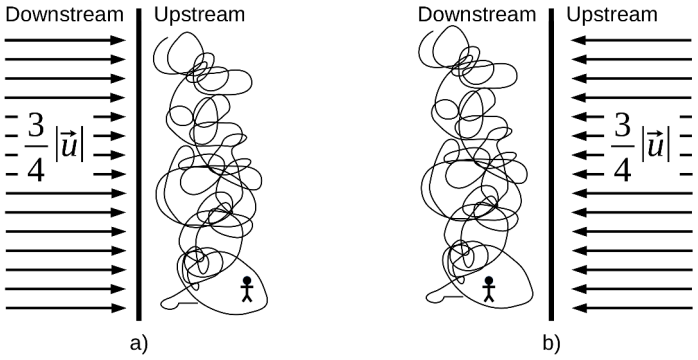

Figure 1.3: Sketch of both sides of a shock: a) in the reference frame of the unperturbed medium in the upstream region, the momenta of the particles are isotropically distributed and the shocked medium advances with 3/4 of the shock velocity u. b) in the reference frame of the shocked medium in the downstream region the momenta of the particles are also isotropic and the gas of the upstream region appears to flow across the shock again with $3/4u$.

energy gain per shock crossing gives:

$$\left\langle \frac{\Delta E}{E} \right\rangle = \frac{4}{3}\beta \tag{1.1}$$

Diffusive shock acceleration allows for an efficient energy transfer from the shock motion to the particles. As with the second-order Fermi acceleration, this mechanism naturally produces power-law energy distributions. The shape of the power-law spectra of the accelerated particles can be derived from the thermodynamic properties of the shock. Assuming reasonable values for the shock compression ratio, the indices for the differential energy spectra are $\sim$2, in agreement with the spectra of CRs at the sources (Bell, 1978).

In this simple exposition of diffusive shock acceleration, many important caveats have been ignored. For example, astrophysical shocks are often relativistic, and the particle momentum distribution can no longer be considered isotropic. The coupling between the particles being accelerated and the magnetic fields responsible for the scatterings introduces non-linear effects, another major complication of the theory (see, e.g., Malkov and Drury, 2001). Perhaps the most severe problem in the shock acceleration mechanism is the so-called 'injection problem'. For shock acceleration to work, the initial energy of the particle has to be high enough for its gyro-radius[1] to be much larger than the size of the shock. This mechanism cannot accelerate particles if their energy is below this threshold.

[1]The gyro-radius is the radius of the circular motion of a charge moving in a magnetic field. The gyro-radius, defined as $R_g = \gamma m v / qB$, with m and γ are the mass and the Lorentz factor of the particle, $v_\perp$ is the component of the particle velocity perpendicular to the direction of the magnetic field, and B is the strength of this field.

1.1.2 Magnetic reconnection

Magnetic reconnection is a fundamental process occurring in plasma in which the topology of the magnetic field rearranges itself and magnetic energy is converted into kinetic energy of the particles and into electric field. It is an efficient acceleration mechanism in magnetically dominated systems and is capable of producing power-law particle distributions. It is also associated with transient and violent events, as solar flares (Su et al., 2013), and it is a plausible explanation for the gamma-ray flares seen from the Crab nebula (Cerutti et al., 2012, see also Section 3.2).

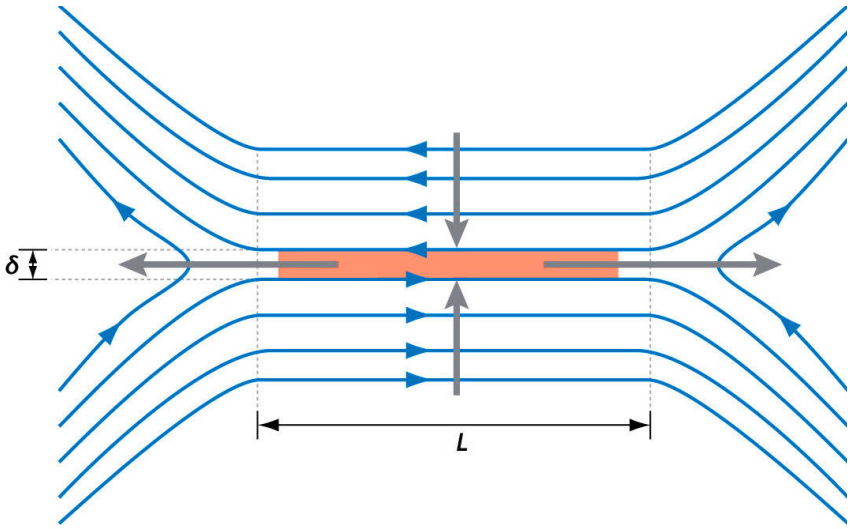

Figure 1.4: Geometry of the Sweet-Parker reconnection. Inside the reconnection layer the magnetic field recombines: plasma is ejected to the left and to the right, and an electric field E_{rec} perpendicular to the page is induced. Adapted from Zweibel and Yamada (2009).

The basic principles of magnetic reconnection were first laid out by Parker and Sweet (Parker, 1957; Sweet, 1958). The geometry of this model is presented in Fig. 1.4. Two opposite magnetic fields $\pm B_0$ in a plasma of density ρ are steadily pushed toward each other at a speed v_i over a region of size L. The fields reconnect in a layer of thickness δ. Both the plasma and the magnetic field[1] are expelled at the sides of the reconnection region with a velocity v_{out}. In the reconnection layer, a current density $J \approx B_0/\mu_0\delta$ is induced, where $\mu_0 = 4\pi \times 10^{-7}$ N/A^2 is the vacuum magnetic permeability. Assuming that δ is small enough, ohmic dissipation heats up the plasma significantly. In a steady state, the pressure of the heated gas P_{gas} in the reconnection layer must be compensated by the magnetic pressure outside $P_{mag} \approx B_0^2/2\mu_0$. Integrating the steady-state equation of state of the plasma gives $P_{gas} = \rho v_{out}^2/2$ (Longair, 1994). Equating P_{gas} to P_{mag} gives $v_{out} \approx B_0/\sqrt{\mu_0\rho}$, equal to the Alfvén speed, the typical

[1] Astrophysical plasmas are highly conductive. In the limit of infinite conductivity, the magnetic field lines are attached to the plasma: the motion of one carries with it the other. This is a consequence of the magnetic flux freezing theorem, and can be observed directly at play in coronal mass ejection of the Sun.

speed of magnetic disturbance in a plasma. Assuming the plasma is incompressible, mass conservation implies $v_{in}L = v_{out}\delta$: large-scale motion of the plasma is converted into fast outflows of hot plasma.

Outside the reconnection layer, the electric field is compensated by the Lorentz force. If the system is in a steady state, the electric field must be constant everywhere[1]. $\mathbf{E}$ inside the reconnection region must be equal to its value outside, $\mathbf{E}_{rec} = (\mathbf{v}_{in} \times \mathbf{B}_0)/c$. Inside the reconnection layer the magnetic field vanishes; there is no Lorentz force to balance $\mathbf{E}_{rec}$ and this field can effectively accelerate particles along the plane of the reconnection. In the Sweet-Parker model, the rate of magnetic reconnection is $v_{in}/v_{out} \approx \delta/L$, which is typically too slow for most astrophysical systems (Zweibel and Yamada, 2009). To achieve higher reconnection rates, the scale L of the reconnection layer must be reduced. The first attempt to overcome this issue was proposed in Petschek (1964), in which standing shock waves surrounding the reconnection region effectively limit its size.

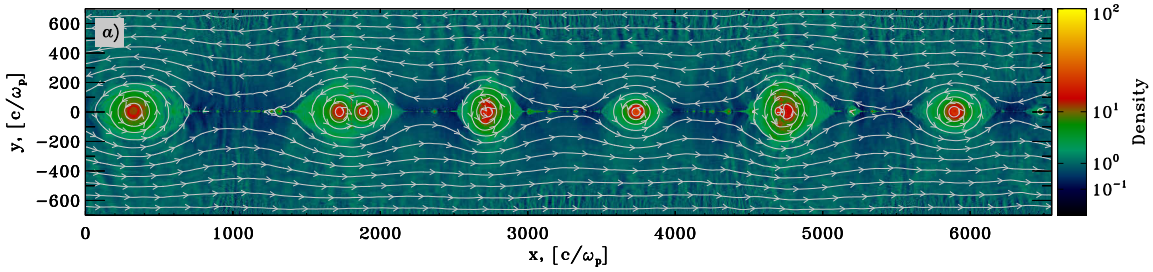

Figure 1.5: Magnetic islands naturally form as a consequence of instabilities in the reconnection layer at $y = 0$. This image presents the structure of the reconnection layer as obtained from numerical 2D simulation. The color encodes the particle density normalized to some value far from the reconnection layer. The white arrows represent the magnetic field lines. Taken from Sironi and Spitkovsky (2014).

Modern models of magnetic reconnection focus on the instability of the flow in the region, called the current sheet, between the two magnetic fields. Mechanisms such as the tearing instability (Furth et al., 1963) spontaneously break the flow in the current sheet into a series of smaller reconnection regions, separated by large flux ropes delimited by closed field lines (magnetic islands, see Fig. 1.5). Particle acceleration in such a setting is thought to proceed in two stages. First, particles are accelerated by the electric fields in the reconnection region. Subsequent acceleration proceeds via the Fermi mechanism as the particles interact with the boundaries of the magnetic islands (see, e.g., Drake et al., 2006; Oka et al., 2010; Sironi and Spitkovsky, 2014). Simulations show that in this scenario particles are accelerated efficiently. As shown in Fig. 1.6, the resulting particle energy distributions have a power-law shape.

The complexity and non-linearity of these models means that they can only be studied in detail through numerical simulations. Despite great progress made in recent years, the theory and modeling

[1]Maxwell's equations for a charge-neutral system in a steady states give $\nabla \cdot \mathbf{E} = 0, \nabla \times \mathbf{E} = 0$.

of particle acceleration in magnetic reconnection is not yet capable of making reliable quantitative predictions, due to limited computing power and uncertainties on the initial conditions of the systems. The basic principles are however established. Magnetic reconnection can efficiently convert a large fraction ($\sim 50\%$) of magnetic energy into particle kinetic energy and it automatically provides a pre-acceleration, thus solving the injection problem affecting pure shock acceleration models.

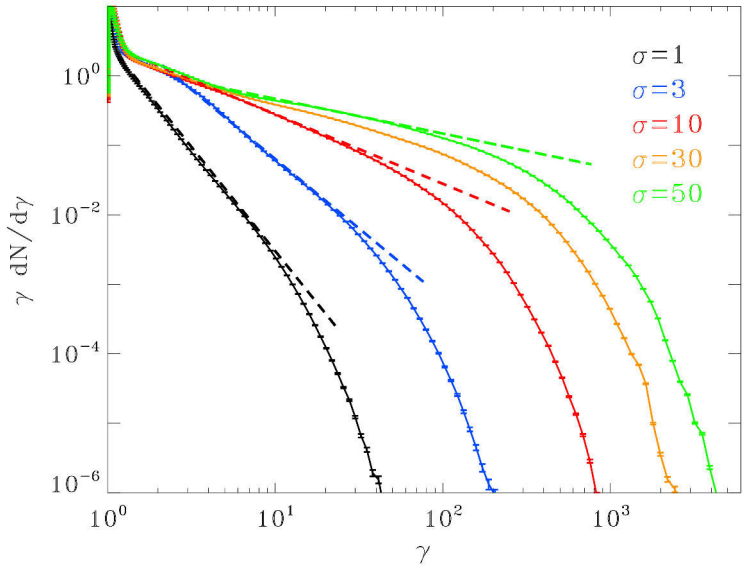

Figure 1.6: Energy distribution of accelerated particles resulting from simulation of magnetic reconnection for different values of the magnetization $\sigma = B_0^2/(4\pi n m_e c^2)$. The straight dotted lines represent power laws with slopes of -4, -3, -2, and -1.5 (from $\sigma = 1$ to $\sigma = 50$ respectively). Taken from Kagan et al. (2015).

1.2 Radiative processes: from cosmic rays to gamma rays

As implied by observations of CRs, the universe contains natural particle accelerators capable of producing power-law energy spectra of the form $dN/dE \propto E^{-\alpha}$ reaching up to the highest energies ever observed. In the environment of these sources, the accelerated particles interact with matter and radiation. Gamma rays are one of the products of these interactions.

In the following we outline the main mechanisms thought to be responsible for the production of high-energy gamma rays, and present the associated energy-loss rates and the spectral and polarization signatures. Once the main characteristics of these radiative processes have been discussed, we will apply them to test proton and electron distributions to compare simple radiative models. Detailed discussions and derivations of the formulae presented in the next paragraphs can be found in Longair (1994), Rybicki and Lightman (1979), and Aharonian (2004).

Synchrotron emission

Electric charges emit electromagnetic radiation when accelerated. For a relativistic particle of charge q, moving with speed $v = \beta c$ and Lorentz factor $\gamma = (1-\beta^2)^{-1/2}$, the energy loss rate can be written as:

$$-\left(\frac{dE}{dt}\right) = \frac{q^2\gamma^4}{6\pi\varepsilon_0 c^3}\left(|a_\perp|^2 + \gamma^2|a_\parallel|^2\right) \tag{1.2}$$

where $\varepsilon_0 \approx 8.9 \times 10^{12}$ F m^{-1} is the vacuum permittivity and $|a_\perp|$, $|a_\parallel|$ are the components of the particle's acceleration perpendicular and parallel to its velocity in the observer's reference frame. This relativistic version of the Larmor formula (Larmor, 1897) can be specialized to treat two cases: bremsstrahlung and synchrotron emission.

Synchrotron emission is produced when a charged particle gyrates at relativistic speed in a magnetic field B. As both energetic particles and magnetic fields are common in our Universe, this emission is ubiquitous in astrophysics, from radio emission of galaxies to non-thermal X- and gamma-ray fluxes of compact objects. The power radiated via this process can be derived from Eq. 1.2 imposing $|a_\parallel| = 0$, and $|a_\perp| = qvB\sin\theta/\gamma m$, as in the case of a particle of charge q and mass m moving with speed v at a pitch angle θ with respect to the magnetic field B. The radiated power, averaged over the angle θ can be written as:

$$-\left\langle\frac{dE}{dt}\right\rangle_{\text{sync}} = \frac{16\pi}{9\mu_0 c^5}\frac{q^4B^2p^2}{m^4} \tag{1.3}$$

The m^4 in the denominator implies that the synchrotron emission of a source is dominated by contributions from the lightest particles present in the system, i.e. electrons. The cooling time τ is the timescale of an energy loss process; it can be defined as $\tau = E/(dE/dt)$. In the case of synchrotron emission of a relativistic particle, τ_{sync} scales with the inverse of the particle energy.

The synchrotron spectrum, i.e. the energy emitted at a given frequency ν per unit time, for a single emitting particle is presented in Fig. 1.7. At low frequencies the spectrum is proportional to $\nu^{1/3}$. It has a broad peak around the critical frequency ν_c, and falls like $e^{-\nu/\nu_c}$ for $\nu \gg \nu_c$. The critical frequency is defined as:

$$\nu_c \sim \gamma^2\frac{qB}{2\pi mc} \tag{1.4}$$

where we have omitted a numerical factor of order $\lesssim 1$. Due to relativistic effects, synchrotron radiation appears collimated to within an angle $\sim 1/\gamma$ of the direction of the emitting particle.

The emission from a single electron is polarized along the direction of the acceleration vector. If the electron velocity is perpendicular to the magnetic field ($\theta = \pi/2$), the observed radiation is linearly polarized in the direction perpendicular to the projection of $\mathbf{B}$ on the sky. In the general case ($\theta \neq \pi/2$), the emission can be decomposed into components parallel and perpendicular to the projection of the magnetic field on the plane of the sky, $I_\parallel$ and $I_\perp$ respectively (see, e.g., Westfold, 1959;

Rybicki and Lightman, 1979). The perpendicular component is associated to the radiation observed when the emitting particle aims directly at the observer, while the parallel component is associated to radiation emitted when the particle velocity is within an angle $\sim 1/\gamma$ of the line of sight. These two components evolve differently as the particle gyrates around the magnetic field lines. As a consequence, the synchrotron emission of a single electron is, in general, elliptically polarized. The major axis of the ellipse is perpendicular to the projection of $\mathbf{B}$ on the sky. For a distribution of pitch angles θ, all the particles directed within an angle $\sim 1/\gamma$ of the line of sight contribute to the observed intensity. The parallel emission components will average out and the observed emission will be linearly polarized in the direction perpendicular to the projection of $\mathbf{B}$ on the sky. The expected degree of linear polarization, defined as:

$$\Pi_0 = \frac{I_\perp - I_\parallel}{I_\perp + I_\parallel} \tag{1.5}$$

is presented in the bottom panel of Fig. 1.7 for the synchrotron emission from a single charge. Considering a distribution of energetic electrons with a power-law energy spectrum $dN/dE/ \propto E^{-p}$ moving in a uniform magnetic field, the expected Π_0 is given by (Rybicki and Lightman, 1979):

$$\Pi_0^{\text{sync}} = \frac{p+1}{p+7/3} \tag{1.6}$$

which can be as high as $\sim 70\%$ for $p = 2$ in the case of a perfectly ordered, uniform magnetic field.

Bremsstrahlung

In the case of bremsstrahlung, the acceleration felt by the charge originates from the interaction with the electrostatic field of the atoms in the traversed material. It is an important energy loss mechanism in dense environments, as, for example, molecular, clouds which typically have densities of $\rho \gtrsim 10$ protons/cm^3, compared to $\rho \sim 1$ protons/cm^3 in the interstellar medium. The kinetic energy lost by the particle in these interactions is carried away by an energetic photon. In the non-relativistic case, bremsstrahlung energy losses are proportional to the square root of the particle energy. For relativistic particles, the power radiated via bremsstrahlung is given by (Bethe and Heitler, 1934):

$$-\left\langle \frac{dE}{dt} \right\rangle_{\text{brems}} \propto \frac{Z(Z+1.3)NE}{m^2} \left[\ln\left(\frac{183}{Z^{1/3}} \right) + \frac{1}{8} \right] \tag{1.7}$$

where N is the number density of target nuclei in the observer reference frame and Z is the atomic number of the target. Note the dependence of the bremsstrahlung energy losses with Z^2. As relativistic bremsstrahlung energy losses are proportional to the energy, an individual particle will loose a significant fraction of its energy in each interaction. A characteristic length scale can be defined for

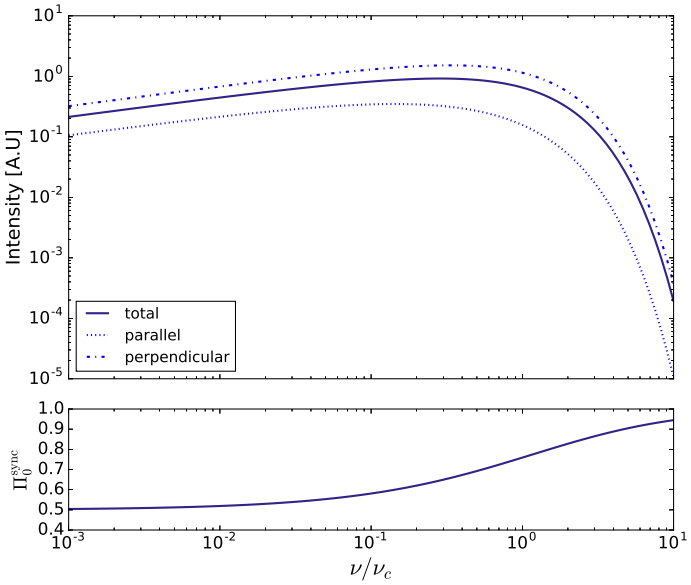

Figure 1.7: Intensity of the synchrotron emission from a single electron as a function of the ratio x of the synchrotron frequency over the critical frequency $x = \nu/\nu_c$. The contributions with polarization parallel and perpendicular to the projection of the magnetic field on a plane orthogonal to the line of sight are shown as dashed and dot-dashed lines respectively. In the bottom panel the variation of the degree of linear polarization $\Pi_0 = (I_\perp - I_\parallel)/(I_\perp + I_\parallel)$ with the frequency is also shown.

this process, the radiation length X_0. This quantity is defined as the mean distance, often expressed as a column density in g cm^{-2}, over which an electron loses $(1 - 1/e)$ of its initial energy through bremsstrahlung. It is given by:

$$X_0[\text{g cm}^{-2}] = \frac{1432.8A}{Z(Z+1)(11.319 - \ln Z)} \tag{1.8}$$

where A and Z are the mass and atomic number of the traversed material, respectively. In the relativistic case, one or two photons are emitted per radiation length, on average. For a relativistic particle of energy E, the average energy of bremsstrahlung photons is $\sim E/3$ (Longair, 1994).

Bremsstrahlung emission can only be polarized only when the distribution of relative velocities of the colliding particles is anisotropic (Ginzburg, 1989). Thermal bremsstrahlung, resulting from the thermal motion of electrons in hot plasma, is weakly, if at all, polarized (see, e.g., Komarov et al., 2016). When considering a particle beam colliding with a dense target, the bremsstrahlung emission is in general polarized and the degree of polarization varies with the energy of the emitted photon (McMaster, 1961). For particles with $\gamma \gg 1$, the linear polarization of bremsstrahlung photons emit-

ted at the end of the bremsstrahlung spectrum is given by (Jackson, 1998):

$$\Pi_0^{\text{brems}} \simeq \frac{2\gamma^2\theta^2}{1+\gamma^4\theta^4} \tag{1.9}$$

where θ is the angle of the emission with respect to the motion of the incoming particles. For $\gamma \gg 1$ the degree of linear polarization of bremsstrahlung emission decreases as $1/\gamma^2$. The high-energy bremsstrahlung emission from relativistic particles is therefore unpolarized.

Inverse Compton scattering

Compton scattering is the inelastic scattering of a photon off a charged particle resulting in a transfer of momentum from the photon to the particle (Compton, 1923). In inverse Compton scattering (IC), the situation is reversed: a charged particle up-scatters a low energy photon to higher energies. The exact cross section for Compton scattering is given by the Klein-Nishina formula (Klein and Nishina, 1929):

$$\sigma_{\text{KN}} = \pi r_e^2 \frac{1}{x}\left\{\left[1-\frac{2(x+1)}{x^2}\right]\ln(2x+1)+\frac{1}{2}+\frac{4}{x}-\frac{1}{2(2x+1)^2}\right\} \tag{1.10}$$

where $x = \hbar\omega/m_e c^2$ is the dimensionless photon energy in the reference frame of the electron and $r_e = e^2/(4\pi\varepsilon_0 m_e c^2)$ is the classical radius of the electron. For low energy photons, $x \ll 1$, this expression reduces to the Thomson cross section $\sigma_T = 8\pi r_e^2/3 \sim 6.6\times10^{-29}$ m^2 . At high photon energies, $x \gg 1$, the cross section decreases with $1/x$, as is shown in Fig.1.8. The energy transfer trough inverse Compton scattering becomes less efficient at high energies.

The average energy gained by the photon through inverse Compton is:

$$\hbar\omega_{out} = \frac{4}{3}\gamma^2\beta^2\hbar\omega_{in}, \tag{1.11}$$

where $\hbar\omega_{in}$, $\hbar\omega_{out}$, and γ are the initial and final energies of the photon, and the Lorentz factor of the electron in the observer's reference frame, respectively Longair (1994). This equation holds as long as the scattering in the rest frame of the electron happens in the Thomson regime, that is, $\hbar\omega'_{in} \ll m_e c^2$. As can be seen from Eq. 1.11, the average energy gain is proportional to γ^2. Through inverse Compton scattering, highly energetic photons can be produced: for example, electrons with $\gamma = 10^3$ can up-scatter optical photons ($\hbar\omega \sim$ eV) to >1 MeV.

In the Thomson regime, the average power radiated via inverse Compton scattering from an electron traveling with momentum p in a electric field with energy density $u_{rad} = \varepsilon_0 E^2/2$ is given by:

$$-\left\langle\frac{dE}{dt}\right\rangle_{\text{IC}} = \frac{4}{3}\sigma_T c u_{rad}\left(\frac{p}{m_e c^2}\right)^2 \tag{1.12}$$

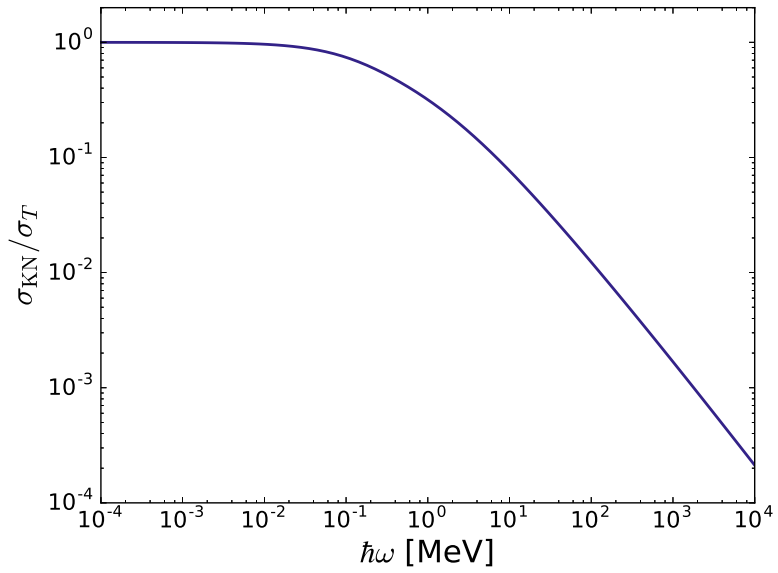

Figure 1.8: Cross section for the Compton scattering of photons on electrons as a function of the photon energy as computed from the Klein-Nishina formula (Eq. 1.10). At low energies it approaches Thomson cross section σ_T, while it decreases as $\sim (\hbar\omega)^{-1}$ for $\hbar\omega \gg m_e c^2$.

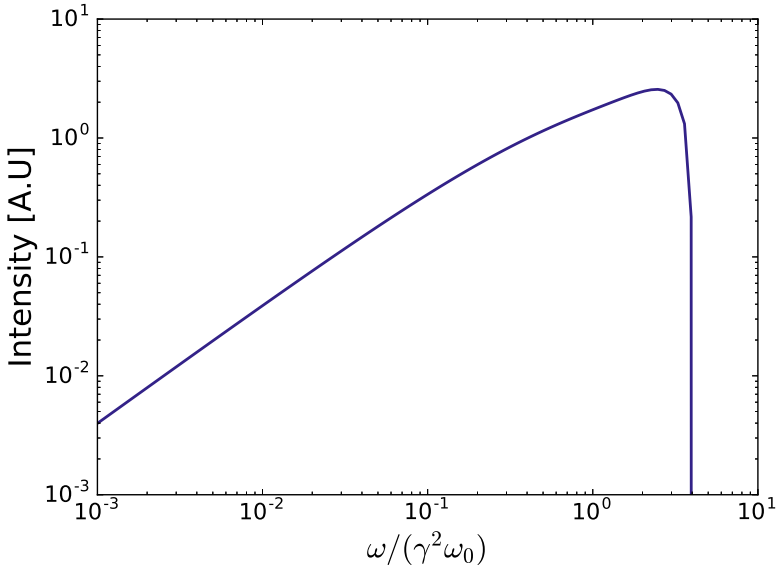

Figure 1.9: Emission spectrum from inverse Compton scattering of a monochromatic and isotropic photon field at a frequency ω_0 from monoenergetic electrons with Lorentz factor γ as computed in Blumenthal and Gould (1970)

It rises quadratically with the electron energy. For higher energies, the Klein-Nishina cross section drops and the radiated power rises logarithmically with the energy[1]. The energy spectrum of the inverse Compton emission from a power-law distribution of electrons $dN_e/dE \propto E^{-p}$ has also a power-law shape $dN_\gamma/dE \propto E^{-\alpha}$ with index $\alpha = (p+1)/2$, provided that the interaction happens in the Thomson regime.

Compton and inverse Compton scattering can both polarize and depolarize incoming radiation. The polarization properties of Compton scattered radiation are presented in Fig. 1.10 for an incoming 1 MeV photon in the two limiting cases of a unpolarized and 100% linearly polarized incoming radiation. As is visible, as the energy increases, both the degree of induced and residual polarization decreases (see Chang et al., 2014, for a more detailed treatment). Scattering can effectively depolarize incoming radiation, especially if multiple collisions are involved. More details on the polarization properties of Compton scattering are presented in Lei et al. (1997) and references therein.

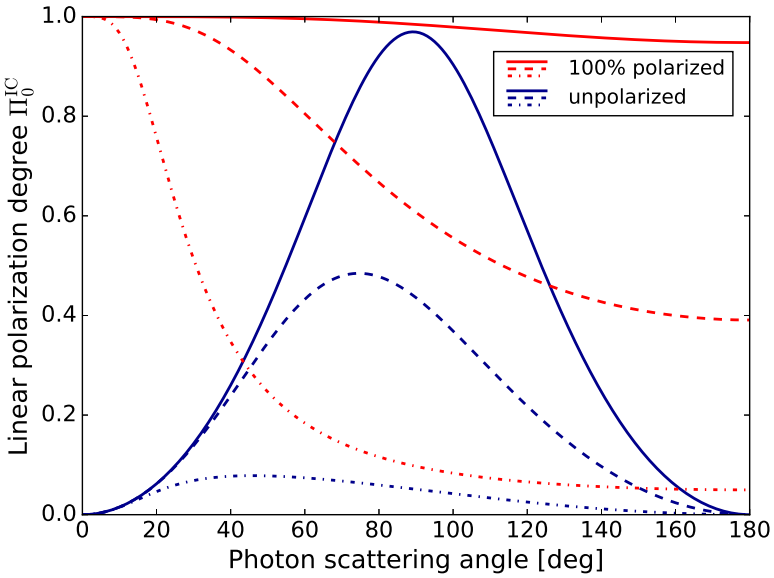

Figure 1.10: Linear polarization of Compton scattering as a function of the scattering angle for three different energies of the incoming photon: 0.1 MeV (solid line), 1 MeV (dashed line), and 10 MeV (dash-dotted line). The blue lines refers to the polarization degree acquired by an unpolarized incident beam as a consequence of the scattering. The red lines illustrates the opposite case: the scattered radiation from a 100% linearly polarized beam partially loses its polarization.

[1]For electrons, the power radiated via synchrotron emission (Eq. 1.3) can be written in the same form as Eq. 1.12, substituting u_{rad} with $u_{mag} = B^2/2\mu_0$. The reason why synchrotron emission and inverse Compton scattering have similar properties is that the energy losses are due to the electric field experienced by the charge in its rest frame (dE/dt is Lorentz invariant), independently of the origin of this field.

Hadronic processes

As seen in the previous paragraphs, the emitted power scales with m^{-4} for synchrotron emission, and with m^{-2} for inverse Compton and bremsstrahlung. These processes are suppressed for protons by factors $(m_e/m_p)^4$ and $(m_e/m_p)^2$ respectively. However, protons of extremely high energies can efficiently radiate gamma rays via synchrotron emission, given a strong enough magnetic field in the emission region (see e.g., Aharonian, 2000; Kundu and Gupta, 2014). Another mechanism through which protons can produce gamma rays is via the production of pions. Pion production proceeds via a delta resonant scattering of the energetic protons either on ambient protons: $p+p \rightarrow \Delta^{++} \rightarrow \pi^0 + \pi^{\pm} + ...$, or photons: $p+\gamma \rightarrow \Delta^{+} \rightarrow \pi^0 + p$. The inelastic cross section for proton-proton interaction is $\sigma_{pp} \approx 35$ mb and is only weakly dependent on the energy (Hinton and Hofmann, 2009). The cross section for $p+\gamma$ interaction is ∼0.1 mb for photon energies $\gtrsim 2$ GeV in the proton rest frame (Mücke et al., 1999). Gamma rays from astrophysical sources can be produced in the electromagnetic decay of the π^0 or via synchrotron and IC emission of the secondary leptons produced in the decay of the charged pions (Mannheim, 1993). The neutral pion decays in two photons with a mean lifetime of 8.3×10^{-17} s. The two gamma rays are produced almost instantaneously and carry away all the energy with which the π^0 was produced. As a rule of thumb, roughly $1/6$ of the proton energy is transferred to the gamma rays from the π^0 (Hinton and Hofmann, 2009). In the rest frame of the π^0, the two gamma rays have an energy $m_{\pi^0}/2 \sim 67.5$ MeV. This introduces a characteristic signature in gamma-ray spectra the so-called pion bump. It was the detection of this feature in the gamma-ray spectra of two supernovae remnants that made it possible to prove that these sources accelerate protons (Ackermann et al., 2013b). As the π^0 is a spin 0 particle, in its rest frame there is no preferred direction. The emitted gamma-rays are therefore unpolarized.

1.3 Simple radiative models

The broad-band emission of a source is customarily presented through the spectral energy distribution (SED), representing the energy flux F_E emitted in a given logarithmic interval of energies: $dF_E/d(\ln E)$. The radiative processes previously discussed produce two distinct bumps in the SEDs of the sources: a low-energy peak in the radio to X-ray energies and a second peak in the X-ray to gamma-ray domain. Such structures are most evident in sources like blazars (see Section 3.1.2), whose electromagnetic emission is completely dominated by the non-thermal radiation of energetic particles (Abdo et al., 2010b). The models invoked to explain the structure of the SED of such sources are divided in two broad families, hadronic or leptonic, depending on the type of particles thought to be responsible for the high energy emission. For a review on both hadronic and leptonic models, see Böttcher et al. (2013) and references therein.

Leptonic models (e.g. Ghisellini et al., 1998) attribute the low-energy peak of the SED to synchrotron radiation, and the high energy one to inverse Compton scattering of ambient low-energy photons. The different target photon fields for IC emission can be the cosmic microwave background (CMB), infrared emission from dust, visible light from stars, and the synchrotron emission from the same energetic electrons. This latter scenario is called synchrotron-self-Compton (SSC, see, e.g. Chiaberge and Ghisellini, 1999).

In hadronic models (Reimer, 2012; Rachen, 2000, e.g.), the high-energy peak of the SED is explained either as resulting from pion decay or, in case of high magnetic fields and proton energies $\gtrsim 10^{19}$ eV, from proton synchrotron emission (see for example Fig. 2 of Hinton and Hofmann, 2009). The low-energy peak of the SED is also interpreted as synchrotron emission from relativistic leptons for hadronic models. These leptons can be initially present in the source and co-accelerated together with the protons, or can be produced as secondaries by the interaction of the protons with ambient matter or radiation fields.

The SEDs for these different processes are illustrated in Fig. 1.11. In this example, we assume that a population of energetic particles is present in a region with a magnetic field $B = 3$ μG and an ion number density $n_0 = 10$ cm^{-3} at a distance of 1 kpc. Both the electron and proton spectra have been modeled with a power-law function with an exponential cutoff: $dN_i/dE_i = KE_i^{-2}\exp(-E_i/E_0)$, $i = \{e, p\}$. The cutoff at high energies accounts for the faster cooling of particles of higher energies, or for a maximum energy of the acceleration process. Both the electron and proton spectra are normalized to a total energy of 10^{47} ergs. In Fig. 1.11, the two types of lines, continuous and dash-dotted, refer to two cutoff energies: E_0 =1 TeV and E_0 =100 TeV, respectively. As shown in the figure, the contribution of the synchrotron emission peaks in the infrared at ~ 0.13 eV (for $E_0 = 1$ TeV), and scales with E_i^2, in agreement with Eq. 1.4. Note also the difference in intensities between the gamma rays from pion decay and those from bremsstrahlung and inverse Compton. As was seen in the previous section, through pion decay only a fraction of the energy of the protons is transferred to the gamma-rays.

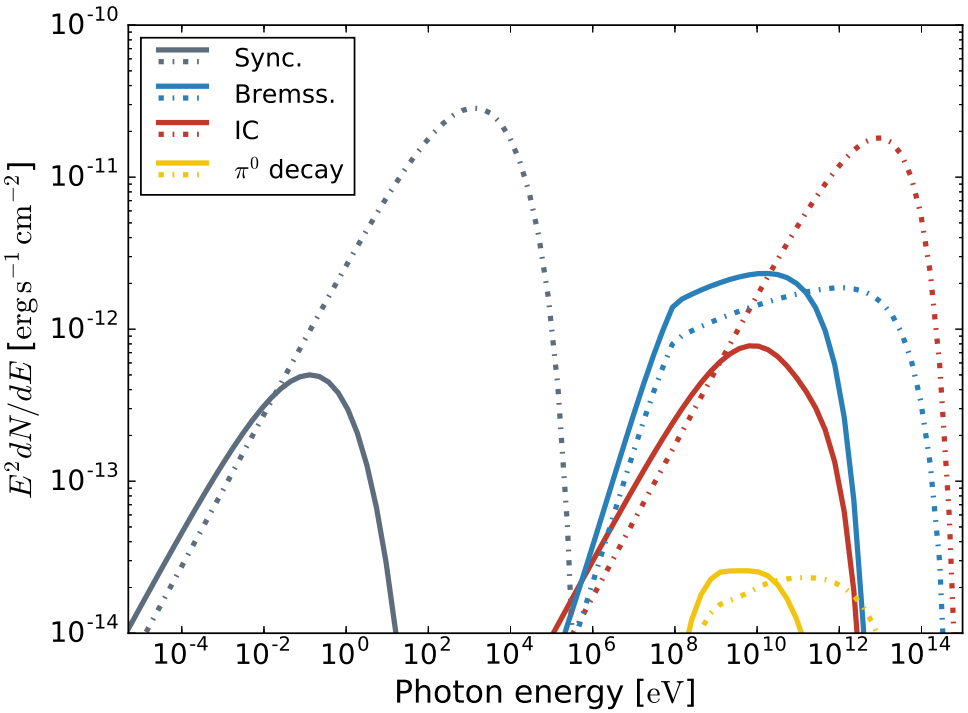

Figure 1.11: SEDs for the different radiative processes presented in this chapter. This plot has been produced with `naima`, a freely available open-source python module for modeling and fitting of non-thermal radiation spectra (Zabalza, 2015). In the environment of the source different target photon fields are available for IC scattering: the cosmic microwave background (CMB, $T = 2.72\,\mathrm{K}$, energy density $\epsilon = 0.26\,\mathrm{eV}^{-1}\,\mathrm{cm}^{-3}$), infrared emission from the dust (IR, $T = 232\,\mathrm{K}$, $\epsilon = 0.26\,\mathrm{eV\ cm}^{-3}$), light from stars ($T = 1.5 \times 10^3\,\mathrm{K}$, $\epsilon = 1\,\mathrm{eV\ cm}^{-3}$), and the synchrotron emission produced by the same electrons.

Chapter 2

Observing high-energy gamma rays

Gamma-ray astronomy is one of the youngest branches of astronomy, the oldest among the natural sciences. It is the study of the Universe at the highest frequencies of the electromagnetic spectrum, from photon energies of $\approx$ MeV up to hundreds of TeV. At higher energies, gamma-ray interaction with ambient photons effectively limits the size of the observable universe: it shrinks to about the size of our galaxy for $\gtrsim$ 1 PeV photons (Gould and Schréder, 1966). Since the recent detection of astrophysical neutrinos and gravitational waves (see, e.g., Aartsen et al., 2014; Abbott et al., 2016) gamma-ray astronomy is now complemented by observations of these new cosmic messengers.

On a practical level, the gamma-ray band is roughly divided into three overlapping ranges, each one characterized by specific observational challenges. The sensitivities of different X-ray and gamma-ray telescopes are presented in Fig. 2.1. The Earth's atmosphere absorbs electromagnetic radiation in these two bands. Direct observation of X- or gamma rays is possible only with space-based detectors.

In the lower part of the gamma-ray band, below some tens of MeV, the photon interaction cross section has a minimum, see Fig. 2.2. The competition between Compton scattering and pair production, two phenomena leaving very different signals in the detector, together with the limited reconstruction accuracy attainable at these energies, makes observation difficult. The last instrument observing in this region of the electromagnetic spectrum was COMPTEL (Schönfelder et al., 1992), launched almost 30 years ago. Several missions have been recently proposed to close this sensitivity gap (the so-called 'MeV Gap'), such as eASTROGAM (De Angelis et al., 2016) or ComPair (Moiseev et al., 2015).

In the high energy (HE) band, from $\lesssim$100 MeV to hundreds of GeV, satellite experiments such as the Fermi Large Area Telescope (LAT, Atwood et al., 2009) and the smaller AGILE (Pittori and Tavani, 2004) provide high sensitivity and good monitoring capabilities.

At very high energies (VHE, roughly above 50 GeV) the steeply declining gamma-ray flux requires photon collection areas that are too large for space-born experiments. Observations at these energies are carried on with ground-based detectors such as the currently operating H.E.S.S. (Aharonian et al.,

2006), MAGIC (Cortina, 2005), VERITAS (Holder et al., 2008), and the upcoming CTA (Actis et al., 2011) imaging atmospheric Cherenkov telescope systems (IACTs), and the High-Altitude Water Cherenkov detector array HAWC (Abeysekara et al., 2017). These instruments detect gamma rays indirectly, measuring or imaging the particle cascade induced by the energetic photons as they interact in the Earth's atmosphere.

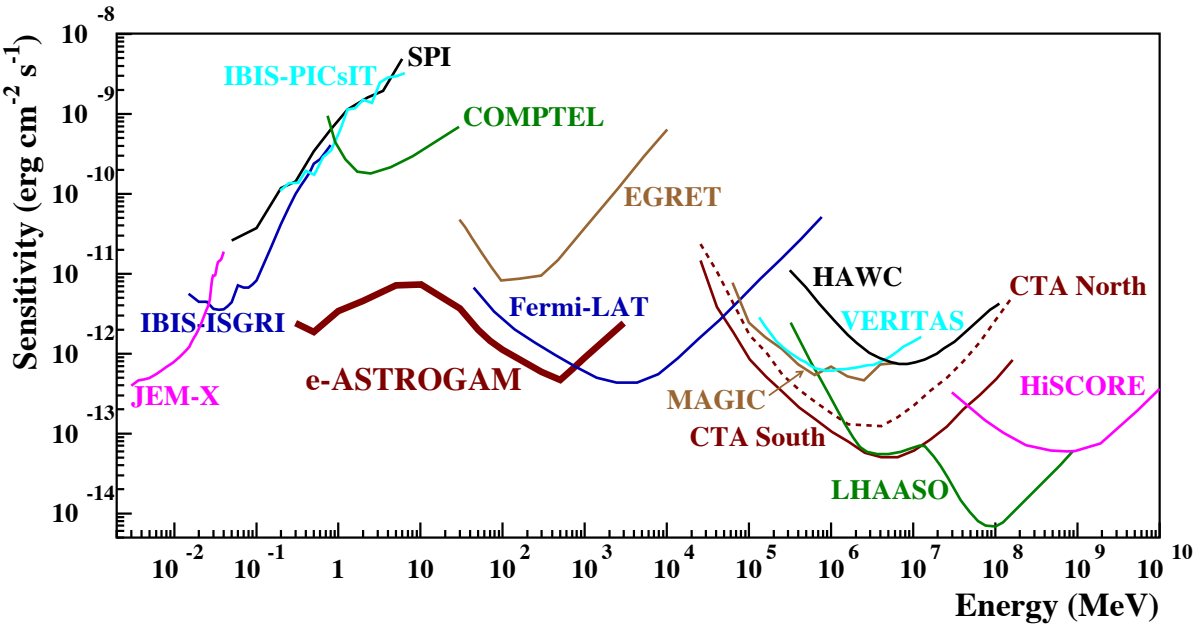

Figure 2.1: Point source differential sensitivity for different past, present, and future X- and gamma-ray observatories. The sensitivity indicates the minimum flux that can be detected by an instrument. Note the bump in the sensitivity curve of eASTROGAM in the energy range where Compton scattering and pair production coexists. The image is taken from De Angelis et al. (2016).

In this chapter, we briefly review the interaction of gamma rays with matter, discussing the main physical processes that influence the design and performance of an HE gamma-ray mission. Finally, we present the *Fermi* Large Area Telescope, currently the most sensitive observatory for gamma-ray astronomy in the energy range between $\sim$ 50 MeV and $\sim$ 100 GeV.

2.1 Detection principle

Different processes govern the interactions of photons with matter, depending on the photon energy and on the target material, and are presented in Fig. 2.2. Below $\sim$ 100 keV the main process is photoelectric absorption: an atomic electron absorbs the photon and is removed from its atom. The kinetic energy of the emitted electron (photoelectron) equals the photon energy minus the atomic binding energy of the electron. At higher energies, from 0.1 MeV to a few MeV, the photon sees the electrons

as essentially free, and Compton scattering is the main interaction mechanism.

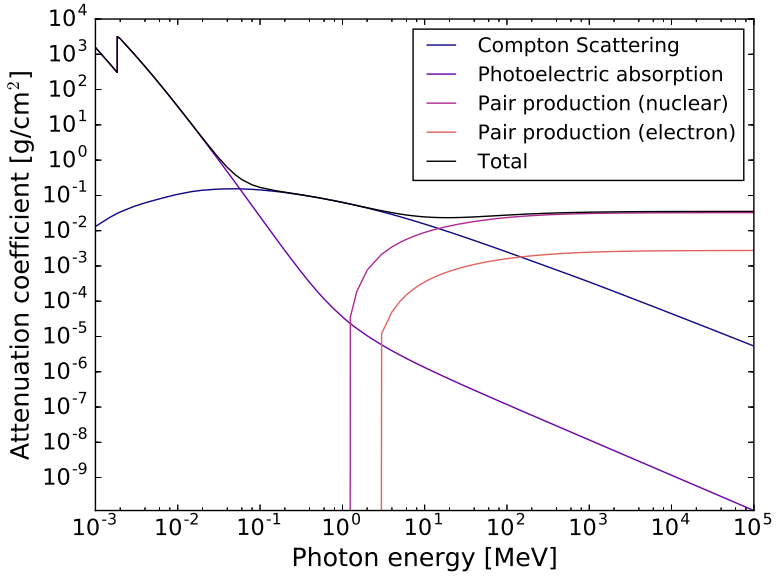

Figure 2.2: Mass absorption coefficient for photons in Silicon as a function of the photon energy. The contributions from photoelectric effect, Compton scattering and pair production are highlighted in different colors. The total attenuation is shown in black. Note the photoelectric peak for the K-shell and the difference between pair production in the field of the nucleus and the one in the electron field (triplet production). The triplet production has a higher threshold: $4m_ec^2$ instead of $2m_ec^2$. Data for the plot is taken from the NIST XCOM database.

For photons above 1.022 MeV, pair production in the Coulomb field of the nucleus is kinematically allowed. It becomes the dominant process above $\gtrsim$ 10 MeV. At intermediate photon energies, $1 \ll E_\gamma/m_ec^2 \ll 1/\alpha Z^3$, where α is the fine structure constant and Z is the atomic number of the material, the pair production cross section rises logarithmically with E_γ:

$$\sigma_{pair} = \alpha r_e^2 Z^2 \left[\frac{28}{9}\ln\frac{2E_\gamma}{m_ec^2} - \frac{218}{27}\right] \tag{2.1}$$

We note here that the fully differential pair production cross section depends on the relative orientation of the momenta of the particles in the final state with respect to the direction of the photon polarization vector. We will return to this dependence of the cross section on the polarization of the photon in Chapter 5, where we will discuss how this can be exploited to measure polarization in gamma rays. The high-energy asymptotic value of the integrated pair production cross section is given by (Patrignani et al., 2016):

$$\sigma_{pair} = \frac{7}{9}A/X_0N_A \tag{2.2}$$

where A is the atomic mass of the absorber material, $N_A = 6.022 \times 10^{23}$ mol^{-1} is Avogadro's number, and X_0 is the radiation length of the material. As can be seen from Eq. 2.2, X_0 is $7/9$ of the mean free path for pair production of photons. Through a sequence of bremsstrahlung and pair production processes, energetic primary particles (electrons or photons in this case) initiate electromagnetic showers when traveling though matter. In these showers the number of particles increases exponentially after each interaction length ($\sim X_0$ for both bremsstrahlung and pair-production processes, at first approximation), while the energy of each particle decreases accordingly. The shower grows until the ionization losses become dominant over bremsstrahlung. This happen at the critical energy E_C which is of the order of $\approx 650\text{MeV}/(Z+1)$ (Patrignani et al., 2016). The maximum number of particles in the shower is $N_{\text{max}} \sim E_0/E_C$ and is attained at a depth of $X_{\text{max}} \sim X_0 \ \ln E_0/E_C$, with E_0 being the energy of the primary particle (see, e.g., Engel et al., 2011, and references therein).

The electron and the positron are produced with opposite momenta in the center of mass reference frame. In the reference frame of the observer, momentum conservation reduces the opening angle of the pair to $\theta_{\text{op}} \sim m_e c^2/E_\gamma$ on average. Reconstructing the paths of the electron and positron pair in the first radiation length allows the measurement of the direction of the incoming photon. The main limitation to the precision of such a measure comes from multiple Coulomb scattering (MS). A charged particle traveling through matter will experience a series of elastic Coulomb scatterings (Rutherford, 2012) off the static electric fields of the nuclei. In each of these interactions, the particle is deflected by a small angle (in most of the cases), as depicted in Fig. 2.3. From the central limit theorem, it follows that, after many such deviations, the net scattering angle will be gaussian distributed. The root-mean-square width of this distribution, as projected on a plane perpendicular to the motion of the particle, is given by:

$$\theta_{\text{MS}} = \frac{13.6\text{MeV}}{\beta c p} q \sqrt{\frac{l}{X_0}} \left[1 + 0.038 \ln\left(l/X_0\right)\right] \tag{2.3}$$

for a particle of charge q, speed βc, and momentum p, respectively, traversing l/X_0 radiation lengths of material. The deflection of the charged particle caused by MS increases with the thickness of the material along the direction of the incoming particle and inversely with the energy of the particle.

To reduce the effect of MS, particle trackers are usually designed to limit the material budget as much as possible (reducing l), which calls additional devices to measure the energy. Calorimeters are dense, instrumented regions where the energy of the incoming particle is deposited, ultimately via ionization losses from the charged particles produced as the shower develops. Calorimeters are designed to contain as much of the particle shower as possible, since the total path length of all the particles in the shower is proportional to the primary energy. In case of imaging calorimeters, the spatial distribution of the energy deposit is also studied, improving the energy estimation and providing information about the type of particle (hadron or lepton) that initiated the shower.

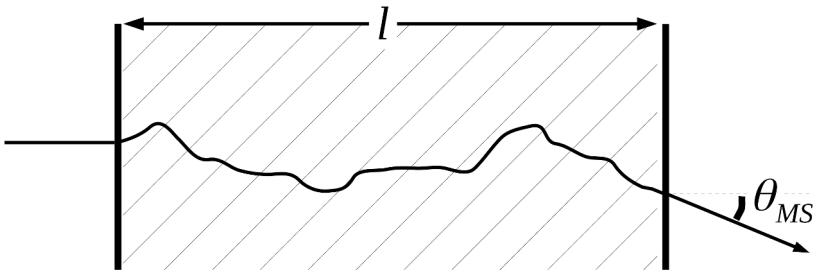

Figure 2.3: Schematic of multiple scattering: the net result of the many small-angle elastic scatterings undergone by a particle traversing a length l of matter.

2.2 The Fermi Large Area Telescope

The *Fermi* Gamma-ray Space Telescope (Gehrels et al., 1999, known as Gamma-ray Large Area Space Telescope, GLAST, before deployment) is a space-born observatory for high-energy gamma-ray astronomy. It is the result of a collaboration between NASA, the United States Department of Energy, and government agencies from France, Italy, Japan, and Sweden.

The two instruments on board *Fermi*, the Large Area Telescope (LAT, Atwood et al., 2009) and the Gamma-ray Burst Monitor (GBM, Meegan et al., 2009) were designed to improve on the legacy of the Energetic Gamma Ray Experiment Telescope (EGRET, Kanbach et al., 1989) and Burst and Transient Spectrometer Experiment (BATSE, Fishman et al., 1982) of the Compton Gamma-Ray Observatory[1] (GCRO Gehrels et al., 1994).

Fermi was successfully launched to low Earth orbit in June 2008. After some testing, both the LAT and the GBM started data acquisition, revealing the first-light all-sky image[2] on August 26. With the exception of an emergency maneuver to dodge a defunct Cold-War spy satellite[3], spacecraft operations have been smooth since launch. Recently, the LAT has reached the milestone of 500 billion triggered event readouts. Due to its huge scientific success and to the excellent condition of the spacecraft, NASA support for the *Fermi* mission has been confirmed until 2018, doubling the initial 5-year duration. After the first year of the mission both the LAT and the GBM have been operating as open observatories, releasing the data to the public as soon as it processed, a policy that has undoubtedly

[1] CGRO was one of the four NASA Great Observatories, the others being the Hubble (Ford et al., 1998, e.g.) and Spitzer (Werner et al., 2004) space telescopes and the Chandra X-ray observatory (Weisskopf et al., 2000). CGRO was a very ambitious project: weighting 17 tons it was, and still is, the heaviest scientific payload to ever be flown in space. Originally scheduled to fly until 2007, it was intentionally deorbited in 2000 after the failure of one of its three stabilizing gyroscopes. While it was still fully capable of operating with the remaining two, an additional failure would have made a controlled de-orbit complex and dangerous. At the time, it was estimated that there was a 1/1000 chance that one person would be killed in case of an uncontrolled reentry of such a massive craft. As a matter of fact, 6-ton debris did survive the re-entry and hit the Earth's surface. More interesting details can be found at this address: http://spaceflightnow.com/cgrodeorbit/status.html.

[2] https://apod.nasa.gov/apod/ap080828.html

[3] More details at https://www.nasa.gov/mission_pages/GLAST/news/bullet-dodge.html.

contributed to the scientific success of the mission.

2.2.1 Design

The LAT is the main instrument on board of the *Fermi* Gamma Ray Space Telescope. It is an imaging pair-conversion telescope sensitive to photon energies from ≈30 MeV to hundreds of GeV. It uses a particle tracker to measure the direction of the incoming photons, an electromagnetic calorimeter to estimate the energy, and an anticoincidence detector to veto charged particle events. The LAT has a modular design, composed of 16 identical towers arranged in a 4×4 grid. Each tower contains a converter-tracker element, a calorimeter module, and the respective electronics. A drawing of the LAT showing these three main components is presented in Fig. 2.4. The entire detector is 0.72 m deep for a surface area of $\sim 1.8 \times 1.8$ m^2; it weighs 2789 kg and consumes 650 W of electrical power. The aspect ratio (height/width) of the LAT is 0.4, giving the instrument a large field of view (FoV).

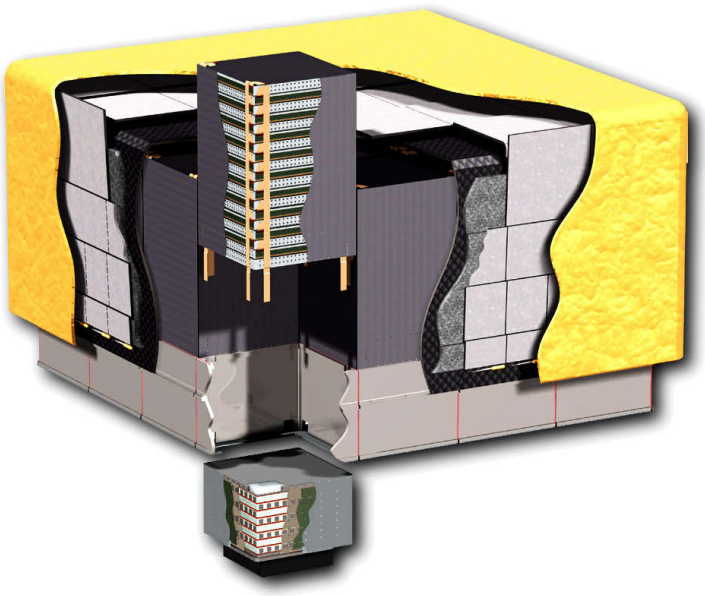

Figure 2.4: Cutaway view of the *Fermi*-LAT. The yellow foil is the thermal/micro-meteorite shield covering the scintillator tiles of the anti-coincidence detectors. The tracker and calorimeter elements of a tower are also exposed. Image adapted from Atwood et al. (2007).

Converter-tracker

At the heart of the LAT is a solid-state converter-tracker, described in detail in Atwood et al. (2007) and Bregeon (2011). It serves the twofold purpose of providing the target material to convert the incoming photons into $e^{\pm}$ pairs and of reconstructing the direction of the gamma rays. It also provides the main

event trigger for the entire instrument. In each tracker module, layers of silicon-strip detectors (SSDs) are interleaved with tungsten converter foils with the purpose of increasing the conversion efficiency. Each SSD is 0.4% radiation lengths (400μm) in thickness and the readout strips in the chip are 228 μm apart. As the SSD are single-sided, the converter foils are followed by a pair of SSDs to record the x and y coordinates of the track hit. There are 18 of such x, y measurement double-layers in each tower. The distance between the lower SSDs in each layer and the next tungsten foil is 30 mm. With more than 70 m^2 of silicon detectors and almost 900000 read-out channels, the LAT is the largest tracker ever flown into space.

To ensure good angular resolution in the lowest part of the energy range, where MS dominates the tracking accuracy, while providing the conversion efficiency needed to extend the effective area up to higher energies, the tracker is divided in two sections. The top 12 layers are equipped with 'thin' converter foils of 0.027 radiation lengths (0.095 mm) thickness and constitute the 'FRONT' of the tracker, while the last 4 (the 'BACK' of the tracker) have thicker converter foils of 0.18 radiation lengths (0.72 mm). The overall material depth of the tracker is $\sim$1.2 radiation lengths at normal incidence, resulting in the conversion of 63% of the incoming gamma rays. It is worth noting that a significant fraction, $\sim 11\%$, of the incoming events are converted in the silicon detectors themselves.

Calorimeter

After traversing the tracker, the $e^{\pm}$ pair enters the calorimeter. Each calorimeter module is composed of 96 CsI(Tl) optically isolated scintillator rods of 2.7 cm$\times$2.0 cm$\times$32.6 cm arranged on 8 layers. Successive layers are rotated by 90° to form an hodoscopic structure (Carlson et al., 1996). Combined together, the 16 calorimeter modules weigh $\sim$1800 kg. The light produced in the crystals is collected at both ends of the scintillator rods using PIN photo-diodes, allowing the reconstruction of the longitudinal position of the energy deposition along the crystal by means of the difference in intensity between the two read-outs. Together with the 2 discrete x and y coordinates given by the position of the crystal, this gives the LAT calorimeter the capability to image the shower and reconstruct its direction. This imaging capability contributes significantly to the background rejection. It also allows the estimation of the energy even for showers that are not fully contained (Fabjan and Gianotti, 2003), extending the high-energy reach of the calorimeter beyond the limit imposed by its depth of 8.9 radiation lengths.

Anti-coincidence detector

The flux of charged CRs is several thousand times higher than the flux of astrophysical gamma rays. To suppress this huge background, the LAT is equipped with an anti-coincidence detector (ACD). Charged particles, in contrast to photons, will produce a signal in this detector that can be used to veto the

event. The ACD is composed of 86 partially overlapping plastic scintillator tiles. The tiled design avoids self-veto from charged particles produced inside the LAT by high-energy gamma rays. Gaps between the tiles are filled with bundles of flexible plastic scintillator fibers. Given the critical importance of this system, each tile is coupled to two photomultiplier tubes (PMTs) for redundancy. These PMTs are the only non-solid state detectors used in the LAT. To ensure the integrity of the light-tight insulation of the tiles throughout the mission, the ACD is completely covered by a micrometeorite shield.

2.2.2 From trigger to high-level science data

The complex architecture of the LAT trigger and event reconstruction is discussed in detail in Ackermann et al. (2012a) and Atwood et al. (2009). Here we recall the main steps that separate a gamma-ray interaction in the LAT from the moment the high-level data is made available and public.

Taking all the LAT sub-systems together, more than a million channels have to be read out for each event. Besides consuming significant electrical power, readout introduces a minimum of 26.5 μs of dead time. The hardware trigger is designed to limit the dead-time fraction to less than $\sim 10\%$, discarding charged particle background events while retaining gamma rays with good efficiency. Each detector subsystem can rise a series of trigger primitives (trigger request). One of the most important is the TKR primitive, which requires the coincidence of 3 consecutive x, y tracker layers recording a signal within a single tower (this is the reason why the last 2 layers of the tracker have no converter foil: events converting there would not be triggered). The trigger primitives are then combined into 'trigger engines' which eventually initiate the read-out of the entire instrument. Triggered events are then analyzed through the onboard filters to further reduce background contamination, in order to meet the limited bandwidth available for data downlink. These filters reduce the $\sim$ 4 kHz average trigger rate to $\sim$ 400 Hz. Comparing it to the $\sim$ 2 Hz average rate of cosmic gamma rays in the LAT, it is clear that the great majority of downlinked events are background.

The on-ground event reconstruction uses track-finding and vertexing algorithms to reconstruct the event topology from the distribution of hits in the tracker. The energy of the event is estimated from the total sum of the energy deposit in the calorimeter, corrected to take into account leakage outside the calorimeter and the energy deposited in the tracker. Several algorithms are used to perform these tasks efficiently over the broad energy range of the LAT. Multivariate analysis methods are then used to combine all the available information into estimators of the event energy and direction, as well as to estimate 'gamma-likeliness' of the event, a measure of the agreement between the measured event topology and what is expected for a gamma-ray of comparable energy and arrival direction. The LAT collaboration releases data in different event classes corresponding to different hardness of the background rejection cuts, from the TRANSIENT event class to the increasingly pure SOURCE, CLEAN and ULTRACLEAN event classes. Combined together, the hardware trigger, the on-board filter, and the

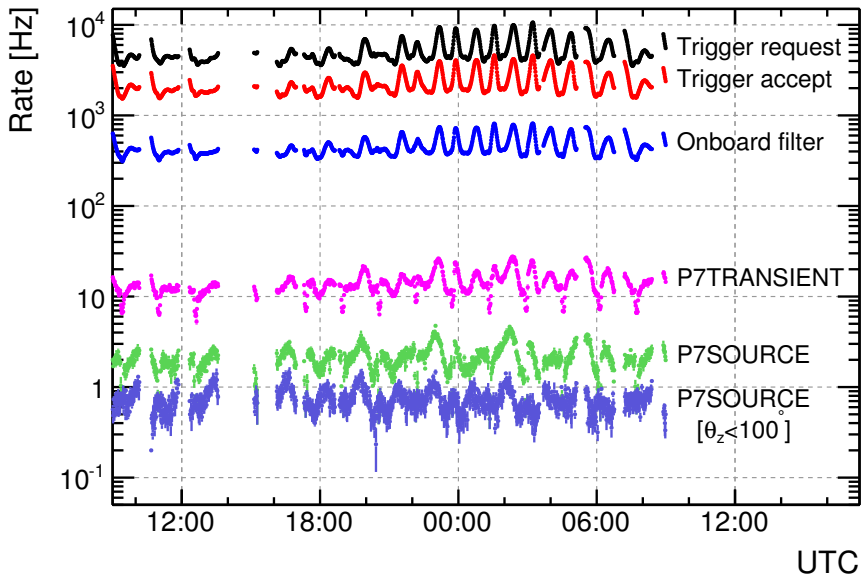

Figure 2.5: Event rates at the different stages of the acquisition and analysis chain for a typical day of the mission. A fraction of the high number of trigger requests (black line) initiate the read out of the instrument (red line). Background contamination of the sample of triggered events is reduced by onboard filters (blue line) before the data is downlinked to Earth where it is processed and classified by event class. The trends in the rates are due to modulation of the charged particle fluxes with the LAT orbit. Image taken from Ackermann et al. (2012a).

background rejection suppress the charged particle background by a factor $\sim 10^6$, while retaining a signal efficiency of $\gtrsim 75\%$.

Since the second year of the mission, all high-level science data collected by both instruments on *Fermi* are non-proprietary and are released as soon as possible, typically within 8-10 hours of triggering, see Fig. 2.6.

2.2.3 Response functions

The instrument response functions (IRFs) provides the mapping from the distribution of event counts in reconstructed energy and instrument coordinates to an astrophysical description of the sky in terms of fluxes. As such, the IRFs provide the basis for the analysis of the LAT data[1]. The IRFs are determined by the design of the instrument and by the reconstruction and event selection algorithms. They are determined using extensive Monte Carlo (MC) simulations that include an accurate description of the detector design, physics interactions, spacecraft conditions in orbit, and event processing.

[1]The analysis of LAT data is based on maximum likelihood methods (Mattox et al., 1996). Extensive documentation and tutorials can be found at https://fermi.gsfc.nasa.gov/ssc/data/analysis/scitools/

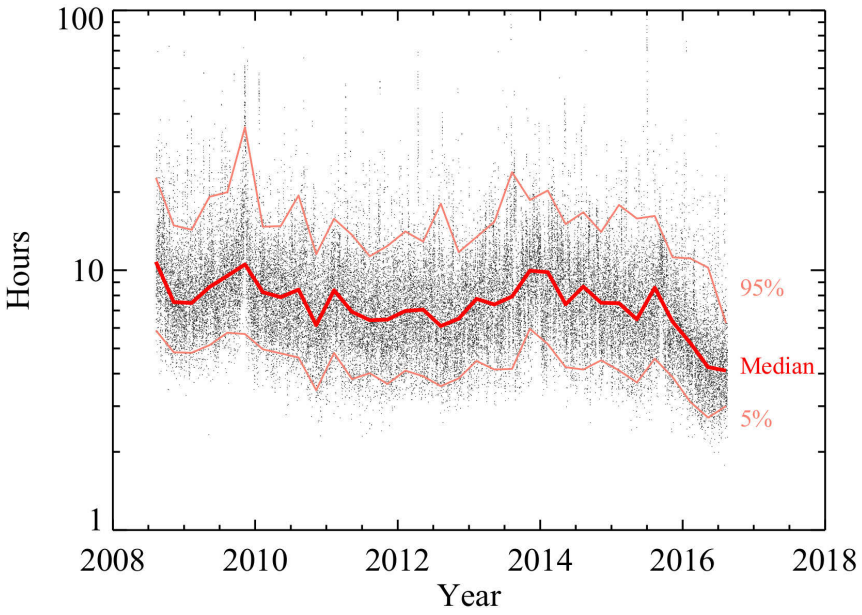

Figure 2.6: Progress of the latency of the LAT data through the mission. The latency is defined as the time difference between the moment in which the processed data-runs are available and the time of the trigger.

The IRFs are verified using on-orbit data. The response of the LAT can be factored in three parts: the point spread function (PSF), the effective area (A_{eff}), and the energy dispersion (E_{disp}). These functions are shown in Fig. 2.7 for the SOURCE event class, the standard event class for point-source analysis. For an event with a given energy E and arrival direction k, the PSF describes the probability that it is measured as coming from a different direction k'. Conversely, the energy dispersion gives the probability of reconstructing an event at energy E'. Finally, A_{eff} is given by the product of the geometrical acceptance of the LAT, the gamma-ray conversion probability, and the detector and reconstruction efficiency. As with the other IRFs, A_{eff} depends on the energy and arrival direction of the event in the reference frame of the instrument.

The LAT PSF is dominated by multiple scattering at low energies and by the finite spacing of the tracker strips at high energies. It strongly depends on the particle energy, varying approximated as $E^{-0.8}$ and reaching an asymptotic value of $\sim 0.2^{\circ}$ (for the acceptance-weighted 95% containment radius) above 20 GeV, see Fig. 2.7a. The FRONT section has roughly a factor two better PSF than the BACK section of the LAT due to the thinner converter foils and hence lower multiple scattering.

The energy resolution is presented in Fig 2.7b. It is of the order of 7% at 10 GeV and degrades to $\geq$ 20% at both ends of the energy range: at high energies the showers are no longer contained in the calorimeter, while at low energies the resolution is limited by stochastic fluctuations in the electromagnetic shower as well as by readout noise.

The LAT effective area is shown in Fig. 2.7d. It saturates at a value of ~ 0.9 m^2 above a few GeV

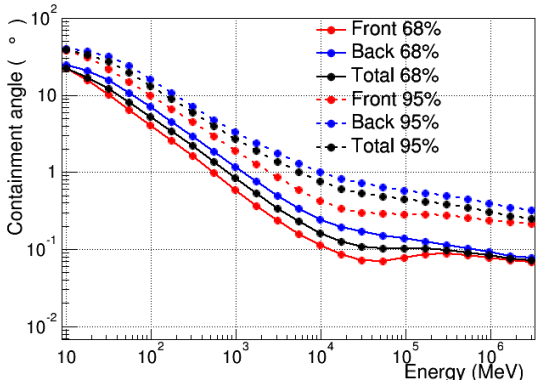

(a) Acceptance-weighted point spread function

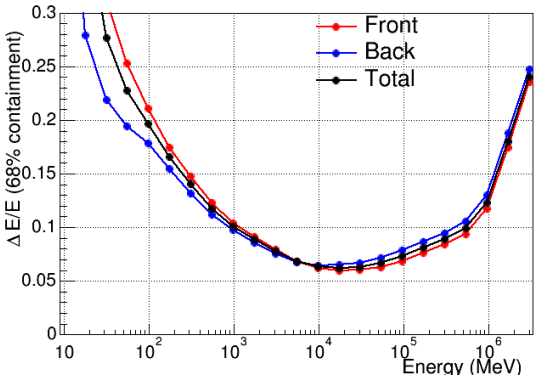

(b) Acceptance-weighted energy resolution

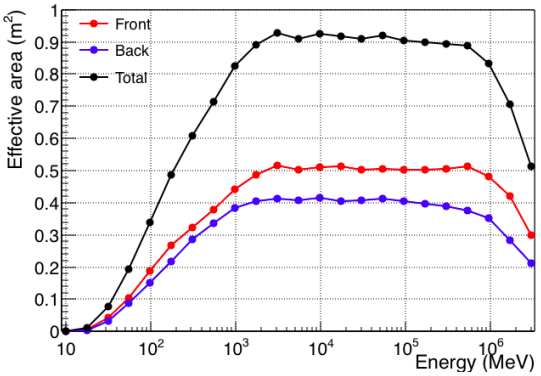

(c) Effective area at normal incidence

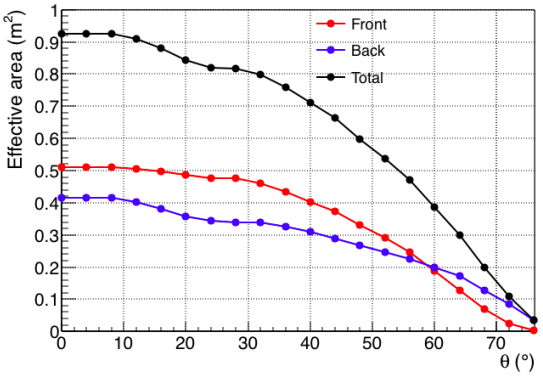

(d) Off-axis angular profile of A_{eff} at 10 GeV

Figure 2.7: LAT IRFs version P8R2_V6 for the SOURCE event class as a function of event energy. The contributions of the FRONT and BACK sections of the tracker are shown in red and blue respectively. The PSF and the energy resolution are weighted by the acceptance, defined as the integral of the effective area over the field of view of the instrument. Images taken from the LAT performance page.

for the SOURCE event class. Thanks to the low aspect-ratio of the LAT, the effective area is relatively independent of the off-axis angle of the event, as shown in Fig. 2.7d, and changes only by ∼15% at 30° off-axis. This gives the LAT a large field of view (FoV) of ~ 2.4 sr. With this large FoV, the LAT observes ∼20% of the entire sky instantaneously.

2.2.4 Observations

The *Fermi* gamma-ray space telescope is orbiting the Earth at 565 Km altitude and 26.5° inclination. The orbital period is 96.5 minutes. Observations are interrupted during the passages through the South Atlantic Anomaly (SAA), a region with a high density of charged particles that are trapped by the configuration of the Earth's magnetic field. This results in the loss of $\sim$ 15% observing time and to

a consequent 15% difference between the northern and southern exposures, as the spacecraft enters the SAA while in the southern part of the orbit. The LAT surveys the sky for $\gtrsim$ 80% of its time. While in survey mode, the LAT boresight looks away from the Earth, pointing above and below the orbital plane between consecutive orbits. This observing mode provides a full image of the sky roughly every two orbits ($\sim$ three hours) with an equivalent on-axis exposure of 30 minutes. Besides the survey, the LAT also performs various types of pointed observations, summarized in Table 2.1. While pointing, the LAT boresight aims a few degrees away from the target and the spacecraft rotates around the line of sight to average out geometrical effects induced by the $x - y$ structure of the tracker. Scheduled observations are regularly performed to increase the exposure on the Galactic center region. Pointed observations after Target of Opportunity (ToO) or Autonomous Repoint Request (ARR) allows the follow-up of interesting transient events. The total amount of time in the scheduled and ToO observations is constrained to be $\lesssim$20% of the total observing time.

Table 2.1: The different observation strategies performed by the LAT and their relative frequency. Source: https://fermi.gsfc.nasa.gov/ssc/proposals/pointing_analysis/

Mode	Frequency	Duration
Survey	$\sim 80\%$	...
Pointed - Scheduled	5-20 per year	few weeks
Pointed - ToO	5-20 per year	$\sim$1 week
Pointed - ARR	$\sim$1/week	5 hours

Chapter 3

The high-energy gamma-ray sky

An overview of the high-energy (HE, $>$ 100 MeV) gamma-ray sky is given by Fig. 3.1. This image presents the GeV sky as seen by the LAT after 8 years of observations. Both large scale structures and point-like sources can be immediately spotted in this image. The bright horizontal region is the

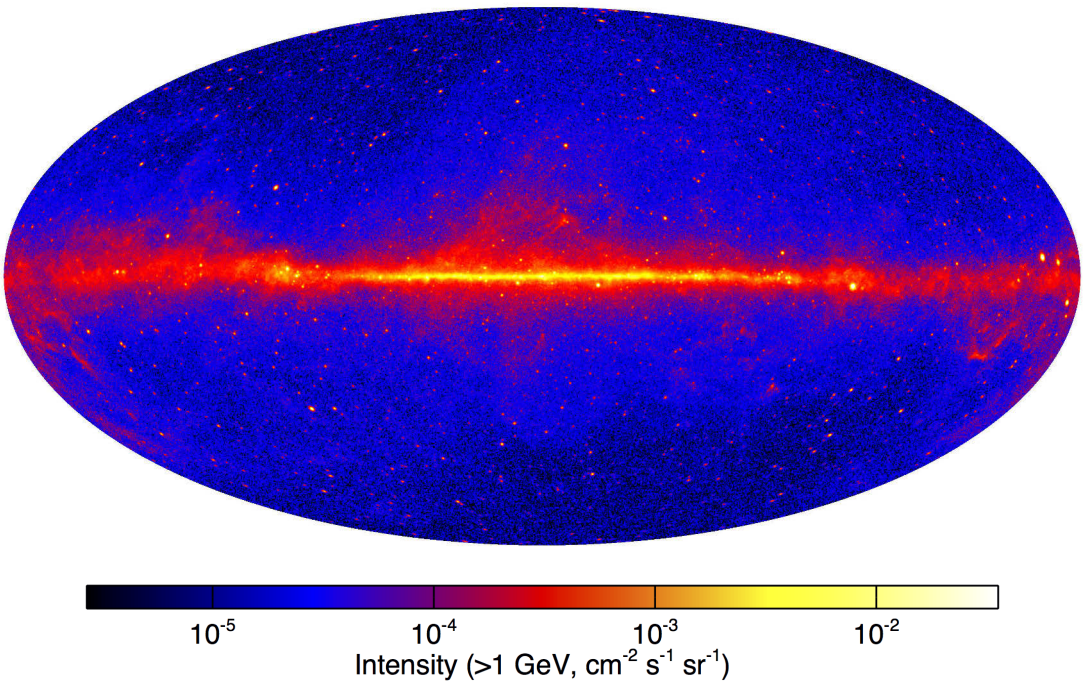

Figure 3.1: All-sky intensity map obtained from 8 years of Fermi Pass 8 data above 1 GeV. The map is in Galactic coordinates and Aitoff projection and has been smoothed with a 0.25° full-width-at-half-maximum Gaussian. The bright Galactic diffuse emission is clearly visible, as well as a wealth of point sources distributed over the entire sky. Image Credit: *Fermi* LAT Collaboration

Galactic diffuse emission. The diffuse gamma-ray emission of our galaxy results from the interaction of energetic CRs with the interstellar medium (via π^0 decay and bremsstrahlung) and with radiation fields (via inverse Compton scattering) in the galaxy (Ackermann et al., 2012d). Other large-scale structures discovered in the LAT sky are the so-called *Fermi* Bubbles: gigantic lobes extending to 55° north and south of the Galactic center region (Dobler et al., 2010; Su et al., 2010; Ackermann et al., 2014b). Besides these local structures, many sources are visible in the image. Gamma-ray sources are intrinsically extended objects. However, in HE, spatial extension has been measured only for a few tens of objects. The great majority of the gamma-ray sources appear point-like due to their distance and the limited angular resolution of the LAT. At the moment of writing, more than 3000 sources have been catalogued in the LAT data (Acero et al., 2015), a factor of 10 improvement over the few hundreds gamma-ray sources known in the EGRET era (Hartman et al., 1999).

As the *Fermi* mission progresses, its scientific outcome has shifted from individual sources and the discovery of new phenomena (see Michelson et al., 2010, for a review of the scientific results from the first year of the mission) to more systematic and general population studies. Since the beginning of the mission, one of the main objectives was to extensively map the entire gamma-ray sky. The main characteristics of the latest *Fermi*-LAT source catalogs are summarized in Table 3.1.

Table 3.1: Summary of the various source catalogs produced with the LAT data. Only the most recent versions of the catalogs are listed here. The catalogs released by the *Fermi*-LAT collaboration are based on likelihood analysis techniques, with the exception of the 1FAV, which uses a photometric technique. The candidate sources in the D^{3}PO catalog are instead found by applying image processing techniques to the LAT photon counts maps.

Catalog	Energy range	Reference
LAT 4-year Point Source Catalog (3FGL)	0.1−300 GeV	Acero et al. (2015)
1^{st} Fermi LAT Supernova Remnant Catalog (1SNR)	1−100 GeV	Acero et al. (2016)
LAT Third High-Energy Source Catalog (3FHL)	50 GeV−2 TeV	Ajello et al. (2017)
LAT 3-year Catalog of Gamma-ray Pulsars	0.1−300 GeV	Abdo et al. (2013)
LAT First Gamma-Ray Burst Catalog	0.1−100 GeV	Ackermann et al. (2013c)
LAT First Inner Galaxy point source Catalog	1−100 GeV	Ajello et al. (2016)
FAVA first flaring source list (1FAV)	0.1−300 GeV	Ackermann et al. (2013a)
D^{3}PO Fermi 6.5-year candidate source list (1DF)	0.6−307.2 GeV	Selig et al. (2015)

So far, the most extensive high-energy gamma-ray catalog is the LAT Third Source Catalog (3FGL, Acero et al., 2015), listing 3033 sources detected during the first 4 years of the *Fermi* mission. The source composition of the 3FGL is presented in Fig. 3.2. As is visible, of the 3FGL sources, more than 1100 have been associated with Active Galactic Nuclei (AGN) of the blazar class. The different source classes will be briefly described in the following sections. Surprisingly, one third of the 3FGL sources

have no known counterpart at other wavelengths. A considerable effort is ongoing to reduce this number through targeted observations at other wavelengths[1].

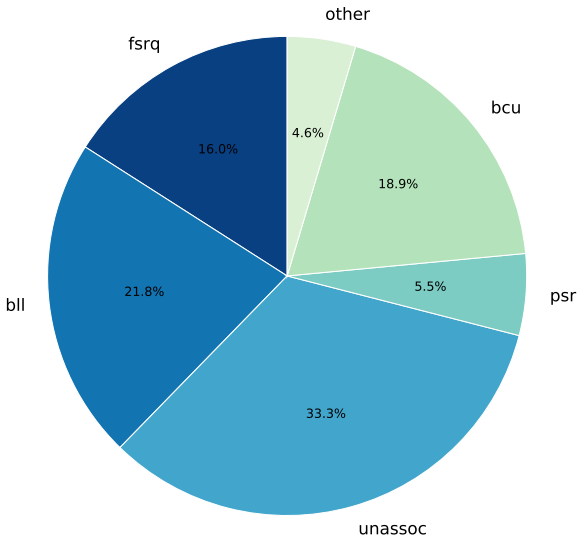

Figure 3.2: Composition of the 3FGL in terms of source classes, showing the fraction of sources in the most populated classes. Blazars, a particular class of active Galactic nuclei, is the most represented class. They are divided into BL Lacertae ('bll') and flat spectrum radio quasar ('fsrq') type objects. The label 'bcu' refers to blazars of uncertain type. The label 'psr' refers to pulsars. Classes with less than 100 members are grouped together in the 'other' slice of the pie chart. These include: binary systems, novae, non-blazar types of AGN, star-forming regions, pulsar wind nebulae, and supernovae remnants.

3.1 Taxonomy of gamma-ray sources

Gamma-ray emission has been now observed from a wide variety of Galactic and extragalactic objects. Gamma-ray sources are very diverse among each other. Yet, all gamma-ray sources must host regions of powerful particle acceleration. The basic energetics of every particle accelerator is governed only by its size and magnetic field. Both compact and highly magnetized objects of $\sim$ 10 km radius, and kpc-scale structures of diluted gas are able to accelerate particles and can be observed in gamma rays (Hillas, 1984). At the moment of writing, 10 broad classes of gamma-ray sources are known. In this section, we briefly outline the basic properties of these source classes and provide relevant references for the interested reader.

[1]For example, the Swift X-ray telescope has a standing program (Stroh and Falcone, 2013) to follow-up *Fermi* unassociated sources, the results of which are available at http://www.swift.psu.edu/unassociated/. An effort to perform optical spectroscopic observations for 3FGL blazars of uncertain type is presented in Álvarez Crespo et al. (2016).

3.1.1 Galactic

Pulsars and Pulsar-wind Nebulae

Figure 3.3: Composite image of the Crab pulsar and nebulae. The X-ray emission observed by the Chandra X-ray Observatory is shown in blue, revealing the complex morphology of the magnetosphere. Red/yellow colors show optical (Hubble Space Telescope) observations and purple represents infrared (from Spitzer Space Telescope). Image credits: X-ray: NASA/CXC/SAO/F.Seward; Optical: NASA/ESA/ASU/J.Hester & A.Loll; Infrared: NASA/JPL-Caltech/Univ. Minn./R.Gehrz.

Pulsars were the first gamma-ray sources to be detected back in the '70s (Kniffen et al., 1974; Thompson et al., 1975). This is the most populated class of Galactic gamma-ray sources, with $\gtrsim 150$ detected so far (Acero et al., 2015; Abdo et al., 2013). Pulsars are rapidly-rotating highly-magnetized neutron stars formed after the collapse of a massive progenitor (Pacini, 1967; Gold, 1968). Magnetic fields extract rotational energy from the system and power relativistic plasma winds which fill the environment of the pulsar, called the magnetosphere. The radiation emitted by the pulsar is believed to be collimated around the direction of the magnetic axis of the system. This axis is generally not aligned with the rotation axis. Pulsed emission is observed as this radiation beam sweeps the Earth. In some cases, the pulsar wind illuminates the remnants of the progenitor star, giving rise to bright nebulae called pulsar wind nebulae (PWN, Gaensler and Slane, 2006). A prominent example of such a system is the Crab nebula, one of the most-studied celestial bodies. A selection of observations of this nebula is shown Fig. 3.3. A recent review of gamma-ray pulsars can be found in Grenier and Harding (2015), while in Cerutti and Beloborodov (2016) the physics of the pulsar magnetosphere is presented.

Supernovae Remnants

Supernovae are catastrophic stellar explosions, of thermonuclear or gravitational nature, in which an enormous amount of energy, of the order of $\sim 10^{51}$ ergs, is released as kinetic energy of stellar ejecta. A supersonic shock wave is blown into the circumstellar medium, see Fig. 3.4, providing the site for particle acceleration. At the shock boundary, charged particles are accelerated via Fermi acceleration up to energies of ∼PeV (Burrows, 2000). At the moment of writing, gamma rays have been detected from 30 supernovae remnants (SNRs) (Acero et al., 2016). SNRs have long been suspected of accelerating CRs up to the knee, based on consideration on the energetics of these sources (see, e.g., Helder et al., 2012). The detection of the pion bump in the gamma-ray spectra of two SNR has provided the first direct evidence for acceleration of hadrons in some of these sources (Ackermann et al., 2013b). However, leptonic models can also explain the emission of some objects.

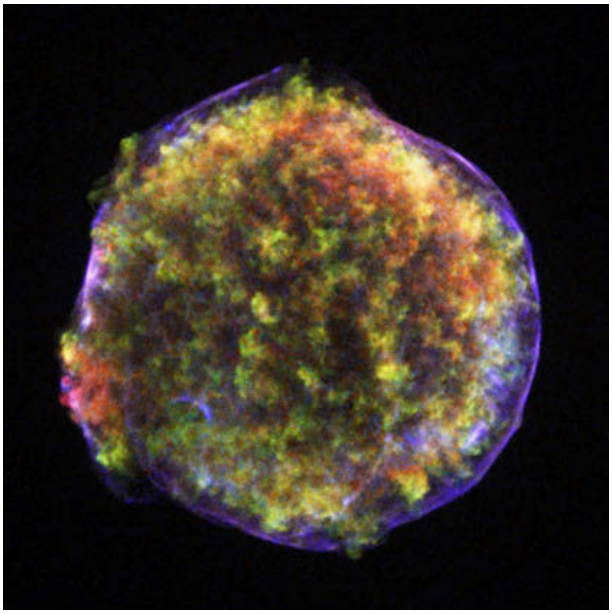

Figure 3.4: Chandra X-ray image of the SNR associated with the supernova observed by Tycho Brahe in 1572. Red/green: stellar debris, blue: high-energy electrons. Credit: NASA/CXC/Rutgers/J.Warren & J.Hughes et al.

Binary systems

Binary systems are systems of two celestial bodies close enough to orbit each other around the barycenter of the system. Following the classification proposed in Dubus (2015), and presented in Fig. 3.5, gamma-ray emitting binary systems can be divided into four different classes, depending on the type of objects constituting the system:

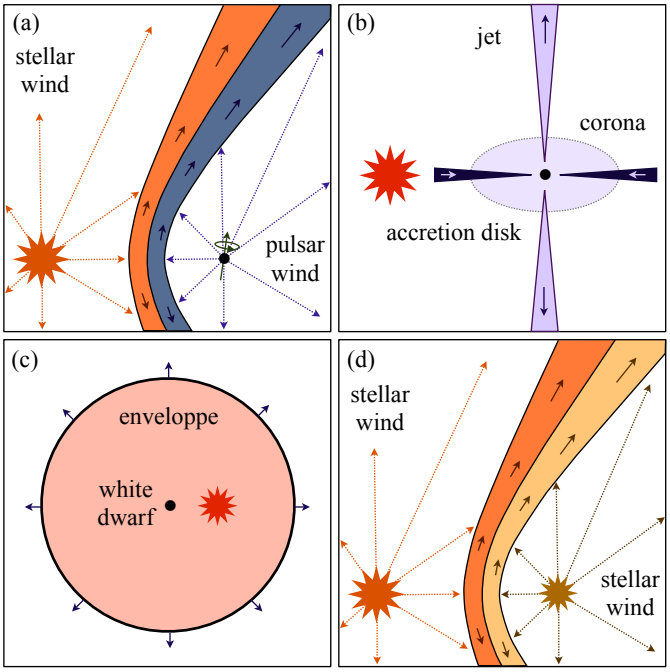

Figure 3.5: Sketches of the geometry of different types of gamma-ray emitting binary systems. a) High-mass gamma-ray binary b) microquasar c) nova d) colliding-wind binary. Taken from Dubus (2015).

- **gamma-ray binaries**: These sources emit most of their power at energies > 1 MeV. At the moment of writing, five gamma-ray binaries have been detected so far in the high-energy band: PSR B1259−63 (Abdo et al., 2011a), LS 5039 (Abdo et al., 2009c), LS I +61 303 (Abdo et al., 2009b), 1FGL J1018.6−5856 (Ackermann et al., 2012e) and CXOU J053600.0−673507, which is located in the Large Magellanic cloud (Corbet et al., 2016). Another gamma-ray binary, HESS J0632+057, was discovered by H.E.S.S. but remains undetected at GeV energies (Caliandro et al., 2013). Gamma-ray binaries are composed of a high- or low-mass ($\geq 10M_{\odot}$ or $\leq 1M_{\odot}$) star and a compact companion, likely a neutron star. Only for PSR B1259-63 has the compact object been identified as a pulsar. VHE emission has been detected only in the case of high-mass binary systems (see, e.g.: Aharonian et al., 2005b,a; Albert et al., 2006). The non-thermal emission from these systems is believed to be ultimately powered by the pulsar rotation and dominates over the thermal emission of the companion star (Dubus, 2013). As we will see in Section 3.2.1, gamma-ray binaries are variable in gamma rays, often showing modulation with the orbital period (see, e.g. Ackermann et al., 2012e).

- **X-ray binaries (microquasars)**: Two such systems have been detected in high-energy gamma rays (Bodaghee et al., 2013): Cyg X-3 (Abdo et al., 2009d) and Cyg X-1 (Del Monte et al., 2010).

In these systems, the compact object is likely to be a black hole that accretes matter from a massive companion star. A fraction of the gravitational energy is lost by the accreted matter and powers relativistic outflows (jets), similar to those observed in radio-loud active galactic nuclei (see Section 3.1.2). Such sources radiate most of their energy in the X-ray band, hence the name.

- **novae**: Novae are thermonuclear explosions on the surface of a white-dwarf star in a binary system. They occur when the accretion of hydrogen from the atmosphere of the companion star onto the surface of the white dwarf eventually builds up the pressure and temperature needed to initiate nuclear fusion. In the first 8 years of the *Fermi* mission, seven novae have been confidently detected in gamma-rays by the LAT[1]. Gamma-ray emission from novae can result from the interaction of the expanding stellar ejecta with the circumstellar medium, as in the case of the 'symbiotic' nova V407 Cygni 2010 (Abdo et al., 2010d), or with the interstellar medium. Novae are inherently transient phenomena, with gamma-ray emission characterized by a 2-3 day long peak and a total duration of the order of $\sim$ 20 days (Ackermann et al., 2014a).

- **colliding-wind binaries**: These systems host two massive stars. A shock front is formed when the two powerful stellar winds collide. At the moment, only one colliding wind binary has been detected in gamma rays: η Carinae (Abdo et al., 2010).

3.1.2 Extragalactic

Active Galactic Nuclei

As was already mentioned, active galactic nuclei (AGN) are the most populated class of gamma-ray sources, totaling $\sim 1/3$ of the known sources (Ackermann et al., 2015b). AGN are compact regions at the center of some galaxies, whose luminosities outshine the host galaxies. Supermassive black holes weighing millions to billions of solar masses are at the center of these galaxies. The gravitational energy lost by matter spiraling into the black hole is believed to power the broad-band emission of these sources. Radio-loud AGN show gigantic outflows of ultrarelativistic plasma (jets) streaming away from the black hole, see Fig. 3.6. Synchrotron emission of the electrons in the jets makes them very bright in the radio band, hence their name.

The appearance of such axially symmetric objects depends strongly on the viewing angle. Based on this consideration, the unified scheme of radio-loud AGN (Barthel, 1989; Urry and Padovani, 1995) explains the different morphologies and spectral properties of the many sub-classes of observed AGN in terms of the viewing angle. A sketch of this scheme is presented in Fig. 3.7. Blazars are a special

[1] An updated list of Galactic novae is maintained at: http://asd.gsfc.nasa.gov/Koji.Mukai/novae/novae.html

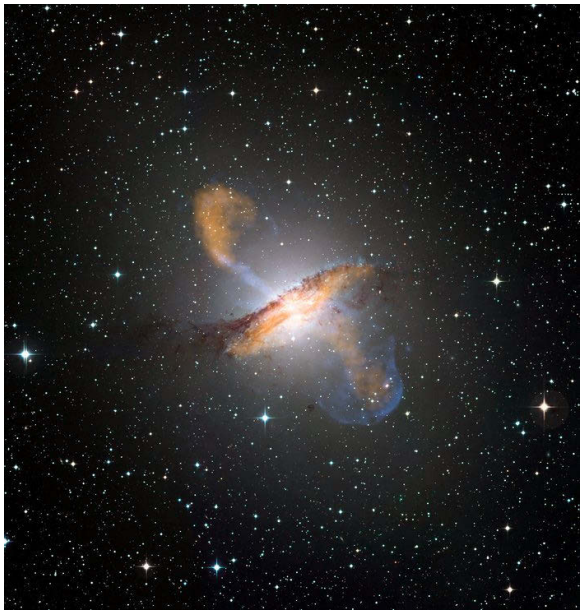

Figure 3.6: A composite radio (orange), optical (colors), and X-ray (blue) image of the nearby AGN Centaurus A. Image credit: ESO/WFI (Optical); MPIfR/ESO/APEX/A.Weiss et al. (Submillimetre); NASA/CXC/CfA/R.Kraft et al. (X-ray).

class of AGN, in which the jets are pointed within a few degrees of the direction of the Earth. Despite the peculiarity of this geometrical arrangement, blazar are by far the most common gamma-ray source class. Relativistic beaming of the jet emission increases their apparent luminosity and shifts the emission to higher frequencies. A recent review of the gamma-ray emission by AGN can be found in Massaro et al. (2016). Another defining characteristic of blazars is their variability, detected at all timescales and wavelengths. The variability properties of blazars will be presented in Section 3.2. According to the properties of their optical spectrum, blazars can be divided in two families: BL Lacertae objects (BL Lacs) and flat-spectrum-radio-quasars (FSRQs). Contrary to what the name suggests, the optical spectra of FSRQs are characterized by the presence of strong and broad emission lines, which are weak or altogether absent in the spectra of BL Lacs objects. The name refers to the appearance of the spectrum at radio frequencies. On average, FSRQs are more luminous than BL Lacs and are located further away from us; the second peak in the SED of FSRQs is located at lower energies than the one of BL Lacs (see, e.g., D'Elia and Cavaliere, 2001). Another common classification of blazars is based on the position of the synchrotron peak ν_{peak} of the SED. According to this scheme we have low-synchrotron-peaked (LSP, for sources with $\nu_{peak} < 10^{14}$Hz), intermediate-synchrotron-peaked (ISP, $10^{14}\text{Hz} < \nu_{peak} < 10^{15}\text{Hz}$), and high-synchrotron-peaked (HSP, $\nu_{peak} > 10^{15}$Hz) blazars.

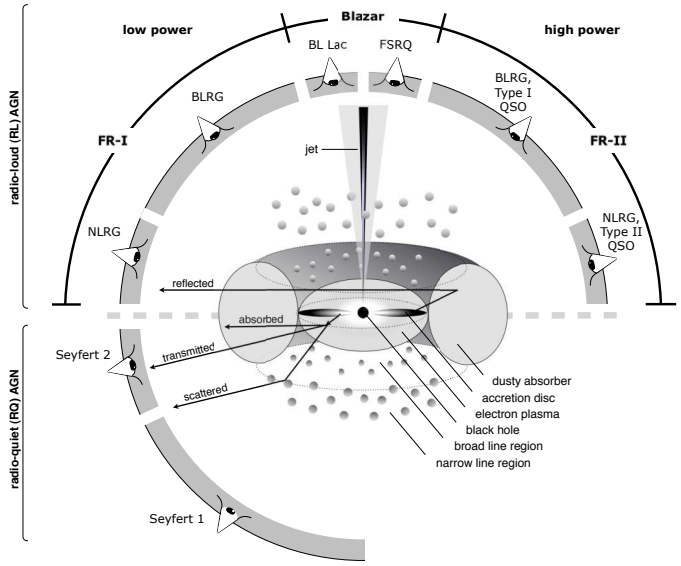

Figure 3.7: The unified scheme of AGN: due to its axial symmetry, the appearance of an AGN is strongly dependent on the viewing angle and on the absorption along the line of sight (Barthel, 1989; Urry and Padovani, 1995). Image take from Beckmann and Shrader (2012).

Starburst galaxies

Starburst galaxies are galaxies undergoing a phase of highly increased star formation. A large flux of CRs is sustained during the starburst phase thanks to the high rate of supernovae explosions. These CRs produce gamma rays upon interaction with the dense interstellar medium (see Ohm, 2016, for a recent review). The gamma-ray emission of these systems is therefore dominated by a diffuse component, rather than individual objects. Two such systems, M82 and NGC 253, have been detected in high energy by the LAT (Abdo et al., 2010c; Ackermann et al., 2012b) and at very-high energies by ground-based Cherenkov telescopes (Acero et al., 2009; Acciari et al., 2009).

Gamma-ray bursts

Gamma-ray bursts (GRBs) are powerful bursts of high-energy radiation from sources at cosmological distances. They are characterized by an intense flash peaking between 0.1-1 MeV and lasting from a few milliseconds to hundreds of seconds, followed by an 'afterglow' phase on the timescale of days/weeks. During the afterglow, the GRB becomes visible also at longer wavelengths (Gomboc, 2012; Piron, 2016). GRBs are detected at a rate of ~ 1 per day and are uniformly distributed over the sky (Meegan et al., 1992). Two types of GRBs can be distinguished: long or short GRBs depending on

Figure 3.8: Mosaic image of the starburst galaxy Messier 82 (M82) obtained with the Hubble Space Telescope with optical and infrared filters. Visible in red is ionized hydrogen blown away by combined stellar winds. This image was released to celebrate 16 years of the Hubble telescope. Credit: NASA, ESA, The Hubble Heritage Team, (STScI/AURA).

the duration of the prompt emission, with the dividing line being set at ~ 2 seconds (Kouveliotou et al., 1993). It is thought that GRBs are related to the formation of black holes either in the collapse of the core of a massive star (for long GRBs), or in the merging of two compact objects such as neutron stars or black holes. More details can be found in Gehrels and Mészáros (2012) and references therein.

3.2 Variability in gamma-rays

The emission of many gamma-ray sources has been observed to vary with time. Roughly 20% of the sources in the 3FGL have been found to be variable on monthly timescales. Often, the fluxes have been found to increase by more than a factor of a few in a matter of days or less. These extreme phenomena, called flares, are far from being rare. Flares have been observed in the gamma-ray emission of a wide variety of objects, most notably from blazars, but also from binary systems and the Crab PWN. In fact, for all classes of gamma-ray sources in which a compact object is responsible for the gamma-ray emission (thus excluding SNRs and starburst galaxies), variability has been detected for at least some members of the class.

Studying the variability patterns and timescales, i.e. the characteristic time intervals over which statistically significant flux variations are observed, provides insight into the size and location of the

emitting region and on the mechanism responsible for the gamma-ray production. If a minimum variability timescale τ has been observed, causality dictates that the size of the emission region cannot be larger than:

$$L < \frac{c\tau(1+z)^{-1}}{\gamma\,(1-\beta\cos\theta)} \tag{3.1}$$

where z is the redshift of the source and the denominator is the inverse of Doppler factor for a source moving with speed βc at an angle θ with respect to the observer. An application of this kind of argument can be found in Rani et al. (2013), for example. The greatest advantages from variability studies come in cases when several instruments, observing in different regions of the electromagnetic spectrum, record the same outburst. In this case correlations, typical timescales, and time lags between the multiwavelength light curves can constrain emission models and the physical properties of the source environment. For example, multiwavelength observations of the variability of the blazar Mkn 421 made it possible to constrain or set limits on: the size of the emitting region, the strength of the magnetic field, and the Lorentz and Doppler factor of the jet (Błażejowski et al., 2005). Finally, observations of correlated variability at different wavelengths provide the key to firmly identify the counterparts of the gamma-ray sources. Due to the relatively poor angular resolution of high-energy gamma-ray observatories, several sources can be often found within the gamma-ray error circle. Detecting correlated variability resolves any ambiguity and in fact has been used to single out the counterparts of many of the 238 firmly identified gamma-ray sources in the 3FGL.

3.2.1 Flux Variability

Based on the properties of their gamma-ray light curves, i.e. the time series of the source fluxes, variable sources can be grouped into three broad families: noisy and aperiodic, periodic, and one-time transients such as novae and GRBs, for which no continuous emission is found.

Gamma-ray light curves from AGN and the Crab nebula often show flares and long-term variability. Two examples are presented in the first two panels of Fig.3.9. The power-spectral density (PSD, Klis, 1989) of their light curves is well approximated by a power-law function of the frequency ν, $\mathrm{PSD}(\nu) \propto \nu^{-\beta}$ over a wide range of frequencies (see, e.g. Abdo et al., 2010a). This relation, characteristic of so-called red-noise processes, implies that fluctuations on longer timescales account for a greater fraction of the power of the light curve than the ones at higher frequencies. Values of β measured for gamma-ray light curves of blazars are around ~ 1.2 on average (Ackermann et al., 2011). Values of β as high as ~ 1.7 were detected from some very bright source (Abdo et al., 2010a). For the Crab nebula β is found to be ~ 0.9 (Buehler et al., 2012). Although AGN are variable at all the observed wavelengths, strong gamma-ray variability of the Crab nebula was unexpected and has not been observed by VHE gamma-ray observatories.

Other features of blazar light curves can be extracted by looking at the distribution of the flux points. These distributions appears skewed to larger flux values (the flares) and often can be well reproduced by log-normal distributions (Ackermann et al., 2015b). The log-normal behavior seems to hint at multiplicative processes at the basis of the emission: it is the natural outcome of a process whose output is the product of a large number of independently varying elements. Log-normality is also linked to a linear relation between the mean flux in a given period and the root mean square (rms) amplitude of flux variations in the time interval (see, e.g., Uttley et al., 2005; Biteau and Giebels, 2012). That is, variability is enhanced when the source is brighter. This rms-flux proportionality implies that variability at the low frequencies (which determines the mean flux of each time range) is coupled to variability at the high frequencies (responsible for the variance inside the time range). This relation has been observed at all the accessible timescales, most notably in X-rays (Vaughan et al., 2003), but also in HE gamma rays (see, e.g., Larsson et al., 2016), and in VHE gamma rays, for example in the case of the bright blazars PKS 2155-304 (Abramowski et al., 2010) and Mkn 421 (Tluczykont et al., 2010). There is some indication that variability properties differ for the two blazar families, BL Lacs and FSRQs. As of today, a larger fraction of FSRQs are found to be variable than BL Lacs (Ackermann et al., 2015b). Looking at the flux distributions and shape of the light curves, BL Lacs seem to have fewer large flares and smoother light curves than FSRQs (Paggi et al., 2011).

In pulsars and binary systems, a varying degree of periodicity is induced by rotation in the former, or orbital motion in the latter. Pulsars are the archetype of a periodic source. Their collimated radiation beams sweep the Earth at regular intervals giving rise to distinct pulses with periods ranging from milliseconds to seconds. This periodicity is not perfect and the period between the pulses constantly increases as the system loses rotational energy. Besides this predictable behavior, several types of timing irregularities have been detected in pulsars (Lyne et al., 2010) such as, for example, glitches and timing noise. Glitches are changes in the rotational state of the neutron star where the rotation frequency abruptly increases, often followed by a decay to its normal value (Espinoza et al., 2011). Timing noise manifests itself as a non-gaussian distribution of the timing residuals (the differences between the expected and measured time of the pulse) which shows quasi-periodic patterns for some objects (Hobbs et al., 2010). Additionally, abrupt changes in the gamma-ray flux of two pulsars have recently been observed. The gamma-ray emission of PSR J2021+4026 dropped abruptly in October 2011 after a slight and gradual increase in the preceding three years (Allafort et al., 2013). For the millisecond pulsar binary PSR J1023+0038, an increase of the gamma-ray flux was observed around June 2013, probably as a consequence of the development of an accretion disk (Takata et al., 2014).

As seen in Section 3.1.1, the emission of gamma-ray binaries originates from the interaction between the stellar and the compact object's winds. It is modulated by the orbital motion of these systems. The orbital periods of the known gamma-ray binaries range from $\lesssim 4$ days for LS 5039 to $\sim$ 3.5 years for PSR B1259−63. The maximum of the HE emission is found at different orbital phases for

each of these objects. Highly variable gamma-ray emission and bright flares have also been observed for PSR B1259−63, roughly a month after its 2010 periastron passage (Tam et al., 2011). In the bottom panel of Fig. 3.9 we report, as an example, the HE gamma-ray light curve of LSI+61 303.

Modulation with the orbital period is also found in high-energy gamma rays in the microquasar Cygnus X−3 (Abdo et al., 2009d). This source also shows very bright gamma-ray flares correlated with radio and X-ray emission (Corbel et al., 2012). The steady-state emission of Cygnus X−1 is not detected in gamma-rays, and the source is only visible during flaring states (Del Monte et al., 2010; Bodaghee et al., 2013). In X-ray, microquasars show red-noise variability similar to the one described in the above paragraph (see e.g. Axelsson et al., 2009). This is not surprising considering the similarity between those two source types.

Like in many other attempts to classify natural phenomena, there are some objects that defy any simplistic scheme such as the one proposed above. For example, some novae can repeat on timescales of tens to one hundred years: these are the so-called recurrent novae (Anupama, 2013). Another example is the blazar PG 1553+113: for this source, quasi-periodic variability of the gamma-ray flux has been observed (Ackermann et al., 2015a). Although the significance of the gamma-ray periodicity is marginal, it is strengthened by correlations with optical and radio observations.

3.2.2 Spectral Variability

In many cases, flux variations are accompanied by variation in the spectral shape of the sources. In blazars, brighter fluxes are often accompanied by harder spectra. This 'harder when brighter' behavior of blazar has been observed in X-rays for a sample of BL Lac objects (see, e.g., Giommi et al., 1990). In HE gamma rays, the hardening of the spectra during flaring states has been significantly detected for FSRQs and for LSP and ISP BL Lacs (Williamson et al., 2014; Abdo et al., 2010b). As we have seen in Section 1.3, the spectral properties of the gamma rays are related to the energy distribution of the emitting particles. Under simplifying assumptions, it can be shown that if the timescale over which particles are accelerated is smaller than the one over which the particles lose their energy, the gamma-ray spectra will harden as the flux increases. Conversely, a softening of the spectra is expected in cases where the acceleration timescale is larger than the cooling time (Kirk et al., 1998). The 'harder when brighter' behavior is not a standard feature of blazar flares and in many cases the situation is reversed, or more complicated, or both. When monitoring the FSRQ PKS1510−089 with the LAT it was found that the spectra was softening as the flux increased. This situation changed above a certain flux value, after which the spectra started to harden for higher fluxes (Abdo et al., 2010a). In the VHE regime, the situation is similar, with a positive detection of this effect (for example, see Aharonian et al., 2002), side by side with more complex cases, similar to the one of PKS 1510−089, as for example Abramowski et al. (2010).

Blazars are not the only source class characterized by this 'harder when brighter' behavior. This behavior has also been observed in other types of active galaxies such as the radio galaxy NGC1275 (Brown and Adams, 2011). The situation for gamma-ray binaries seems to be completely reversed. In these sources, the high-energy spectra tend to soften as the flux increases (Dubus, 2013).

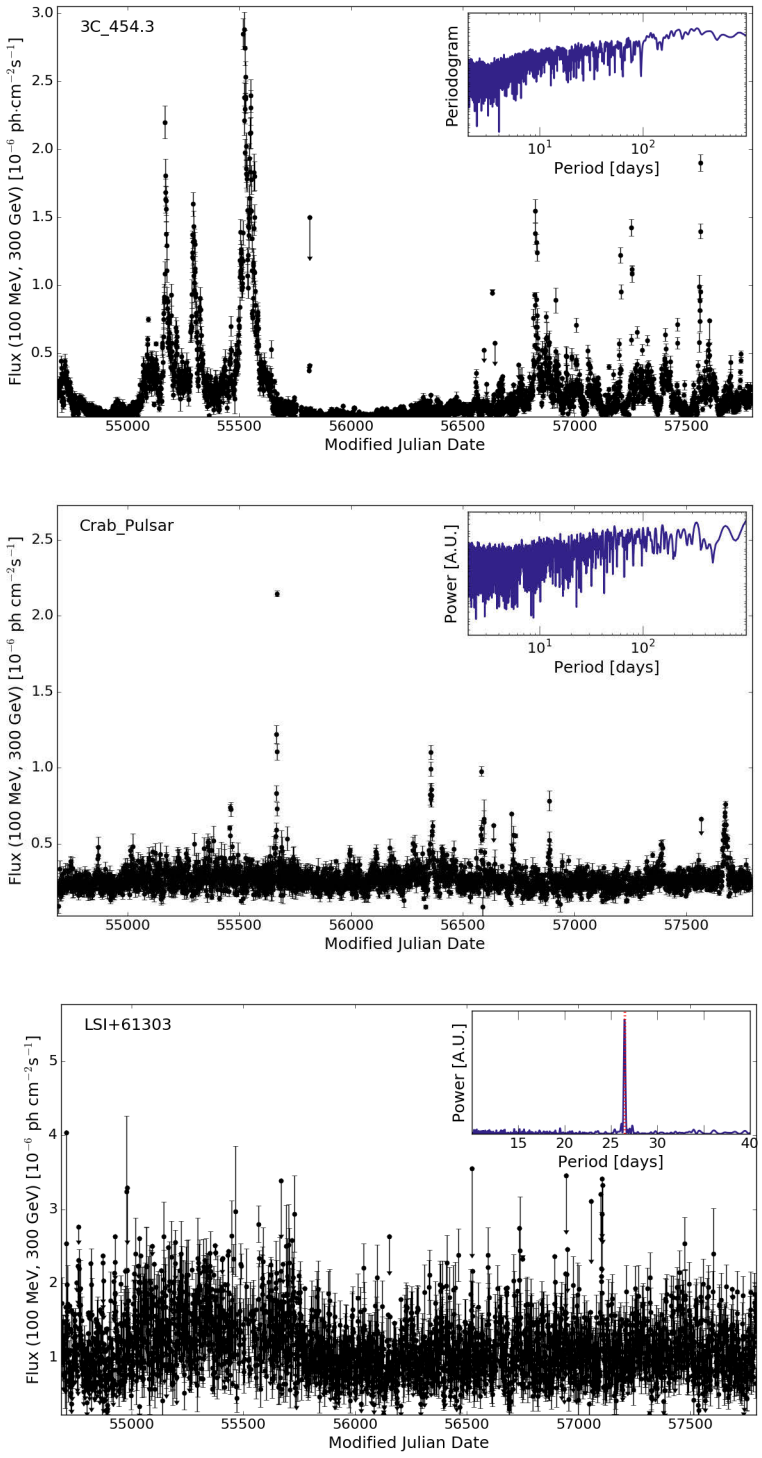

Figure 3.9: Examples of gamma-ray light curves and their periodograms (in inset plots). Top: the FSRQ 3C 454.3, middle: the Crab pulsar, bottom: the gamma-ray binary system LS I +61 303. Although at first glance the light curve from LSI+61 303 does not look periodic, a clear spike corresponding to the orbital period of $\sim$ 26.5 days appears in the periodogram. The data used to produce these plot can be downloaded from the *Fermi*-LAT Monitored Source List page: https://fermi.gsfc.nasa.gov/ssc/data/access/lat/msl_lc/.

Chapter 4

The Second Fermi All-sky Variability Analysis Catalog

This chapter presents a catalog of variable gamma-ray sources discovered in the first 7.4 years of *Fermi*-LAT data using the Fermi All-sky Variability Analysis (FAVA). This second FAVA catalog (2FAV, Abdollahi et al., 2016) contains 4547 gamma-ray flares detected with a pre-trial significance of 6σ over the timescale of a week and in two energy bands: 100−800 MeV and 0.8−300 GeV. Studying the positions of these transients, we identify 518 variable gamma-ray sources, 77 of which have no likely counterpart in other gamma-ray and blazar catalogs. The spectra of the 2FAV flares is studied for the different source classes. A significant hardening of the flare spectra with higher flux levels is established as a general feature of flares associated with FSRQs, and of high-energy flares associated with BL Lacs. An observed limit on the spectral hardness of the flares ($\Gamma \gtrsim 1.5$) translate, under a simple leptonic scenario, to a constraint on spectra of the injected electrons, which cannot be harder than $p \sim 2$. In the 2FAV, both the sources and the flares are provided together with likely gamma-ray counterparts of the sources, and detailed spatial and spectral information on every flare.

We note that an initial version of FAVA was already used by the *Fermi*-LAT collaboration since 2012 as an online monitoring tool and to produce a first catalog of flaring sources (1FAV, Ackermann et al., 2013a). The work presented here consisted in a major upgrade and extension of the analysis pipeline and in the data analysis and catalog preparation which lead to the 2FAV. In addition to the analysis upgrade and the construction of the catalog, I have also prepared a publication presenting the resulting source list. The initial version of the paper has already been released (Abdollahi et al., 2016). This chapter necessarily shares the results from this publication, but expands on the description of the methods.

4.1 Introduction

With its large field of view covering 20% of the sky at any moment and almost continuous operations in survey mode, the LAT is perfectly suited to monitor the gamma-ray sky and to study variable and transient phenomena. To exploit this capability, the *Fermi*-LAT Collaboration maintains different analysis pipelines dedicated to the search for and monitoring of variable gamma-ray sources. Of these, FAVA and the *Fermi* Flare Advocate program (Ciprini and Fermi-LAT Collaboration, 2012) are both blind, all-sky variability searches. The Flare Advocate variability search uses wavelet decomposition of the all-sky counts maps to initially locate the transients. With this method, shifters monitor the variability of the gamma-ray sky on timescales of 6 hours and 1 day. FAVA is instead fully automated and requires no human intervention. The reports from the FAVA online monitoring are forwarded to the Flare Advocate shifters, often leading to the circulation of an Astronomer's Telegram when new flaring sources are discovered (see, e.g., Ajello et al., 2014; Kocevski et al., 2015).

The current version of FAVA consists of two sequential steps. As a first step, a photometric analysis is used to blindly scan the entire sky and to provide a coarse localization of the transients. Statistically significant excesses are further analyzed, in a second step, using maximum likelihood techniques (see, e.g., Mattox et al., 1996). Prior to this work, FAVA consisted only of the photometric analysis. This photometric analysis searches for variability by comparing, for every direction in the sky, the number of counts detected in a given time bin Δt with the number of counts one would expect based on a long term ($\gg \Delta t$) average emission. With respect to maximum likelihood analysis methods, the photometric analysis has several advantages:

- it is model independent: the expected counts are derived from the data itself. The photometric analysis does not require any model of the gamma-ray diffuse emission. FAVA assumes only that this diffuse emission does not vary on timescales comparable to the duration of the *Fermi* mission. When comparing the observed counts to the expected ones, any such constant term will cancel out. FAVA is also insensitive to the spectral shape of the flares.

- it is equally sensitive to both positive and negative flux variations. In the following, we will use the word 'flare' to refer to both absence and excess of counts.

- it is a robust technique and it is computationally inexpensive. It can be used to perform all-sky variability searches in different energy bands and over different timescales.

Despite these advantages, the usefulness of the photometric analysis is hampered by a poor localization accuracy. As the method does not rely on a fit of the spatial distribution of the events, the uncertainties on the position of any counts excess is determined by the LAT PSF. As seen in Section 2.2.3, the 68% containment radius of the LAT PSF is $\sim 0.8^{\circ}$ at 1 GeV and rapidly degrades for lower energies,

reaching $\sim 5^\circ$ at 100 MeV. As a consequence, the positions of low-energy flares of a single source, as reconstructed by the photometric analysis, are often scattered over scales of one degree or more. Another disadvantage of the photometric approach is that it cannot measure the spectra of the flares. These issues motivated the extension of the analysis that constitutes part of the work presented here.

4.2 FAVA analysis

FAVA now proceeds in two steps: a photometric technique is used to blindly scan the entire sky and to provide a coarse localization of the transients, and a likelihood analysis to accurately measure the flare position and its spectra. These two steps are described in this section. We stress again that the photometric part of the analysis was not developed during this work. The 1FAV catalog was constructed using only the photometric step of the analysis (Ackermann et al., 2013a).

In the analysis presented here, FAVA runs in weekly time bins and two energy bands: low energy (100−800 MeV) and high energy (0.8−300 GeV). Week-long time bins were also used in the 1FAV. The energy bands are now independent from one another (in the 1FAV the energy bands were defined as > 100 MeV and > 800 MeV). This allows the combination of two weak signals detected simultaneously in the two energy bands into a more significant overall detection. With respect to the 1FAV, FAVA is now using data from the Pass 8 data release (Atwood et al., 2013). We use the `P8R2_SOURCE` event class and cut on the zenith angle at 95° in order to reduce the contamination from the Earth's limb. Due to spacecraft motion, the Earth's limb emission appears variable in time and needs to be removed.

Besides being used to construct the 2FAV, the analysis pipeline developed in this thesis is running in real time, continuously monitoring the gamma-ray sky in search of new transients. Every week, the findings of the FAVA on-line analysis are released to the public via a web page at NASA's *Fermi* Science Support Center[1]. Thanks to its all-sky capabilities, FAVA was used by the *Fermi*-LAT collaboration to search for electromagnetic counterparts of the poorly localized gravitational waves recently detected (Abbott et al., 2016; Ackermann et al., 2016a) by the Laser Interferometer Gravitational-Wave Observatory (LIGO, Abbott et al., 2009).

4.2.1 Photometric all-sky search

The photometric step of FAVA is presented in detail in Ackermann et al. (2013a). Here it will be described briefly for reference and completeness. To account for the dependence of the LAT exposure and PSF on the energy and incident angle θ of the events, FAVA internally works in 12 logarithmic energy bins between 100 MeV and 300 GeV, and in four bins in $\cos\theta$. For each bin in energy E_i, time t_j, and angle θ_k, FAVA computes all-sky maps of the number of observed $N_{obs}(\mathbf{r}, E_i, t_j, \theta_k)$ and expected

[1] http://fermi.gsfc.nasa.gov/ssc/data/access/lat/FAVA/

$N_{exp}(\mathbf{r}, E_i, t_j, \theta_k)$ counts from the direction $\mathbf{r}$. These maps are binned with a resolution of $0.5^\circ \times 0.5^\circ$ per pixel. The number of total counts $N_{tot}(\mathbf{r}, E_i, \theta_k)$ observed from the pixel corresponding to $\mathbf{r}$ over a time range $T_{tot} > \Delta t$ is given by:

$$N_{tot}(\mathbf{r}, E_i, \theta_k) = \sum_{t_j=0}^{T_{tot}} N_{obs}(\mathbf{r}, E_i, t_j, \theta_k) \tag{4.1}$$

The number of expected counts in a given time bin is derived from $N_{tot}(\mathbf{r}, E_i, \theta_k)$, after accounting for the different exposures $\epsilon_{week}(\mathbf{r}, E_i, \theta_k)$ and $\epsilon_{tot}(\mathbf{r}, E_i, \theta_k)$:

$$N_{exp}(\mathbf{r}, E_i, t_j, \theta_k) = N_{tot}(\mathbf{r}, E_i, \theta_k) \frac{\epsilon_{week}(\mathbf{r}, E_i, \theta_k)}{\epsilon_{tot}(\mathbf{r}, E_i, \theta_k)} \tag{4.2}$$

For each energy and θ bin, the expected and observed counts maps are smoothed with the LAT PSF: each pixel is assigned the sum of all counts within the 68% containment radius of the PSF. After the exposure and PSF have been accounted for, the maps are integrated in θ and in energy. To improve the sensitivity of the analysis for flares with hard and soft spectra, the integration over the energy is performed separately in the two energy ranges: 100−800 MeV and 0.8−300 GeV. The probability for any excess/deficit of the number of observed counts with respect to the expected ones is computed with Poisson statistics, and then converted into gaussian significance, $S_{\rm LE/HE}$, for convenience. Hereafter, the symbols $S_{\rm LE/HE}$ will indicate the significance of the flares as measured solely by the photometric analysis. The corresponding quantity for the likelihood is the test-statistic (TS). As a result, for every time bin and energy band, all-sky maps of the number of expected and observed counts, as well as of the significance of the flux variation, are produced, see for example Fig. 4.1.

Local maxima and minima in the significance maps indicate positive and negative flux variations, respectively. A peak-finding algorithm (Morháč et al., 2000) is used to locate the flares in both the low- and high-energy significance maps. When, in the same week, a low energy flare is found within 3° of a significant ($S_{\rm HE} > 5.5\sigma$) high-energy flare, the two flares are assumed to originate from the same astrophysical event. In these cases the position assigned to the flare is the one measured by the high-energy analysis, which is more accurate due to the better PSF of the LAT at high energies. This distance threshold of 3°, already used in the 1FAV, gives a good compromise between the spatial density of flares recorded in one week, and the angular resolution of the photometric analysis.

To construct the 2FAV, we choose to limit the time range T_{tot} used to create the expected counts maps (see Eq. 4.1) to the 4-year period analyzed in the 3FGL, from 2008 August 4 to 2012 July 31. The statistical errors on the photometric technique are dominated by the low statistics of the weekly observed counts. Restricting T_{tot} to 4 years, instead of considering the full, 7.4-year long dataset of the 2FAV, does not introduce any significant error. As the number of expected counts is based on the 3FGL

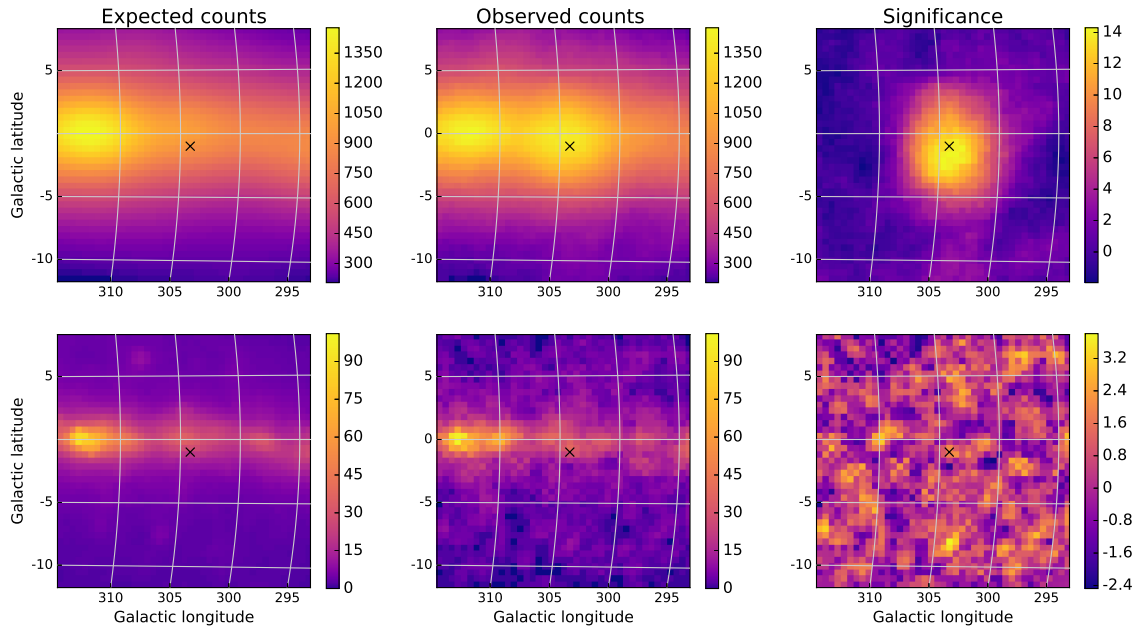

Figure 4.1: Sky maps from the FAVA photometric analysis step. The various panels show: expected counts (left), observed counts (center), and significance (right). The maps from the low- and high-energy analysis are shown in the top and bottom row respectively. All the maps are in Galactic coordinates. Shown is a $20^\circ \times 20^\circ$ portion of these all-sky maps, centered on the position of the binary system PSR B1259-63/LS 2883. The maps are relative to the week around MJD 55582, when the source flared in coincidence of one of the periastron passages. The position of this source is marked with a black 'X' . Adapted from Abdollahi et al. (2016).

time span, the photometric significance of the flares measured by FAVA refers to excess of counts with respect to the static, time-integrated 3FGL sky. As we will see in the next section, this choice of T_{tot} allows us to compare meaningfully the statistical significance of the flares as measured by the photometric and the likelihood analysis.

As seen in Sec. 3.2, the flux distribution of variable sources is skewed towards high fluxes: the mean value is typically greater than the mode of the flux distribution. For sources with frequent and bright flares the number of expected counts (derived from the time average) sensibly over-predict the level of the quiescent state emission of the source. As a consequence, such sources are often accompanied by a number of negative flares, corresponding to the quiescent periods. For the 2FAV such behavior has been corrected only in the case of the bright solar flare of 2012 March 7 (Ajello et al., 2014). To do this, a circular patch of 10° radius around the position of the Sun on the date of the flare has been masked out in the N_{obs} maps of the corresponding time bin. If not corrected, the solar flare would increase the level of the expected counts around its position. This excess of expected counts would introduce spurious negative flares in the catalog. Other solar flares occurred during the 3FGL time range had no measurable effect on the expected counts maps.

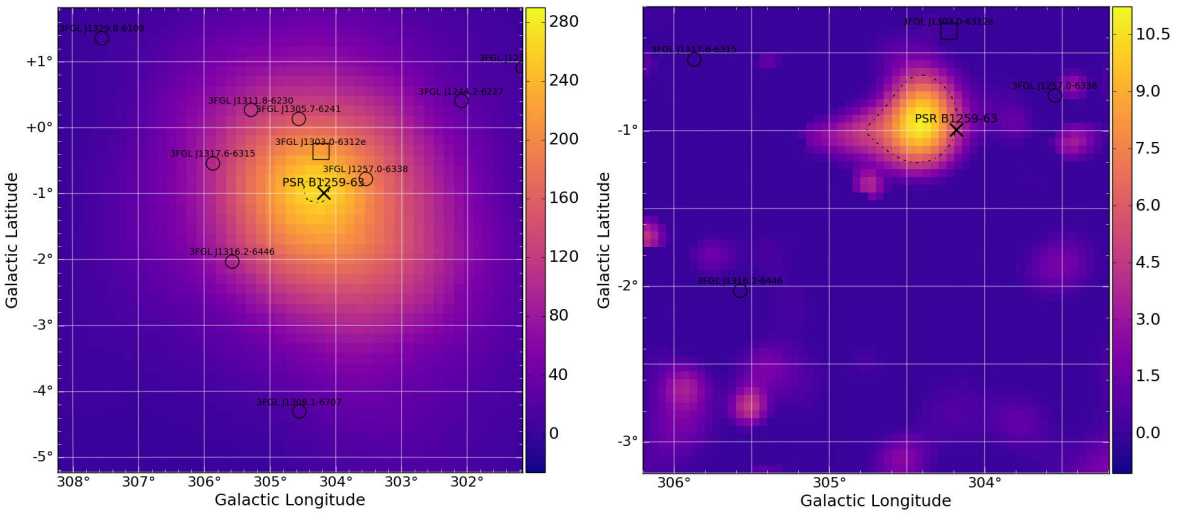

(a) Low-energy band, 100−800 MeV

(b) High-energy band, 0.8−300 GeV

Figure 4.2: TS maps from FAVA likelihood follow-up analysis. These maps target the bright flare of PSR B1259-63/LS 2883 during its first periastron passage. The photometric maps for this same flares are shown in Fig. 4.1. The photon index of the flare is $\Gamma = 3$ and the detection significance is higher in the low-energy band. The two TS maps are in Galactic coordinates. The maps for the low- and high-energy analysis are shown in the left and right panel respectively. The dashed lines show the 95% CL contour. In black, the nearby 3FGL sources (included in the sky model used in the likelihood fit) are shown. The position of PSR B1259-63/LS 2883 is indicated by a black 'X' . Adapted from Abdollahi et al. (2016).

4.2.2 Likelihood follow-up analysis

The likelihood follow-up analysis has the goal of providing a more accurate position for the flares, as well as of measuring their spectra. The photometric part of the analysis is used as a seed finder. Maximum likelihood techniques are computationally intensive. The likelihood follow-up is performed only on flares having a photometric significance greater than 4σ in at least one of the two energy bands. When this 'seed' condition is satisfied, the likelihood follow-up is executed for both energy bands. As the likelihood analysis methods available in the *Fermi* Science Tools cannot measure an absence of flux, negative flares are not processed by this analysis step.

The likelihood follow-up is based on the generation of maximum likelihood test-statistic (TS) maps using the `gttsmap` tool from the *Fermi* Science Tools[1] (ST). The TS is defined as:

$$\mathrm{TS} = -2 \log \left(\frac{\mathcal{L}_{\mathrm{max},0}}{\mathcal{L}_{\mathrm{max},1}} \right) \tag{4.3}$$

where $\mathcal{L}_{\mathrm{max},1}$ is the value of the maximum likelihood for a model that includes a candidate point source

[1] https://fermi.gsfc.nasa.gov/ssc/data/analysis/documentation/Cicerone/

with a power-law spectrum with a free in index and normalization, and $\mathcal{L}_{\max,0}$ is the maximum likelihood value for the same model, but without the additional source (the so-called 'null-hypothesis'). A TS map is the result of a series of likelihood fits obtained by moving the candidate point source over a grid of positions in the sky. Examples of these maps are shown in Fig 4.2.

The TS maps are centered on the position of the seed flares provided by the photometric analysis. The null-hypothesis model comprises of all the 3FGL sources within 30° and 12° of the seed position, at low and high energies respectively, and the templates for the Galactic and isotropic diffuse emissions for the Pass 8 `SOURCE` event class. The spatial morphology of the extended sources is also considered, using the templates provided by the *Fermi*-LAT collaboration[1]. In the fit, the spectra of the 3FGL sources are fixed to their catalog values. The index and normalization of the Galactic diffuse component are instead free parameters, as is the normalization of the isotropic diffuse component. The diffuse emission templates have a nominal normalization of 1 and are scaled in order to minimize the all-sky residuals for the 3FGL catalog analysis. Treating them as free fit parameters makes it possible to compensate for local large-scale residuals. It is a more conservative approach with respect to flare detection. The fitted values of the Galactic diffuse normalization are compatible with the nominal value of 1 within the statistical errors.

To summarize, the sky model used in the FAVA likelihood follow-up comprises of all the 3FGL sources (fixed) and the diffuse emission templates (free). The flare spectra are modeled with power laws with free indices and normalizations. The resulting values of TS measure the significance of an excess in flux, above a static 3FGL source population.

The analysis is binned in the low-energy band, unbinned at high energies. An unbinned analysis is more precise than a binned one as it exploits the full information from the event sample. However this comes at the price of increased computing times. As the gamma-ray fluxes steeply decline with energy, only in the high-energy band is the number of events is small enough to make an unbinned analysis viable. The parameters of the analysis are presented in Table 4.1. The TS maps computed at high energies are smaller in size and have a finer pixelization than the ones at low energies, taking advantage of the better PSF of the LAT in that energy band. The size and resolution of the TS maps are the result of a compromise between the accuracy of the flare localization (small pixels are required), the ability to accommodate misplaced positions of the seed (large maps are required), and the time constraints of the FAVA online monitoring tool (the computation timescales with the square of the number of pixels). With these settings, the average runtimes are $\sim$5 and $\sim$9 hours for the low- and high-energy band analyses, respectively (see Fig. 4.3). Using multiple cpus, the entire FAVA pipeline, including the photometric analysis, processes one week of data in $\sim$ 20 hours.

Once the TS maps are completed, they are used to measure the flare position and the corresponding statistical uncertainty, see Fig. 4.5. The position of the flare is estimated as the center of the pixel of

[1] https://fermi.gsfc.nasa.gov/ssc/data/access/lat/4yr_catalog/LAT_extended_sources_v15.tgz

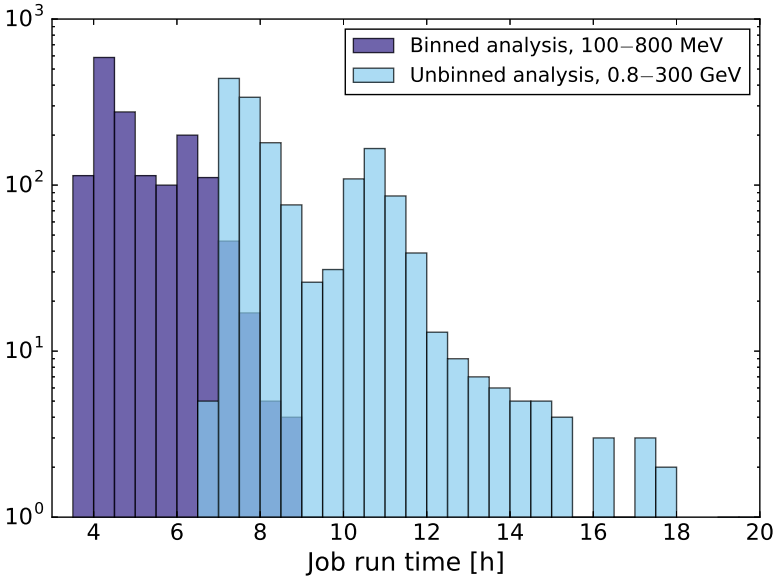

Figure 4.3: Distribution of the runtime for $\sim$ 1600 jobs of the FAVA likelihood analysis, including the TS map generation, the flare localization, and the second likelihood fit that measures the flare spectra. The distribution of the jobs of the unbinned analysis in the high-energy band is shown in dark-blue and in light-blue for the binned analysis jobs, performed at low energies.

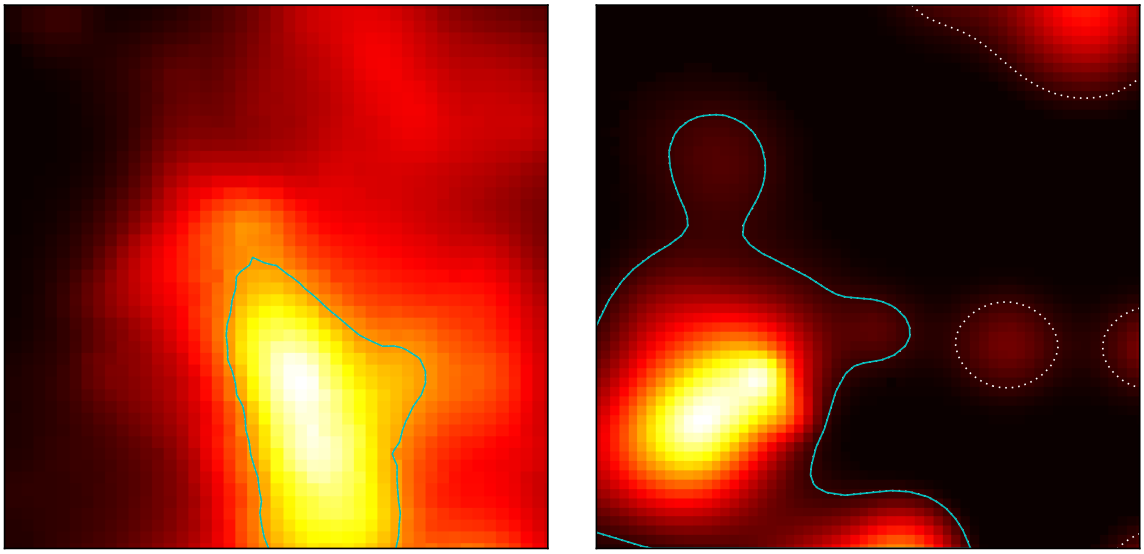

Figure 4.4: Examples of the results of the ray-casting algorithm used to identify and analyze the TS-map contours (shown here in arbitrary units). The paths of the contour are represented by the dotted white lines. The algorithm finds the path containing the maximum TS (cyan solid line). On the left is shown a TS map computed by the analysis in the low-energy band, on the right a TS map computed in the high-energy band.

Table 4.1: Parameters of the FAVA likelihood follow-up analysis in the two energy bands.

Parameter	Low-energy band	High-energy band
Analysis type	binned (10 logarithmic bins)	unbinned
Sky-model radius	30°	12°
Radius of the fitted region	15°	8°
TS map size	$7^\circ \times 7^\circ$	$3^\circ \times 3^\circ$
TS map pixel size	$0.15^\circ \times 0.15^\circ$	$0.05^\circ \times 0.05^\circ$

coordinates $(x_{\text{max}}, y_{\text{max}})$ corresponding to the maximum value of TS. The contour of the TS profile at the 95% confidence level is found by slicing the image horizontally, to find the contour where TS is a $\Delta\text{TS} = 5.99$ below the maximum value (James, 1994). This value of ΔTS corresponds to a 95% confidence level for a TS distribution with two degrees of freedom. In case of low maximum TS or irregularly-shaped TS profiles, this contour can be composed of a number of different paths, possibly closing on the border of the images, as is shown in Fig. 4.4 for one example. To analyze the topology of the contour and to select the contour path containing $(x_{\text{max}}, y_{\text{max}})$, we implemented a ray-casting algorithm[1] based on the point-in-polygon algorithm (Shimrat, 1962). Straight lines are drawn radially from $(x_{\text{max}}, y_{\text{max}})$ towards the borders of the TS map. For each of these rays we find the contour path closest to $(x_{\text{max}}, y_{\text{max}})$ that is intersected by the ray an odd number of times. The 95% contour is obtained joining all the found paths (just one in case of well-localized excesses in the TS map).

The estimate of the 95% statistical error radius (r_{95}) on the flare position is computed as the average distance of $(x_{\text{max}}, y_{\text{max}})$ from the 95% confidence-level contour. For very bright flares the 95% contour can be smaller than the pixel of the TS maps. In these cases, the r_{95} is constrained to be equal to the half-diagonal of the pixel (0.11° and 0.035° at low and high energies, respectively). The number of contour paths found by the contour-finding algorithm is used to construct a boolean flag, called `contour_f`, indicating the quality of the flare localization. This flag is `TRUE` only if the 95% contour is composed of a single closed path not touching the borders of the TS map and containing $(x_{\text{max}}, y_{\text{max}})$.

Once the more refined position of the flare is measured from the TS maps, the flare spectrum is estimated with an additional likelihood fit. The fit is performed using the `gtlike` code from the Science Tools. This fit shares the same data and analysis settings as the TS map generation. The flare is modeled as a point source, located at the position of the maximum TS, with a power-law spectrum free in index and normalization. In the 2FAV catalog we include only flares for which the minimizer has converged successfully. In Fig. 4.5 the structure of the likelihood follow-up analysis of FAVA is summarized.

[1] https://en.wikipedia.org/wiki/Point_in_polygon

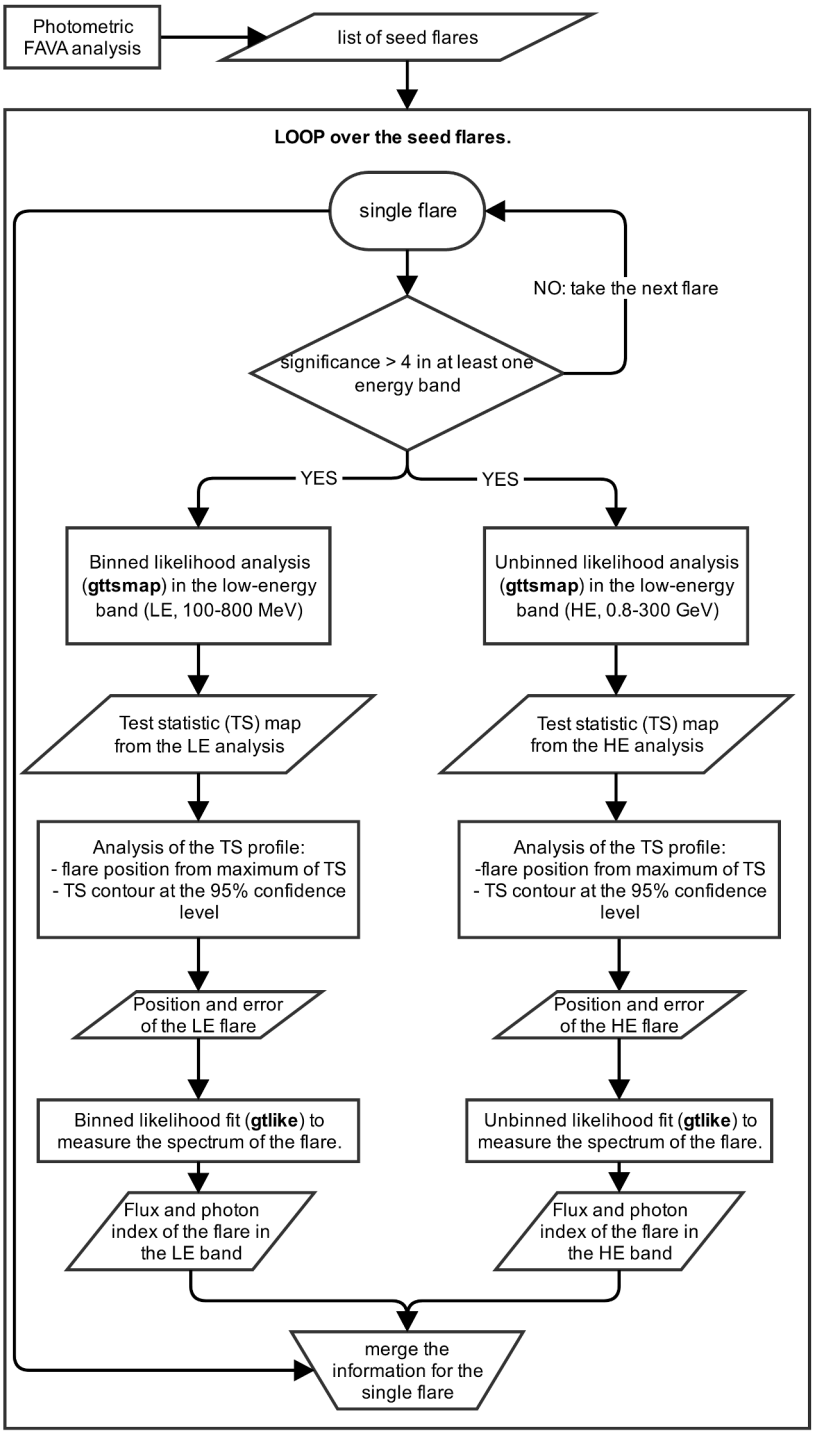

Figure 4.5: Flow chart of the likelihood analysis follow-up of FAVA

4.2.3 Angular resolution and sensitivity

The FAVA analysis provides three different estimators for the position of each seed flare: one from the photometric analysis (the peak-finder position in the two energy bands are merged together), and two from the TS maps at low and high energies. The peak-finding algorithm used in the photometric step does not provide a measure of the uncertainty on the flare position. To estimate its accuracy we compare the photometric positions of the flares with the positions of known and variable sources, as was done for the 1FAV. The average r_{95} from the photometric analysis is $\sim 1^\circ$ for flares detected only in the low-energy band (whose high-energy significance $S_{\mathrm{HE}} < 5.5$) and $\sim 0.8^\circ$ for flares detected also in the high-energy band.

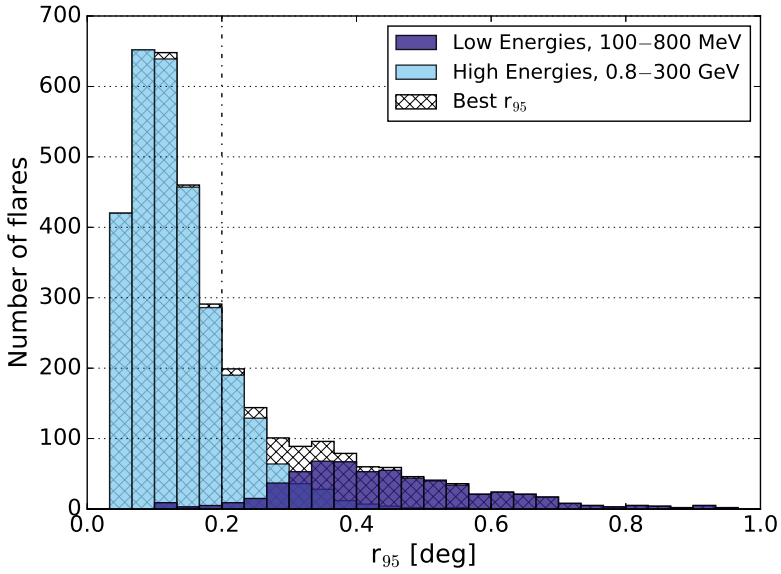

Figure 4.6: Distribution of the average radii for the 95% confidence-level contour of the TS maps of the flares in the 2FAV catalog. The colors show this distribution for flare positions coming from the low- and high-energy analysis (in light and dark blue, respectively) and the total of the distribution (hatched black area). The dash-dotted line corresponds to $r_{95} = 0.2^\circ$ and indicates the division between more and less accurately localized flares used in the first step of the clustering (see Section 4.3.3). Figure reproduced from Abdollahi et al. (2016).

The distribution of r_{95} as measured from the TS maps for the flares in the 2FAV catalog is presented in Fig. 4.6. The two distributions peak at 0.35° and $\sim 0.1^\circ$ at low and high energies, respectively. These values corresponds to roughly twice the size of the pixels of the TS maps (0.15° at low energies and 0.05° at energies). Although coarse, the resolution of the TS maps is small compared to the typical statistical uncertainties of an analysis covering one week. With respect to the average photometric localization, for most of the flares, the improvement in localization accuracy brought by the likelihood follow-up is a factor of $\sim$8 at high energies, and $\sim$3 at low energies. Having an estimate of the local-

ization accuracy of each flare is another advantage brought by the likelihood follow-up. In the online analysis, this additional information facilitates the search for possible counterparts of each flare. To construct the catalog, the best estimator of the flare position can be selected on a flare-by-flare basis by comparing the corresponding r_{95}. As is visible in Fig. 4.6, the analysis in the high-energy band on average provides the smallest containment radii. There are, however, cases in which the low-energy analysis provides more accurate localization.

Besides providing more accurate positions of the flares, the likelihood analysis is also slightly more sensitive. Figure 4.7 shows the comparison between the photometric significance $S_{\mathrm{LE\,/\,HE}}$ and the corresponding gaussian significance derived from the value of TS. To convert the TS into a probability, and then into a gaussian significance $S(\mathrm{TS}_{LE/HE})$, we use a χ^2 distribution, according to the Wilk's theorem (Wilks, 1938). Assuming two degrees of freedom for the TS map (corresponding to the parameters of the flare spectra), we find that, on average, $S(\mathrm{TS_{LE}}) \sim 1.26 S_{\mathrm{LE}}$ and $S(\mathrm{TS_{HE}}) \sim 1.1 S_{\mathrm{HE}}$ for the comparison in the low- and high-energy bands respectively. If we consider 4 degrees of freedom for the TS map (the two spectral parameters and the two coordinates of the test source position), the linear coefficient changes only slightly, from 1.26 to 1.25 at low energies and from 1.11 to 1.09 at high energies.

4.3 Construction of the catalog

We apply this upgraded version of FAVA to the first 387 weeks of *Fermi* data, starting from 2008-08-04 (Modified Julian Date, MJD 54682) to 2016-01-04 (MDJ 57391). Figure 4.8 presents, for every location in the sky, the maximum significance found by the photometric analysis during this 7.4-year long time-span, in either the low- or the high-energy band. This picture summarizes the results of the photometric analysis, and gives a qualitative overview on the widespread variability of the gamma-ray sky.

In the considered time range, a total of 10709 flare candidates have been detected by the photometric analysis. Of these, 7106 (on average $\sim$ 18 per week) satisfy the seed condition (photometric significance greater than 4σ) and have been processed with the likelihood follow-up. The second FAVA catalog is based on the resulting lists of flare candidates. The construction of the catalog has involved:

- selecting statistically significant flares,
- clustering the position of the flares in order to identify the 2FAV sources, and
- searching for counterparts of the found sources.

These steps are detailed in the following. The catalog is presented and discussed in Section 4.4.

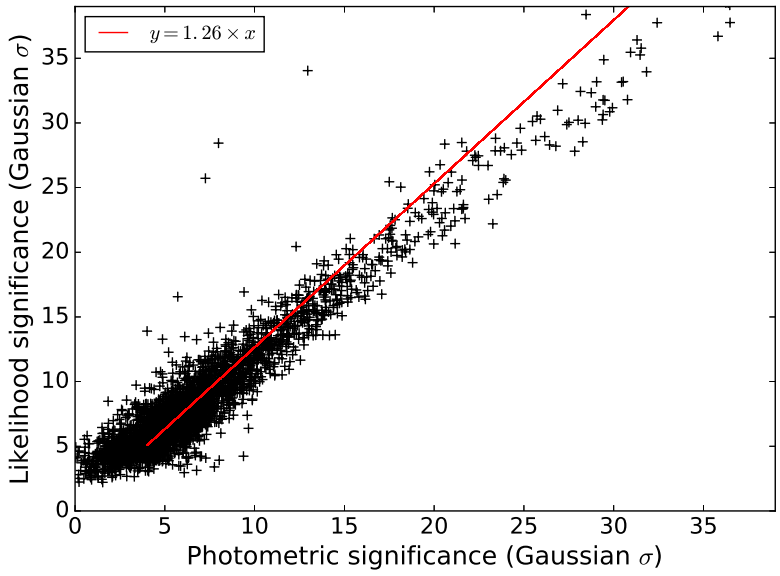

(a) Low-energy band, 100−800 MeV

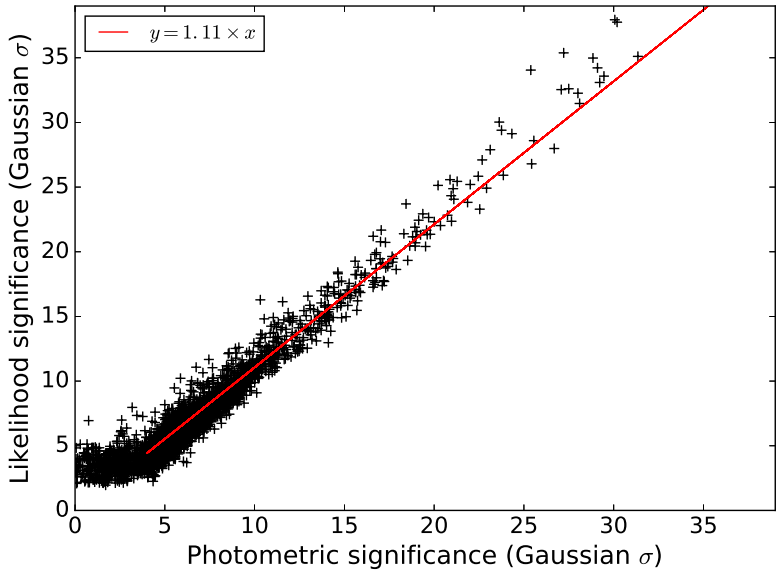

(b) High-energy band, 0.8−300 GeV

Figure 4.7: Comparison of the significance of the flare as measured by the photometric technique (x axis) and by the likelihood analysis (y axis). Top: low-energy band, bottom: high-energy band. The TS of the flare is converted into gaussian significance using a χ^2 distribution with 2 degrees of freedom (the two parameters of the flare spectrum: photon index and normalization). The red line shows the best linear fit to the data.

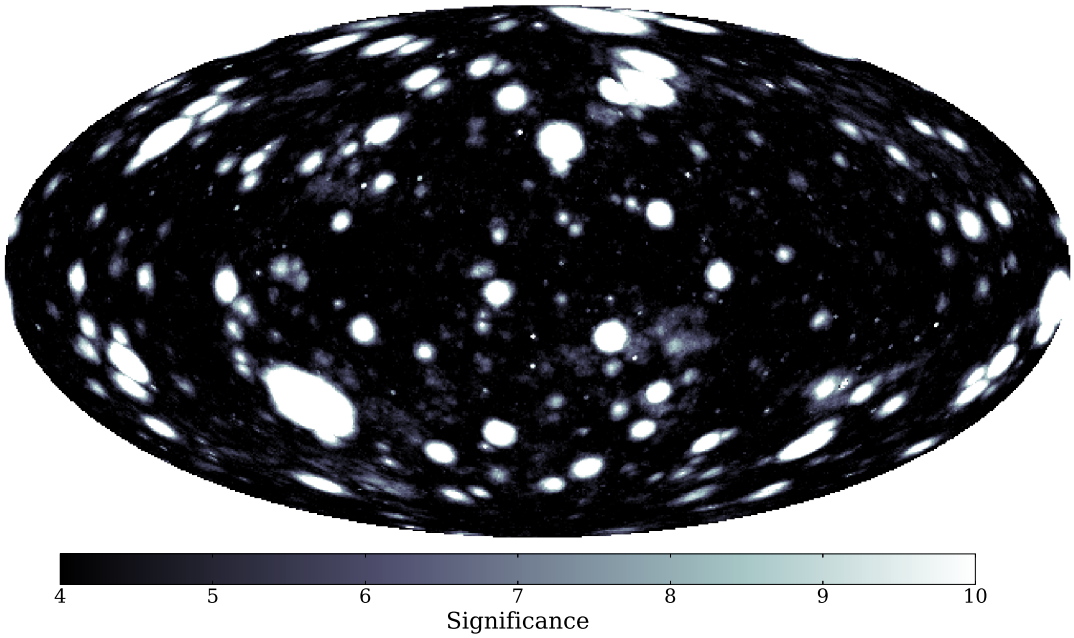

Figure 4.8: All-sky map of the maximum significance of the flux variations measured, in either the low- or the high-energy band, during the time-span of the 2FAV. The difference of the LAT PSF between the two FAVA energy bands can be appreciated from this image. High energy flares results in well-localized maxima, in general a few pixels in diameter. Low-energy flares produce much broader peaks. The very large spots corresponds to bright low-energy flares saturating the tails of the LAT PSF. The map is in Galactic coordinates and in Hammer-Aitoff projection.

4.3.1 Flare selection

In every time bin, FAVA scans the entire sky searching for excesses of counts. For every time bin, the number of trials of the photometric analysis is estimated as the number of times the PSF fits on the entire sky. The average values for the PSF 68% containment radius are $\sim 3^\circ$ and $\sim 0.6^\circ$, in the low- and high-energy bands respectively. Multiplying by the number of time bins ($N_{\rm week} = 387$) analyzed for the 2FAV, the total number of trials in the two energy bands are $N^{\rm LE}_{\rm trial} \sim 5.6 \times 10^5$ and $N^{\rm HE}_{\rm trial} \sim 1.4 \times 10^7$.

The many trials of the FAVA analysis enhance the probability of measuring, by chance, high significance values caused by fluctuations of the noise. To compensate for this, we apply strong cuts on the statistical significance of the flares that will be used to build the 2FAV. The cuts are applied separately in the two energy bands, and for the photometric and likelihood analysis separately. To be included in the 2FAV, a flare must satisfy at least one of the following conditions (we remind the reader that $S_{\rm LE/HE}$ and $\mathrm{TS}_{\rm LE/HE}$ denote the photometric significance and the TS in the respective energy bands):

- $|S_{\rm LE/HE}| > 6\sigma$ in a single energy band.

- $TS_{LE/HE} > 39$ in a single energy band.
- $|S_{LE}| > 4\sigma$ and $|S_{HE}| > 4\sigma$ with a distance between the photometric low- and high-energy positions smaller than $3°$.
- $TS_{LE} > 18$ and $TS_{HE} > 18$ with a distance between the positions of the flare measured from the low- and high-energy TS map smaller than $1.5°$.

Since the two energy band are independent, a spatially coincident and simultaneous detection at the 4σ level in the two energy bands corresponds to a global significance of $\sim 6\sigma$. The number of false positives at the 6σ level can be estimated using the number of trials computed before. Each of these cuts corresponds to a significance threshold of $\sim 6\sigma$. Above this threshold, we expect ≈0.001 false flares at low energies and ≈0.03 in the high-energy band.

Additional cuts are applied to the flares detected by the likelihood analysis. We discard information coming from the TS maps if the 95% confidence-level contour intersects the borders of the map, or if it is composed of more than one closed path. In the case of such an irregular contour, we also discard the photometric information on the flare if the corresponding TS is greater than 18. That is, poorly-localized significant excesses are removed. This latter requirement accounts for seed flares with misplaced positions. It is the only case in which the two analysis are used to veto each other. In all other cases, the photometric and likelihood analyses are fully independent. The advantages of the photometric technique (see Section 4.2.1) are maintained, and the likelihood analysis is used to provide more accurate and sensitive information on the flares.

Another potential source of spurious flares is our Sun. Besides occasional flares, the Sun is a steady source of > 100 MeV gamma-rays caused by the interaction of CRs in the solar atmosphere and in the heliosphere (Abdo et al., 2011b). As the Earth orbits the Sun, the sky position of our star moves along the ecliptic plane with a speed of $\sim 7°$ per week. This motion, and the solar flares, causes many FAVA detections, visible in Fig. 4.9a. To remove these spurious detections, flares are not included in the catalog if they are within $6°$ of the position occupied by the Sun at in the middle of the time bin.

In total, 4547 flares pass the above mentioned cuts and will be used to construct the catalog. In Table 4.2, the number of flares passing the different sets of cuts is presented. The majority of the catalog flares have valid likelihood information. The distribution of the flares on the sky is shown in Fig. 4.9b. Note how the positions of these flares correlates with the maxima of the photometric significance map shown in the background.

4.3.2 Sensitivity

The background of the photometric analysis is determined only by the expected counts map. This makes it possible to compute all-sky sensitivity maps corresponding to an arbitrary significance thresh-

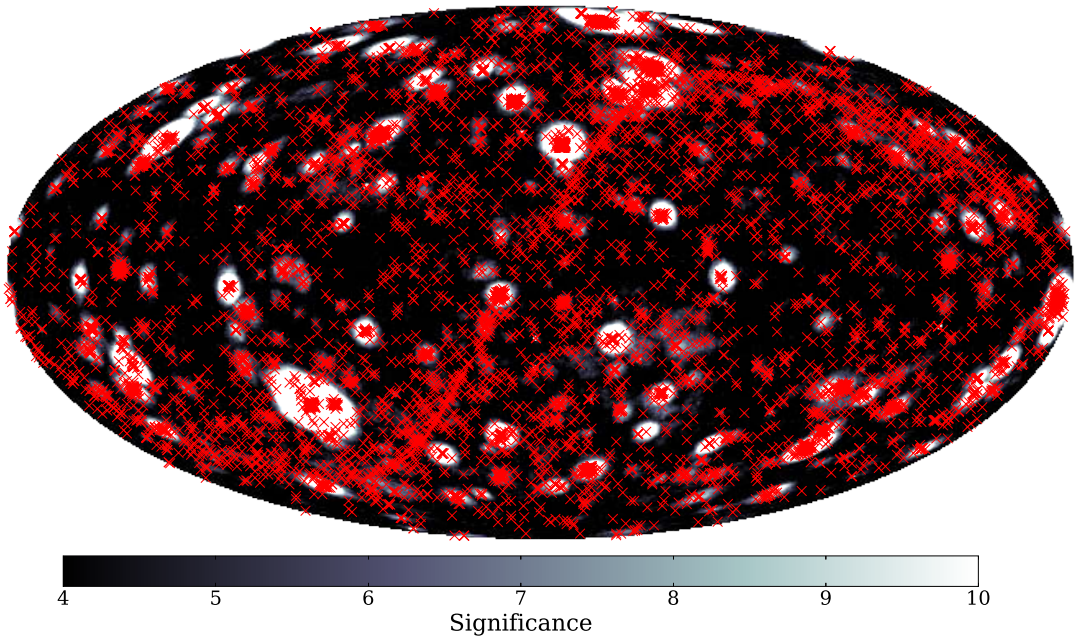

(a) Flare candidates

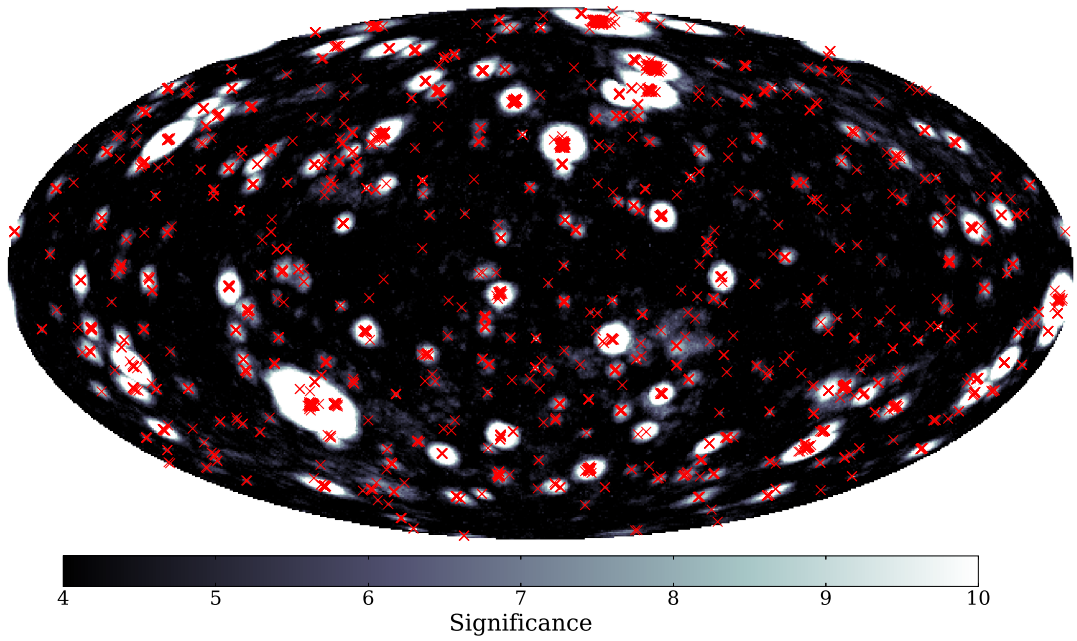

(b) Catalog flares

Figure 4.9: Sky position of all the flare candidates found by FAVA in the first 387 weeks of *Fermi* data (top), and of the flares satisfying the cuts for the 2FAV catalog (bottom). The maps are in Galactic coordinates and we have used Fig. 4.8 as a background image. In the top panel, note how the plane of the ecliptic is traced by the many spurious detections from the Sun.

Table 4.2: Number of catalog flares in the different cut classes. Since a given flare can satisfy more than one cut, to produce this table the cuts are evaluated in hierarchical order to avoid double-counting: first likelihood then the photometric analysis; for each analysis methods the energy bands are evaluated in the order: high, low, and combined. The number of flares satisfying the cuts on the photometric properties are divided into positive flares (excesses of counts) and negative flares (deficits of counts).

Energy band	Likelihood	Photometric (positive)	Photometric (negative)	total
High Energy	1748	18	228	1994
Low Energy	1156	57	579	1792
Combined	524	77	160	761
Total	3428	152	967	4547

old. We compute the average exposure of a weekly time bin and we assume power-law spectra for the flares. For each sky position we derive the minimum flux that is necessary to produce an excess of counts above the threshold used to construct the catalog: a significance greater than 6σ in a single energy band, or above 4σ in both energy bands. The resulting sensitivity maps are presented in Fig. 4.10 for two values of the flare photon index Γ, representative of hard ($\Gamma = 1.5$) and soft ($\Gamma = 3.5$) flares. As we will see in Section 4.5, most of the 2FAV flares have photon indices between these two values. For convenience, the sensitivity is expressed as the integral flare flux above 100 MeV. As is visible from Fig. 4.10, FAVA has a considerably worse sensitivity along the Galactic plane, due to the bright background of the Galactic diffuse emission. In Fig. 4.11, the dependence of the average sensitivity (at the position of the 2FAV sources) on the spectral index of the flare is presented. The high-energy band ($S_{\mathrm{HE}} > 6\sigma$) provides the best sensitivity for flares harder than $\Gamma \sim 2$, while the low-energy one ($S_{\mathrm{LE}} > 6\sigma$) is most sensitive for flares softer than $\Gamma \sim 2.5$. In the intermediate photon index range, the combined requirement ($S_{\mathrm{LE}} > 4\sigma$ and $S_{\mathrm{HE}} > 4\sigma$) provides better sensitivity.

The sensitivity presented here refers to the photometric analysis only and does not take into account the effects of the likelihood analysis. These sensitivity maps are upper limits on the actual sensitivity of the 2FAV catalog, as the likelihood analysis is slightly more sensitive than the photometric one and the flare selection cuts are applied independently on the results from the two analysis methods. As the significance is proportional to the flux, the photometric sensitivity could be scaled, to first approximation, by the measured correlations between the photometric significance and the TS derived in Section 4.2.3: $S(TS_{\mathrm{LE}}) \sim 1.26 S_{\mathrm{LE}}$ and $S(TS_{\mathrm{LE}}) \sim 1.11 S_{\mathrm{LE}}$.

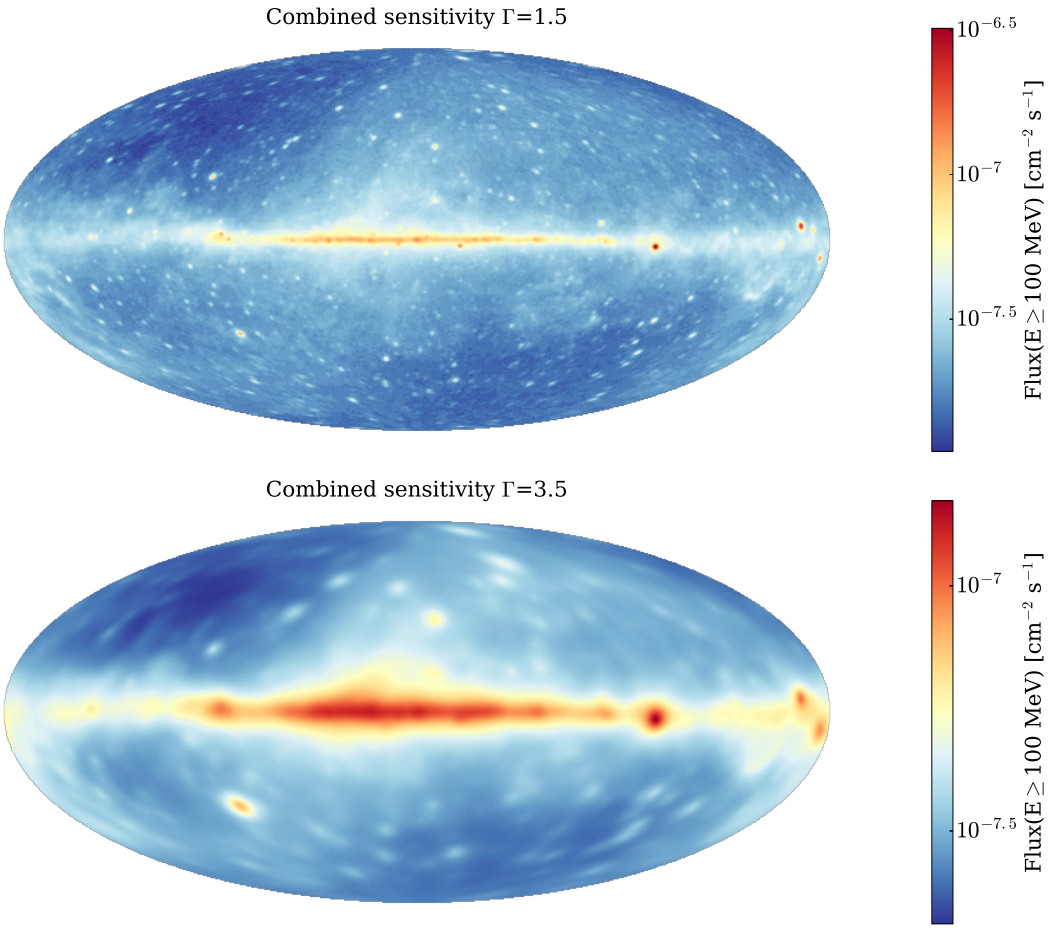

Figure 4.10: All-sky sensitivity maps for the photometric analysis of the 2FAV. The maps are in Galactic coordinates and in Hammer-Aitoff projection. To compute these maps we have used the average weekly exposure, and assumed a power-law shape for the flare spectra. The sensitivity depends on the photon index of the flare. Here the maps are shown for reference for hard flares ($\Gamma = 1.5$, top) and soft flares ($\Gamma = 3.5$, bottom). As the PSF varies strongly with the energy, the map for $\Gamma = 1.5$, where the analysis in the high energy band is the most sensitive, has a better spatial resolution. Taken from Abdollahi et al. (2016).

4.3.3 Clustering of the flares

We perform a clustering analysis of the positions of the 4547 catalog flares. A source in the 2FAV is defined as a cluster of flares. To identify the clusters, we use the implementation of the Kruskal's Minimum Spanning Tree (MST) algorithm (Nesetril et al., 2001; Kruskal, 1956) already in place for the 1FAV. A MST is a way to connect the points in a graph that minimizes the total length (defined according to some metric) of the connections (called edges). Once the algorithm identifies the MST connecting the flares, we separate the clusters by cutting the edges of the graph which are longer than

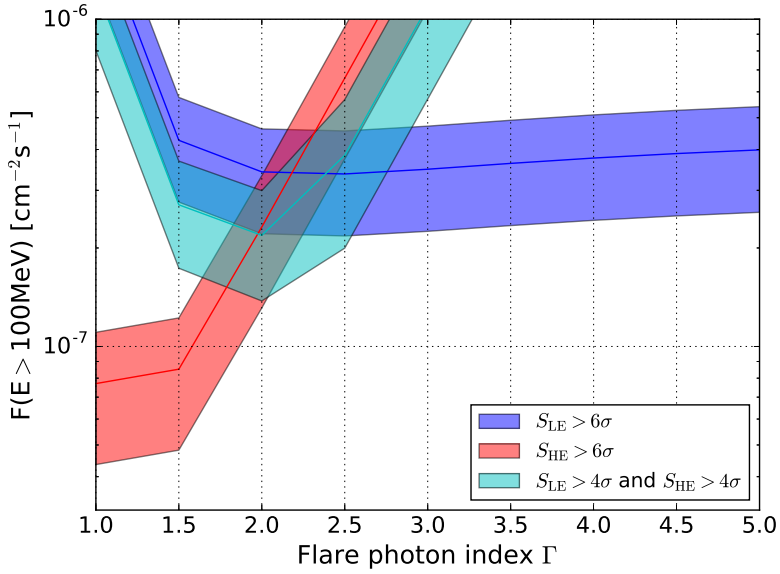

Figure 4.11: Sensitivity of the photometric analysis as a function of the flare photon index. The curves are produced by averaging the sensitivity at the position of all the 2FAV sources (solid lines). The shaded area corresponds to a deviation of plus-minus one standard deviation from the average.

a given threshold: nearby points are assigned to the same cluster if the separation between them is smaller than the threshold. This approach could result in spurious clusters due to the presence of poorly localized flares. Such flares can act as 'bridges' , effectively reducing the distance between more separated clusters of better localized flares. To account for this, the clustering is performed in multiple stages, starting with better localized flares and and gradually adding less precise information in each following step.

The catalog flares are divided in 3 different groups, according to the accuracy of their position. These groups are presented in Table 4.3. The flares of group A and B have positions measured by the likelihood analysis, mostly from the high- and low-energy band, respectively (see Fig. 4.6). For these flares, the measured r_{95} is used to scale the angular distance $d(i,j)[\mathrm{deg}]$ between a pair (i,j) of flares used in the MST algorithm:

$$d'(i,j) = \frac{d(i,j)[\mathrm{deg}]}{1.62\sqrt{r_{95}^2(i) + r_{95}^2(j)}} \tag{4.4}$$

where we have used the fact that, for a 2D symmetric gaussian, $r_{95} \simeq 1.62 \times r_{68}$. The metric $d'(i,j)$ expresses the separation between these flares in terms of r_{68}. Group C flares only have positions from the photometric analysis (967 are negative). In clustering these flares, the edges of the graph are defined as the angular flare-to-flare distance.

Each group of flares is used in a separate step of the clustering. At each of these steps, flares are

Table 4.3: Definitions and population counts of the three groups of flares used in the different stages of the clustering.

Name	Position from	Selection	Number of flares
Group A	Likelihood	$r_{95} < 0.2^\circ$	2471
Group B	Likelihood	$r_{95} > 0.2^\circ$	1087
Group C	Photometric		989

added to pre-existing clusters if they are within a certain distance d_{add} of a cluster. Then, the clustering algorithm is applied to the remaining flares and new clusters are identified by cutting the edges of the MST longer than a given threshold d_{cut}. As a first step, we build the MST of the flares of group A, and identify 437 clusters by cutting the edges for which $d' > 4r_{68}$. Flares of group B are then considered: 988 of them are within $4r_{68}$ of some cluster of group A flares and are assigned to the nearby cluster. The 99 group B flares that remain are separately clustered (again using $d_{\text{cut}} = 4r_{68}$), resulting in 72 additional clusters. In the last step we add flares of the group C. 980 of these flares are within 3.5° of existing clusters and are assigned to them. The remaining 9 group-C flares are widely separated. Each one defines a cluster by itself. We choose to set $d_{\text{add}} = d_{\text{cut}}$ in each step of the clustering for the sake of simplicity. The selected values of $4r_{68}$ and 3.5° have been determined through a series of tests and are found to give good results. With larger distance thresholds, some nearby clusters would be merged together, and the corresponding sources would be lost to the catalog. On the other hand, with smaller thresholds new sources would be created, often from dubious clustering solutions. In these cases we prefer to be conservative.

With this procedure, the 4547 flares are grouped in 518 clusters. Each one of these clusters identifies a source in the 2FAV. The source position $\mathbf{r}$ and the associated statistical error r_{95} are defined as:

$$\mathbf{r} = \frac{\sum_{i=0}^{N^*} \mathbf{r}(i) r_{95}^{-2}(i)}{\sum_{i=0}^{N^*} r_{95}^{-2}(i)} \qquad r_{95} = \left(\sum_{i=0}^{N^*} r_{95}^{-2}(i) \right)^{-\frac{1}{2}} \tag{4.5}$$

where, for each source, the sum includes only the N^* best localized flares contained in the cluster, i.e: group A flares if present, if not, group B flares, in the absence of these, group C flares. In this latter case, the 95% error radius is not measured directly for each flare, and we use the average values of 1° and 0.8° estimated in Section 4.2.3. The r_{95} of the source is constrained to be not smaller than the finest pixel of the highest resolution map used to derive the position of the flares in the cluster. Finally, we estimate the systematic uncertainty on the position of the sources as was done in the 1FAV,

by comparing the position of the 2FAV source to those of known flaring gamma-ray sources. The resulting systematic uncertainty is $r_{sys} = 0.1^{\circ}$. The position on the sky of the 2FAV sources, and of the flares is shown in Fig. 4.12.

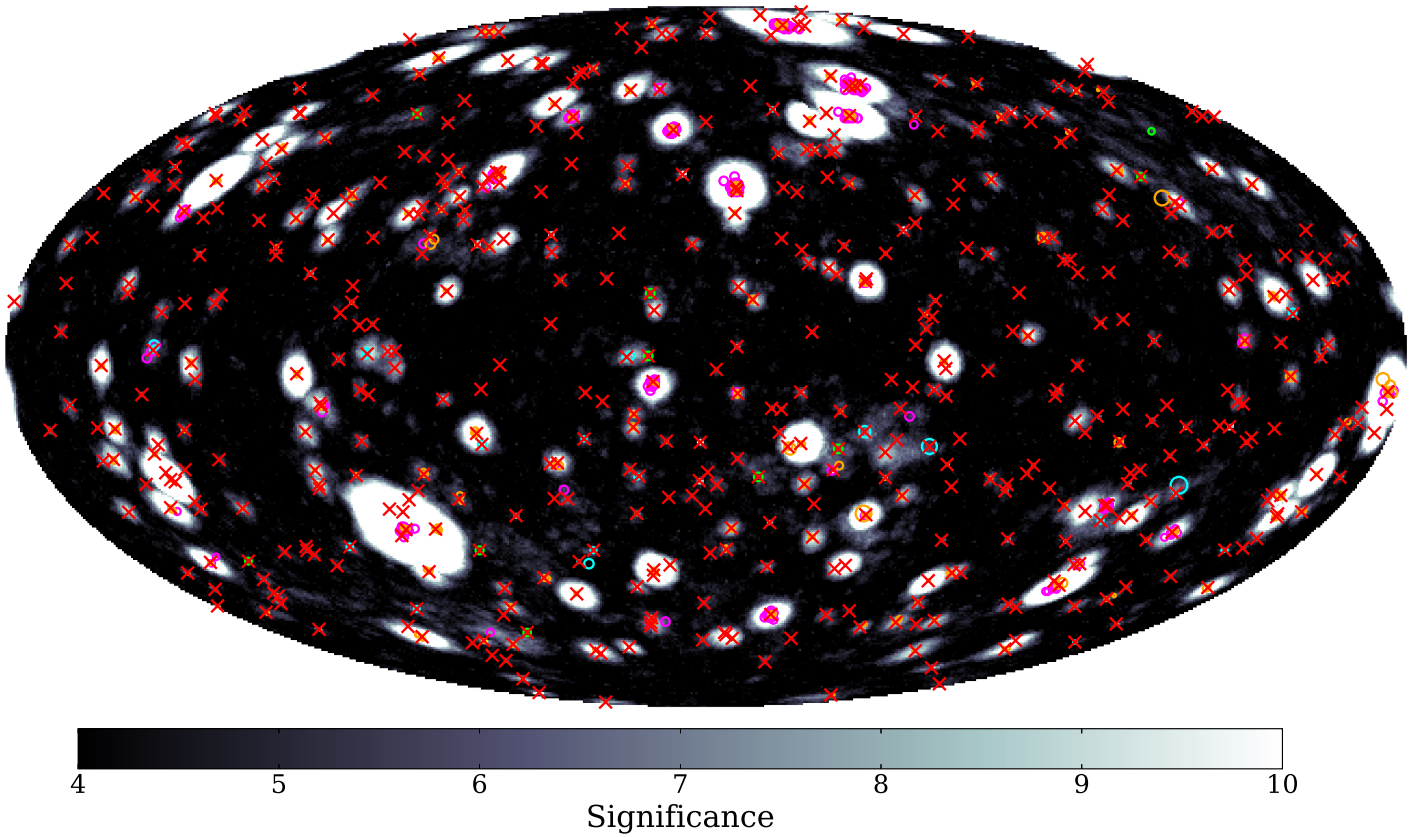

Figure 4.12: Positions of the catalog flares and sources on the sky. The background image, in Galactic coordinates and Hammer-Aitoff projection, is the maximum significance map shown in Fig. 4.8. The 2FAV sources are marked with red crosses. The flares are shown as colored circles, with radii defined by their r_{95}. The flares are color-coded according to the accuracy of their localization. Different colors refers to the different flare-groups used in the clustering analysis. Group A flares ($r_{95} < 0.2°$) are in yellow, group B flares ($r_{95} > 0.2°$) are in orange if they have been merged to a cluster, cyan otherwise. Group C flares (the ones with only the photometric position) are magenta if they have been assigned to a cluster, green otherwise. Figure reproduced from (Abdollahi et al., 2016)

4.3.4 Association procedure

The association procedure aims to find plausible counterparts for the 2FAV sources, explicitly prioritizing known variable gamma-ray sources or blazars. The catalogs used to look for counterparts of the 518 2FAV sources are listed in Table 4.4. All the *Fermi*-LAT, AGILE, and EGRET gamma-ray source catalogs available when the 2FAV was constructed are used. We also include the *Roma-BZCAT* (5BZ), a multiwavelength catalog of blazars detected at high confidence. Besides these source catalogs, we also considered the list of *Fermi*-issued Astronomer's telegrams (FERATels) and of the LAT-detected GRBs.

Table 4.4: Catalogs used to search for possible associations of 2FAV sources. The second column shows the number of counterparts of 2FAV sources found in each catalog. For the FGL catalogs, the numbers in parentheses refer to the counterparts that were not flagged as variable in the corresponding catalogs.

Catalog	Number of counterparts	Reference
Third *Fermi* LAT Source catalog (3FGL)	352 (12)	Acero et al. (2015)
Second *Fermi* LAT Source catalog (2FGL)	5 (1)	Nolan et al. (2012)
First *Fermi* LAT Source catalog (1FGL)	0 (0)	Abdo et al. (2010)
First AGILE catalog (1AGL)	1	Pittori et al. (2009)
Updated AGILE catalog (1AGLR)	0	Verrecchia et al. (2013)
Third EGRET catalog (3EG)	1	Hartman et al. (1999)
Roma-BZCAT blazar catalog (5^{th} edition)	39	Massaro et al. (2015)
Fermi-issued ATels (FERATels)	16	†
LAT detected GRBs	14	‡

Notes — † :The list of FERATels used was current as of 2016-05-30. The most recent version can be found at: http://www.asdc.asi.it/feratel/

‡ The list of LAT-detected GRBs can be found at: http://fermi.gsfc.nasa.gov/ssc/observations/types/grbs/lat_grbs/.

The association procedure is based only on positional coincidence, but prioritizes counterparts that are known to be variable, when available. It has been adapted from the one used in the 1FAV catalog. As no spectral or temporal information on the sources is used, the results of the associations have to be considered as likely counterparts, rather than confident identification. Counterparts are looked for within a search radius R_s from each 2FAV source. The search radius is defined as the sum of the systematic uncertainty and the 99% statistical error on the 2FAV source position: $R_s = r_{99} + r_{sys}$.

The association procedure has several steps, and stops as soon as a counterpart is found. For each 2FAV source we search:

1. among variable gamma-ray sources from the *Fermi* LAT point-source catalogs (from the most recent to the oldest: 3FGL, 2FGL, and 1FGL). These sources are selected requiring variability

indices greater than 23.21 (241 sources), 41.64 (458 sources), and 72.44 (647 sources) in the 1FGL, 2FGL, and 3FGL respectively (Abdo et al., 2010; Nolan et al., 2012; Acero et al., 2015). Such sources have less than 1% probability of being constant on monthly timescales.

2. among gamma-ray sources announced in the FERATels.

3. among blazars in the 5BZ catalog.

These first steps consider sources that are known (or likely, in the case of the 5BZ blazars) to be variable. At this stage, we found 352 variable counterparts of 2FAV sources in the 3FGL, 5 in the 2FGL, and none in the 1FGL. 16 2FAV sources have counterparts among sources featured in some LAT-issued ATel, and 39 have been associated with blazars from the 5BZ.

For the 2FAV sources that are still unassociated, we search again in the LAT point source catalogs (in the same order) but including all the sources, not just the variable ones. We find 12 and 1 new counterparts, from the 3FGL and the 2FGL respectively. Since the number of possible counterparts is much larger at this step, chance coincidence associations are more likely. In the 2FAV, the names of these FGL counterparts are therefore marked with a '*', to suggest additional caution in interpreting these associations.

As a next step, we look for counterparts in the 1AGLR, 1AGL, and 3EG catalogs, finding one counterpart in the 1AGL and one in the 3EG. Finally, we search for associations of 2FAV sources with GRBs detected by the LAT. A 2FAV source is associated with a GRB only if: $i)$ a single flare is associated to the 2FAV source, $ii)$ the position of the source's flare and of the GRB are compatible within the errors, and $iii)$ the GRB time is contained in the weekly time bin when the flare is detected. 14 FAVA sources have been associated with GRBs. For none of these 2FAV sources, were other counterparts found in the other catalogs.

With this procedure, 441 2FAV sources have been associated with likely counterparts, while 77 of them remain unassociated. In total, six sources in the 2FAV catalog have counterparts coming from the 2FGL. In three cases, the 2FGL sources are no longer included the 3FGL (details on sources that are 'lost' in the 3FGL can be found in Acero et al., 2015, sec. 4.2). For the other three sources, the 2FGL counterpart is also associated to a 3FGL source. There are two reasons why these three 2FAV sources have not been directly associated with the 3FGL counterpart: *i)* the variability index in the 3FGL has dropped below the threshold used to identify sources that are variable at the 99% confidence level. In this case, the 3FGL counterpart is excluded from the first iteration of the association procedure, and the 2FGL source is found. *ii)* The position of the source measured in the 3FGL has shifted with respect to the one given in the 2FGL, bringing the 3FGL counterpart outside the search radius. Table 4.5 summarizes the details on these associations with 2FGL sources.

Table 4.5: 2FAV sources with a counterpart from the 2FGL and the eventual 3FGL counterpart. In the first two columns are shown the name and the search radius used by the association procedure. The following columns present the name of the 2FGL counterpart of the 2FAV source, its distance to the 2FAV source, and its variability index. The last three columns shows the same quantities for the 3FGL source to which the 2FGL one is associated. In the second part of the table are listed the 2FAV sources whose 2FGL counterpart is 'lost' in the 3FGL.

2FAV ID	R_s	2FGL assoc.	2FGL dist.	2FGL var. index	3FGL assoc	3FGL dist.	3FGL var. index
2FAV J0709+22.7	0.21°	2FGL J0709.0+2236	0.11°	45.63	3FGL J0708.9+2239	0.07°	56.60
2FAV J2022+76.2	0.19°	2FGL J2022.5+7614	0.03°	57.89	3FGL J2022.5+7612	0.02°	66.59
2FAV J0059-56.9	0.43°	2FGL J0059.7-5700	0.13°	43.01	3FGL J0059.1-5701	0.15°	64.37
2FAV J0910-50.8	0.19°	2FGL J0910.4-5050	0.07°	59.12	...	...	...
2FAV J1023+0.7	0.18°	2FGL J1023.6+0040	0.02°	15.32	...	...	...
2FAV J2032+41.0	0.30°	2FGL J2032.1+4049	0.16°	121.21	...	...	...

4.4 The second FAVA catalog

The 2FAV catalog contains both the 518 sources and the 4547 flares. The first release of the catalog is publicly available at the *Fermi* Science Support Center[1]. Table 4.6 presents, for reference, the first sources of the catalog. The 2FAV sources are identified as 2FAV JHHMM+DD.d: HHMM is the Right Ascension of the source expressed in hours and minutes, and DD.d is the source declination in degrees, truncated to one decimal digit. The sky position of the 2FAV sources, color-coded according to the class of the counterpart, is presented in Fig. 4.13.

For 155 of the 518 2FAV sources, only low-energy flares have been detected. Negative flares have been assigned to 35 sources, the majority of which are blazar (18 FSRQs and 8 BL Lacs), but also from some unassociated sources (8 cases). Negative flare are also detected from the Crab PWN (2FAV J0534+21.9) and from the high-mass X-ray binary system (HMB) LS I+61 303 (2FAV J0240+61.4). As discussed in Section 4.2.1, negative flares corresponds to quiescent periods of the most variable sources, at flux levels which are below the average emission of the source.

In the 2FAV there are 9 sources detected only by the photometric analysis. In each of these cases, only one flare is associated to each source (see Section 4.3.3). Four of these 9 flares were detected only in the low-energy band, while the remaining 5 reached more than 4σ in both energy bands. In most of the cases, the TS measured with the likelihood analysis is below threshold and the 95% contour is irregular. Beside these features, the analysis for these flares shows nothing which might point to a technical problem. However, the disagreement between the two analysis methods suggests that caution must be used with these photometric-only sources. They are flagged by appending an 'f' to their names, i.e. 2FAV J0159+19.6f.

[1] https://fermi.gsfc.nasa.gov/ssc/data/access/lat/fava_catalog/

Table 4.6: 2FAV source table (only the first sources are shown). The 2FAV identification number (ID) is shown in the first column. The source position in Galactic and Equatorial (J2000) coordinates, together with the 95% statistical error r_{95} on this position are presented in columns 1 to 5. The following columns show the number of flares associated to that source: total N^f, high-energy flares only (N^f_{he}), and negative flares (N^f_{neg}). The last columns presents the search radius used to look for counterparts (R_s), the name of the gamma-ray counterpart (Gamma assoc.), the identification number of ATels associated to the source, and the name of the multiwavelength counterpart (Assoc.). Taken from Abdollahi et al. (2016).

2FAV ID	RA [°]	Dec [°]	l [°]	b [°]	r_{95}[°]	N^f	N^f_{he}	N^f_{neg}	R_s [°]	Gamma assoc.	Assoc.	class	ATel
J0001+20.6	0.39	20.65	107.50	−40.70	0.87	1	0	0	1.18	3FGL J0001.4+2120	TXS 2358+209	fsrq	...
J0002+75.0	0.71	75.03	119.70	12.50	0.14	1	1	0	0.27	...	...	...	...
J0017−05.1	4.48	−5.15	101.50	−66.60	0.13	6	1	0	0.27	3FGL J0017.6−0512	PMN J0017−0512	fsrq	...
J0019+73.4	4.97	73.48	120.70	10.70	0.05	5	4	0	0.16	...	5BZQ J0019+7327	fsrq	...
J0025−48.1	6.42	−48.10	314.70	−68.40	0.08	2	2	0	0.20	3FGL J0026.2−4812*	...	...	...
J0028+06.9	7.21	6.93	113.00	−55.50	0.84	1	0	0	1.14	...	5BZQ J0029+0554	fsrq	...
J0030−02.2	7.66	−2.22	110.80	−64.60	0.05	11	7	0	0.16	3FGL J0030.7−0209	PKS B0027−024	bcu	...
J0032−55.2	8.12	−55.29	308.60	−61.60	0.08	2	2	0	0.19	3FGL J0032.3−5522	...	...	...
J0033−41.3	8.46	−41.32	316.10	−75.40	0.15	1	1	0	0.28	...	...	...	...
J0037+18.5	9.34	18.52	118.30	−44.20	0.09	2	2	0	0.21	...	...	...	...
J0042−01.7	10.54	−1.74	117.50	−64.50	0.06	1	1	0	0.18	GRB131231A	GRB131231A	grb	...
J0043+23.3	10.99	23.33	120.70	−39.50	0.24	1	1	0	0.40	...	...	...	...
J0045+21.4	11.36	21.49	121.10	−41.40	0.04	2	2	0	0.15	...	5BZB J0045+2127	bll	...
J0047+22.5	11.90	22.55	121.80	−40.30	0.29	1	1	0	0.46	3FGL J0048.0+2236	NVSS J004802+223525	fsrq	...
J0050−04.9	12.74	−4.97	122.60	−67.80	0.13	1	1	0	0.26	...	5BZQ J0050−0452	fsrq	...
J0051−06.6	12.86	−6.63	122.90	−69.50	0.26	1	1	0	0.42	3FGL J0051.0−0649	PKS 0048−071	fsrq	...
J0059−56.8	14.89	−56.88	300.70	−60.20	0.27	1	0	0	0.43	2FGL J0059.7−5700	PKS 0056−572	bcu	...
J0102+42.2	15.66	42.28	125.10	−20.50	0.14	1	0	0	0.28	3FGL J0102.3+4217	GB6 J0102+4214	fsrq	...
J0102+58.3	15.68	58.39	124.40	−4.50	0.04	12	6	0	0.14	3FGL J0102.8+5825	TXS 0059+581	fsrq	...
J0102+04.2	15.71	4.27	128.40	−58.50	0.08	1	0	0	0.20	...	...	...	...
J0108+01.5	17.16	1.59	131.80	−61.00	0.04	34	14	0	0.14	3FGL J0108.7+0134	4C +01.02	fsrq	...
J0109+61.5	17.41	61.56	125.10	−1.20	0.05	9	4	0	0.17	3FGL J0109.8+6132	TXS 0106+612	fsrq	...
J0111+22.7	18.00	22.73	129.10	−39.90	0.05	3	1	0	0.17	3FGL J0112.1+2245	S2 0109+22	bll	...
J0112+32.1	18.24	32.17	128.20	−30.50	0.04	11	3	0	0.15	3FGL J0112.8+3207	4C +31.03	fsrq	...
J0116−11.5	19.02	−11.60	144.60	−73.40	0.06	5	5	0	0.17	3FGL J0116.0−1134	PKS 0113−118	fsrq	...
J0118−21.7	19.70	−21.73	173.50	−81.80	0.06	3	2	0	0.18	3FGL J0118.8−2142	PKS 0116−219	fsrq	...
J0132−16.9	23.18	−16.91	168.10	−76.00	0.05	2	2	0	0.16	3FGL J0132.6−1655	PKS 0130−17	fsrq	...
J0132−52.0	23.22	−52.00	288.30	−63.90	0.16	3	1	0	0.30	3FGL J0133.2−5159	PKS 0131−522	bcu	6223
J0137+47.8	24.36	47.85	130.90	−14.30	0.07	6	1	0	0.19	3FGL J0137.0+4752	OC 457	fsrq	...
J0137−24.6	24.45	−24.66	202.20	−79.30	0.19	2	0	0	0.34	3FGL J0137.6−2430	PKS 0135−247	fsrq	...
J0156+39.2	29.15	39.22	136.50	−21.90	0.14	1	0	0	0.27	3FGL J0156.3+3913	MG4 J015630+3913	bcu	...
J0159+19.6f	29.92	19.66	144.20	−40.40	1.00	1	0	0	1.34	...	...	...	...
J0203+30.7	30.93	30.73	140.80	−29.60	0.04	8	7	0	0.14	3FGL J0203.6+3043	NVSS J020344+304238	bll	...
J0204−17.0	31.17	−17.00	185.80	−70.30	0.15	1	0	0	0.29	3FGL J0205.2−1700	PKS 0202−17	fsrq	...
J0204+15.2	31.23	15.20	148.00	−44.10	0.11	1	1	0	0.23	3FGL J0205.0+1510	4C +15.05	bcu	...
J0205+32.2	31.32	32.26	140.60	−28.10	0.18	1	1	0	0.33	3FGL J0204.8+3212	B2 0202+31	fsrq	...
J0210+72.4	32.67	72.45	128.90	10.50	0.10	1	1	0	0.23	...	5BZU J0209+7229	bcu	...
J0210−51.0	32.68	−51.01	276.10	−61.80	0.04	16	7	0	0.14	3FGL J0210.7−5101	PKS 0208−512	bcu	...
J0211+10.8	32.76	10.84	152.50	−47.40	0.05	4	2	0	0.16	3FGL J0211.2+1051	MG1 J021114+1051	bll	...
J0211+11.6	32.78	11.65	152.00	−46.70	0.16	1	0	0	0.30	...	...	...	...
J0216+35.7	34.09	35.77	141.70	−24.00	0.16	1	0	0	0.29	...	...	...	...
J0217+08.6	34.29	8.62	156.10	−48.70	0.05	2	2	0	0.17	3FGL J0217.2+0837	ZS 0214+083	bll	...

Note — The complete table is 17 pages long and will not included in this thesis for ecological reasons. The full 2FAV catalog is available in `fits` file format at https://fermi.gsfc.nasa.gov/ssc/data/access/lat/fava_catalog/.

4.4.1 Likely counterparts

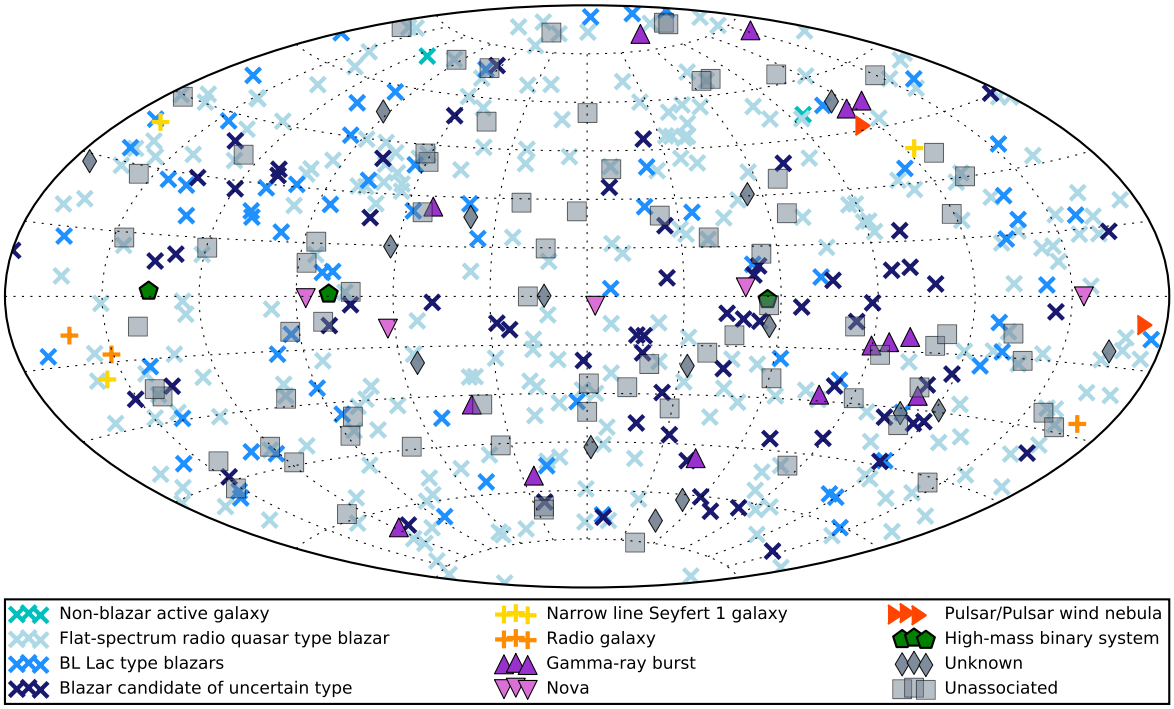

Figure 4.13: Sky position of the 2FAV sources, marked according to the class of the found counterpart. The map is in Galactic coordinates and in Aitoff projection.

We found likely counterparts for 441 of the 518 2FAV sources. Table 4.7 presents the breakdown of the 2FAV according to the classes of the counterparts. We adopt the classifications used in the 3FGL. All the different classes of variable gamma-ray sources (see Section 3.2) are represented in the 2FAV. Roughly 90% of the counterparts of 2FAV sources belong to the AGN class, with FSRQs being the most common (253 sources), followed by BL Lacs (73 sources), and by AGN of uncertain type (bcu, 67 sources in the 2FAV).

Table 4.8 lists the individual 2FAV sources that have non-blazar and non-GRB counterparts. These include three Narrow-line Seyfert 1 galaxies (nlsy1) and three radio galaxies (rdg). For five 2FAV sources we found counterparts among LAT-detected Novae (nov), announced via ATel. Two additional novae were observed by the LAT in the timespan covered by the 2FAV: the recurrent nova V745 Sco (Cheung et al., 2014), and V5668 Sgr (Cheung et al., 2015). These two novae were too faint to reach the 6σ threshold used to construct this catalog. Galactic 2FAV sources include also the Crab nebula and three high-mass gamma-ray binaries (hmb). The gamma-ray binaries 1FGL J1018.6−5856 and LS 5039 are not included in this catalog. The variability of LS 5039 is modulated with a ~ 4 day period (Abdo

Table 4.7: Composition of the 2FAV in terms of source classes. The designators of the classes have been adopted from the 3FGL. The class names of all the 2FAV sources are reported in lowercase, following the convention that reserves uppercase class names to firmly identified sources. Taken from (Abdollahi et al., 2016).

Source class	Designator	Number of associated sources
Pulsar wind nebula	pwn	1
Pulsar	psr	1
Non-blazar active galaxy	agn	2
High-mass binary	hmb	3
Radio galaxy	rdg	3
Narrow line Seyfert 1	nlsy1	3
Nova	nov	5
Gamma-ray burst	grb	14
AGN candidate of uncertain type	bcu	67
BL Lac	bll	73
FSRQ	fsrq	253

et al., 2009c), smaller than the size of the FAVA time bins. 1FGL J1018.6−5856 has a longer period, ~ 16.5 days. The peak flux of this source is about $\sim 5.6 \times 10^{-7}$ ph cm^{-2}s^{-1} above 100 MeV, and the spectrum is well described by a broken power law with indices $\Gamma_1 \sim 2$ and $\Gamma_2 \sim 3$ below and above 1 GeV, respectively (Ackermann et al., 2012e). This flux is smaller than the sensitivity at the position of the source in the low-energy band ($\sim 7.6 \times 10^{-7}$ ph cm^{-2}s^{-1} assuming $\Gamma = 2$) and slightly above the sensitivity limit in the high-energy band ($\sim 5.4 \times 10^{-7}$ ph cm^{-2}s^{-1} for $\Gamma = 3$). Considering also that the peaks of the light-curve of 1FGL J1018.6−5856 are shorter than one week, the non-detection of this source by FAVA is expected.

GRBs

Fourteen 2FAV sources have been associated with LAT-detected GRBs. As the association with GRBs requires both time and spatial coincidence of a single flare, these associations can be made with confidence. The duration of GRBs is of the order of hundreds of seconds, yet 14 of them have been detected by FAVA over the timescale of one week. The GRBs included in the 2FAV are in fact among the brightest ones observed by the LAT, as shown in Fig. 4.14. The average energy fluence in the 100 MeV − 100 GeV range of the GRBs included in the 2FAV is $\sim 8.5 \times 10^{-5}$ ergs cm^{-2}, while it is $\sim 3.2 \times 10^{-5}$ ergs cm^{-2} for the entire sample of LAT-detected GRBs.

Table 4.8: List of 2FAV sources with non-blazar and non-GRB counterparts.

2FAV ID	Class	Counterpart	Reference
2FAV J0948+00.3	Narrow-line Seyfert 1 galaxy	PMN J0948+0022	D'Ammando et al. (2015)
2FAV J0849+51.1	Narrow-line Seyfert 1 galaxy	SBS 0846+513	D'Ammando et al. (2012)
2FAV J0324+34.3	Narrow-line Seyfert 1 galaxy	1H 0323+342	Paliya et al. (2014)
2FAV J0419+38.2	Radio galaxy	3C 111	Grandi et al. (2012)
2FAV J0319+41.5	Radio galaxy	NGC 1275	Abdo et al. (2009a)
2FAV J0433+05.5	Radio galaxy	3C 120	Tanaka et al. (2015)
2FAV J2102+45.8	Nova	V407 Cyg	Abdo et al. (2010d)
2FAV J0639+05.8	Nova	V959 Mon 2012	Cheung et al. (2012b)
2FAV J1751−32.6	Nova	V1324 Sco 2012	Cheung et al. (2012a)
2FAV J2023+20.7	Nova	V339 Del 2013	Hays et al. (2013)
2FAV J1354−59.2	Nova	V1369 Cen 2013	Cheung et al. (2013)
2FAV J2032+41.0	high-mass gamma-ray binary	Cyg X−3	Abdo et al. (2009d)
2FAV J0240+61.4	high-mass gamma-ray binary	LS I+61 303	Abdo et al. (2009b)
2FAV J1302−63.8	high-mass gamma-ray binary	PSR B1259−63/LS 2883	Abdo et al. (2010e); Caliandro et al. (2015)
2FAV J0534+22.0	pulsar-wind nebula	Crab	Abdo et al. (2011); Tavani et al. (2011) Buehler et al. (2012); Mayer et al. (2013)
2FAV J1023+00.7	pulsar	PSR J1023+0038	Stappers et al. (2014)

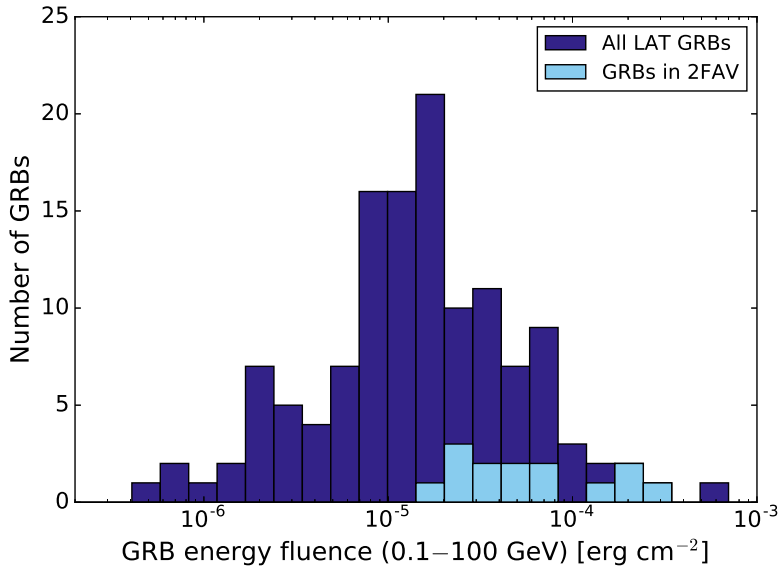

Figure 4.14: Comparison of the energy fluence between 100 MeV and 100 GeV of the LAT-detected GRBs and of those included in the 2FAV.

Counterparts of unknown type

In the 2FAV, 16 sources have gamma-ray counterparts for which no plausible counterpart at other wavelengths is listed in the respective catalogs. 12 of these unassociated counterparts are found in

the 3FGL, two among LAT-issued ATels, one in the 3EG, and one in the 1AGL. In the 3FGL, 33% of the sources are unassociated. In the 2FAV these unassociated 3FGL sources represent only $\simeq 3\%$ of the found counterparts. The fraction of unassociated sources in the 3FGL increases steeply for fainter sources. We check for a possible instrumental cause (due to the different sensitivities of the two catalogs) of this marked difference in the percentages of unassociated gamma-ray sources. Figure 4.15 shows the fraction of unassociated 3FGL sources in different bins of the energy flux. As is visible, this fraction has already reached ∼30% in the region populated by the 2FAV sources. The smaller fraction of unassociated 3FGL sources in the 2FAV suggests that the 3FGL sources without counterpart, regardless of their class, are less likely to be variable on weekly timescales. This is confirmed looking at the distribution of variability indices for the unassociated 3FGL sources shown in Fig. 4.16. The vast majority of the sources have a small variability index, indicating little or no probability of being variable on the monthly timescales.

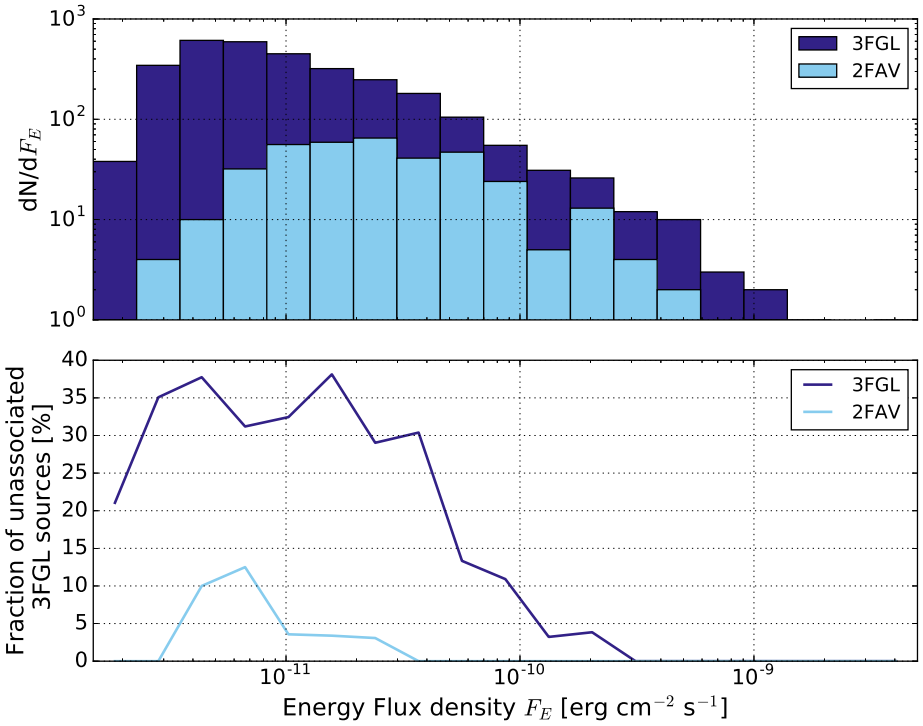

Figure 4.15: Top: distribution of the energy flux F_E [erg cm^{-2} s^{-1}] in the 100 MeV to 100 GeV range for the 3FGL sources and the 2FAV sources with 3FGL counterpart. The values of F_E are read from the 3FGL catalog. Bottom: evolution of the fraction of unassociated sources in the two catalogs as a function of the energy flux.

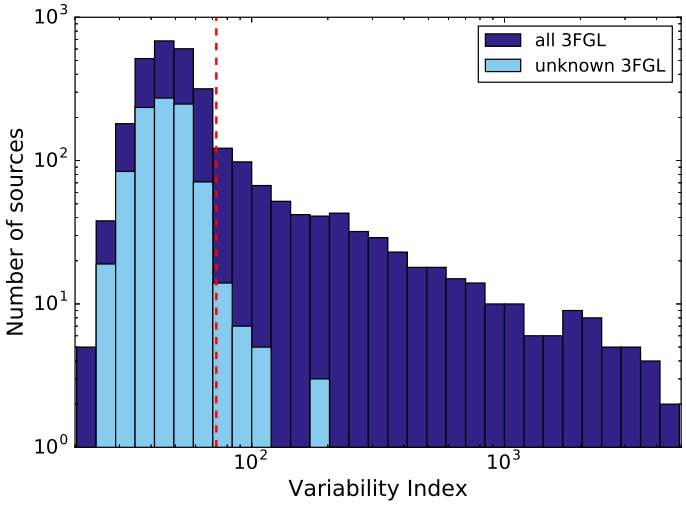

Figure 4.16: Distribution of the variability index for the entire 3FGL sample (dark blue) and for the 3FGL sources for which no counterpart at other wavelengths has been found (cyan). Sources with a variability index larger than 72.44 (red dashed line) have less than 1% probability of being constant on monthly timescales.

Pulsar counterparts

For 2FAV J1023+00.7 and 2FAV J1824−13.0, pulsar counterparts have been found in the step of the association procedure that considers non-variable 3FGL sources. The counterpart of 2FAV J1023+00.7 is the millisecond pulsar binary PSR J1023+0038. The gamma-ray flux of this source increased by roughly a factor 5 between June and July 2013 and remained high for several months afterwards (Stappers et al., 2014). This sudden change in the source emission is possibly associated with a transition between a rotation- and accretion-powered state of the system (Papitto et al., 2014; Papitto and Torres, 2015; Takata et al., 2014). A transition in gamma rays has also been detected by the LAT for the pulsar PSR J2021+4026 (Allafort et al., 2013), which is not included in this catalog. The flux of this source dropped by $\approx 20\%$ around MJD 55850 (MET 340416002). On that occasion, the photometric analysis recorded a $\approx 3.8\sigma$ transition in the high-energy emission of the source[1], smaller than both the catalog and the seed threshold of this analysis. The reduced significance measured for this flux transition is due to the lower sensitivity of FAVA along the Galactic plane (PSR J2021+4026 is at Galactic latitude $b \simeq 2.1°$).

The position of 2FAV J1824−13.0 is compatible with the pulsar PSR J1826−1256, discovered in the *Fermi*-LAT data using a blind periodicity search (Abdo et al., 2009). This source has a frequency of 9 Hz and a characteristic age of 1.44×10^3 years. Its spin-down power is $\dot{E} \sim 3.6 \times 10^{36}$ ergs s^{-1}, roughly two orders of magnitude smaller than that of the Crab pulsar. PSR J1826−1256 is thought to be the energy source powering the 'Eel ' PWN (Roberts et al., 2001).

[1] http://fermi.gsfc.nasa.gov/ssc/data/access/lat/FAVA/LightCurve.php?ra=305.386&dec=40.448

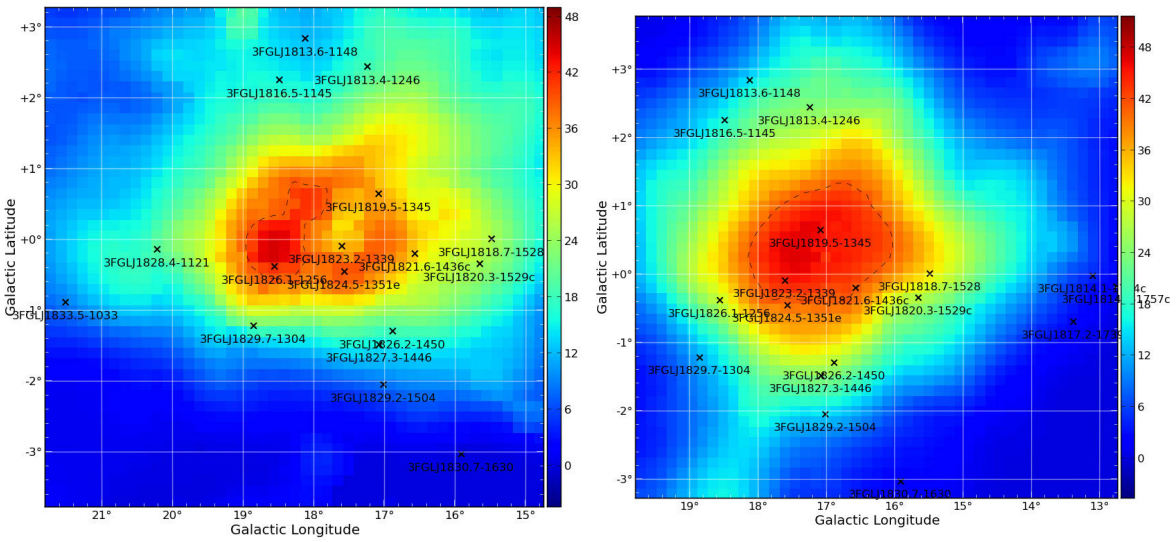

(a) Flare 9323

(b) Flare 9360

Figure 4.17: TS maps from the low-energy analysis of the two flares assigned to 2FAV J1824−13.0. The black crosses marks the position of the 3FGL sources included in the sky model. Flare number 9323 is shown on the left panel. Its position is compatible with the position of PSR J1826−1256 (3FGL J1826.1−1256). The excess of TS in this second outburst associated to 2FAV J1824−13.0 (flare number 9360, right panel) is broad and the flare position is compatible with two 3FGL sources, contained in the 95% contour: 3FGL J1819.5−1345 and 3FGL J1823.2−1339, whose counterpart at other wavelengths is unknown.

Two flares detected by FAVA in the low-energy band have been associated to this source: flares number 9323 and 9360. The corresponding TS maps are shown in Fig. 4.17. As is visible, only in one case (flare 9323, Fig. 4.17a) is PSR J1826−1256 the sole 3FGL source (3FGL J1826.1−1256) contained inside the 95% confidence-level contour. The low-energy photometric significance of the flare is $\sim 9.7\sigma$ and the maximum of the low-energy TS map, located at Galactic coordinates $l = 18.57°$ $b = -0.10°$, is ∼45. This flare has a flux of $(5.3 \pm 1.0) \times 10^{-7}$ ph cm^{-2}s^{-1} between 100 and 800 MeV, and a photon index of 2.1 ± 0.3. Flare 9360 is located at $l = 17.46°$ $b = -0.25°$. It has a photometric significance of 7.1σ in the low-energy band and a TS of ~ 47. The flare is slightly brighter than 9323, with a low-energy flux of $(7.5 \pm 1.2) \times 10^{-7}$ ph cm^{-2}s^{-1}. With a photon index of 3.6 ± 0.4, flare 9360 is considerably softer than 9323 and hence has a larger 95% error radius: $0.96°$ compared to $0.61°$ for flare 9323. As is visible in Fig. 4.17b, the 95% contour of 9360 is broad and contains two 3FGL sources: 3FGL J1819.5−1345 and 3FGL J1823.2−1339, both gamma-ray sources with unknown counterparts.

Flare 9323 happened in the time bin [448818218, 449423018] MET, centered on 2015-03-27. During this week, the LAT performed a long ToO observation of the nova V5668 Srg 2015 (Cheung et al., 2016) and was pointing just 2.3 degrees away from the pulsar. Previous experience with transients detected

in coincidence with ToOs suggest caution, as incorrect modeling of the exposure for the ToO might lead to systematic uncertainties. Although there are indications of the presence of a variable gamma-ray emitter in this region of the sky (see also Neronov et al., 2012), the association of the flares with PSR J1826−1256 cannot be firmly established and we list 2FAV J1824−13.0 as unassociated in the 2FAV.

4.4.2 Unassociated sources

For 77 2FAV sources we found no counterpart in the catalogs used in the association procedure. As is visible in Fig. 4.13, the great majority of the unassociated sources are extragalactic, with only 3 objects close to the Galactic plane ($|b| < 5°$): 2FAV J1259-65.4, 2FAV J2010+35.7, and 2FAV J1824-13.0. The positional coincidence of the latter with PSR J1826−1256 has been discussed in the previous paragraphs. For these low-latitude sources, we made a dedicated search for counterparts using the SIMBAD database (Wenger et al., 2000). A plausible counterpart for 2FAV J2010+35.7 is the bright flat-spectrum radio source B2 2008+35 (VERA J20089+3543, Petrov et al., 2007), located $\sim 0.08°$ (the search radius for this 2FAV source is $0.16°$) away from the 2FAV source. No plausible counterpart could be found for 2FAV J1259-65.4.

We inspect the distribution of the unassociated 2FAV sources in the sky to test the hypothesis of an isotropic distribution, as one might expect in the case of extragalactic sources such as blazars. As was seen in Section 4.3.2, the sensitivity of FAVA is not uniform over the entire sky. In particular, it is reduced along the Galactic plane due to the bright Galactic gamma-ray diffuse emission. We account for this effect by convolving an isotropic distribution of points with the photometric sensitivity of FAVA, using the all-sky maps of expected counts computed with the average weekly exposure (see Section 4.3.2). We randomize the positions of each unassociated 2FAV source according to $l_{\rm rand} = 360°u, b_{\rm rand} = 180° \arcsin(2v-1)/\pi$ (u and v are random variables drawn from a uniform probability distribution between 0 and 1), and test if the source would still be detected by the photometric analysis at this new position. To test the detection of the source, we use the number of observed counts for all the flares associated to the source and compare them to the number of expected counts at the random position of the source. The significance of the flare excess of counts is computed using Poisson statistics as in the photometric analysis (Section 4.2.1). The same cuts on the flare significance used to construct the 2FAV are applied to test the detection of this randomly located source. With this algorithm, we generate 500 samples of randomly distributed sky positions. Each sample contains 77 points, the number of unassociated 2FAV sources. We compare the distribution of the source-source distance for the unassociated 2FAV sources and for the many random realizations of isotropic points, see Fig. 4.18. The agreement of the distributions indicates that the unassociated 2FAV sources are compatible with an isotropic population.

The large number of unassociated sources in the 2FAV could be explained, at least partially, by the

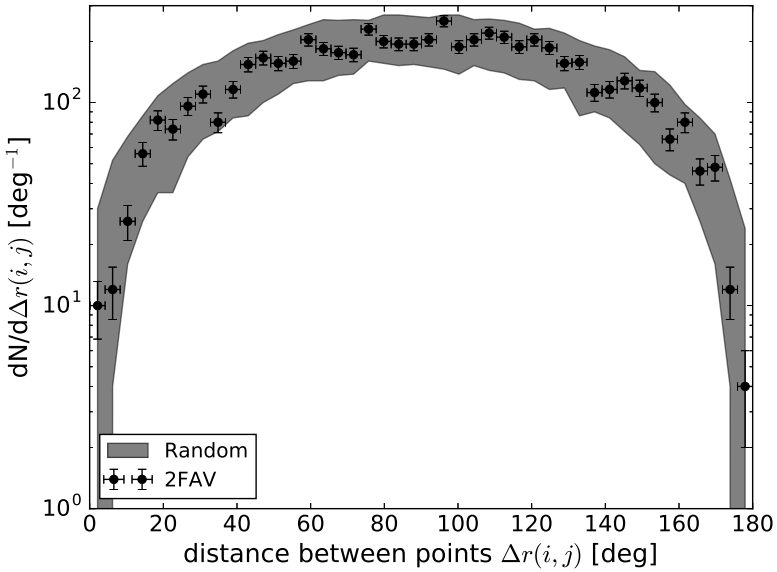

Figure 4.18: Distribution of the source-source distance for the 77 unassociated 2FAV sources (black points), and for the 500 sets of randomly distributed points, each one with 77 objects (shaded area). The width of the shaded area corresponds to the difference between the maximum and minimum value of the corresponding bin content found in the 500 realizations.

longer time span covered by this analysis, with respect to the 4 years of the 3FGL. Of the unassociated 2FAV sources, 21 flared solely during the 3FGL period, while 49 have the first detected flare outside of the 3FGL time range. All of the 21 sources that flared only during the 3FGL time span are associated to a single flare, with the exception of 2FAV J0905+01.4 for which 2 flares have been detected. After the release of the 2FAV catalog, the The Third Catalog of Hard *Fermi*-LAT Sources (3FHL, Ajello et al., 2017) was published. This catalog is based on 7 years of *Fermi*-LAT data and contains 214 sources which have no counterpart in any of the FGL catalogs. We correlate the positions of the sources in the preliminary release of the 3FHL[1] with those of the unassociated 2FAV sources. We find 3FHL counterparts for 2 2FAV sources (in addition to PSR J1826−1256) that are listed as unassociated in the 2FAV: 2FAV J1650+04.2 is associated with 3FHL J1650.9+0430 (unknown class) and 2FAV J1514−09.8 is associated with 3FHL J1514.7−0949 (classified as bcu).

4.4.3 Comparison with the 1FAV

The analysis presented here differs from the one used to construct the 1FAV in two ways: it includes the likelihood follow-up and, for both the likelihood and photometric analysis, uses the Pass 8 data release (Atwood et al., 2013), as opposed to the Pass 7 reprocessed (`P7SOURCE_V6`) of the 1FAV (Ack-

[1] https://fermi.gsfc.nasa.gov/ssc/data/access/lat/3FHL/

ermann et al., 2013a). The 2FAV analysis covers, with the same time binning, the same time range as the 1FAV, from 2008-08-04 to 2012-07-16 (47 months). The list of flares found in the two catalogs during this common time range can be compared, in order to quantify the improvements brought by the updated analysis. Even though the significance threshold used to include flares in the 1FAV is lower (5.5σ in the 1FAV, 6σ in the 2FAV), the 2FAV catalog lists $\sim 43\%$ more flares than the 1FAV (2025 in the 2FAV, 1419 in the 1FAV) for the common time range. This increase in the number of detections is mostly due to the higher sensitivity of the likelihood follow-up and the inclusion of flares detected simultaneously above 4σ in both energy bands. As seen in Section 4.3.2, this cut provides better sensitivity for flares with photon index between $\sim$2 and $\sim$2.5. Of the 761 flares detected in this combined energy band for the entire 2FAV, roughly ~ 370 happen in the 1FAV time range.

A direct, flare-by-flare comparison between the 2FAV catalogs can be done only for the photometric analysis. Since this analysis is the same for both catalogs, such a comparison gives information on the effect of the new Pass 8 data release. Comparing the distributions of the source-flare distance d_{s-f} (see Fig. 4.19b), we see that the harmonic mean (the average of d_{s-f} weighted by $1/d_{s-f}$ to account for the effect of the annular geometry) of this distance has decreased from 0.42° in the 1FAV to 0.34° in the 2FAV. The improvement on the photometric sensitivity is less marked, see Fig. 4.19a. The high-energy photometric significances of 2FAV flares are, on average, $\sim 6\%$ higher than the ones measured in the 1FAV for the same flares. No significant improvement in the sensitivity is measured for the photometric analysis in the low-energy band.

When comparing the sources in the two catalogs, we find no 2FAV counterpart for 15 of the 215 sources in the 1FAV. 10 of these missing sources are due to the higher significance threshold used in the 2FAV. For the flares associated to the remaining 5 1FAV sources, some have a 1FAV significance just above 6σ, and may have fallen below threshold in the 2FAV. In other cases, the 1FAV flares are spatially coincident with a 2FAV source, even if the 1FAV source to which they are associated is not compatible with the position of any source in the 2FAV. This discrepancy is a consequence of different clustering solutions in the 2FAV (based on more and better localized flares) that shift the position of the cluster centroids away from the 1FAV sources.

4.5 2FAV flare spectra

We look at the spectral properties of the flares included in the 2FAV. This discussion will consider first flares associated to blazars (the vast majority of the flares in the 2FAV catalog), then those associated to sources in other classes. To make this study, we will consider all catalog flares that have TS>18, a well defined 95% confidence level TS map contour, and that located are more than 6° from the Sun. We note here that this cut is less stringent than the one used to locate the sources, which considered only the best localized flares of each cluster.

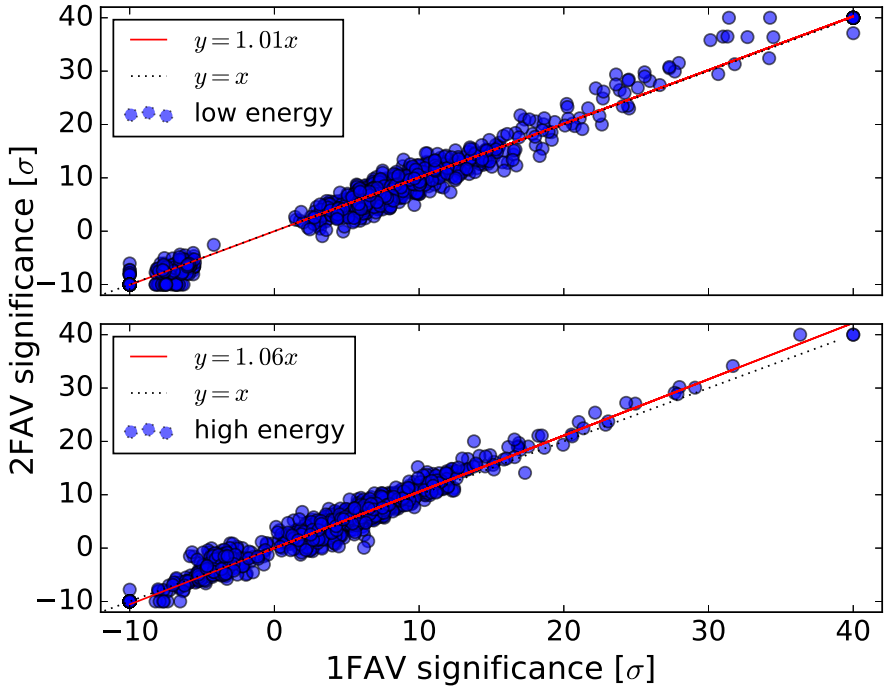

(a) Photometric significance. Top: low energy band, bottom: high energy band.

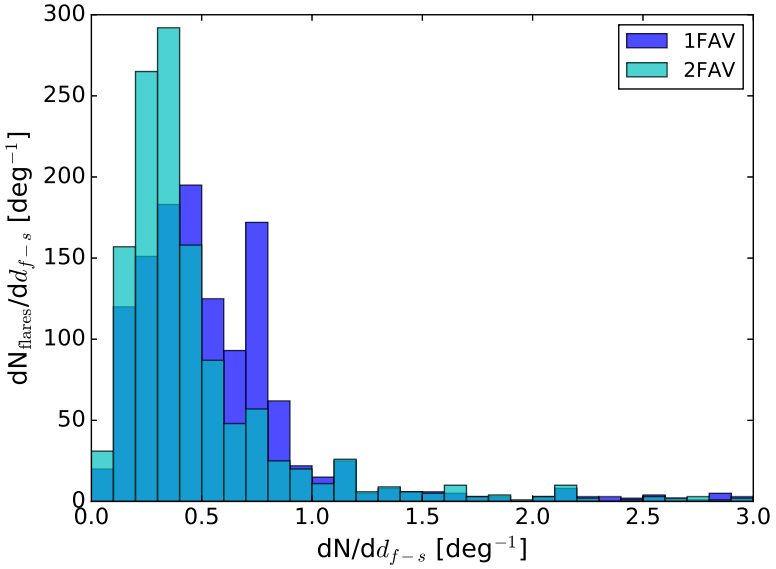

(b) Angular resolution

Figure 4.19: Comparison of the photometric significances (top) and angular resolution (bottom panel) for flares measured in the both the 1FAV and in the 2FAV. The bottom plot shows the distribution of the distance of the flares to the FGL counterparts of the 1FAV and 2FAV sources to which the flares are assigned. The spike at $\sim 0.7^\circ$ is caused by the $0.5^\circ \times 0.5^\circ$ pixelization of the photometric maps. We remind the reader that the photometric analysis merges the flare positions found in the two energy bands, and provides a unique estimator of the flare position.

The absorption of the gamma rays on the Extragalactic Background Light (EBL) affects the SED of distant sources. As a result of the pair-production interaction of the gamma rays with diffuse radiation fields in the Universe, the observed spectrum of a source at redshift z is attenuated for energies higher than $\sim 170(1+z)^{-2.38}$ GeV (Ackermann et al., 2012c). The most distant associated 2FAV source is 2FAV J0539−28.8 (FSRQ PKS 0537−286), located at $z = 3.1$. For this source, the EBL is expected to affect the spectrum above ~ 6 GeV. Spectral measurements in the low-energy band are therefore always unaffected. The high energy band of FAVA starts at 800 MeV. Measurements of the spectral shape in this band are still dominated by the lowest-energy events in the band. The effect of the EBL on the high-energy spectra of the 2FAV flares is expected to be small, and will be neglected.

4.5.1 Blazars

To extract source-intrinsic information from the sample of 2FAV flares associated with blazars, the flux limit of the analysis has to be accounted for. We use the sensitivity maps computed for a range of different spectral indices (see Section 4.3.2). The flux limits we apply are computed as the average sensitivity at the position of the 2FAV blazars, plus one standard deviation (std), see Fig.4.20. As the sensitivity in the two energy bands depends on the spectral index, for each energy band we choose the spectral index corresponding to the worst sensitivity: $\Gamma = 3.5$ in the low-energy band and $\Gamma = 1.5$ in the high-energy band. For the positions of 2FAV sources associated with blazars, the resulting flux limits are $F_{\rm LE}^{sens} = 3.67 \times 10^{-7}{\rm cm}^{-2}{\rm s}^{-1}$ in the low-energy band, and $F_{\rm HE}^{sens} = 3.24 \times 10^{-8}{\rm cm}^{-2}{\rm s}^{-1}$ in the high-energy band. In the following, we consider only flares above these limits. We remind that these sensitivity limits are conservative, as they only account for the photometric part of the analysis.

The flux $F_{\rm LE/HE}$ and photon index $\Gamma_{\rm LE/HE}$ of the 2FAV flares associated with FSRQs and BL Lacs are presented in Fig. 4.20 for the analysis in the two energy bands. The flares associated with BL Lacs are on average harder than the ones associated with FSRQs (top panels of Fig. 4.20). This difference between the two source populations is already known from the time-averaged spectra. The mean and std of the distributions of Γ for FSRQs and BL Lacs flares above the flux limits are 2.19 ± 0.33 and 1.97 ± 0.27 in the low-energy band, and 2.50 ± 0.36 and 2.14 ± 0.32 in the high-energy band, respectively. These values are in agreement with the average photon index found for the whole sample of BL Lacs and FSRQs in the Third *Fermi* LAT AGN catalog (3LAC, Ackermann et al., 2015b): 2.44 ± 0.20 for FSRQs and 2.01 ± 0.25 for BL Lacs.

As discussed in Section 3.2, blazar flares are often accompanied by a change in the photon index, which decreases (the flare becomes harder) as the flux increases. To test the variation of the photon index with flux level, we divide the entire sample of flares in flux bins (3 for FSRQs and 2 for BL Lacs), each one containing the same number of flares. In each flux bin we compute the mean $\langle\Gamma\rangle$ and the standard deviation σ_Γ of the photon index. For each energy band, the harder-when-brighter behavior

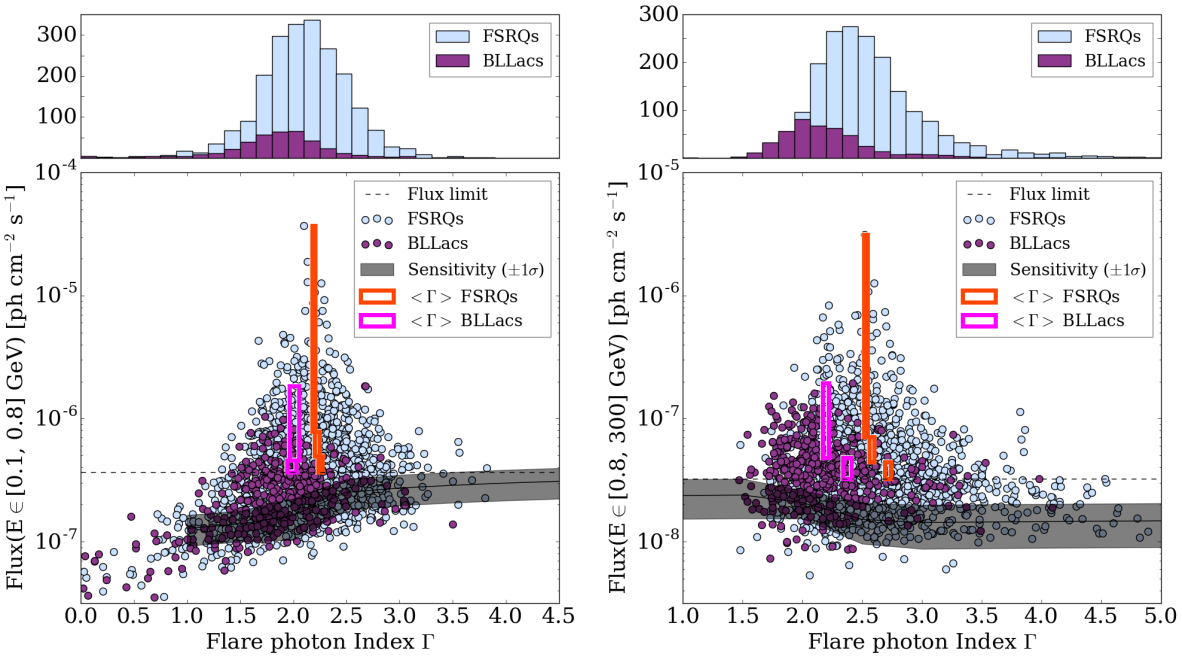

Figure 4.20: Scatter plot of the spectral parameters (Flux and photon index Γ) of the 2FAV flares associated with blazars. Low-energy band: left panel; high-energy band: right panel. The grey-shaded area represents, for each value of Γ, the average sensitivity at the position of the blazars (solid black line) plus/minus one standard deviation (std). The flux limit is chosen as the sensitivity plus one std for $\Gamma = 3.5$ at low energies and $\Gamma = 1.5$ at high energies (dotted lines). Flares associated with FSRQs are in light-blue, the ones associated with BL Lacs are in violet. The boxes shows the binned representation of the data in equally populated flux-bins (magenta for BL Lacs, orange for FSRQs). The width in the x direction is given by the error on the mean Γ for the corresponding bin. In the top panels, the distributions of Γ for the two source classes are presented. Taken from (Abdollahi et al., 2016).

of the entire sample of flares is quantified as the difference in $\langle\Gamma\rangle$ computed in the lowest- and highest-flux bin, divided by the combined error on the corresponding means:

$$H = \frac{\langle\Gamma\rangle^{\text{high}} - \langle\Gamma\rangle^{\text{low}}}{\sqrt{\left(\sigma_\Gamma^{\text{high}}/\sqrt{N^{\text{high}}}\right)^2 + \left(\sigma_\Gamma^{\text{low}}/\sqrt{N^{\text{low}}}\right)^2}} \tag{4.6}$$

For the analysis in the low-energy band, this difference is found to be $H = 2.4\sigma$ and $H = 0.4\sigma$ for FSRQs and BL Lacs, respectively. In the high-energy band, the difference between the average spectral index in the low- and high-flux bin is $H = 6.2\sigma$ for FSRQs and $H = 4.3\sigma$ for BL Lacs. Excluding low-energy flares associated with BL Lacs, the anticorrelation between the photon index and the flux of the flares is measured for the collective sample of the 2FAV blazar flares, not only for specific sources

(like, e.g, Albert et al., 2007; Aharonian et al., 2009; Britto et al., 2015). For both energy bands, the effect is more significant for FSRQs than for BL Lacs flares. Roughly 60% of the low-energy flares associated with BL Lacs comes from three sources (2FAV J2202+42.3, 2FAV J0238+16.6, and 2FAV J0428-37.9 respectively BL Lacertae, AO 0235+164, and PKS 0426−380). For these objects, a mild (2.7σ) spectral hardening for higher fluxes is measured only for 2FAV J0238+16.6.

Blazars can also be subdivided into low synchrotron peaked (LSP), intermediate synchrotron peaked (ISP), and high synchrotron peaked (HSP), according to the position of the low-energy bump in their SED (see Section 3.1.2). The 349 2FAV sources that have SED classification in the 3LAC are thus subdivided: 295 LSPs, 46 ISPs, and 19 HSPs. With the procedure described above we measure the harder-when-brighter behavior in the three SED classes. We use 3 flux bins for LSPs and 2 for ISPs and HSPs. The results are summarized in Table 4.9. The effect is significant only for high-energy flares from LSPs, the great majority of which are FSRQs.

Table 4.9: Significance of the difference between the average spectral index in the lowest- and highest-flux bin (Eq. 4.6) for flares associated to LSP, ISP, and HSP objects. The third and fifth columns show the number of flares (sources) that are above the flux limit and contribute to the measurement.

	100−800 MeV		0.8−300 GeV	
SED class	Signif. (σ)	$N_{flares}(N_{sources})$	Signif. (σ)	$N_{flares}(N_{sources})$
LSP	1.6	901 (107)	5.4	1159 (149)
ISP	0.5	65 (7)	0.8	28 (10)
HSP	0.2	5 (4)	2.3	91 (15)

In both the low- and high-energy band, no flare with photon index smaller than ~ 1.5 is detected. This limit on the hardness of the flare spectra, here detected for newly accelerated particles, is consistent with the known properties of the time-integrated emission of blazars (see e.g. Dermer and Giebels, 2016; Malkov and Drury, 2001). As higher energy photons carry more information than lower-energy ones, the fact that flares with similar fluxes but softer indices have been detected disfavors an instrumental explanation for this observed limit on the photon index. Under the simple assumptions of leptonic emission and of isotropy of both electrons and target photon fields, the observed constraint of $\Gamma \gtrsim 1.5$ implies that the spectrum of the freshly injected electrons ($dN/dE \propto E^{-p}$) must be softer than $p_{min} \sim 2$. For photon indices smaller than 2, the SED of the source rises with the energy. In a leptonic scenario, this suggests that the IC interaction happens in the Thomson regime (see Section 1.2). The IC cross section drops sharply in the Klein-Nishina regime and the energy transport from leptons to gamma rays becomes too inefficient to produce rising SEDs. For IC interaction in the Thomson limit and among isotropic particle and radiation fields $\Gamma = (p+1)/2$ (Rybicki and Lightman, 1979). Hence, $\Gamma \gtrsim 1.5$ implies $p \gtrsim 2$. This limit is compatible with shock acceleration mechanisms and

magnetic acceleration of particles (e.g. Malkov and Drury, 2001; Blandford and Eichler, 1987; Sironi et al., 2015; Kagan et al., 2015). Simulations of magnetic reconnection models seem to suggest that electron spectra softer than 2 are produced only in cases of low magnetization ($\sigma \lesssim 10$, see Fig. 1.6 in Section 1.1).

4.5.2 Non-blazar sources

Figures 4.21 and 4.22 present the spectral parameters of all the low- and high-energy flares in the 2FAV not associated with blazars. In the low-energy band, flares associated with the binary systems Cyg X−3, LS I+61 303, and PSR B1259−63/LS 2883 and the Crab nebula are located in a different region of the parameter space (bottom-left panel of Fig. 4.21). The flares associated to these Galactic sources have higher fluxes and softer indices than the rest of the 2FAV flare sample. This seems to suggest that the flaring mechanisms of these objects might be different than the one at play in the other sources. At least in the case of the Crab nebula, magnetic reconnection mechanisms are favored over shock acceleration models (Bühler and Blandford, 2014).

The flares associated with non-blazar active galaxies (agn) are harder than those associated with blazars. The medians of the distribution of photon indices for the flares associated to the two non-blazar active galaxies in the 2FAV are 1.7 and 2.1 in the low- and high-energy band, respectively. For the entire blazar sample, the median Γ is 2.1 and 2.4 at low and high energies, respectively. The median low-energy photon index of flares associated to radio galaxies (rdg) is 2.0, compatible with that of blazars. High-energy flares from rdg are, however, harder than those from blazar (median of 2.2). Narrow-line Seyfert galaxies have median flare photon indices of 2.2 in the low-energy band and of 2.4 at high energies.

A small number of high-energy flares from unassociated 2FAV sources are faint and hard (see bottom-left panel of Fig. 4.22). These flares are characterized by a flux in the 0.8−300 GeV band smaller than 10^{-8} ph cm^{-2}s^{-1} and a photon index smaller than 2. These flares are not bright enough to reach the TS $>$ 39 (or photometric significance greater than 6σ) threshold in the high-energy band. They are included in the catalog as they have been detected with TS $>$ 18 simultaneously in the two energy bands. The average significance of the detection in the high-energy band is $\sim$ 20 and in five cases the detection in the low energy band reached a TS of 39 or a photometric significance greater than 6. The low- and high-energy positions of the faint flares for which 18 $<$ TS $<$ 39 in both energy bands are compatible or marginally compatible with each other in all cases. These faint high energy flares appear to have hard spectra. Due to their low fluxes, the error bars are, however, large and the photon indices of these flares are all compatible with $\Gamma = 1.5$ within one and a half sigma.

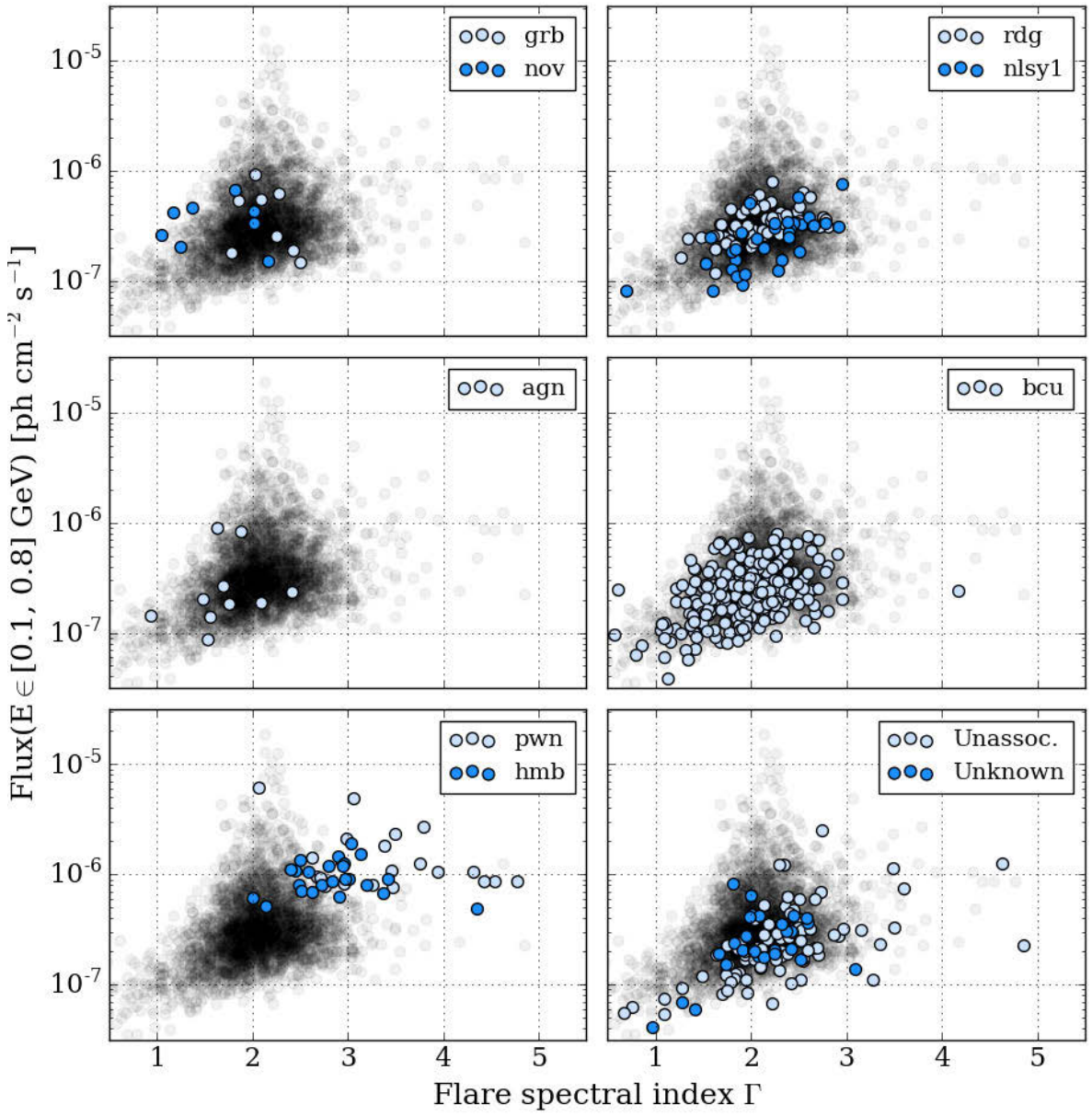

Figure 4.21: Spectral parameters of the low-energy flares for all the non-blazar sources in the 2FAV (see Fig. 4.20 for BL Lacsa and FSRQs). In each panel, the colored points represent flares from specific source classes (see Table 4.4). In grey is presented for reference the entire sample of low-energy 2FAV flares. Taken from Abdollahi et al. (2016).

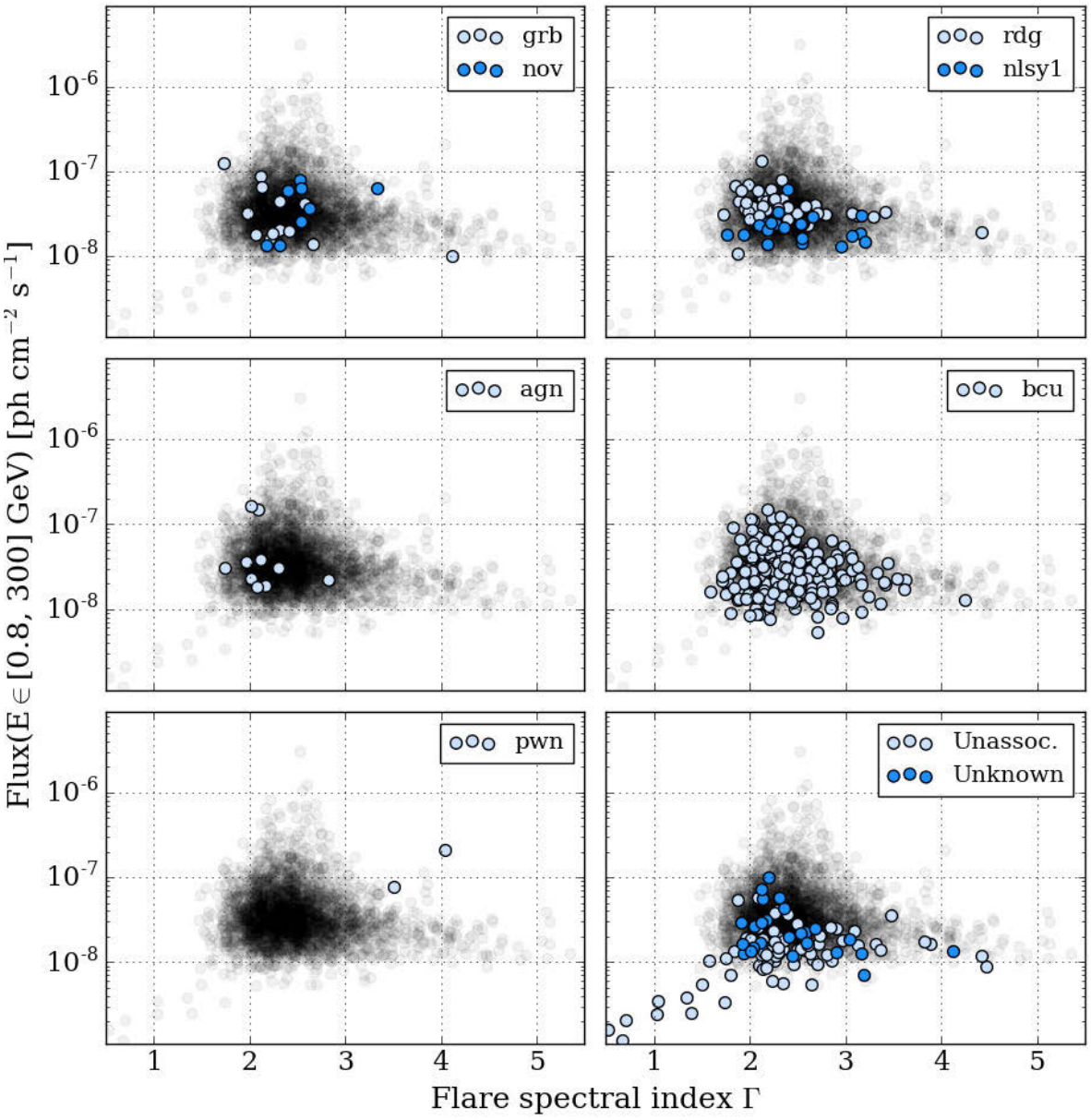

Figure 4.22: Parameters of the spectra of the high-energy 2FAV flares not associated with blazar sources. The high-energy flares from BL Lacs and FSRQs are presented in Fig. 4.20. The grey points shows, for comparison, the parameters for the 2FAV flares detected at high-energies. Taken from Abdollahi et al. (2016).

4.6 Outlook and conclusions

For this thesis, we have extended and upgraded the FAVA analysis pipeline and used it to construct a catalog of flaring gamma-ray sources. The upgraded FAVA analysis consists of an all-sky, model-

independent, photometric variability search that provides a rough estimate of the flare position. In a second stage of the analysis, developed for this thesis, emission from these preliminary positions is analyzed with maximum likelihood methods. The likelihood follow-up provides accurate measurement of the flare position (with a factor of $\sim$3 and $\sim$8 improvement at low and high energies, respectively) and of its spectrum.

We apply this upgraded analysis to the first 7.4 years of *Fermi*-LAT data, searching for gamma-ray variability on the timescale of one week and in two energy bands, 100$-$800 MeV and 0.8$-$300 GeV. This systematic search resulted in 4547 flares with a statistical significance (pre-trials) greater than 6σ. A clustering analysis of the positions of these flares made it possible to single out 518 variable gamma-ray sources which constitute the 2FAV catalog. We provide likely counterparts for these sources, as well as detailed positional and spectral information for all the flares assigned to each source. Among the 441 associated 2FAV sources, the great majority are blazars. For 77 sources, we found no counterpart in the catalogs used in the association procedure.

Studying the spectra of the flares, we observe a spectral hardening with higher fluxes for the entire sample of flares associated with FSQRs, as well as for high-energy flares associated with BL Lacs. The spectra of the observed flares are never significantly harder than $\Gamma = 1.5$. Under simple assumptions of leptonic origin of the flare and of isotropy of the particle distributions in the source reference frames, this limit on the hardness of the flare spectra implies that the injected particles generating the flares is never harder than $dN/dE \propto E^{-2}$.

The analysis developed for this catalog is running in real time, and its results are released to the public at NASA's *Fermi* Science Support Center[1]. This web-page provides a summary of the weekly variability of the gamma-ray sky, listing all the flares and their properties. Photometric aperture light curves can also be generated for a grid of directions on the sky.

There are no theoretical limits to the timescales that can be probed with FAVA. For this study, a weekly binning has been chosen in order to maintain compatibility with the 1FAV. A possible future upgrade of FAVA would be to run the analysis at the smallest possible timescale of $\sim$ 3 hours, and then combine the results to inspect variability at longer timescales. With comparatively little effort, this would provide a comprehensive and systematic study of the variability of the gamma-ray sky. Besides providing the multiwavelength community with an open, all-sky monitoring in the gamma-ray band, it would greatly contribute to the legacy of the *Fermi* LAT.

[1] http://fermi.gsfc.nasa.gov/ssc/data/access/lat/FAVA/

Chapter 5

Estimate of the *Fermi*-LAT sensitivity to gamma-ray polarization

Polarization is a fundamental property of an electromagnetic (EM) wave which describes the geometry of the oscillation of the wave's electric field. Electromagnetic waves are transverse waves in which the electric and magnetic fields ($\mathbf{E}$, $\mathbf{B}$ respectively) oscillate on a plane perpendicular to the wave propagation direction $\mathbf{k}$. In an EM wave, $\mathbf{B}$ is perpendicular to $\mathbf{E}$ and its amplitude $B = E/c$ is fixed. For an EM wave with angular frequency ω traveling along $\hat{z}$, $\mathbf{E}$ can be decomposed into its components on the plane perpendicular to the wave vector $\mathbf{k} = (0, 0, k)$. Considering the wave at $\mathbf{x} = (0, 0, 0)$:

$$E_x(t) = E_x(0)\cos(\omega t - \varphi_1) \qquad E_y(t) = E_y(0)\cos(\omega t - \varphi_2) \tag{5.1}$$

These are the parametric equations for an ellipse. The axes and orientation of this ellipse are fixed in time and are given by the relative values of $E_x(0)$, $E_y(0)$, φ_1, and φ_2 (e.g, Rybicki and Lightman, 1979). The angle χ between $\mathbf{E}(t)$ and $\hat{x}$ is called the polarization angle. This is the most general polarization state of an EM wave and is called elliptical polarization. Linear and circular polarization are degenerate cases. Linear polarization, when $\varphi_1 = \varphi_2$, implies that the orientation of $\mathbf{E}$ is fixed (χ is constant) but its magnitude changes. An EM wave is circularly polarized when $\varphi_1 = \varphi_2 \pm n\pi/2$ and $E_x(0) = E_y(0)$: the magnitude of $\mathbf{E}$ is fixed but it rotates constantly in the xy plane. A comprehensive review of the formalism used to describe polarization can be found in Trippe (2014) and McMaster (1961).

When dealing with a superposition of waves, as customary in astronomy, a net polarization arises only in case of anisotropies in the source or in the medium traversed by the radiation. In such cases

the radiation is partially polarized with a polarization degree Π of:

$$\Pi = \frac{I_{\text{pol}}}{I_{\text{tot}}} \in [0, 1] \tag{5.2}$$

where I_{tot} is the total intensity of the radiation, and I_{pol} is the intensity of the polarized radiation. In astrophysics the polarization degree is traditionally quoted as a percentage and the polarization angle is conventionally measured from the celestial north going east.

Measuring the polarization degree and angle of a source's emission gives important information on the astrophysical environment of the source such as the strength, orientation, and degree of turbulence of the magnetic field and, when combined with other observables, on the location of the emission region, the emission mechanisms, and the types of particles involved. All of this information is often not accessible if one considers just the scalar properties of the radiation.

Since the first observation of the polarization of starlight by Hiltner and Hall (Hiltner, 1949; Hall, 1949), polarimetry has become a useful probe of astrophysical environments. Optical polarimetry makes it possible to measure the properties of the interstellar medium and of the magnetic field in our Galaxy, and to detect and characterize the atmosphere of exoplanets (Snik and Keller, 2013). In cosmology, the study of the polarization of the CMB provides important tests of our understanding of the early universe, and makes it possible to measure some of its properties (see, e.g., Kovac et al., 2002; Kogut et al., 2003). In astrobiology, polarization of light could also be the cause of the homochirality of amino acids found in biological molecules on Earth (Clark, 1999). At X-ray energies, the first measurements date back to the 1970s when a polarization degree of $\sim 16\%$ at an angle of $\sim 160°$ was measured for the Crab nebula, thus establishing the synchrotron nature of the keV emission of this source (Weisskopf et al., 1976, 1978). More recent measurements of the $\lesssim$ MeV emission of the Crab nebula (Dean et al., 2008), of the black hole binary system Cygnus X1 (Laurent et al., 2011), as well as of some bright GRBs (e.g., Götz et al., 2013; McGlynn et al., 2007; Götz et al., 2009) have been performed with the International Gamma-Ray Astrophysics Laboratory (INTEGRAL, Winkler et al., 2003).

As seen in the first chapter of this thesis, a certain degree of linear polarization is expected for all the processes thought to produce gamma-rays, with the exception of π^0 decay. In the case of a uniform magnetic field, synchrotron radiation can be highly polarized up to a maximum polarization degree of $\approx 60\% - 70\%$. Inverse Compton scattering can either induce or reduce the polarization degree of the target photon field, depending on the geometry of the interaction. The degree of polarization of high energy photons emitted through bremsstrahlung is suppressed by the square of the Lorentz factor of the emitting particles. As the polarization properties of these processes differ, observing gamma-ray polarization would provide strong constraints on the emission mechanism. For example, it could help in distinguishing between hadronic and leptonic emission models of blazars. As seen in Section 1.3, some hadronic models interprets the gamma-ray emission as proton synchrotron radiation, while

leptonic models invoke inverse Compton scattering. Theoretical studies of the polarization degrees of blazars indicates maximum values of $\approx 70\%$ in case of hadronic synchrotron emission and $\lesssim 40\%$ for leptonic models, depending on the target photon field (e.g., Zhang and Böttcher, 2013; Chakraborty et al., 2015). For many other gamma-ray sources, like pulsars and GRBs, the polarization signatures of the gamma-ray emission differ greatly between proposed emission models. Constraining these models with measurements of the gamma-ray polarization is discussed in Bernard (2013); Gros and Bernard (2017) and references therein.

As of today, polarization of astrophysical sources above the MeV has never been measured due to the lack of dedicated instrumentation. Recent proposals of future MeV missions, such as e-ASTROGAM (De Angelis et al., 2016) or the Compton-Pair Production Space Telescope (ComPair Moiseev et al., 2015) all feature polarimetric capabilities. However, it is likely that no such mission will be operative in the next few years. For this reason, we perform a preliminary estimate of the sensitivity of the *Fermi* LAT to gamma-ray polarization, presenting the principle of the measurement and discussing both statistical and systematic uncertainties. This chapter is based and expands on the work already published as part of the proceedings of the 6^{th} International Symposium on Gamma-Ray Astronomy 2016 (Giomi et al., 2016). It is the result of the work done in the first year of my PhD. As it became clear that the scope of the analysis implementation was too large to be accomplished within the three year duration of my studies, I focused on the 2FAV catalog (Chapter 4). As a consequence, the analysis presented here could still be optimized. We will discuss its limitations and the possible improvements in the last section of this chapter.

5.1 Principle of the measurement

In the sensitivity range of the LAT, above $\sim$ 30MeV, the interaction of gamma rays with matter is dominated by pair-production in the electrostatic fields of the nuclei. The pair production cross section for linearly-polarized photons has been computed by Berlin and Madansky (Berlin and Madansky, 1950) and shows a dependence on the orientation of the plane in which the $e^{\pm}$ pair is produced with respect to the direction of the polarization vector of the photon (see also May, 1951; Maximon and Olsen, 1962).

The geometry of a pair creation event is sketched in Fig. 5.1. The photon is moving along the z axis and its polarization vector lies on the x axis. The final state is described by 5 kinematic variables that are customarily chosen to be the azimuthal and polar angles (ψ, φ and θ_-, θ_+, respectively) and the energy of one of the two leptons. The definition of the relevant angles is given in Fig. 5.1. In case of an infinitely massive nucleus, the momenta of the electron and the positron, and that of the incoming photon, lay on a plane. The deviation from this planar situation is measured by the coplanarity angle φ. For a given φ, the azimuthal angle ψ measures the orientation of the pair with respect to the

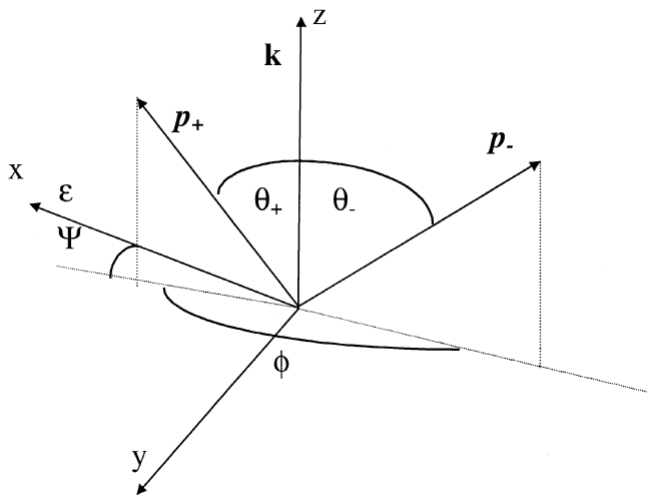

Figure 5.1: Geometry of a pair production interaction. The photon is coming along the z axis and its polarization vector is on the x axis. The pair production interaction happens in the origin. The electron and positron momenta are indicated by $\mathbf{p}_-$ and $\mathbf{p}_+$, respectively. Image taken from Depaola et al. (1999).

direction of the photon polarization vector. Integrating over polar angles and energy, one obtains the so-called spatial azimuthal distribution, that is, the cross section as a function of the coplanarity angle φ and the azimuthal angle ψ. In Fig. 5.2, this distribution is shown for a gamma-ray of 100 MeV. For nearly-coplanar events ($\varphi \simeq \pi$) there is higher probability of producing the pair at $\psi = \pi/2$, in the plane perpendicular to the polarization vector. The situation reverses for smaller φ, and for $\varphi \lesssim 3$ the distribution monotonically decreases to zero.

At high photon energies, the nuclear recoil energy is usually too small to be observed in a silicon tracker (Rosenbaum, 1950) and the spatial azimuthal distribution has to be integrated over the coplanarity angle φ. What is left is a distribution of events modulated in the azimuthal angle ψ, hereafter azimuthal distribution. This distribution has the form:

$$\frac{dN(\psi)}{d\psi} \propto 1 - A_{100}\Pi\cos^2(\psi - \psi_0) \tag{5.3}$$

where A_{100} is the polarization asymmetry for a 100% polarized radiation and Π and ψ_0 are the polarization degree and angle of the incoming photons, respectively. Examples of the shape of the azimuthal distribution for different energies of the gamma-ray are shown in Fig. 5.3. We note that this equation holds true regardless of the choice of the angle ψ that describes the azimuthal orientation of the final state with respect to the polarization vector (Bernard, 2013). The measurable quantities in Eq. 5.3 are the polarization angle ψ_0 and the product $A_{100}\Pi$. To derive the polarization degree of

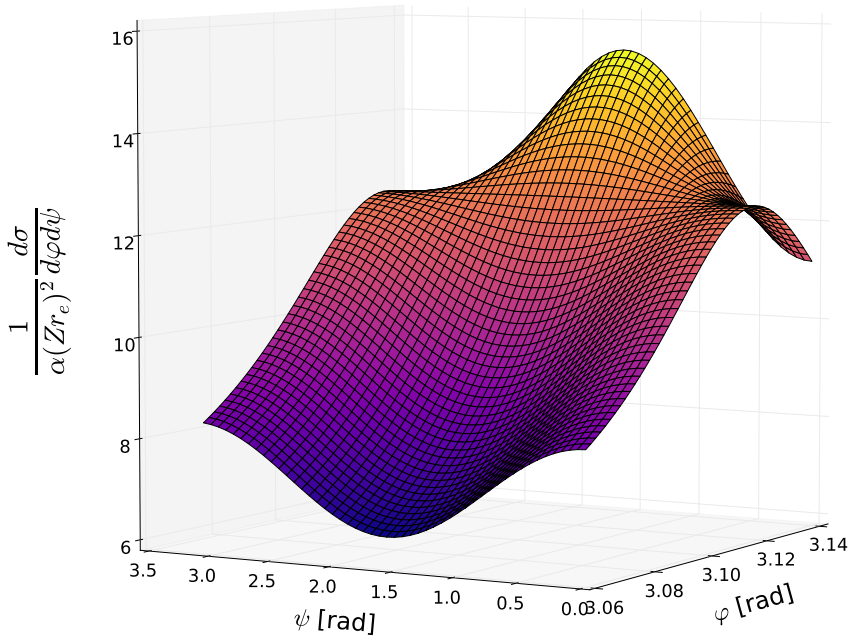

Figure 5.2: Pair production cross section for a 100 MeV gamma ray, after integrating over the electron and positron energies and polar angles θ_+ and θ_-. To produce this figure, we have used the parametric expression of the spatial azimuthal distribution provided in Depaola et al. (1999). Note how the maximum at $\psi = \pi/2$, $\varphi = \pi$ becomes a minimum as the coplanarity angle φ decreases.

the source, A_{100} has to be calculated by integrating the cross section within the 5-dimensional event phase space covered by the measurement. A_{100} depends strongly on the energy. It varies between $\pi/4 \approx 79\%$ at the pair-production threshold and $1/7 \approx 14\%$ in the high-energy ($\gg 100$ MeV) limit. As a result, the amplitude of the polarization-induced modulation of the azimuthal distribution of the events decreases with the gamma-ray energy, as is visible in Fig. 5.3. For intermediate energies the measurable amplitude of the asymmetry depends on the actual definition of the azimuthal angle ψ (Gros and Bernard, 2017). In this study we assume $A_{100} = 20\%$ as computed in Depaola et al. (1999) for a 100 MeV photon.

The key to measuring polarization is to be able to reconstruct the azimuthal angle ψ of each event. As seen in chapter 2, the precision of the tracker is limited by multiple Coulomb scattering (MS) at low energies and by the finite spacing between the tracker strips at high energies. Combining these two effects, the angular resolution for the reconstruction of a track can be approximated by:

$$\theta_{\text{res}} = \sqrt{\theta_{\text{MS}}^2 + \theta_{\text{geo}}^2} \tag{5.4}$$

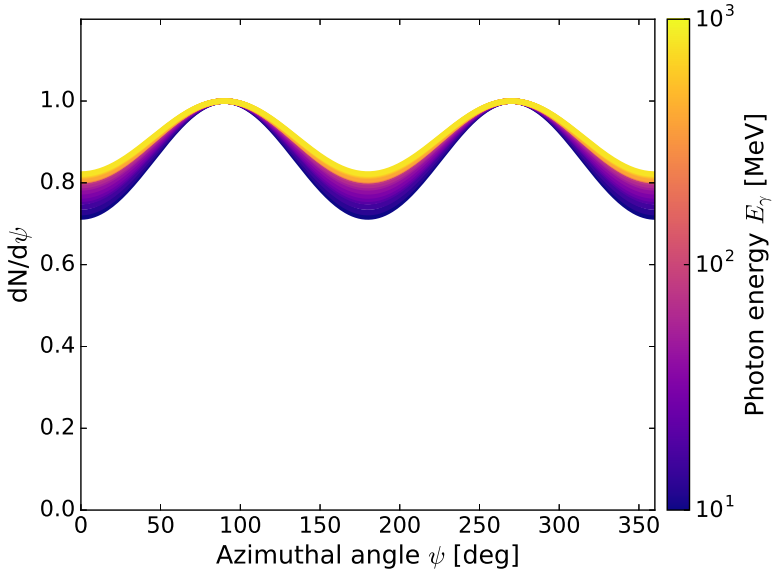

Figure 5.3: Shape of the azimuthal distribution of the events for different energies of the incoming gamma ray. The amplitude A of the modulation decreases with the energy. To produce this plot we used the values of $A(E_\gamma)$ given in Gros and Bernard (2017), for the case in which the azimuthal angle ψ is defined as the bisector angle of the electron/positron momenta. This definition of the azimuthal angle is the most sensitive to the polarization asymmetry at energies $\lesssim 20$ MeV.

where $\theta_{\rm MS}$ is the rms width of the MS angle distribution and $\theta_{\rm geo} = 7.6$ mrad is the smallest angle that can be distinguished, for events coming from the zenith with two planes of the LAT tracker (strip pitch of 228 μm) separated by 30 mm from each other. The azimuthal angle ψ can be reconstructed whenever the opening angle of the pair $\theta_{\rm op}$ is appreciably larger than $\theta_{\rm res}$. The distribution of the opening angle of the pair for different values of the photon energy is shown in Fig. 5.4.

In Fig. 5.5 we compare $\theta_{\rm res}$ with the average pair opening angle $\langle\theta_{\rm op}\rangle \approx m_e c^2/E_\gamma$ as a function of the energy. We consider photons converting in the middle of a ('FRONT') tungsten layer or in the middle of a silicon detector element. As shown in the figure, for events converting in the silicon layers with energies $\leq$200 MeV, the angular resolution $\theta_{\rm res}$ is smaller than the average pair opening angle $\theta_{\rm op}$ and the $e^\pm$ tracks can be resolved, given a sufficient accuracy of the track-reconstruction algorithms.

5.2 Selection of silicon-converted events

With the *Fermi*-LAT, polarization can only be measured using low energy ($\lesssim$ 200 MeV) events that convert in the silicon elements of the tracker. Only for these events can the azimuthal angle of the $e^\pm$ pair be measured with sufficient precision. Before describing how these events can be selected, we

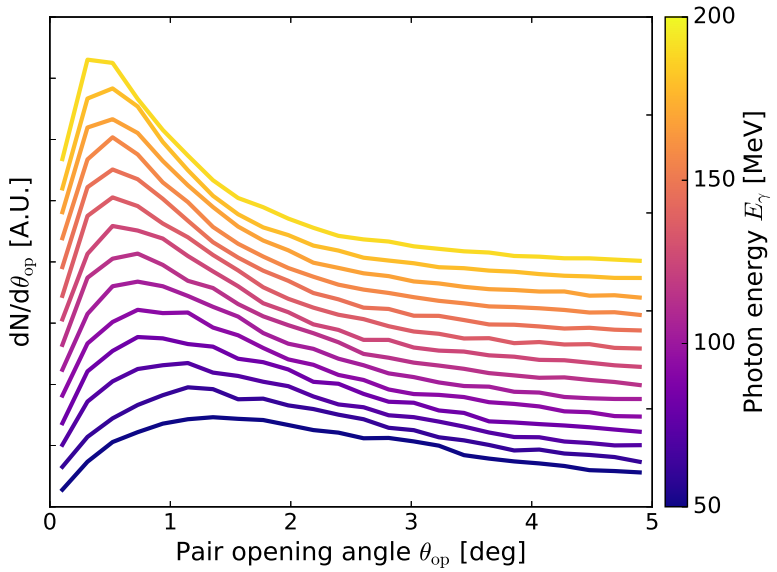

Figure 5.4: Distribution of the pair opening angle $\theta_{\rm op}$ as a function of the photon energy. The curves shows the profile of the normalized $\theta_{\rm op}$ distribution in different energy bins, whose center value can be read from the color scale. To separate the curves corresponding to different energies, an offset has been applied. To produce this plot we have used MC simulated interactions of gamma-rays in the LAT.

briefly review the structure of the LAT-tracker (see Section 2.2.1) for the convenience of the reader. Each tower module of the tracker is composed of a stack of 18 trays. The topmost 16 trays carry one converter foil followed by two SSDs on a support structure based on aluminum honeycomb and carbon walls. The arrangement of these components is visible in Fig. 5.6. The depth of each tray in the FRONT (BACK) section of the tracker is 0.042 (0.194) radiation lengths, divided in 0.008 radiation lengths in the SSDs, 0.006 radiation lengths in the electronics and support structure, and 0.027 (0.18) radiation lengths for the converter foils of the FRONT (BACK) section (Bregeon, 2011; Atwood et al., 2009). At normal incidence, 11% of incoming gamma rays are expected to convert in one of the silicon SSDs of the LAT.

To classify the events we use boosted decision trees (BDT, see e.g., Ivezić et al., 2014) with gradient boosting (BDTG), a machine learning algorithm routinely employed in Physics (see, e.g. Roe et al., 2005; Yang et al., 2005). Compared with other classification algorithms, BDTG gave the best performance. A decision tree is a collection of binary questions (nodes) of the form $x_i \gtrless c_j$ for some variable x_i and cut value c_j. These binary nodes are connected with each other in subsequent layers, depending on the the depth of the tree. At the bottom of the decision tree, events are classified into sets of leaves: in our case, one set for signal-like events and one for background-like events. BDT are ensembles of many decision trees. In the training process, a set of events is fed to the algorithm, together with the

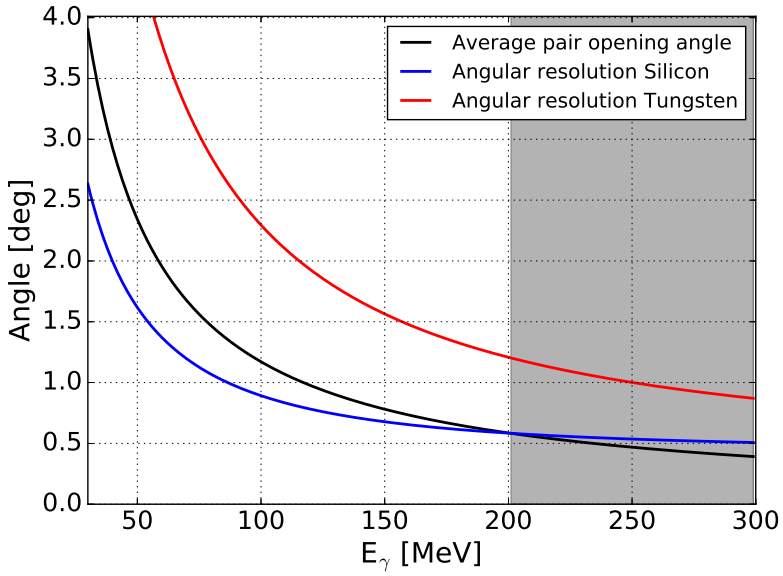

Figure 5.5: Angles at play in the reconstruction of the tracks of the $e^{\pm}$ pair in the LAT tracker. To be able to resolve the two tracks the average pair opening angle ($\langle\theta_{\rm op}\rangle$, black line) must be larger than the achievable angular resolution $\theta_{\rm res}$, which depends on the photon energy and on where the pair is created (middle of a silicon detector plane in blue, middle of a FRONT tungsten converter foil in red). For photon energy $\gtrsim$ 200 MeV (shaded region), the opening angle of the pair is, on average, too small for the two tracks to be resolved.

true value of the target variable (signal or background, in our case). At each iteration, the variables x_i and cuts c_j of each nodes are varied in order to cover the phase space of the input data. The algorithm searches for the combinations of x_i, c_j that maximize the performances of the classifier, measured according to some cost function. The classifier output a continuous variable c with values between -1 (background-like) and 1 (signal-like). The classification of the events into the signal and background classes is done applying a cut on c.

The selection of silicon-converted events is based on intermediate-level LAT data products, called `merit` files. These `ROOT` (Brun and Rademakers, 1997) trees contain, for each event, $\sim$ 1200 variables[1]. These variables describe the signals in the various detectors and spacecraft sub-systems, as well as intermediate quantities characterizing the response and behavior of the different event reconstruction and background suppression algorithms. `Merit` files are intermediate data products, between the raw LAT data and the high-level science ready-photon files. An example of the level of abstraction of the information contained in the `merit` files: they do not contain the position of all the hits in the tracker, but rather quantities like the number of strips with signal in each SSD, the number of tracks found by the reconstruction algorithm and the direction and length of each of them.

[1]This holds true for Pass 8 `merit` files. In the initial data release (Pass 6) there were $\sim$200 variables in the `merit` files.

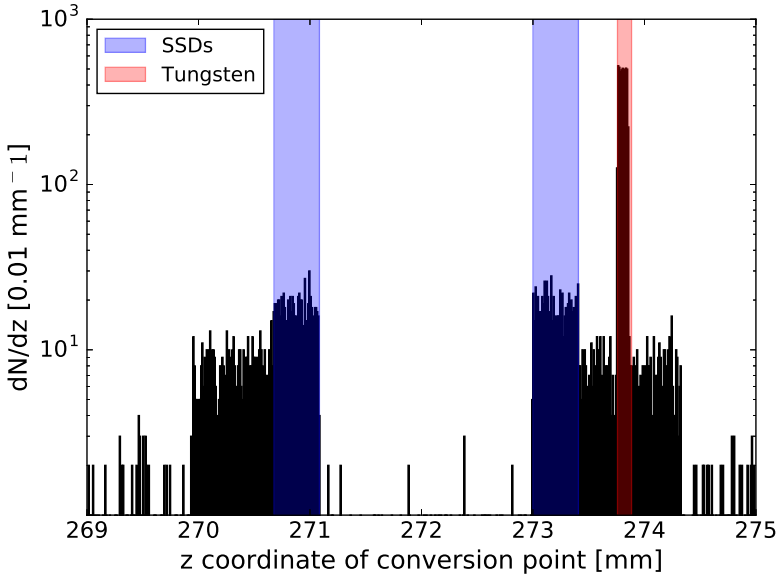

Figure 5.6: 'Tomographic' view of layer 7 of the LAT tracker. This histogram bins the z-coordinate (in mm, going from the calorimeter to the top) of the photon conversion point, as resulting from a MC simulation. With a logarithmic scale on the y axis, the positions of the silicon detectors (shaded in light blue), the support and electronics, and of the converter foil (shaded in light red) are clearly visible.

In order to successfully classify silicon-converted events, the number of `merit` variables must be reduced and correlations have to be eliminated. For every `merit` variable x_i, we perform a χ^2 test (Gagunashvili, 2006) checking the compatibility of its distribution for events converting in the SSDs (signal) and for all other events (background, events converting in the tungsten layers or in the electronics or in the support structure) as obtained from MC simulations (see Section 5.4.2 for a description of the simulations). Using the results of this test, we pre-select the 50 variables whose distributions are most sensitive to the conversion type. We proceed then via a series of tests, training a classifier and then removing variables that yield little separating power or that are highly correlated with a more sensitive variable. The remaining 24 variables, are listed in Table 5.1 in order of importance in the classifier hierarchy. The distributions for signal and background events, for the three variables with the most discriminating power are presented in Fig. 5.7. As is visible in the first panel, the reconstructed tracks of silicon-converted events are more likely to start in the lower SSD of each measurement layer (the z coordinate of the beginning of the best track, `Tkr1Z0` is set in the reconstruction either in the middle of the converted foils, or in the middle of the lower SSDs). In signal events, the $e^{\pm}$ pair is created inside the silicon detectors. These events deposit a smaller amount of ionization charge in the SSD in which they convert, as opposed to background events for which the $e^{\pm}$ pair can travel trough the

entire detector layer. The time over threshold (ToT[1]) of the first layer of the track (`Tkr1ToTFirst`), which estimate the amount of charge deposited in that layer, tends to be smaller for signal events (third panel of Fig. 5.7). Leaving a weaker signal in the very first conversion layer, signal events are also more likely to leave a hit in an odd number of SSDs, as opposed to background events (second panel of Fig. 5.7).

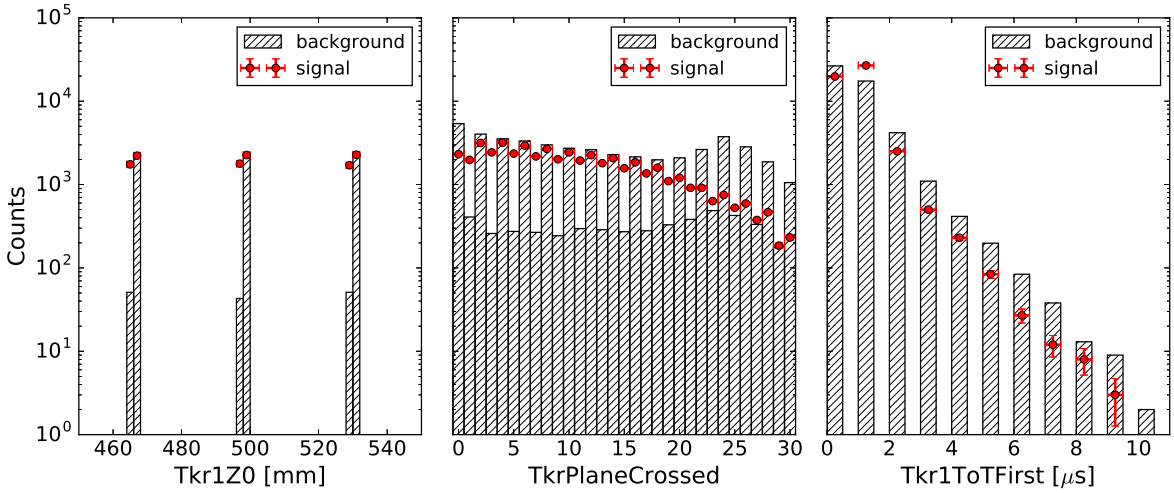

Figure 5.7: Distributions of three of the most useful `merit` variables that are used to select silicon-converted (signal) events. The distributions of the variables are drawn in dark blue for signal events, in cyan for background events. The histograms for both event classes have 5×10^4 entries. The variable carrying the highest discriminating power is `Tkr1Z0`, the z coordinate of the start of the reconstructed track. For the sake of clarity, the distribution of this variable is presented on a restricted range, showing three layers of the FRONT section of the tracker.

We use the implementation of the BDTG algorithm provided with the Toolkit for Multivariate Data Analysis (`TMVA`, Hoecker et al., 2007) library. The classifier uses a collection of 2000 trees with a maximum allowed depth of 3 and is trained to select events converted in any of the SSDs, which will constitute our signal sample. All other events fall into the background class. The input variables are pre-processed by the algorithm with a principal component analysis[2] to further reduce correlations among them.

To train the classifier, we use a sample of MC generated events with 7×10^5 signal and $\sim 7 \times 10^6$ background events. These events belong to the P8V3_SOURCE class, and have energies between 30 and 250 MeV. The energy range is wider than the one we will use in the analysis, to compensate for

[1]The ToT of a layer is defined as the time the total signal from the layer (digital OR of all the strips) remains above a fixed threshold. It is an estimate of the charge deposited in the layer.

[2]The principal component analysis (PCA) is an unsupervised learning algorithm. It searches for a set of rotations in the parameter space of the data with the aim of finding a base of uncorrelated variables that retains as large a fraction as possible of the initial variance of the data.

Table 5.1: `Merit` variables used to select silicon-converted events, listed in order of separating power (more important first). The ranking of the variables is measured by the `TMVA` method, which accounts for the the frequency the variable is used in any tree node and for the signal/background separation this variable achieved at each node.

Variable name	Description
`Tkr1Z0`	Z position of the first hit of the best track.
`TkrPlaneCrossed`	Number of layers crossed by the track.
`Tkr1ToTFirst`†	ToT associated with the first hit on best track.
`TkrHDCount`	Number of unused clusters in top x-y layer of the best track within 30 mm.
`Tkr1SSDVeto`	Counts the number of hit-clusters found close to non-sensitive region of the tracker.
`TkrRadLength`*	Radiation lengths traversed by the best track.
`TkrThinHits`	Number of clusters in the above cone in the thin-converter layers.
`Tkr2FirstLayer`	First layer in the second track.
`Tkr1ToTAsym`†	Asymmetry between last two and first two ToTs for the best track.
`EvtTkr1PSFMdRat`	Ratio of errors from covariance matrix to PSF expected from simple model.
`Tkr1DifHits`	Difference between the number of x and y clusters associated with track.
`Tkr1TwrEdge`	Distance from tower edge of initial point.
`Tkr1DieEdge`	Distance from wafer edge of initial point.
`TkrStripsZCntr`	Z position of the strips centroid in the tracker.
`Tkr1ToTAve`†	Average ToT for the hits on the best track.
`GrbYHits`	Number of hits in Y projection of the best track.
`Tkr1Hits`	Number of clusters associated to the best track.
`VtxNumVertices`	Number of vertices in the event.
`TkrNumHits`	Total number of TKR clusters.
`GrbXHits`	Number of hits in X projection of the best track.
`EvtTkr1EFrac`	Approximates the fraction of energy carried by best track.
`Tkr1KalThetaMS`‡	Multiple scattering angle for the best track, referenced to first layer.
`Vtx2LongDoca`	Longitudinal distance of the 2^{nd} vertex along the axis of the first vertex.
`EvtEVtxDoca`	Distance of closest approach between the two tracks.

Notes — †: The Time over Threshold (ToT) of a tracker layer is the time the total signal from the layer (digital OR of all the strips) remains above a fixed threshold. It is thus an estimate of the charge deposited in the layer.
‡: The MS scattering angle is computed by adjusting the contributions from all the layers in the track for the predicted energy in each layer, and weighting accordingly. It is sensitive to the particle type and the chosen energy-loss mechanism.
∗: The number of radiation lengths are counted from half-way through the initial converter to the lowest bi-plane in the tracker, whether or not the track actually gets to the end..

energy dispersion. A zenith angle cut of 80° is applied to eliminate the contamination from the Earth's gamma-ray albedo. More details on the production of MC `merit` files are given in Section 5.4.2. After the training, the response of the classifier is evaluated on an sample of events for which the algorithm has not been given the true values (test sample). The agreement between the distributions of the classifier output, as evaluated on the training and test sample, is measured with a Kolmogorov-Smirnov test, which measures the statistical compatibility between two distributions on a scale from KS $= 0$ (non-compatible) to KS $= 1$ (compatible) (e.g., Chakravarti et al., 1967). We measure a KS $= 0.31$ for the sample of signal events, and KS $= 0.92$ for the sample of background events. The agreement of the classifier responses on the training and test sample is satisfactory. The classifier is not overtrained: it behaves equally well on both the samples.

Once a cut c_{BDT} on the classifier response is set, the input data is classified into the signal and background samples. The performance of a classifier is evaluated based on two quantities, the efficiency ε and the purity η, defined as:

$$\varepsilon = \frac{N_{\mathrm{MC\_True}}^{\mathrm{Reco\_True}}}{N_{\mathrm{MC\_True}}} \qquad \eta = \frac{N_{\mathrm{MC\_True}}^{\mathrm{Reco\_True}}}{N_{\mathrm{Reco\_True}}} \tag{5.5}$$

where $N_{\mathrm{MC\_True}}^{\mathrm{Reco\_True}}$ is the number of true signal events that are correctly classified as signal, $N_{\mathrm{MC\_True}}$ the total number of true signal events, and $N_{\mathrm{Reco\_True}}$ the total number of reconstructed signal events. The curves $\varepsilon(c_{\mathrm{BDT}})$ and $\eta(c_{\mathrm{BDT}})$ are shown in Fig. 5.8, together with $f_{\mathrm{BDT}}(c_{\mathrm{BDT}})$, the fraction of events passing the cut. As is often the case, efficiency and purity are partially anticorrelated: as the cut is made more stringent the sample of selected events becomes purer at the expense of discarding a larger and larger fraction of signal events. The threshold value of c_{BDT} to be used in the analysis is found by requiring the quantity:

$$S(c_{\mathrm{BDT}}) = \frac{N_{\mathrm{MC\_True}}(c > c_{\mathrm{BDT}})}{\sqrt{N_{\mathrm{MC\_False}}(c > c_{\mathrm{BDT}}) + N_{\mathrm{MC\_True}}(c > c_{\mathrm{BDT}})}} \tag{5.6}$$

to be maximal. This happens for $c_{\mathrm{BDT}} = 0.675$, corresponding to an efficiency of $\varepsilon = 0.50$, a purity of $\eta = 0.64$, and a fraction $f_{\mathrm{BDT}} = 7\%$ of the events remaining after the cuts.

5.2.1 Instrument Response Functions for silicon events

For what will follow, we need to estimate the LAT effective area $A_{\mathrm{eff}}^{\mathrm{pol}}$ and the point spread function radius R_{95}^{pol} for low-energy silicon-converted events. The basis for our calculations will be version P8V3_SOURCE of the IRFs. For simplicity, we will consider both FRONT and BACK events together. These preliminary estimates of the IRFs for silicon-converted events will be used to characterize, for a given source, the level of signal and background events of astrophysical origin.

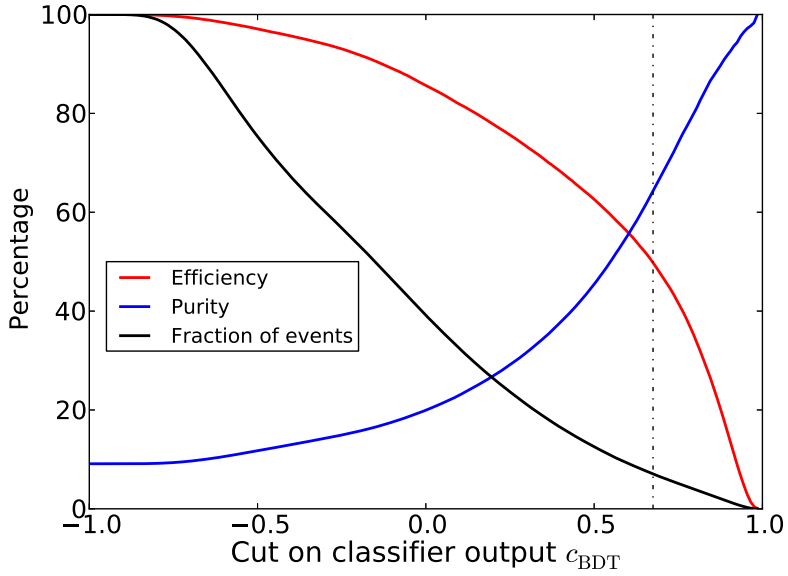

Figure 5.8: Performance of the classifier used to select silicon-converted events: efficiency (red), purity (blue), and fraction of events after the cut (black) as a function of the cut on classifier output c_{BDT}. The dash-dotted line at $c_{\mathrm{BDT}} = 0.675$ marks the value of the cut that will be used in the analysis.

We average the effective area between 50 and 200 MeV and over incident angles θ between $0°$ and $60°$. In every energy bin E_i, the effective area A_{eff} is weighted by E_i^{-2} to account for the average spectra of the sources:

$$\langle A'_{\mathrm{eff}} \rangle = \frac{\sum_{E_i=50}^{200\mathrm{MeV}} \sum_{\theta_i=0°}^{60°} A_{\mathrm{eff}}(E_i, \theta_i) E_i^{-2}}{\sum_{E_i=50}^{200\mathrm{MeV}} E_i^{-2}} \tag{5.7}$$

resulting in $\langle A'_{\mathrm{eff}} \rangle \sim 1.9 \times 10^3$ cm^2. This value has to be scaled by the fraction of events converting in the silicon and passing the analysis cuts. This scaling factor is estimated from a MC simulation of point source observations to account for a realistic distribution of incoming directions. The resulting scaling factor is $\sim 9.5\%$, and the LAT effective area for silicon-converted events becomes $A_{\mathrm{eff}}^{\mathrm{pol}} \approx 180$ cm^2.

To estimate the effective PSF for silicon-converted events, we use a MC simulation of a point source observation and compute the radial distance to that source that contains a given fraction of the silicon-converted events. The distribution of the source-event distance, for events of the SOURCE class in the $[50, 200]$ MeV energy range and with angles in $[0°, 60°]$, is presented in Fig. 5.9. Without selecting on the conversion point, we measure $R'_{95} \approx 11.6°$. Considering silicon-converted events (selected using MC truth) we have $R_{95}^{\mathrm{pol}} \approx 7.5°$. The same exercise for the 68% containment radius

gives $2.8°$ for all events and $1.8°$ for the silicon-converted ones, in reasonable agreement with the simple predictions of Fig. 5.5.

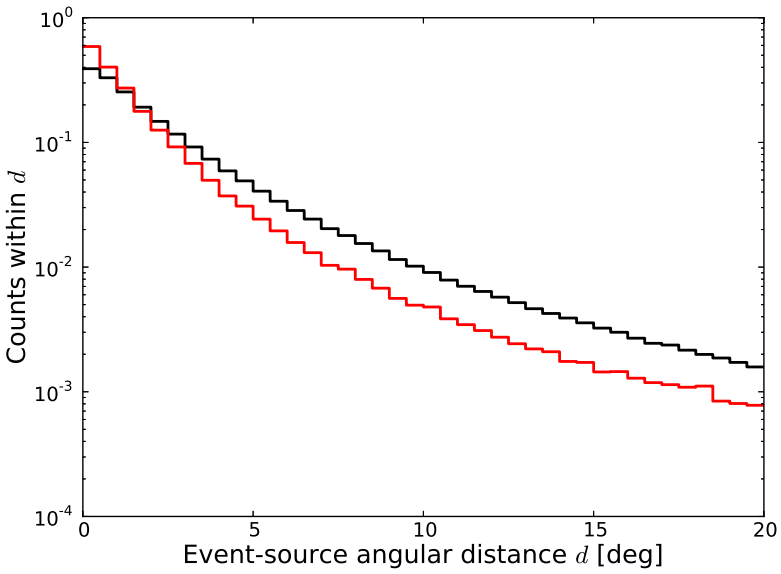

Figure 5.9: Distribution of the event-source distance d as computed from a MC simulation of a point source. The energy range is [50, 200] MeV and the incident angles are below $60°$. To account for the increasing solid angle at larger distances, the events are weighted by $1/d$. In red is the distribution for silicon-converted events (selected on MC truth) and in black the one of all events. The histograms have been normalized to facilitate the comparison.

5.3 The minimum detectable polarization

The statistical sensitivity of a polarimeter is quantified with the minimum detectable polarization (MDP, Weisskopf et al., 2010). For a given probability p, MDP(p) represents the minimum polarization degree corresponding to a modulation amplitude that has less than a probability p of being exceeded by chance, in the case of the absence of a signal.

$$\mathrm{MDP}(p) = \frac{2}{A_{100}} \frac{\sqrt{-\ln(p)}}{R_S} \sqrt{\frac{R_S + R_B}{0.2T}} \tag{5.8}$$

Here R_S and R_B are the rate of signal and background events, respectively, and T is the observation time. As the LAT observes $\sim 20\%$ of the sky at any given moment, each individual source is observed for $\sim 20\%$ of the time, hence the factor 0.2 scaling the total observation time.

We estimate the rates of signal and background events R_S and R_B using the results from the 3FGL

catalog and the corresponding diffuse templates. The flux of each source in the 50-200 MeV energy range is estimated by extrapolating its spectrum as given in the 3FGL.

$$F_{\rm src} = F_{300-1000}\frac{50^{\Gamma-1} - 200^{\Gamma-1}}{300^{\Gamma-1} - 1000^{\Gamma-1}} \tag{5.9}$$

where $F_{300-1000}$ and Γ are the flux measured in the 0.3−1 GeV energy range and the power-law photon index, as measured in the 3FGL. Similarly, the contribution of the Galactic and isotropic diffuse emission $F^{\rm diff} = F^{\rm diff}_{\rm gal} + F^{\rm diff}_{\rm iso}$ in the vicinity of each source is found by integrating the corresponding templates[1]) over the average PSF radius computed in the previous section.

Using the values η and $f_{\rm BDT}$ for the classifier purity and fraction of retained events at the chosen cut value of $c_{\rm BDT} = 0.675$, the rates of signal and background events after the analysis cuts are given by:

$$\begin{aligned} R_S &= 0.95F^{\rm src}A_{\rm eff}f_{\rm BDT}f_{op}\eta \\ R_B &= [(1-\eta)0.95F^{\rm src} + F^{\rm diff}]A_{\rm eff}f_{\rm BDT}f_{op} \end{aligned} \tag{5.10}$$

where $f_{op} \sim 0.8$ is the expected fraction of the events with opening angle larger than the rms multiple scattering angle, as computed from MC simulations of gamma-ray interactions in the LAT (see Fig. 5.4).

In Fig. 5.10, we present the MDP as a function of the Gaussian significance corresponding to the confidence level p for the three most promising gamma-ray sources[2]: the blazar 3C 454.3 (3FGL J2254.0+1608), the Crab pulsar and synchrotron nebula (3FGL J0534.5+2201 and 3FGL J0534.5+2201s, respectively), and the Vela pulsar (3FGL J0835.3−4510 Abdo et al., 2010). After 10 years of observations, a 5σ MDP of $\sim 30\%$ is within reach for Vela, the brightest point source in the *Fermi*-LAT sky. Despite the lower diffuse background near the Galactic anticenter, the 5σ MDP for the Crab pulsar is higher than $\sim 50\%$ after 10 years. Recent studies on the linear polarization degrees of the synchrotron emission of pulsars suggests values between $\sim 10\% - 30\%$. Unfortunately, higher polarization is expected for the off-pulse emission (Cerutti et al., 2016). In the case of 3C 454.3, the 5σ MDP after ten years is $\sim 40\%$. As seen in the beginning of the chapter, polarization degrees of this order are expected in blazar emission models. Perhaps more interesting is the case of the Crab synchrotron nebulae whose MDP is similar to the one for 3C 454.3. Below 100 MeV, the synchrotron nebula becomes brighter than the pulsar (Bühler and Blandford, 2014). As was seen in the introduction to this chapter, the polarization angle for this source to the value is known from observations in other wavelengths. The number of free parameters for a gamma-ray measurement could be reduced, and the sensitivity should increase.

[1] Available at http://fermi.gsfc.nasa.gov/ssc/data/access/lat/BackgroundModels.html

[2] This analysis considers only the steady state emission of the sources. Bright flares from blazars, if not anticorrelated with the polarization degree, could increase the chances of a positive detection of the polarization of these sources (Chakraborty et al., 2015).

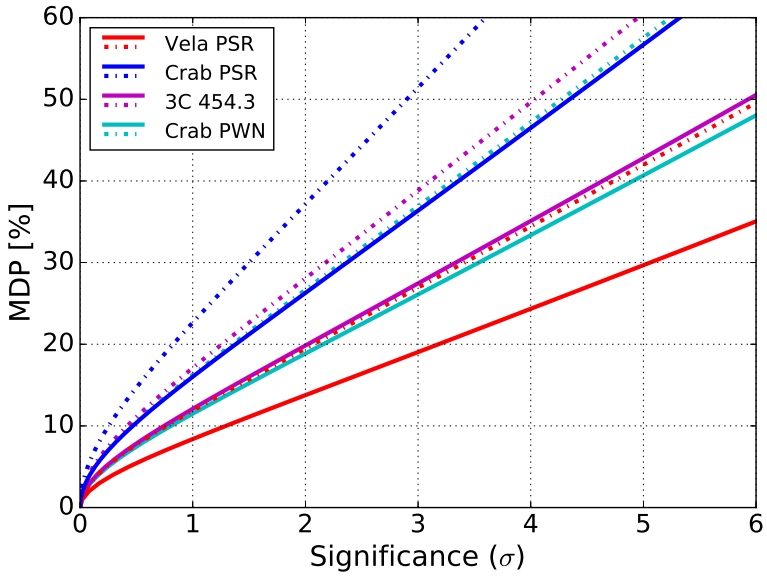

Figure 5.10: Minimum detectable polarization at different significance levels for the Crab and Vela pulsar, the Crab PWN, and 3C 454.3 assuming 10 years (solid lines) and 5 years (dash-dotted lines) of observation.

With such a simple event selection, the measurement of HE-gamma-ray polarization would be possible for the first time with a MDP at the level of $30\% - 40\%$ for 10 years of observations of the brightest sources. For comparison, the design goal of the e-ASTROGAM mission states a MDP$< 20\%$ for a 10 mCrab source (De Angelis et al., 2016). This basic analysis could be improved in many ways, in particular by reducing the PSF radius, and hence the background contamination, and by improving the event selection. We will discuss these points in more detail at the end of the chapter.

5.4 Estimating systematic uncertainties

When, as in this case, statistical errors dominate the sensitivity, one is often allowed to relax the treatment of the systematic uncertainties. However, as this measurement depends on a sample of 'special' events, a careful treatment of the systematic uncertainties is needed. To measure the polarization of a source, one would compare the azimuthal distribution of the events with the one obtained from a MC simulation of the unpolarized emission of the source. The MC should reproduce, as accurately as possible, both the astrophysical and the instrumental conditions of the observation. Systematic errors might arise both as a consequence of incorrect modeling of the source or of the detector. Particularly important is the second, as it might introduce unexpected asymmetries in the azimuthal distribution.

To estimate the overall sensitivity, including both statistical and systematic uncertainties, we build an unpolarized test source by stacking several AGN and set up a crude reconstruction of the azimuthal

angle ψ. Simulating the test source and comparing the MC results with the data, we assess the precision with which the null signal from the AGN stack can be measured.

5.4.1 A stack of AGN as a test source

As no individual gamma-ray source can be considered unpolarized[1], we use a stack of AGN as a test source to estimate the magnitude of the systematic uncertainties affecting the measurement. Even if the emission of individual AGN is polarized, the polarization angles of the individual sources are expected to be uncorrelated. The total flux of a stack of many sources will have low residual polarization. Another reason for using the AGN stack is that, by not looking directly at individual sources, we do not add significant trials to any future analysis.

We set up a simple model of the sources in order to decide the best composition of the stack. The basic idea is to represent the total emission of the stack ($N^{\text{stack}}(\psi)$) as a sum of partially polarized signals $n_i(\psi)$ from the N_{srcs} sources of the stack:

$$N^{\text{stack}}(\psi) = \sum_{i}^{N_{\text{srcs}}} n_i(\psi) \tag{5.11}$$

where each $n_i(\psi)$ has the form of Eq. 5.3. The contribution $n_i(\psi)$ of each source to the global azimuthal distribution of the stack is made up of two components: a point source emission assumed to be polarized in a random direction with a high degree of polarization, $\Pi_{\text{AGN}} = 60\%$, and the integrated Galactic and isotropic diffuse emission in the vicinity of the source. This diffuse component, n_i^{diff} is assumed to be unpolarized, therefore:

$$n_i(\psi) = K_i \left[1 - A_{100}\Pi_{\text{AGN}} \cos^2(\psi - \psi_i)\right] + n_i^{\text{diff}} \tag{5.12}$$

The point source contribution is normalized to the total number of counts expected from the source N_i: $K_i = N_i/\pi[1 - (A_{100}\Pi_{\text{AGN}}/2)]$. To compute N_i we proceed as in the previous section, using the 3FGL spectra of the sources and the IRFs for silicon-converted events. For the rest of the analysis, we will assume an observation time corresponding to 5 years of the mission.

All 3FGL AGN are ranked in descending order of $F_{\text{src}}/F_{\text{diff}}$ in order to maximize the signal-to-noise ratio in the global emission. As seen in Section 5.3, the bright blazar 3C 454.3 is a good candidate for a real measurement, and is therefore excluded from the stack. The two FSRQs 3FGL J1833.6−2103 and 3FGL J0109.8+6132 are also removed from the stack. The simulation of the sky region around these sources, located close the Galactic plane (Galactic latitudes of 5.71° and -1.24° respectively) was not

[1]The only exception is the Moon, whose gamma-ray glow is mostly due to the decay of π^0 produced by inelastic collisions of CRs on its surface (Ackermann et al., 2016b). Unfortunately our Moon is an extended source and is not so bright in gamma rays, both attributes that disqualify it as a good test source.

in a satisfactory agreement with the data. The stack is then constructed by adding one source at a time, but excluding candidates within 20° of any source already included in the stack. For each new source that is added to the stack, we estimate the amplitude of the azimuthal modulation of the stack using a MC procedure: all the signals $n_i(\psi)$ from the sources of the stack are summed, each with a random phase, and the amplitude of the azimuthal modulation of the stack ($A_{\rm stack}$) is measured[1]. This procedure is repeated 10^3 times, randomizing the phases at each new realization. The first moments of the distribution of $A_{\rm stack}$ are used to characterize the residual polarization of the stack. We continue to add sources to the stack until our sample satisfies the following requirements:

- **Brightness:** the total flux from the stacked sources must be greater than 10^{-5} ph cm^{-2}s^{-1}
- **Low residual polarization:** The mean residual amplitude modulation $\langle A_{\rm stack} \rangle$ is at least 2σ below 2%.

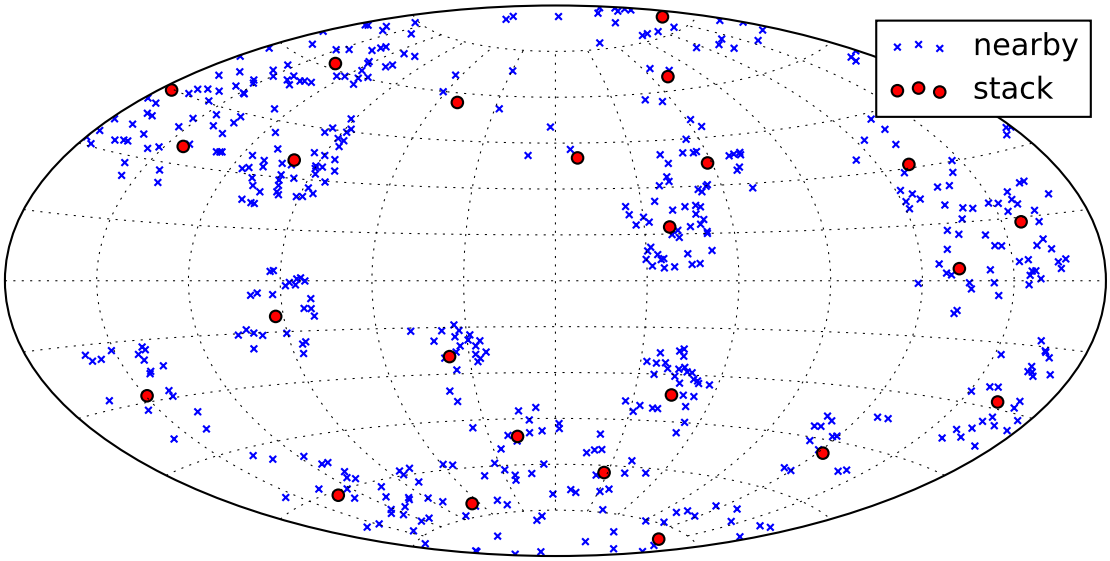

Figure 5.11: Positions, in galactic coordinates and in Aitoff projection, of the AGN constituting the stack (red dots) and of the nearby sources which are also included in the simulation (blue crosses). For 3 AGN of the stack, visible towards the center of the norther hemisphere, less than 10 neighboring sources have been considered. Although there are more 3FGL sources in the vicinity of these AGN, only a few of them are bright enough to be included in the analysis. Details on how the neighboring sources are selected are given in Section 5.4.2.

The resulting 24 sources in the stack are listed in Table 5.2 and their position on the sky is shown

[1]The sum of sinusoids with equal frequencies is still a sinusoid with the same frequency. To see this we can think of taking the Fourier transform $\mathcal{F}[N^{\rm stack}(\psi)]$ of the stack emission. The Fourier transform is linear: $\mathcal{F}(\sum x) = \sum F(x)$ and $\mathcal{F}[\sin(\omega_0 t)] \sim \delta(\omega - \omega_0)$. It follows that $\mathcal{F}[N^{\rm stack}(\psi)] \sim \delta(\omega - \omega_0)$; the reverse transformation returns a sinusoid at the frequency ω_0.

in Fig. 5.11. The total flux of these sources between 50 and 200 MeV is $\sim 1.3 \times 10^{-5}$ ph cm^{-2}s^{-1}, while the total diffuse emission in the same energy range and within 3° of the sources is $\approx 7.9 \times 10^{-6}$ ph cm^{-2}s^{-1}.

Table 5.2: Composition of the AGN stack. As is customary in the LAT catalogs, uppercase (lowercase) class designations indicate identified (associated) sources. Γ is the source photon index computed with a power-law spectrum over the 0.1−300 GeV energy range. The integral source and diffuse fluxes $F^{\rm src}$ and $F^{\rm diff}$ are computed by integrating in energy between 50 and 200 MeV, and within 4° from the source.

Source Name	l [deg.]	b [deg.]	$F^{\rm src}$ [10^{-7}ph cm^{-2}s^{-1}]	Γ	$F^{\rm diff}$ [10^{-7}ph cm^{-2}s^{-1}]	class
3FGL J1512.8−0906	351.29	40.13	19.61	2.36	2.48	FSRQ
3FGL J1229.1+0202	289.98	64.35	12.90	2.66	0.61	FSRQ
3FGL J1522.1+3144	50.16	57.02	8.19	2.35	0.75	fsrq
3FGL J2329.3−4955	332.01	-62.31	4.87	2.27	0.55	fsrq
3FGL J0403.9−3604	237.73	-48.47	4.41	2.49	0.65	FSRQ
3FGL J0237.9+2848	149.48	-28.52	4.24	2.35	2.10	FSRQ
3FGL J2151.8−3025	17.13	-50.76	3.32	2.97	1.05	fsrq
3FGL J0841.4+7053	143.54	34.43	3.39	2.84	1.14	FSRQ
3FGL J0730.2−1141	227.76	3.14	6.08	2.28	6.64	fsrq
3FGL J2202.7+4217	92.60	-10.44	5.32	2.25	5.17	BLL
3FGL J1427.9−4206	321.45	17.26	4.69	2.21	5.27	FSRQ
3FGL J2147.3−7536	315.79	-36.53	3.51	2.47	2.14	FSRQ
3FGL J0108.7+0134	131.87	-60.99	2.75	2.39	0.60	fsrq
3FGL J1246.7−2547	301.61	37.07	3.18	2.28	2.25	fsrq
3FGL J1159.5+2914	199.45	78.37	2.20	2.21	0.20	fsrq
3FGL J2025.6−0736	36.90	-24.39	2.46	2.33	3.08	fsrq
3FGL J0920.9+4442	175.69	44.81	2.04	2.29	0.69	fsrq
3FGL J0442.6−0017	197.20	-28.46	2.63	2.50	1.58	fsrq
3FGL J2345.2−1554	65.70	-70.99	1.92	2.09	0.37	FSRQ
3FGL J0909.1+0121	228.95	30.93	2.16	2.41	1.19	fsrq
3FGL J0725.2+1425	203.64	13.92	2.09	2.23	1.95	FSRQ
3FGL J1700.1+6829	99.54	35.20	1.69	2.40	1.31	fsrq
3FGL J0145.1−2732	217.96	-78.07	1.22	2.57	0.20	fsrq
3FGL J1208.7+5442	135.82	61.34	1.30	2.54	0.47	fsrq

5.4.2 Data and Monte Carlo simulation

The analysis presented here covers ∼5 years of observations, from 2008-08-04 to 2013-05-10 (MET 239560179 to 389884599). The MC `merit` files are produced with the GLAST LAT Event Analysis Ma-

chine (*Gleam*, Boinee et al., 2003). The input for the simulation is a sky model defining the position and spectra of the sources. This model is then folded with the spacecraft motion and pointing history to derive the fluxes impinging on the LAT. The particle interactions with the detector are simulated using `Geant4` (Agostinelli et al., 2003) and a detailed physical description of the spacecraft. A dedicated simulation of the detector electronics and responses converts the physical processes into electronic signals. The synthetic data is then processed through the entire LAT data acquisition and analysis pipeline, from the trigger primitives to the highest event classes.

For this simulation, we have used a real pointing history file spanning the whole 5 years. The sky model of the sources we want to simulate is derived from the 3FGL. It includes the AGN in the stack as well as the nearby sources within $15°$ to any stack source if their flux is brighter than $> 5\%$ of the AGN flux, shown in Fig. 5.11 as blue crosses. Dim nearby sources not included in the simulation are not expected to introduce significant residuals in the azimuthal distribution. The Galactic and isotropic diffuse emission is also simulated using the diffuse templates for the P8V3_SOURCE event class.

We note that our preliminary MC model is not complete. In particular, the charged-particle background from CRs impinging on the LAT is not simulated. The residual CR contamination of the `SOURCE` event class is accounted for in the isotropic diffuse template, which includes the contribution from misclassified CR events. The emission from the Earth's limb is also not included in the simulation. We account for this by applying a hard cut on the zenith arrival direction, discarding events with zenith angle $> 80°$. The first energy bin for which the galactic and isotropic templates are computed is centered at ≈ 60 MeV. As a consequence, the simulation cannot account for the energy dispersion in the lower part of this energy range. As seen in Section 2.2.3, the energy resolution for the `SOURCE` event class is of the order of $\Delta E \sim 23\%$ around 60 MeV (see Fig. 2.7b). For the rest of the analysis we will consider events with energies greater than 90 MeV, roughly $2\Delta E$ higher than the energy of the first bin of the simulated diffuse gamma-ray emission components.

Figure 5.12 presents the comparison of the energy distribution of the data and simulated events classified as silicon-converted and within $3°$ of the stacked source. As is visible in Fig. 5.12, the simulation under-predicts the number of counts at the higher energies. Within $3°$ of the stack sources, the total residuals are of the order of 8.3% over the considered [90, 200] MeV energy range. As the model of the simulated sky is not complete, a deficit of MC counts is to be expected. Possible causes of this discrepancy are the non-simulated Earth limb emission and CR background, and the contribution from the point sources not included in the simulation. Only a few sources in the stack are located at low galactic latitudes, see Fig. 5.11. A difference between the normalization of the galactic diffuse emission in the vicinity of these sources and the all-sky nominal value used in the MC simulation could also be responsible for part of the discrepancy. The variability of the sources is not considered in the simulation. As is visible in Fig. 5.13, which shows the time series of the Data-MC counts, significant variability is present in the data.

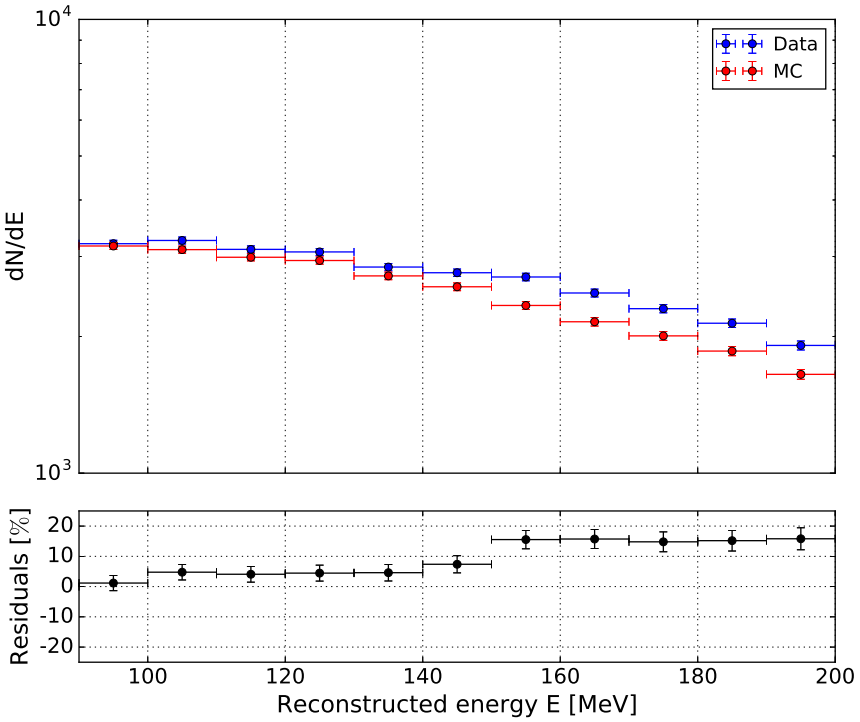

Figure 5.12: Distribution of reconstructed energy for data (blue crosses) and simulated (red crosses) events reconstructed as converting in the silicon layers. The bottom panel shows the relative residuals, (Data-MC)/MC, in each energy bin.

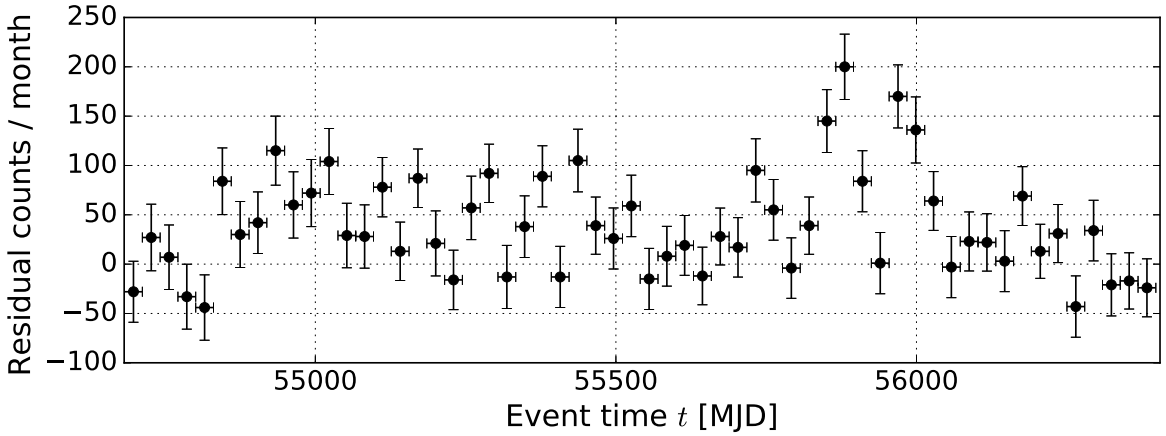

Figure 5.13: Time series of the difference between data and MC counts from the AGN stack. Real events have on average a higher rate than what predicted from the simulation. The abrupt increase in the residuals around MJD 55900 is probably due to a flare of one of the sources in the stack. The data shown here are classified as converted in silicon, have energies between 90 and 200 MeV and are collected within 3° of the AGN of the stack.

Figure 5.14 shows the distribution of the classifier output variable c as evaluated on data and simulated events. Some inconsistencies between the two distributions are visible, especially in the region $c \lesssim 0.1$. Besides the possible causes of a disagreement between data and MC discussed in the above paragraphs, we remind that the training of the classifier considered a wider energy range (30−250 MeV) than the one of the analysis. In the signal region, for $c > 0.675$, the two distributions agrees reasonably well. The contribution to the distributions from signal and background events (selected using the MC truth) are also shown for comparison. As is visible, the fraction of background events decreases smoothly for $c \gtrsim 0$. At around $c \gtrsim 0.6$, a shoulder is visible in the distribution of c for both the data and MC sample. This rise is due to the increased fraction of silicon-converted events that are rightly classified. This is an important check of the of the effectiveness of the event selection and of the accuracy of the simulations.

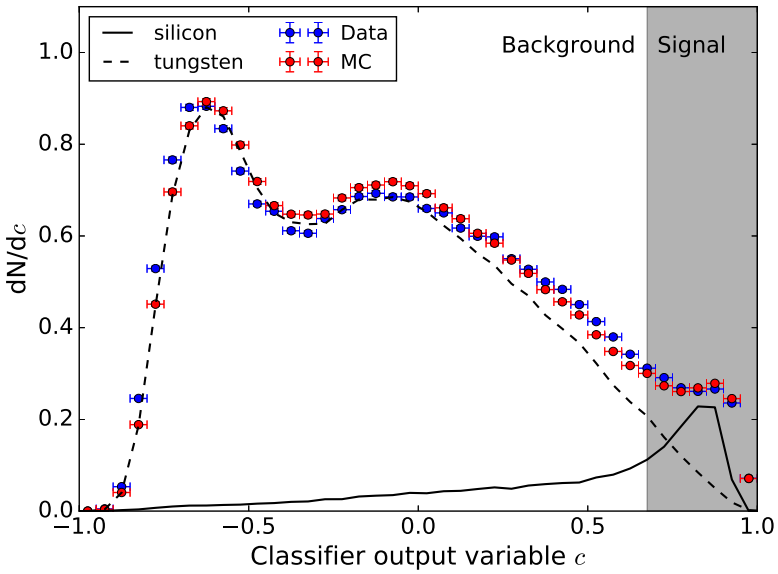

Figure 5.14: Distributions of the classifier output variable for data (blue crosses) and simulated events (red crosses) in the 90−200 MeV range and with zenith angles smaller than 80°. Both curves are normalized. The shaded area on the left of the plot highlights the signal region ($c > 0.675$). The solid and dashed lines show the contributions to the MC distribution from 'true' signal and 'true' background events, respectively.

Finally, in Fig. 5.15, we present the spatial distribution of the data and MC events. The different sky-regions around the AGN of the stack have been rotated to a common reference direction in order to produce an image of the stack emission. As is visible in the bottom panel, showing the significance of the residuals, some $\gtrsim 5\sigma$ spots are presents towards the border of the analysis region, possibly associated with non-simulated point sources. Beside these features, the uniformity of the residuals across the analysis region can be considered satisfactory. Different sizes of the analysis region have been

tested, from radii of 3° up to 10°. The absolute magnitude of the residuals increases approximately with the square of the radius of the analysis region as expected in the case of both a population of faint sources not included in the simulation and a mismatch in the level of diffuse gamma-ray emission.

5.5 Azimuthal distributions

The tracking and vertexing algorithms implemented in the Pass 8 event reconstruction have been developed with the aim of reconstructing the direction of the incoming gamma rays. For polarization measurements, the quantities of interest are the directions of the $e^{\pm}$ tracks. The LAT event reconstruction algorithms have been optimized for higher energies than the ones which are of interest for polarization. As a consequence, for many low-energy events the two-track solution is not accurate. To account for this, we only rely on the longest and straightest of the found tracks (best track) for the reconstruction of the azimuthal angle ψ. The second direction we need to determine ψ is given by the sky position of the source. We therefore make the assumption that all events in the region of interest come from the point source at its center, an assumption that is justified only for sources with a high signal-to-background ratio. A disadvantage of this method is that it requires to consider rather large portions of the sky around the sources, with the consequent dilution of the signal. The best events for polarization are in fact the ones with large opening angles. In the absence of an effective vertexing algorithm the reconstructed directions of these events are likely to have large offsets from the source position.

Our one-track reconstruction of the azimuthal angle is sketched in Fig. 5.16. We define $\hat{s}$ and $\hat{t}$ as the unit vectors identifying the true source position and the best track direction in the celestial sphere. We take Ω to be the plane tangent to the sphere and perpendicular to $\hat{s}$, and $\hat{n'}$ to be the unit vector pointing to the local north, applied on $\hat{s}$ and projected on Ω. We define ψ as the angle between $\hat{n'}$ and $\hat{t'}$, the projection of $\hat{t}$ on the tangent plane:

$$\psi = \arccos\left(\frac{\hat{t'}\cdot\hat{n'}}{|\hat{t'}||\hat{n'}|}\right) \tag{5.13}$$

With this method, we compute the azimuthal angle ψ for data and MC events. The resulting distributions are shown in the top panel of Fig. 5.17. We use 8 coarse bins in ψ, each 45° wide, to reduce the statistical uncertainty on each point as well as to average out the spatial distribution of the residuals (Fig. 5.15, bottom panel). The azimuthal distribution of the residuals (Data-MC)/MC is shown in the bottom panel of Fig. 5.17. The agreement with a constant term is satisfactory (p-value of 42%). Fitting this distribution with the expected shape for the polarization signal (Eq. 5.3) yields a modulation amplitude of $\sim 2\%$ and has a p-value of 44%.

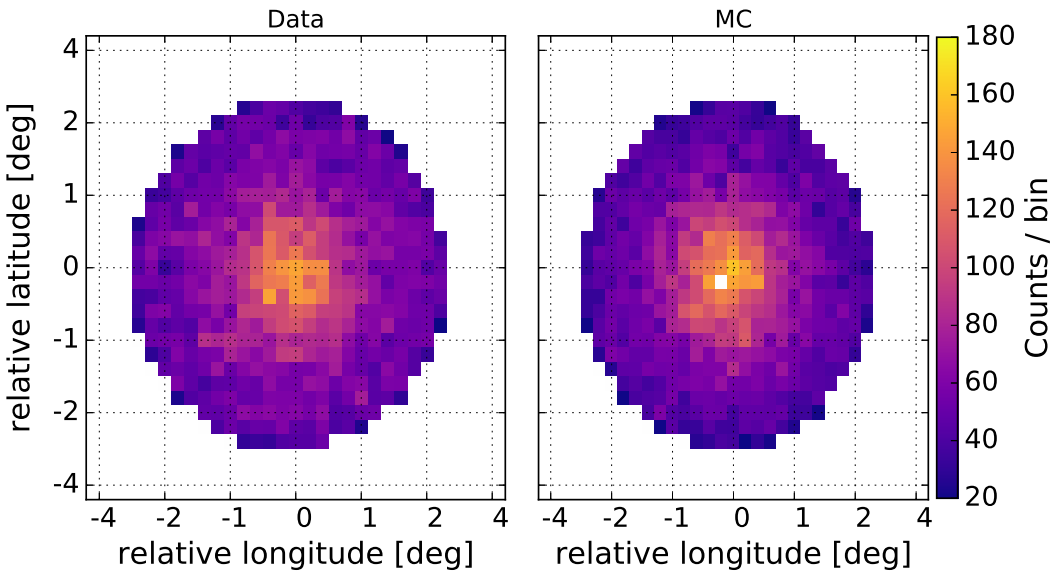

(a) Counts.

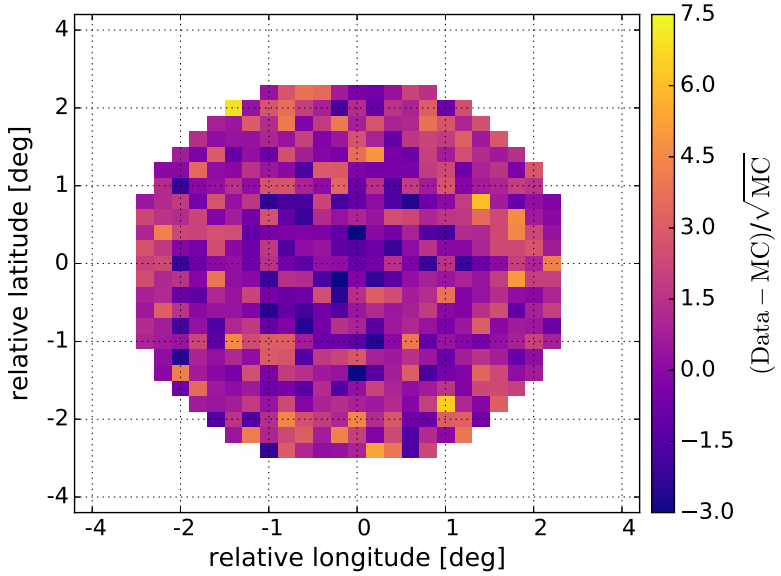

(b) Significance of the residuals.

Figure 5.15: Spatial distribution of the data and MC counts classified as silicon-converted (top panel). To produce this plot, the analysis region centered on each AGN of the stack has been rotated to a reference position. The bins of these histograms are $0.25° \times 0.25°$ in size. The bottom panel shows the significance of the residuals, defined as (Data-MC)/$\sqrt{\mathrm{MC}}$.

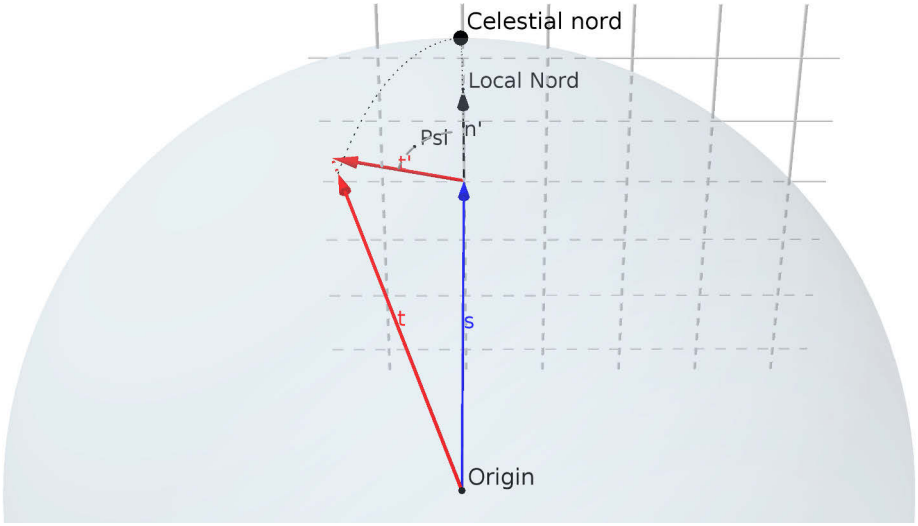

Figure 5.16: Simple reconstruction of the azimuthal angle ψ (dashed arc). The red and blue arrows indicates the reconstructed arrival direction of the event and the source position, $\hat{t}$ and $\hat{s}$ respectively. The black arrow points to the local north. The primed vectors are projected on the plane tangent to the celestial sphere and perpendicular to $\hat{s}$ (shaded area with a grid of dashed lines).

The residual azimuthal distribution is used to estimate the global sensitivity of this analysis, accounting for both statistical and systematic uncertainties. We fit the distribution with polarization signals of the form of Eq. 5.3, gradually increasing the amplitude of the modulation until we find the minimum signal amplitude $A_{5\sigma}$ that is not compatible with the residual azimuthal distribution at the 5σ level. Using $A_{100} = 0.2$, the resulting $A_{5\sigma} = 9.2\%$ corresponds to a polarization degree of $A_{5\sigma}/A_{100} \sim 46\%$. The purely statistical MDP estimate for the stack, computed for the 90−200 MeV range, using 3°-radius regions around the AGN, and including the contributions from the nearby sources, is $\sim 47\%$. The agreement between the sensitivity estimated with this analysis and the one resulting from a purely statistical calculation suggests that the systematic errors are sub-dominant with respect to the statistical uncertainties.

We tested different sizes of the analysis region, up to 10°. The values of A_{sens} for the larger analysis regions are always smaller than or comparable with the one measured using a 3° analysis radius around the sources of the stack.

5.6 Conclusions and outlook

In the pair production regime, linear polarization of the photon induces a sinusoidal modulation in the azimuthal distribution of the events. The period of this modulation is 180°. Around 100 MeV, the amplitude of this modulation is of the order of 20% for a 100% polarized flux. Accurately reconstructing

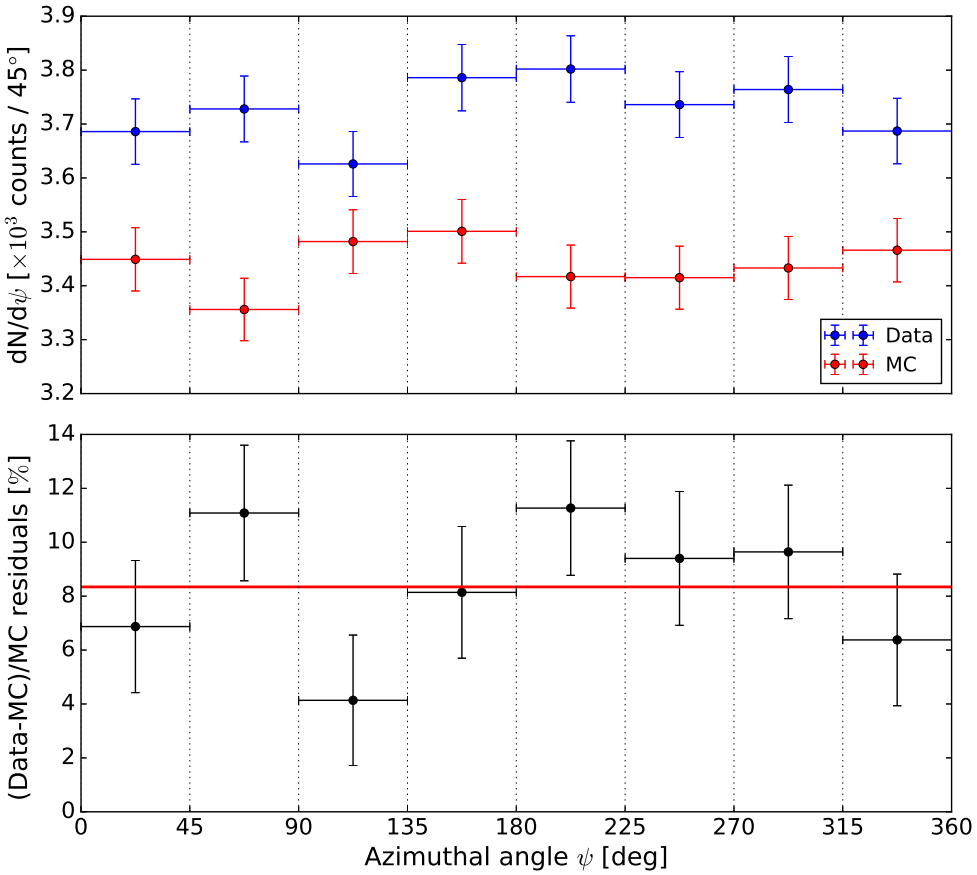

Figure 5.17: Top panel: azimuthal distributions for data (blue) and MC (red) events with energies in the 90−200 MeV range and reconstructed as converting in the SSD of the tracker. Bottom panel: residual azimuthal distribution, computed as (Data-MC)/MC. The red line is a constant term at 8.3%, the overall level of the residuals.

this distribution is the key to measuring the degree of linear polarization and the polarization angle of the sources. In this chapter, we have studied the possibility of performing such a measurement with the *Fermi* LAT, discussing the many challenges presented by this measurement and evaluating the purely statistical sensitivity for the most promising sources. Finally, we have presented a preliminary event selection and reconstruction and used it to estimate the overall sensitivity of the measurement and the level of systematic uncertainty.

Although the LAT has not been designed as a polarimeter, a basic calculation shows that low energy (< 200 MeV) events that convert in the silicon detectors of the LAT tracker could carry enough information to allow the reconstruction of the azimuthal angle ψ. A simple selection of silicon-converted events based on boosted decision trees have an efficiency of 50%, with 64% purity and an acceptance of only $\sim 7\%$ of the events. The statistical uncertainties are large and play a major role in limiting the sensitivity. With this basic event selection, the purely statistical minimum detectable polarization for the brightest sources such as the Vela pulsar, the Crab pulsar and PWN, and the blazar 3C 454.3 is estimated to be around $\approx 30 - 50\%$ after 10 years of observations. To estimate the level of the systematic uncertainties we build a stack of AGN to be used as an unpolarized test source. Comparing the stack emission over 5 years with a detailed simulation we measure a 5σ sensitivity corresponding to a polarization degree of $\approx 46\%$. This is in agreement with the purely statistical estimate for the stack, suggesting that systematic uncertainties are small as compared to the statistical ones.

The analysis presented here could still be improved in many regards. I conclude this chapter (and this thesis) with a list of suggested improvements, hoping to clarify the limits of this analysis and to provide a proposal of possible future development. The two main areas of possible improvement are:

- Using the lowest-level LAT data products (`RECON` files), instead of the `merit` files to select silicon-converted events. The variables included in the `merit` files have been optimized for the standard LAT analysis, more focused on the >100 MeV energy range. The `RECON` files contain the position of the individual hits in the LAT tracker. Access to this information will greatly improve the selection of silicon-converted events. For example, events converting in the bottom-most silicon detector of a tray could be easily identified by requiring no signal from the detector plane immediately above it (the single strips have an efficiency of $> 99\%$).

- Developing a dedicated vertexing algorithm, optimized for low energy events and focusing on the first few layers traversed by the tracks. If successful, this would allow the reconstruction of the azimuthal angle with greater accuracy, eliminating the limitations of the one-track analysis. To improve on the algorithms already implemented by the LAT team is not an easy task. There are however two reasons to hope that this could be accomplished: a) the LAT analysis is optimized for a different energy range, and b) new machine learning algorithms, such as deep convolutional neural networks, are remarkably good when it comes to pattern recognition and

completion.

More specific remarks and comments on my analysis are listed in the following, in order of importance:

- To validate the analysis, as well as to refine and optimize the event selection and reconstruction, a dedicated *Gleam* simulation which includes the polarized pair production cross section is needed. An effort in this direction is ongoing in the *Fermi*-LAT collaboration.
- The sky model used in the MC simulation of the stack could be refined, including all the sources (maybe based on the upcoming *Fermi*-LAT fourth source catalog) and fitting every sky region to optimize the data-MC agreement.
- A much larger MC production is needed in order to decrease the statistical uncertainties on the simulated data, allowing a more precise estimate of the sensitivity.
- The analysis could be optimize separately for the FRONT and BACK tracker sections. The two parts of the tracker are indeed very different when it comes to selecting the silicon events. Silicon selection cuts for events in the FRONT section can be less stringent than the ones used for BACK converting events. On an even finer level, one could also develop a multiclass event selection, treating separately the upper and lower silicon layers and the electronic chips (also made of silicon). As shown in Fig. 5.6, the fraction of events converting in the electronic chips is not marginal.

Apart from being instrumental to an actual polarization measure, a successful silicon-event selection and a dedicated vertexing algorithm for low energy events will improve the angular resolution of the LAT below 100 MeV, since the first hits of a track are the ones that carry most of the directional information. As seen in Section 2.2.3 the sensitivity of the LAT is limited in the lowest end of the energy range by the large PSF radius. Improving the angular resolution through the selection of silicon-converted events would also improve the sensitivity of the LAT at low energies.

List of Figures

1.1 Spectrum of Cosmic rays above 100 TeV. 2
1.2 Geometry of the second-order Fermi acceleration mechanism. 4
1.3 Schematic representation of the particle momenta distribution on both sides of a shock. 5
1.4 Geometry of the Sweet-Parker model of magnetic reconnection 6
1.5 Orientation of the magnetic field and density of particles in the vicinity of the reconnection layer as resulting from 2D simulations. 7
1.6 Energy spectra of particles accelerated via magnetic reconnection. 8
1.7 Intensity and degree of liner polarization of the synchrotron emission of a single electron. 11
1.8 Compton scattering cross section as a function of the photon energy. 13
1.9 Emission spectrum from inverse Compton scattering of a monochromatic and isotropic photon field from monoenergetic electrons. 13
1.10 Linear polarization of Compton scattering as a function of the scattering angle for different energies of the incoming photon. 14
1.11 Spectral energy distributions for synchrotron, inverse Compton, bremsstrahlung, and π^0 decay. 17

2.1 Point source differential sensitivity for different X- and gamma-ray observatories. . . . 20
2.2 Mass absorption coefficient for photons in Silicon as a function of the photon energy. . 21
2.3 Schematic of multiple Coulomb scattering. 23
2.4 Cutaway view of the *Fermi*-LAT. 24
2.5 Event rates at the different stages of the *Fermi*-LAT acquisition and analysis chain. . . . 27
2.6 Progress of the latency of the LAT data through the mission. 28
2.7 LAT IRFs version P8R2_V6 for the SOURCE event class as a function of event energy. . . 29

3.1 All-sky intensity map obtained from 8 years of Fermi Pass 8 data above 1 GeV. 31
3.2 Composition of the 3FGL in terms of source classes. 33

3.3 Composite image of the Crab pulsar and its nebula in the X-ray, optical and infrared bands. . . . 34
3.4 The Tycho supernovae remnant as imaged by the Chandra X-ray telescope. . . . 35
3.5 Geometry of different types of gamma-ray emitting binary systems. . . . 36
3.6 Composite radio, optical, and X-ray image of the nearby AGN Centaurus A. . . . 38
3.7 Schematic model of an active galactic nuclei. . . . 39
3.8 The starburst galaxy Messier 82 seen with the Hubble Space Telescope. . . . 40
3.9 Examples of gamma-ray light curves and their periodograms. . . . 45

4.1 Sky maps produced by the photometric step of FAVA. . . . 51
4.2 TS maps produced by the FAVA likelihood follow-up analysis. . . . 52
4.3 Distribution of the runtime for the jobs of the FAVA likelihood analysis. . . . 54
4.4 Examples of the ray-casting algorithm used to analyze the TS-map contours. . . . 54
4.5 Flow chart of the likelihood analysis follow-up of FAVA. . . . 56
4.6 Distribution r_{95} error radius of the flares in the 2FAV catalog. . . . 57
4.7 Comparison of the significance of the flare as measured by the photometric technique and by the likelihood analysis. . . . 59
4.8 All-sky map of the maximum photometric significance of the flux variations measured in the time-span of the 2FAV. . . . 60
4.9 Sky position of all the flare candidates and of the catalog flares. . . . 62
4.10 All-sky sensitivity maps for the photometric analysis of the 2FAV. . . . 64
4.11 Sensitivity of the photometric analysis as a function of the flare photon index. . . . 65
4.12 Positions of the catalog flares and sources on the sky. . . . 68
4.13 Sky position of the 2FAV sources, marked according to the class of the found counterpart. 73
4.14 Comparison of the energy fluence of the LAT-detected GRBs and of those included in the 2FAV. . . . 75
4.15 Distribution of the energy flux for the 3FGL source and the 2FAV sources with 3FGL counterpart. . . . 76
4.16 Distribution of the variability index for the entire 3FGL sample and for the unassociated 3FGL sources. . . . 77
4.17 TS maps from the low-energy analysis of the two flares assigned to 2FAV J1824−13.0. . 78
4.18 Comparison between the source-source distance of the unassociated 2FAV sources and of randomly distributed points. . . . 80
4.19 Comparison of the photometric significances and angular resolution measured in the 1FAV and in the 2FAV. . . . 82

4.20 Scatter plot of the spectral parameters (flux and photon index Γ) of the 2FAV flares associated with blazars. 84
4.21 Spectral parameters of the low-energy flares for all the non-blazar sources in the 2FAV. 87
4.22 Spectral parameters of the high-energy flares for all the non-blazar sources in the 2FAV. 88

5.1 Geometry of a pair production interaction. 94
5.2 Pair production cross section for a 100 MeV gamma ray as a function of the azimuthal and coplanarity angles. 95
5.3 Shape of the azimuthal distribution of the events for different energies of the incoming gamma ray. 96
5.4 Distribution of the pair opening angle $\theta_{\rm op}$ as a function of the photon energy. 97
5.5 Angles at play in the reconstruction of the tracks of the $e^{\pm}$ pair in the LAT tracker. . . . 98
5.6 'Tomographic' view of layer 7 of the LAT tracker. 99
5.7 Distributions of three of the most useful `merit` variables used in the selection of silicon-converted. 100
5.8 Performance of the classifier used to select silicon-converted events: efficiency, purity, and fraction of retained events. 103
5.9 Distribution of the event-source distance d as computed from a MC simulation of a point source. 104
5.10 Minimum detectable polarization at different significance levels for the Crab and Vela pulsar, the Crab PWN, and 3C 454.3 106
5.11 Positions on the sky of the AGN constituting the stack and their nearby sources. 108
5.12 Distribution of reconstructed energy for data and simulated events from the AGN stack. 111
5.13 Time series of the difference between data and MC counts for the AGN stack. 111
5.14 Distribution of the classifier output variable for data and simulated events from the AGN stack. 112
5.15 Spatial distribution of the data and MC counts. 114
5.16 Sketch of the geometry used in the one-track reconstruction of the azimuthal angle. . . 115
5.17 Azimuthal distributions of data and simulated events and residual azimuthal distribution. 116

List of Tables

2.1 The different observation strategies performed by the LAT and their relative frequency. 30

3.1 Summary of the various source catalogs produced with the LAT data. 32

4.1 Parameters of the FAVA likelihood follow-up analysis. 55
4.2 Number of catalog flares in the different cut classes. 63
4.3 Definitions and population counts of the three groups of flares used in the clustering. . 66
4.4 Catalogs used to search for possible associations of 2FAV sources. 69
4.5 2FAV sources with a counterpart from the 2FGL and the eventual 3FGL counterpart. . . 71
4.6 2FAV source table. 72
4.7 Composition of the 2FAV in terms of source classes. 74
4.8 List of 2FAV sources with non-blazar counterparts. 75
4.9 Significance of the harder-when-brighter behavior for flares associated to LSP, ISP, and HSP objects. 85

5.1 `Merit` variables used to select silicon-converted events. 101
5.2 3FGL sources included in the AGN stack. 109

Bibliography

Aab, A., Abreu, P., Aglietta, M., et al. (2015). Searches for Anisotropies in the Arrival Directions of the Highest Energy Cosmic Rays Detected by the Pierre Auger Observatory. ApJ, 804:15, arXiv:1411.6111.

Aartsen, M. G., Ackermann, M., Adams, J., et al. (2014). Observation of High-Energy Astrophysical Neutrinos in Three Years of IceCube Data. *Physical Review Letters*, 113(10):101101, arXiv:1405.5303.

Abbott, B. P., Abbott, R., Abbott, T. D., et al. (2016). Observation of Gravitational Waves from a Binary Black Hole Merger. *Physical Review Letters*, 116(6):061102, arXiv:1602.03837.

Abbott, B. P., Abbott, R., Adhikari, R., et al. (2009). LIGO: the Laser Interferometer Gravitational-Wave Observatory. *Reports on Progress in Physics*, 72(7):076901, arXiv:0711.3041.

Abdo, A. A., Ackermann, M., Agudo, I., et al. (2010a). Fermi Large Area Telescope and Multi-wavelength Observations of the Flaring Activity of PKS 1510-089 between 2008 September and 2009 June. ApJ, 721:1425–1447, arXiv:1007.1237.

Abdo, A. A., Ackermann, M., Agudo, I., et al. (2010b). The Spectral Energy Distribution of Fermi Bright Blazars. ApJ, 716:30–70, arXiv:0912.2040.

Abdo, A. A., Ackermann, M., Ajello, M., et al. (2010). Fermi Large Area Telescope First Source Catalog. *ApJS*, 188(2):405–436.

Abdo, A. A., Ackermann, M., Ajello, M., et al. (2010). The Vela Pulsar: Results from the First Year of Fermi LAT Observations. ApJ, 713:154–165, arXiv:1002.4050.

Abdo, A. A., Ackermann, M., Ajello, M., et al. (2011). Gamma-Ray Flares from the Crab Nebula. *Science*, 331(6018):739–742.

Abdo, A. A., Ackermann, M., Ajello, M., et al. (2010). Fermi large area telescope observation of a gamma-ray source at the position of eta carinae. *The Astrophysical Journal*, 723(1):649.

Abdo, A. A., Ackermann, M., Ajello, M., et al. (2011a). Discovery of High-energy Gamma-ray Emission from the Binary System PSR B1259-63/LS 2883 around Periastron with Fermi. ApJ, 736:L11, arXiv:1103.4108.

Abdo, A. A., Ackermann, M., Ajello, M., et al. (2009). Detection of 16 gamma-ray pulsars through blind frequency searches using the fermi lat. *Science*, 325(5942):840–844.

Abdo, A. A., Ackermann, M., Ajello, M., et al. (2010a). Gamma-ray Light Curves and Variability of Bright Fermi-detected Blazars. ApJ, 722:520–542, arXiv:1004.0348.

Abdo, A. A., Ackermann, M., Ajello, M., et al. (2009a). Fermi Discovery of Gamma-ray Emission from NGC 1275. ApJ, 699:31–39, arXiv:0904.1904.

Abdo, A. A., Ackermann, M., Ajello, M., et al. (2009b). Fermi LAT Observations of LS I +61deg303: First Detection of an Orbital Modulation in GeV Gamma Rays. ApJ, 701:L123–L128, arXiv:0907.4307.

Abdo, A. A., Ackermann, M., Ajello, M., et al. (2009c). Fermi/LAT observations of LS 5039. ApJ, 706:L56–L61, arXiv:0910.5520.

Abdo, A. A., Ackermann, M., Ajello, M., et al. (2010b). Spectral Properties of Bright Fermi-Detected Blazars in the Gamma-Ray Band. ApJ, 710:1271–1285, arXiv:1001.4097.

Abdo, A. A., Ackermann, M., Ajello, M., et al. (2010c). Detection of Gamma-Ray Emission from the Starburst Galaxies M82 and NGC 253 with the Large Area Telescope on Fermi. ApJ, 709:L152–L157, arXiv:0911.5327.

Abdo, A. A., Ackermann, M., Ajello, M., et al. (2010d). Gamma-Ray Emission Concurrent with the Nova in the Symbiotic Binary V407 Cygni. *Science*, 329:817–821, arXiv:1008.3912.

Abdo, A. A., Ackermann, M., Ajello, M., et al. (2009d). Modulated High-Energy Gamma-Ray Emission from the Microquasar Cygnus X-3. *Science*, 326:1512.

Abdo, A. A., Ackermann, M., Ajello, M., et al. (2011b). Fermi Large Area Telescope Observations of Two Gamma-Ray Emission Components from the Quiescent Sun. ApJ, 734:116, arXiv:1104.2093.

Abdo, A. A., Ajello, M., Allafort, A., et al. (2013). The Second Fermi Large Area Telescope Catalog of Gamma-Ray Pulsars. ApJS, 208:17, arXiv:1305.4385.

Abdo, A. A., Parent, D., Grove, J. E., et al. (2010e). Fermi LAT Detection of GeV Gamma-Ray Emission from the Binary System PSRB1259-63. *The Astronomer's Telegram*, 3085.

Abdollahi, S., Ackermann, M., Ajello, M., et al. (2016). The second catalog of flaring gamma-ray sources from the Fermi All-sky Variability Analysis. *ArXiv e-prints*, arXiv:1612.03165.

Abeysekara, A. U., Albert, A., Alfaro, R., et al. (2017). Observation of the Crab Nebula with the HAWC Gamma-Ray Observatory. *ArXiv e-prints*, arXiv:1701.01778.

Abramowski, A., Acero, F., Aharonian, F., et al. (2010). VHE γ-ray emission of PKS 2155-304: spectral and temporal variability. A&A, 520:A83, arXiv:1005.3702.

Acciari, V. A., Aliu, E., Arlen, T., et al. (2009). A connection between star formation activity and cosmic rays in the starburst galaxy M82. Nature, 462:770–772, arXiv:0911.0873.

Acero, F., Ackermann, M., Ajello, M., et al. (2015). Fermi Large Area Telescope Third Source Catalog. *ApJS*, 218(2):23.

Acero, F., Ackermann, M., Ajello, M., et al. (2016). The First Fermi LAT Supernova Remnant Catalog. ApJS, 224:8, arXiv:1511.06778.

Acero, F., Aharonian, F., Akhperjanian, A. G., et al. (2009). Detection of Gamma Rays from a Starburst Galaxy. *Science*, 326:1080, arXiv:0909.4651.

Ackermann, M., Ajello, M., Albert, A., et al. (2013a). The Fermi All-sky Variability Analysis: A List of Flaring Gamma-Ray Sources and the Search for Transients in Our Galaxy. ApJ, 771:57, arXiv:1304.6082.

Ackermann, M., Ajello, M., Albert, A., et al. (2012a). The Fermi Large Area Telescope on Orbit: Event Classification, Instrument Response Functions, and Calibration. ApJS, 203:4, arXiv:1206.1896.

Ackermann, M., Ajello, M., Albert, A., et al. (2016a). Fermi-LAT Observations of the LIGO Event GW150914. ApJ, 823:L2, arXiv:1602.04488.

Ackermann, M., Ajello, M., Albert, A., et al. (2015a). Multiwavelength Evidence for Quasi-periodic Modulation in the Gamma-Ray Blazar PG 1553+113. ApJ, 813:L41, arXiv:1509.02063.

Ackermann, M., Ajello, M., Albert, A., et al. (2016b). Measurement of the high-energy gamma-ray emission from the Moon with the Fermi Large Area Telescope. Phys. Rev. D, 93(8):082001, arXiv:1604.03349.

Ackermann, M., Ajello, M., Albert, A., et al. (2014a). Fermi establishes classical novae as a distinct class of gamma-ray sources. *Science*, 345:554–558, arXiv:1408.0735.

Ackermann, M., Ajello, M., Allafort, A., et al. (2011). THE SECOND CATALOG OF ACTIVE GALACTIC NUCLEI DETECTED BY THE FERMI LARGE AREA TELESCOPE. *ApJ*, 743(2):171.

Ackermann, M., Ajello, M., Allafort, A., et al. (2013b). Detection of the Characteristic Pion-Decay Signature in Supernova Remnants. *Science*, 339:807–811, arXiv:1302.3307.

Ackermann, M., Ajello, M., Allafort, A., et al. (2012b). GeV Observations of Star-forming Galaxies with the Fermi Large Area Telescope. ApJ, 755:164, arXiv:1206.1346.

Ackermann, M., Ajello, M., Allafort, A., et al. (2012c). The Imprint of the Extragalactic Background Light in the Gamma-Ray Spectra of Blazars. *Science*, 338:1190, arXiv:1211.1671.

Ackermann, M., Ajello, M., Asano, K., et al. (2013c). The First Fermi-LAT Gamma-Ray Burst Catalog. ApJS, 209:11, arXiv:1303.2908.

Ackermann, M., Ajello, M., Atwood, W. B., et al. (2015b). The Third Catalog of Active Galactic Nuclei Detected by the Fermi Large Area Telescope. ApJ, 810:14, arXiv:1501.06054.

Ackermann, M., Ajello, M., Atwood, W. B., et al. (2012d). Fermi-LAT Observations of the Diffuse γ-Ray Emission: Implications for Cosmic Rays and the Interstellar Medium. ApJ, 750:3, arXiv:1202.4039.

Ackermann, M., Ajello, M., Ballet, J., et al. (2012e). Periodic Emission from the Gamma-Ray Binary 1FGL J1018.6-5856. *Science*, 335:189, arXiv:1202.3164.

Ackermann, M., Albert, A., Atwood, W. B., et al. (2014b). The Spectrum and Morphology of the Fermi Bubbles. ApJ, 793:64, arXiv:1407.7905.

Actis, M., Agnetta, G., Aharonian, F., et al. (2011). Design concepts for the Cherenkov Telescope Array CTA: an advanced facility for ground-based high-energy gamma-ray astronomy. *Experimental Astronomy*, 32:193–316, arXiv:1008.3703.

Agostinelli, S., Allison, J., Amako, K., et al. (2003). G EANT4—a simulation toolkit. *Nuclear Instruments and Methods in Physics Research A*, 506:250–303.

Aharonian, F. (2000). TeV gamma rays from BL Lac objects due to synchrotron radiation of extremely high energy protons. *New Astronomy*, 5(7):377 – 395.

Aharonian, F., Akhperjanian, A., Beilicke, M., et al. (2002). Variations of the TeV energy spectrum at different flux levels of Mkn 421 observed with the HEGRA system of Cherenkov telescopes. A&A, 393:89–99, arXiv:astro-ph/0205499.

Aharonian, F., Akhperjanian, A. G., Anton, G., et al. (2009). Simultaneous multiwavelength observations of the second exceptional γ-ray flare of PKS 2155-304 in July 2006. A&A, 502:749–770, arXiv:0906.2002.

Aharonian, F., Akhperjanian, A. G., Aye, K.-M., et al. (2005a). Discovery of Very High Energy Gamma Rays Associated with an X-ray Binary. *Science*, 309:746–749, arXiv:astro-ph/0508298.

Aharonian, F., Akhperjanian, A. G., Aye, K.-M., et al. (2005b). Discovery of the binary pulsar PSR B1259-63 in very-high-energy gamma rays around periastron with HESS. A&A, 442:1–10, arXiv:astro-ph/0506280.

Aharonian, F., Akhperjanian, A. G., Bazer-Bachi, A. R., et al. (2006). Observations of the Crab nebula with HESS. A&A, 457:899–915, arXiv:astro-ph/0607333.

Aharonian, F., Bykov, A., Parizot, E., et al. (2012). Cosmic Rays in Galactic and Extragalactic Magnetic Fields. Space Sci. Rev., 166:97–132, arXiv:1105.0131.

Aharonian, F. A. (2004). *Very high energy cosmic gamma radiation : a crucial window on the extreme Universe*. World Scientific Publishing Co.

Ajello, M., Albert, A., Allafort, A., et al. (2014). IMPULSIVE AND LONG DURATION HIGH-ENERGY GAMMA-RAY EMISSION FROM THE VERY BRIGHT 2012 MARCH 7 SOLAR FLARES. *ApJ*, 789(1):20.

Ajello, M., Albert, A., Atwood, W. B., et al. (2016). Fermi-LAT Observations of High-Energy Gamma-Ray Emission toward the Galactic Center. ApJ, 819:44, arXiv:1511.02938.

Ajello, M., Atwood, W. B., Baldini, L., et al. (2017). 3FHL: The Third Catalog of Hard Fermi-LAT Sources. *ArXiv e-prints*, arXiv:1702.00664.

Ajello, M., Kocevski, D., Gasparrini, D., et al. (2014). Fermi LAT detection of gamma-ray flaring activity from the blazar MG J221916+1806 through the Fermi All-sky Variability Analysis (FAVA). *The Astronomer's Telegram*, 6020.

Albert, J., Aliu, E., Anderhub, H., et al. (2006). Variable Very-High-Energy Gamma-Ray Emission from the Microquasar LS I +61 303. *Science*, 312:1771–1773, arXiv:astro-ph/0605549.

Albert, J., Aliu, E., Anderhub, H., et al. (2007). Variable Very High Energy γ-Ray Emission from Markarian 501. ApJ, 669:862–883, arXiv:astro-ph/0702008.

Allafort, A., Baldini, L., Ballet, J., et al. (2013). PSR J2021+4026 in the Gamma Cygni Region: The First Variable γ-Ray Pulsar Seen by the Fermi LAT. ApJ, 777:L2.

Álvarez Crespo, N., Masetti, N., Ricci, F., et al. (2016). Optical Spectroscopic Observations of Gamma-ray Blazar Candidates. V. TNG, KPNO, and OAN Observations of Blazar Candidates of Uncertain Type in the Northern Hemisphere. AJ, 151:32, arXiv:1609.04829.

Anupama, G. C. (2013). Recurrent Novae: What Do We Know about Them? In Di Stefano, R., Orio, M., and Moe, M., editors, *Binary Paths to Type Ia Supernovae Explosions*, volume 281 of *IAU Symposium*, pages 154–161.

Atwood, W. et al. (2013). Pass 8: Toward the Full Realization of the Fermi-LAT Scientific Potential. *ArXiv e-prints*, arXiv:1303.3514.

Atwood, W. B., Abdo, A. A., et al. (2009). The Large Area Telescope on the Fermi Gamma-Ray Space Telescope Mission. ApJ, 697:1071–1102 , arXiv:0902.1089.

Atwood, W. B., Bagagli, R., Baldini, L., et al. (2007). Design and initial tests of the Tracker-converter of the Gamma-ray Large Area Space Telescope. *Astroparticle Physics*, 28:422–434.

Axelsson, M., Larsson, S., and Hjalmarsdotter, L. (2009). The aperiodic broad-band X-ray variability of Cygnus X-3. *Monthly Notices of the Royal Astronomical Society*, 394:1544–1550, arXiv:0902.4007.

Barthel, P. D. (1989). Is every quasar beamed? ApJ, 336:606–611.

Beckmann, V. and Shrader, C. (2012). The AGN phenomenon: open issues. In *Proceedings of An INTEGRAL view of the high-energy sky (the first 10 years)*, page 69. 9th INTEGRAL Workshop and celebration of the 10th anniversary of the launch (INTEGRAL 2012). 15-19 October 2012. Bibliotheque Nationale de France, Paris, France.

Bell, A. R. (1978). The acceleration of cosmic rays in shock fronts. I. MNRAS, 182:147–156.

Berlin, T. H. and Madansky, L. (1950). On the Detection of γ-Ray Polarization by Pair Production. *Physical Review*, 78:623–623.

Bernard, D. (2013). Polarimetry of cosmic gamma-ray sources above e^+e^- pair creation threshold. *Nuclear Instruments and Methods in Physics Research A*, 729:765–780 , arXiv:1307.3892.

Bethe, H. and Heitler, W. (1934). On the Stopping of Fast Particles and on the Creation of Positive Electrons. *Proceedings of the Royal Society of London A: Mathematical, Physical and Engineering Sciences*, 146(856):83–112.

Biteau, J. and Giebels, B. (2012). The minijets-in-a-jet statistical model and the rms-flux correlation. *Astronomy & Astrophysics*, 548:A123, arXiv:1210.2045.

Blandford, R. and Eichler, D. (1987). Particle acceleration at astrophysical shocks: A theory of cosmic ray origin. Phys. Rep., 154:1–75.

Błażejowski, M., Blaylock, G., Bond, I. H., et al. (2005). A Multiwavelength View of the TeV Blazar Markarian 421: Correlated Variability, Flaring, and Spectral Evolution. ApJ, 630:130–141, arXiv:astro-ph/0505325.

Blumenthal, G. R. and Gould, R. J. (1970). Bremsstrahlung, synchrotron radiation, and compton scattering of high-energy electrons traversing dilute gases. *Rev. Mod. Phys.*, 42:237–270.

Bodaghee, A., Tomsick, J. A., Pottschmidt, K., et al. (2013). Gamma-Ray Observations of the Microquasars Cygnus X-1, Cygnus X-3, GRS 1915+105, and GX 339-4 with the Fermi Large Area Telescope. ApJ, 775:98, arXiv:1307.3264.

Boinee, P. et al. (2003). GLEAM: The GLAST Large Area Telescope Simulation Framework. In *Proceedings, 1st Workshop on Science with the New Generation of High Energy Gamma-ray Experiments : Between Astrophysics and Astroparticle Physics. (SceNeGHE 2003): Perugia, Italy, May 21, 2003*, pages 141–151.

Böttcher, M., Reimer, A., Sweeney, K., et al. (2013). Leptonic and Hadronic Modeling of Fermi-detected Blazars. ApJ, 768:54, arXiv:1304.0605.

Bregeon, J. (2011). Design and performance of the silicon strip tracker of the Fermi Large Area Telescope. *Journal of Instrumentation*, 6(12):C12043.

Britto, R. J. G., Buson, S., Lott, B., et al. (2015). Fermi-LAT Observations of 2014 May-July outburst from 3C 454.3. *ArXiv e-prints*, arXiv:1511.02280.

Brown, A. M. and Adams, J. (2011). High-energy γ-ray properties of the Fanaroff-Riley type I radio galaxy NGC 1275. MNRAS, 413:2785–2790, arXiv:1101.2687.

Brun, R. and Rademakers, F. (1997). Root — an object oriented data analysis framework. *Nuclear Instruments and Methods in Physics Research Section A: Accelerators, Spectrometers, Detectors and Associated Equipment*, 389(1):81 – 86. New Computing Techniques in Physics Research V.

Buehler, R., Scargle, J. D., Blandford, R. D., et al. (2012). Gamma-Ray Activity in the Crab Nebula: The Exceptional Flare of 2011 April. ApJ, 749:26, arXiv:1112.1979.

Bühler, R. and Blandford, R. (2014). The surprising Crab pulsar and its nebula: a review. *Reports on Progress in Physics*, 77(6):066901, arXiv:1309.7046.

Burrows, A. (2000). Supernova explosions in the Universe. Nature, 403:727–733.

Caliandro, G. A., Cheung, C. C., Li, J., et al. (2015). Gamma-Ray Flare Activity from PSR B1259-63 during 2014 Periastron Passage and Comparison to Its 2010 Passage. ApJ, 811:68, arXiv:1509.02856.

Caliandro, G. A., Hill, A. B., Torres, D. F., et al. (2013). The missing GeV γ-ray binary: searching for HESS J0632+057 with Fermi-LAT. MNRAS, 436:740–749, arXiv:1308.5234.

Carlson, P. and de Angelis, A. (2010). Nationalism and internationalism in science: the case of the discovery of cosmic rays. *European Physical Journal H*, 35:309–329, arXiv:1012.5068.

Carlson, P., Francke, T., Fuglesang, C., et al. (1996). Long narrow CsI(T1) rods as calorimeter elements. *Nuclear Instruments and Methods in Physics Research A*, 376:271–274.

Cerutti, B. and Beloborodov, A. M. (2016). Electrodynamics of Pulsar Magnetospheres. Space Sci. Rev., arXiv:1611.04331.

Cerutti, B., Mortier, J., et al. (2016). Polarized synchrotron emission from the equatorial current sheet in gamma-ray pulsars. *ArXiv e-prints*, arXiv:1609.00021.

Cerutti, B., Uzdensky, D. A., and Begelman, M. C. (2012). Extreme Particle Acceleration in Magnetic Reconnection Layers: Application to the Gamma-Ray Flares in the Crab Nebula. ApJ, 746:148, arXiv:1110.0557.

Chakraborty, N., Pavlidou, V., and Fields, B. D. (2015). High Energy Polarization of Blazars: Detection Prospects. ApJ, 798:16, arXiv:1502.00453.

Chakravarti, I. M., Laha, R. G., and Roy, J. (1967). *Handbook of Methods of Applied Statistics*, volume I. John Wiley and Sons.

Chang, Z., Jiang, Y., and Lin, H.-N. (2014). Polarization of Photons Scattered by Electrons in Any Spectral Distribution. ApJ, 780:68, arXiv:1306.3733.

Cheung, C. C., Glanzman, T., and Hill, A. B. (2012a). Fermi LAT Detection of a New Galactic Bulge Gamma-ray Transient in the Scorpius Region: Fermi J1750-3243, and its Possible Association with Nova Sco 2012. *The Astronomer's Telegram*, 4284.

Cheung, C. C., Hays, E., Venters, T., et al. (2012b). Fermi LAT Detection of a New Gamma-ray Transient in the Galactic Plane: Fermi J0639+0548. *The Astronomer's Telegram*, 4224.

Cheung, C. C., Jean, P., and Shore, S. N. (2013). Fermi-LAT Gamma-ray Observations of Nova Centauri 2013. *The Astronomer's Telegram*, 5649.

Cheung, C. C., Jean, P., and Shore, S. N. (2014). Fermi-LAT Gamma-ray Observations of Recurrent Nova V745 Sco. *The Astronomer's Telegram*, 5879.

Cheung, C. C., Jean, P., and Shore, S. N. (2015). Further Fermi-LAT Gamma-ray Observations of Nova Sagittarii 2015 No. 2. *The Astronomer's Telegram*, 7315.

Cheung, C. C., Jean, P., Shore, S. N., et al. (2016). Fermi-LAT Gamma-Ray Detections of Classical Novae V1369 Centauri 2013 and V5668 Sagittarii 2015. ApJ, 826:142, arXiv:1605.04216.

Chiaberge, M. and Ghisellini, G. (1999). Rapid variability in the synchrotron self-Compton model for blazars. MNRAS, 306:551–560, arXiv:astro-ph/9810263.

Ciprini, S. and Fermi-LAT Collaboration (2012). Four years of Fermi LAT flare advocate activity. In Aharonian, F. A., Hofmann, W., and Rieger, F. M., editors, *American Institute of Physics Conference Series*, volume 1505, pages 697–700.

Clark, S. (1999). Polarized Starlight and the Handedness of Life. *American Scientist*, 87:336.

Compton, A. H. (1923). A Quantum Theory of the Scattering of X-rays by Light Elements. *Phys. Rev.*, 21:483–502.

Corbel, S., Dubus, G., Tomsick, J. A., et al. (2012). A giant radio flare from Cygnus X-3 with associated γ-ray emission. MNRAS, 421:2947–2955, arXiv:1201.3356.

Corbet, R. H. D., Chomiuk, L., Coe, M. J., et al. (2016). A Luminous Gamma-ray Binary in the Large Magellanic Cloud. ApJ, 829:105, arXiv:1608.06647.

Cortina, J. (2005). Status and First Results of the Magic Telescope. Ap&SS, 297:245–255, arXiv:astro-ph/0407475.

D'Ammando, F., Orienti, M., Finke, J., et al. (2012). SBS 0846+513: a new γ-ray-emitting narrow-line Seyfert 1 galaxy. MNRAS, 426:317–329, arXiv:1207.3092.

D'Ammando, F., Orienti, M., Finke, J., et al. (2015). The most powerful flaring activity from the NLSy1 PMN J0948+0022. MNRAS, 446:2456–2467, arXiv:1410.7144.

De Angelis, A., Tatischeff, V., Tavani, M., et al. (2016). The e-ASTROGAM mission (exploring the extreme Universe with gamma rays in the MeV-GeV range). *ArXiv e-prints*, arXiv:1611.02232.

Dean, A. J., Clark, D. J., et al. (2008). Polarized Gamma-Ray Emission from the Crab. *Science*, 321:1183 .

Del Monte, E., Feroci, M., Evangelista, Y., et al. (2010). A year-long AGILE observation of Cygnus X-1 in hard spectral state. A&A, 520:A67, arXiv:1004.0849.

D'Elia, V. and Cavaliere, A. (2001). The Connection between BL Lacs and Flat-Spectrum Radio Quasars. In Padovani, P. and Urry, C. M., editors, *Blazar Demographics and Physics*, volume 227 of *Astronomical Society of the Pacific Conference Series*, page 252.

Depaola, G. O., Kozameh, et al. (1999). A method to determine the polarization of high energy gamma rays. *Astroparticle Physics*, 10:175–183 , arXiv:astro-ph/9806302.

Dermer, C. D. and Giebels, B. (2016). Active galactic nuclei at gamma-ray energies. *Comptes Rendus Physique*, 17:594–616, arXiv:1602.06592.

Dobler, G., Finkbeiner, D. P., Cholis, I., et al. (2010). The Fermi Haze: A Gamma-ray Counterpart to the Microwave Haze. ApJ, 717:825–842, arXiv:0910.4583.

Drake, J. F., Swisdak, M., Che, H., et al. (2006). Electron acceleration from contracting magnetic islands during reconnection. *Nature*, 443(7111):553–556.

Dubus, G. (2013). Gamma-ray binaries and related systems. A&A Rev., 21:64, arXiv:1307.7083.

Dubus, G. (2015). Gamma-ray emission from binaries in context. *Comptes Rendus Physique*, 16:661–673, arXiv:1507.00935.

Engel, R., Heck, D., and Pierog, T. (2011). Extensive Air Showers and Hadronic Interactions at High Energy. *Annual Review of Nuclear and Particle Science*, 61(1):467–489.

Espinoza, C. M., Lyne, A. G., Stappers, B. W., et al. (2011). A study of 315 glitches in the rotation of 102 pulsars. MNRAS, 414:1679–1704, arXiv:1102.1743.

Fabjan, C. W. and Gianotti, F. (2003). Calorimetry for particle physics. *Rev. Mod. Phys.*, 75:1243–1286.

Fermi, E. (1949). On the origin of the cosmic radiation. *Phys. Rev.*, 75:1169–1174.

Fishman, G. J., Meegan, C. A., Parnell, T. A., et al. (1982). The burst and transient source experiment for the gamma-ray observatory. *AIP Conference Proceedings*, 77(1):443–451.

Ford, H. C., Bartko, F., Bely, P. Y., et al. (1998). Advanced camera for the Hubble Space Telescope. In Bely, P. Y. and Breckinridge, J. B., editors, *Space Telescopes and Instruments V*, volume 3356 of Proc. SPIE, pages 234–248.

Furth, H. P., Killeen, J., and Rosenbluth, M. N. (1963). Finite-resistivity instabilities of a sheet pinch. *The Physics of Fluids*, 6(4):459–484.

Gaensler, B. M. and Slane, P. O. (2006). The Evolution and Structure of Pulsar Wind Nebulae. *Annual Review of Astronomy and Astrophysics*, 44(1):17–47, arXiv:0601081.

Gagunashvili, N. D. (2006). Comparison of weighted and unweighted histograms. *ArXiv Physics e-prints*, arXiv:physics/0605123.

Gehrels, N., Chipman, E., and Kniffen, D. (1994). The Compton Gamma Ray Observatory. ApJS, 92:351–362.

Gehrels, N. and Mészáros, P. (2012). Gamma-Ray Bursts. *Science*, 337:932, arXiv:1208.6522.

Gehrels, N., Michelson, P., and GLAST Facility Science Team (1999). GLAST: the next-generation high energy gamma-ray astronomy mission. *Astroparticle Physics*, 11:277–282.

Ghisellini, G., Celotti, A., Fossati, G., et al. (1998). A theoretical unifying scheme for gamma-ray bright blazars. MNRAS, 301:451–468, arXiv:astro-ph/9807317.

Ginzburg, V. L. (1989). *Applications of electrodynamics in theoretical physics and astrophysics.* Gordon and Breach, New York, NY (USA).

Ginzburg, V. L. and Syrovatskii, S. I. (1964). *The Origin of Cosmic Rays*. Macmillan, New York (NY), USA.

Giomi, M., Bühler, R., Sgrò, C., et al. (2016). Estimate of the Fermi Large Area Telescope sensitivity to gamma-ray polarization. *ArXiv e-prints*, arXiv:1610.06729.

Giommi, P., Barr, P., Pollock, A. M. T., et al. (1990). A study of BL Lacertae-type objects with Exosat. I - Flux correlations, luminosity variability, and spectral variability. ApJ, 356:432–455.

Gold, T. (1968). Rotating Neutron Stars as the Origin of the Pulsating Radio Sources. Nature, 218:731–732.

Gomboc, A. (2012). Unveiling the secrets of gamma ray bursts. *Contemporary Physics*, 53:339–355, arXiv:1206.3127.

Götz, D., Covino, et al. (2013). The polarized gamma-ray burst GRB 061122. MNRAS, 431:3550–3556 , arXiv:1303.4186.

Götz, D., Laurent, P., et al. (2009). Variable Polarization Measured in the Prompt Emission of GRB 041219A Using IBIS on Board INTEGRAL. ApJ, 695:L208–L212 , arXiv:0903.1712.

Gould, R. J. and Schréder, G. (1966). Opacity of the Universe to High-Energy Photons. *Physical Review Letters*, 16:252–254.

Grandi, P., Torresi, E., and Stanghellini, C. (2012). The γ-Ray Emission Region in the Fanaroff-Riley II Radio Galaxy 3C 111. ApJ, 751:L3, arXiv:1204.2268.

Greisen, K. (1966). End to the Cosmic-Ray Spectrum? *Physical Review Letters*, 16:748–750.

Grenier, I. A. and Harding, A. K. (2015). Gamma-ray pulsars: A gold mine. *Comptes Rendus Physique*, 16:641–660, arXiv:1509.08823.

Gros, P. and Bernard, D. (2017). γ-Ray polarimetry with conversions to e^+e^- pairs: Polarization asymmetry and the way to measure it. *Astroparticle Physics*, 88:30–37, arXiv:1611.05179.

Hall, J. S. (1949). Observations of the Polarized Light from Stars. *Science*, 109:166–167.

Hartman, R. C., Bertsch, D. L., Bloom, S. D., et al. (1999). The Third EGRET Catalog of High-Energy Gamma-Ray Sources. ApJS, 123:79–202.

Hays, E., Cheung, T., and Ciprini, S. (2013). Detection of gamma rays from Nova Delphini 2013. *The Astronomer's Telegram*, 5302.

Helder, E. A., Vink, J., Bykov, A. M., et al. (2012). Observational Signatures of Particle Acceleration in Supernova Remnants. Space Sci. Rev., 173:369–431, arXiv:1206.1593.

Hess, V. F. (1912). Über Beobachtungen der durchdringenden Strahlung bei sieben Freiballonfahrten. *Z. Phys.*, 13:1084.

Hillas, A. M. (1984). The origin of ultra-high-energy cosmic rays. *Annual Review of Astronomy and Astrophysics*, 22(1):425–444.

Hiltner, W. A. (1949). Polarization of light from distant stars by interstellar medium. *Science*, 109(2825):165–165.

Hinton, J. A. and Hofmann, W. (2009). Teraelectronvolt Astronomy. ARA&A, 47:523–565, arXiv:1006.5210.

Hobbs, G., Lyne, A. G., and Kramer, M. (2010). An analysis of the timing irregularities for 366 pulsars. MNRAS, 402:1027–1048, arXiv:0912.4537.

Hoecker, A., Speckmayer, P., Stelzer, J., et al. (2007). TMVA - Toolkit for Multivariate Data Analysis. *ArXiv Physics e-prints*, arXiv:physics/0703039.

Holder, J., Acciari, V. A., Aliu, E., et al. (2008). Status of the VERITAS Observatory. In Aharonian, F. A., Hofmann, W., and Rieger, F., editors, *American Institute of Physics Conference Series*, volume 1085 of *American Institute of Physics Conference Series*, pages 657–660.

Ivezić, Ž., Connolly, A. J., VanderPlas, J. T., et al. (2014). *Statistics, Data Mining, and Machine Learning in Astronomy: A Practical Python Guide for the Analysis of Survey Data*. Princeton University Press.

Jackson, J. D. (1998). *Classical Electrodynamics, 3rd Edition*.

James, F. (1994). MINUIT Function Minimization and Error Analysis: Reference Manual Version 94.1.

Kagan, D., Sironi, L., Cerutti, B., et al. (2015). Relativistic Magnetic Reconnection in Pair Plasmas and Its Astrophysical Applications. Space Sci. Rev., 191:545–573, arXiv:1412.2451.

Kanbach, G., Bertsch, D. L., Favale, A., et al. (1989). The project egret (energetic gamma-ray experiment telescope) on nasa's gamma-ray observatory gro. *Space Science Reviews*, 49(1):69–84.

Kirk, J. G., Rieger, F. M., and Mastichiadis, A. (1998). Particle acceleration and synchrotron emission in blazar jets. A&A, 333:452–458, arXiv:astro-ph/9801265.

Klein, O. and Nishina, T. (1929). Über die Streuung von Strahlung durch freie Elektronen nach der neuen relativistischen Quantendynamik von Dirac. *Zeitschrift fur Physik*, 52:853–868.

Klis, M. (1989). Fourier Techniques in X-Ray Timing. In *Timing Neutron Stars*, pages 27–69. Springer Netherlands, Dordrecht.

Kniffen, D. A., Hartman, R. C., Thompson, D. J., et al. (1974). Gamma radiation from the Crab Nebula above 35 MeV. Nature, 251:397–399.

Kocevski, D., Ajello, M., and Buehler, R. (2015). Fermi LAT detection and Swift follow up observation of Fermi J0617-4026: a new transient gamma-ray source. *The Astronomer's Telegram*, 6912.

Kogut, A., Spergel, D. N., Barnes, C., et al. (2003). First-Year Wilkinson Microwave Anisotropy Probe (WMAP) Observations: Temperature-Polarization Correlation. ApJS, 148:161–173, arXiv:astro-ph/0302213.

Komarov, S. V., Khabibullin, I. I., Churazov, E. M., et al. (2016). Polarization of thermal bremsstrahlung emission due to electron pressure anisotropy. MNRAS, 461:2162–2173, arXiv:1604.08669.

Kouveliotou, C., Meegan, C. A., Fishman, G. J., et al. (1993). Identification of two classes of gamma-ray bursts. ApJ, 413:L101–L104.

Kovac, J. M., Leitch, E. M., Pryke, C., et al. (2002). Detection of polarization in the cosmic microwave background using DASI. Nature, 420:772–787, arXiv:astro-ph/0209478.

Kruskal, J. B. (1956). On the shortest spanning subtree of a graph and the traveling salesman problem. *Proceedings of the American Mathematical Society*, 7(1):48–50.

Kundu, E. and Gupta, N. (2014). Possible proton synchrotron origin of X-ray and gamma-ray emission in large-scale jet of 3C 273. MNRAS, 444:L16–L19, arXiv:1406.5978.

Larmor, J. (1897). A Dynamical Theory of the Electric and Luminiferous Medium. Part III. Relations with Material Media. *Philosophical Transactions of the Royal Society of London A: Mathematical, Physical and Engineering Sciences*, 190:205–493.

Larsson, S., Buson, S., Fuhrmann, L., et al. (2016). Multi-Timescale Variability in Gamma-ray Blazars. presented at the conference: Blazars through Sharp Multi-Wavelength Eyes, Malaga, Spain.

Laurent, P., Rodriguez, J., et al. (2011). Polarized Gamma-Ray Emission from the Galactic Black Hole Cygnus X-1. *Science*, 332:438 , arXiv:1104.4282.

Lei, F., Dean, A. J., et al. (1997). Compton polarimetry in gamma-ray astronomy. *Space Science Reviews*, 82(3):309–388.

Longair, M. S. (1994). *High Energy Astrophysic*, volume 1. Cambridge University Press, second edition.

Lyne, A., Hobbs, G., Kramer, M., et al. (2010). Switched Magnetospheric Regulation of Pulsar Spin-Down. *Science*, 329:408, arXiv:1006.5184.

Maestro, P. (2015). Cosmic rays: direct measurements. In Borisov, A. S., Denisova, V. G., Guseva, Z. M., et al., editors, *34th International Cosmic Ray Conference (ICRC2015)*, volume 34 of *International Cosmic Ray Conference*, page 16.

Malkov, M. A. and Drury, L. O. (2001). Nonlinear theory of diffusive acceleration of particles by shock waves. *Reports on Progress in Physics*, 64:429–481.

Mannheim, K. (1993). The proton blazar. A&A, 269:67–76, arXiv:astro-ph/9302006.

Massaro, E., Maselli, A., Leto, C., et al. (2015). The 5th edition of the Roma-BZCAT. A short presentation. Ap&SS, 357:75, arXiv:1502.07755.

Massaro, F., Thompson, D. J., and Ferrara, E. C. (2016). The extragalactic gamma-ray sky in the Fermi era. A&A Rev., 24:2, arXiv:1510.07660.

Mattox, J. R., Bertsch, D. L., Chiang, J., et al. (1996). The Likelihood Analysis of EGRET Data. ApJ, 461:396.

Maximon, L. C. and Olsen, H. (1962). Measurement of linear photon polarization by pair production. *Phys. Rev.*, 126:310–319 .

May, M. M. (1951). On the Polarization of High Energy Bremsstrahlung and of High Energy Pairs. *Physical Review*, 84:265–270.

Mayer, M., Buehler, R., Hays, E., et al. (2013). Rapid Gamma-Ray Flux Variability during the 2013 March Crab Nebula Flare. ApJ, 775:L37, arXiv:1308.6698.

McGlynn, S., Clark, D. J., et al. (2007). Polarisation studies of the prompt gamma-ray emission from GRB 041219a using the spectrometer aboard INTEGRAL. A&A, 466:895–904 , arXiv:astro-ph/0702738.

McMaster, W. H. (1961). Matrix representation of polarization. *Rev. Mod. Phys.*, 33:8–28.

Meegan, C., Lichti, G., Bhat, P. N., et al. (2009). The Fermi Gamma-ray Burst Monitor. ApJ, 702:791–804, arXiv:0908.0450.

Meegan, C. A., Fishman, G. J., Wilson, R. B., et al. (1992). Spatial distribution of gamma-ray bursts observed by BATSE. Nature, 355:143–145.

Michelson, P. F., Atwood, W. B., and Ritz, S. (2010). Fermi Gamma-ray Space Telescope: high-energy results from the first year. *Reports on Progress in Physics*, 73(7):074901, arXiv:1011.0213.

Moiseev, A. A. et al. (2015). Compton-Pair Production Space Telescope (ComPair) for MeV Gamma-ray Astronomy. *ArXiv e-prints*, arXiv:1508.07349.

Morháč, M., Kliman, J., Matoušek, V., et al. (2000). Identification of peaks in multidimensional coincidence γ-ray spectra. *Nuclear Instruments and Methods in Physics Research Section A: Accelerators, Spectrometers, Detectors and Associated Equipment*, 443(1):108 – 125.

Mücke, A., Rachen, J. P., Engel, R., et al. (1999). Photohadronic Processes in Astrophysical Environments. PASA, 16:160–166, arXiv:astro-ph/9808279.

Neronov, A., Malyshev, D., Chernyakova, M., et al. (2012). Search for variable gamma-ray emission from the Galactic plane in the Fermi data. A&A, 543:L9, arXiv:1207.1991.

Nesetril, J., Milková, E., and Nesetrilová, H. (2001). Otakar boruvka on minimum spanning tree problem translation of both the 1926 papers, comments, history. *Discrete Mathematics*, 233(1-3):3–36.

Newman, M. E. J. (2005). Power laws, Pareto distributions and Zipf's law. *Power laws, Pareto distributions and Zipf's law. Contemporary physics*, 46(5):323–351, arXiv:0412004.

Nolan, P. L., Abdo, A. A., Ackermann, M., et al. (2012). Fermi Large Area Telescope Second Source Catalog. *ApJS*, 199(2):31.

Ohm, S. (2016). Starburst galaxies as seen by gamma-ray telescopes. *Comptes Rendus Physique*, 17:585–593, arXiv:1601.06386.

Oka, M., Phan, T.-D., Krucker, S., et al. (2010). Electron Acceleration by Multi-Island Coalescence. ApJ, 714:915–926, arXiv:1004.1154.

Pacini, D. (2010). Penetrating Radiation at the Surface of and in Water. *ArXiv e-prints*, arXiv:1002.1810.

Pacini, F. (1967). Energy Emission from a Neutron Star. Nature, 216:567–568.

Paggi, A., Cavaliere, A., Vittorini, V., et al. (2011). Flaring Patterns in Blazars. ApJ, 736:128, arXiv:1105.2887.

Paliya, V. S., Sahayanathan, S., Parker, M. L., et al. (2014). The Peculiar Radio-loud Narrow Line Seyfert 1 Galaxy 1H 0323+342. ApJ, 789:143, arXiv:1405.0715.

Papitto, A. and Torres, D. F. (2015). A Propeller Model for the Sub-luminous State of the Transitional Millisecond Pulsar PSR J1023+0038. ApJ, 807:33, arXiv:1504.05029.

Papitto, A., Torres, D. F., and Li, J. (2014). A propeller scenario for the gamma-ray emission of low-mass X-ray binaries: the case of XSS J12270-4859. MNRAS, 438:2105–2116, arXiv:1312.0456.

Parker, E. N. (1957). Sweet's Mechanism for Merging Magnetic Fields in Conducting Fluids. J. Geophys. Res., 62:509–520.

Patrignani, C. et al. (2016). Review of Particle Physics. *Chin. Phys.*, C40(10):100001.

Petrov, L., Hirota, T., Honma, M., et al. (2007). VERA 22 GHz Fringe Search Survey. AJ, 133:2487–2494, arXiv:astro-ph/0609557.

Petschek, H. E. (1964). Magnetic Field Annihilation. *NASA Special Publication*, 50:425.

Piron, F. (2016). Gamma-ray bursts at high and very high energies. *Comptes Rendus Physique*, 17:617–631, arXiv:1512.04241.

Pittori, C. and Tavani, M. (2004). Scientific Goals and Instrument Performance of the Gamma-Ray Imaging Detector AGILE. *Nuclear Physics B - Proceedings Supplements*, 134:72 – 74. Proceedings of the Second International Conference on Particle and Fundamental Physics in Space (SpacePart '03).

Pittori, C., Verrecchia, F., Chen, A. W., et al. (2009). First AGILE catalog of high-confidence gamma-ray sources. A&A, 506:1563–1574, arXiv:0902.2959.

Rachen, J. P. (2000). Hadronic blazar models and correlated X-ray/TeV flares. In Dingus, B. L., Salamon, M. H., and Kieda, D. B., editors, *American Institute of Physics Conference Series*, volume 515 of *American Institute of Physics Conference Series*, pages 41–52.

Rani, B., Lott, B., Krichbaum, T. P., et al. (2013). Constraining the location of rapid gamma-ray flares in the flat spectrum radio quasar 3C 273. A&A, 557:A71, arXiv:1307.0854.

Reimer, A. (2012). On the physics of hadronic blazar emission models. *J. Phys. Conf. Ser.*, 355:012011.

Roberts, M. S. E., Romani, R. W., and Kawai, N. (2001). The ASCA Catalog of Potential X-Ray Counterparts of GEV Sources. ApJS, 133:451–465, arXiv:astro-ph/0012304.

Roe, B. P., Yang, H.-J., Zhu, J., et al. (2005). Boosted decision trees as an alternative to artificial neural networks for particle identification. *Nuclear Instruments and Methods in Physics Research A*, 543:577–584, arXiv:physics/0408124.

Rosenbaum, B. (1950). Nuclear recoil momentum in pair production. *Phys. Rev.*, 78:628–628.

Rutherford, E. (2012). The scattering of α and β particles by matter and the structure of the atom. *Philosophical Magazine*, 92(4):379–398.

Rybicki, G. B. and Lightman, A. P. (1979). *Radiative processes in astrophysics*.

Schönfelder, V., Bennett, K., Collmar, W., et al. (1992). *The GRO - COMPTEL Mission: Instrument Description and Scientific Objectives*, pages 185–200. Springer US, Boston, MA.

Selig, M., Vacca, V., Oppermann, N., et al. (2015). The denoised, deconvolved, and decomposed Fermi γ-ray sky. An application of the D^{3}PO algorithm. A&A, 581:A126, arXiv:1410.4562.

Shimrat, M. (1962). Algorithm 112: Position of point relative to polygon. *Commun. ACM*, 5(8):434–.

Sironi, L., Keshet, U., and Lemoine, M. (2015). Relativistic Shocks: Particle Acceleration and Magnetization. Space Sci. Rev., 191:519–544, arXiv:1506.02034.

Sironi, L. and Spitkovsky, A. (2014). Relativistic Reconnection: An Efficient Source of Non-thermal Particles. ApJ, 783:L21, arXiv:1401.5471.

Snik, F. and Keller, C. U. (2013). *Astronomical Polarimetry: Polarized Views of Stars and Planets*, pages 175–221. Springer Netherlands, Dordrecht.

Stappers, B. W., Archibald, A. M., Hessels, J. W. T., et al. (2014). A State Change in the Missing Link Binary Pulsar System PSR J1023+0038. ApJ, 790:39, arXiv:1311.7506.

Stroh, M. C. and Falcone, A. D. (2013). Swift X-Ray Telescope Monitoring of Fermi-LAT Gamma-Ray Sources of Interest. ApJS, 207:28, arXiv:1305.4949.

Su, M., Slatyer, T. R., and Finkbeiner, D. P. (2010). Giant Gamma-ray Bubbles from Fermi-LAT: Active Galactic Nucleus Activity or Bipolar Galactic Wind? ApJ, 724:1044–1082, arXiv:1005.5480.

Su, Y., Veronig, A. M., Holman, G. D., et al. (2013). Imaging coronal magnetic-field reconnection in a solar flare. *Nature Phys.*, 9:489, arXiv:1307.4527.

Sweet, P. A. (1958). The Neutral Point Theory of Solar Flares. In Lehnert, B., editor, *Electromagnetic Phenomena in Cosmical Physics*, volume 6 of *IAU Symposium*, page 123.

Takata, J., Li, K. L., Leung, G. C. K., et al. (2014). MULTI-WAVELENGTH EMISSIONS FROM THE MILLISECOND PULSAR BINARY PSR J1023+0038 DURING AN ACCRETION ACTIVE STATE. *ApJ*, 785(2):131.

Tam, P. H. T., Huang, R. H. H., Takata, J., et al. (2011). Discovery of GeV γ-ray Emission from PSR B1259-63/LS 2883. ApJ, 736:L10, arXiv:1103.3129.

Tanaka, Y. T., Doi, A., Inoue, Y., et al. (2015). Six Years of Fermi-LAT and Multi-Wavelength Monitoring of the Broad-Line Radio Galaxy 3c 120: Jet Dissipation At Sub-Parsec Scales from the Central Engine. ApJ, 799:L18, arXiv:1412.3903.

Tavani, M., Bulgarelli, A., Vittorini, V., et al. (2011). Discovery of Powerful Gamma-Ray Flares from the Crab Nebula. *Science*, 331:736, arXiv:1101.2311.

Thompson, D. J., Fichtel, C. E., Kniffen, D. A., et al. (1975). SAS-2 high-energy gamma-ray observations of the VELA pulsar. ApJ, 200:L79–L82.

Tluczykont, M., Bernardini, E., Satalecka, K., et al. (2010). Long-term lightcurves from combined unified very high energy γ-ray data. *Astronomy and Astrophysics*, 524:A48, arXiv:1010.5659.

Trippe, S. (2014). [Review] Polarization and Polarimetry. *Journal of Korean Astronomical Society*, 47:15–39 , arXiv:1401.1911.

Urry, C. M. and Padovani, P. (1995). Unified Schemes for Radio-Loud Active Galactic Nuclei. *Pasp*, 107:803, arXiv:9506063.

Uttley, P., McHardy, I. M., and Vaughan, S. (2005). Non-linear X-ray variability in X-ray binaries and active galaxies. *Monthly Notices of the Royal Astronomical Society*, 359:345–362, arXiv:arXiv:astro-ph/0502112.

Vaughan, S., Edelson, R., Warwick, R. S., et al. (2003). On characterizing the variability properties of X-ray light curves from active galaxies. *Monthly Notices of the Royal Astronomical Society*, 345:1271–1284, arXiv:arXiv:astro-ph/0307420.

Verrecchia, F., Pittori, C., Chen, A. W., et al. (2013). An updated list of AGILE bright γ-ray sources and their variability in pointing mode. A&A, 558:A137, arXiv:1310.4029.

Verzi, V. (2016). Cosmic rays: air showers from low to high energies. *PoS*, ICRC2015:015.

Weisskopf, M. C., Cohen, G. G., et al. (1976). Measurement of the X-ray polarization of the Crab Nebula. ApJ, 208:L125–L128 .

Weisskopf, M. C., Elsner, R. F., and O'Dell, S. L. (2010). On understanding the figures of merit for detection and measurement of x-ray polarization. *Proc. SPIE Int. Soc. Opt. Eng.*, 7732:0E, arXiv:1006.3711.

Weisskopf, M. C., Silver, E. H., et al. (1978). A precision measurement of the X-ray polarization of the Crab Nebula without pulsar contamination. ApJ, 220:L117–L121 .

Weisskopf, M. C., Tananbaum, H. D., Van Speybroeck, L. P., et al. (2000). Chandra X-ray Observatory (CXO): overview. In Truemper, J. E. and Aschenbach, B., editors, *X-Ray Optics, Instruments, and Missions III*, volume 4012 of Proc. SPIE, pages 2–16.

Wenger, M., Ochsenbein, F., Egret, D., et al. (2000). The SIMBAD astronomical database. The CDS reference database for astronomical objects. A&AS, 143:9–22, arXiv:astro-ph/0002110.

Werner, M. W., Roellig, T. L., Low, F. J., et al. (2004). The Spitzer Space Telescope Mission. ApJS, 154:1–9, arXiv:astro-ph/0406223.

Westfold, K. C. (1959). The Polarization of Synchrotron Radiation. ApJ, 130:241.

Wilks, S. S. (1938). The large-sample distribution of the likelihood ratio for testing composite hypotheses. *Ann. Math. Statist.*, 9(1):60–62.

Williamson, K. E., Jorstad, S. G., Marscher, A. P., et al. (2014). Comprehensive Monitoring of Gamma-Ray Bright Blazars. I. Statistical Study of Optical, X-Ray, and Gamma-Ray Spectral Slopes. ApJ, 789:135, arXiv:1406.2719.

Winkler, C., Courvoisier, T. J.-L., Di Cocco, G., et al. (2003). The INTEGRAL mission. A&A, 411:L1–L6.

Yang, H.-J., Roe, B. P., and Zhu, J. (2005). Studies of boosted decision trees for MiniBooNE particle identification. *Nuclear Instruments and Methods in Physics Research A*, 555:370–385, arXiv:physics/0508045.

Zabalza, V. (2015). naima: a Python package for inference of relativistic particle energy distributions from observed nonthermal spectra. *ArXiv e-prints*, arXiv:1509.03319.

Zatsepin, G. T. and Kuz'min, V. A. (1966). Upper Limit of the Spectrum of Cosmic Rays. *Soviet Journal of Experimental and Theoretical Physics Letters*, 4:78.

Zhang, H. and Böttcher, M. (2013). X-Ray and Gamma-Ray Polarization in Leptonic and Hadronic Jet Models of Blazars. ApJ, 774:18 , arXiv:1307.4187.

Zweibel, E. G. and Yamada, M. (2009). Magnetic Reconnection in Astrophysical and Laboratory Plasmas. ARA&A, 47:291–332.

Acknowledgment

There are many people that have supported me, in a way or another, during this PhD. Making a complete list of them is a daunting task. As always in difficult situations, this quote by the King of Hearts in Alice's Adventures in Wonderland comes to my mind:

"Begin at the beginning," the King said, very gravely, "and go on till you come to the end: then stop."

So, to begin from the beginning. I would like to thank the following people:

- my supervisor Rolf, for being such a knowledgeable scientist, intrepid learner, wonderful boss, awesome Human Being, and real friend. He guided me throughout my PhD, and taught me more than I can realize now. I wish him all the luck for his future plans, scientific (be a spaceman Rolf!) and not.
- Gernot, for his teaching and support since my early years at Desy. After all, you cannot write your PhD thesis without having first completed your master.
- the other members of my committee: Thomas Lohse, Jamie Holder, Elisa Bernardini, and Burkhard Priemer. Reviewing a PhD thesis takes time and effort. I am grateful to them for that.
- all the gentle, knowledgeable, and helpful souls who have reviewed big and small parts of this thesis: Moritz, Cosimo, Markus, Anna, Stefan O., Nora, Carmelo, and James (that was a bet). Elisa earned my eternal gratitude for the scrupulous proof-reading of the entire manuscript.
- fellow PhD students (some of them already doctores rerum naturalium): Andrea, Cosimo, Federica, Galo, Henrike, Maria, Matthias, Moritz, Nathan, and Nora (the order is alphabetical), for the discussions, the help, and the fun. Maria and Moritz also showed me the bureaucratic steps needed to hand in the thesis. Moreover, Moritz helped me with the Zusammenfassung and the bibliography style. Maria, on the other hand, provided me with a LaTeX template for this document, which hopefully complies to the required standards.
- il Porelli, storico (e stoico) compagno di ufficio sin dal primissimo giorno, e Cosimo e la Federica, che mi sono venuti a prendere con i biscotti.
- Markus P. Lindhout, my kindred spirit.
- Peter and Simon, with whom I shared many (never enough!) hours making really cool music together.
- The ranking algorithms of Youtube, for the awesome music they have suggested me.

Un ringraziamento speciale va a i miei genitori e la mia sorella Alessandra, per il supporto, l'incoraggiamento e l'educazione che mi hanno dato e che mi danno, senza i qual probabilmente non potrei scrivere qui queste parole. Vorrei anche ringraziare di cuore la mia nonna Elisa, che con pazienza e amore (ma non senza rigore), mi insegnò l'algebra e la geometria. Infine ringrazio la Giada e la Mia, che mi hanno cambiato la vita e a cui questa tesi è giustamente dedicata.

And here I stop, as the King advised.

Selbständigkeitserklärung

Ich erkläre, dass ich die Dissertation selbständig und nur unter Verwendung der von mir gemäß §7 Abs. 3 der Promotionsordnung der Mathematisch-Naturwissenschaftlichen Fakultät, veröffentlicht im Amtlichen Mitteilungsblatt der Humboldt-Universität zu Berlin Nr. 126/2014 am 18.11.2014 angegebenen Hilfsmittel angefertigt habe.

Berlin, den 15. Juni 2017.

Matteo Giomi